Ultracold fermions in periodically-driven superlattices

Dissertation
zur
Erlangung des Doktorgrades (Dr. rer. nat.)
der
Mathematisch-Naturwissenschaftlichen Fakultät
der
Rheinischen Friedrich-Wilhelms-Universität Bonn

vorgelegt von
Nick Klemmer
aus
Heidelberg

Bonn 2024

Angefertigt mit Genehmigung der Mathematisch-Naturwissenschaftlichen Fakultät der Rheinischen Friedrich-Wilhelms-Universität Bonn

Gutachter / Betreuer: Prof. Dr. Michael Köhl
Gutachter Prof. Dr. Stefan Linden

Tag der Promotion: **14.01.2025**
Erscheinungsjahr: **2025**

Abstract

This thesis presents quantum simulation of strongly-correlated systems beyond standard Hubbard models, using ultracold fermionic potassium atoms in both static and periodically-driven optical superlattices. For this study, we utilize a three-dimensional optical lattice setup, controlling particle interactions via magnetic Feshbach resonances and tunneling between lattice sites through optical lattice intensity. High-resolution absorption imaging combined with radio-frequency spectroscopy distinguishes between singly and doubly occupied sites.

To enhance our systems capabilities beyond the standard Hubbard model, we extend the apparatus with an in-plane optical superlattice, creating a bi-chromatic structure by superposition of two optical lattices with commensurate lattice spacings. Using a phase locked loop with an environmental feed forward, we create an excellent phase stability of the superlattice exceeding 3 mrad. This precision allows us to explore both static and periodically-driven one-dimensional tight-binding models with strong interactions.

We characterize the static superlattice through radio-frequency spectroscopy and Rabi oscillations, and validate the experimental data against theoretical calculations. In a tilted superlattice configuration, we successfully prepare and detect repulsively bound atom pairs, representing a highly excited eigenstate of the system.

Furthermore, we demonstrate control over pair tunneling dynamics in a double-well potential using Floquet engineering, employing a low-noise periodic modulation of the optical superlattice tilt. Using an adiabatic band mapping technique, we directly observe the tunneling dynamics in the driven superlattice. We realize dynamic localization in quarter-filled wells and density-assisted tunneling up to the third harmonic order in half-filled wells. We observe a crossover from density-assited tunneling to dominant pair tunneling by tuning the effective interactions. Remarkably, the pair tunneling is not only enhanced relative to the suppressed single-particle tunneling but also exceeds the superexchange rate of a static double-well by more than a factor of two.

This opens the possibility to study many-body systems with dominant pair tunneling, that extend beyond the standard Hubbard model.

Acknowledgements

Over the course of this four-year PhD project, many people have supported me in many ways and I would like to use this section to acknowledge their contributions.

First of all, I would like to thank my supervisor Michael Köhl. Thank you for inspiring me to study ultracold atomic gases with your insightful lectures and giving me the opportunity to work in your lab. You have supported me in many ways throughout this project, and I am especially thankful for many helpful discussions and your always inspiring intuitive understanding of physics.

I would like to thank the people who have worked alongside me on our experiment, without whom none of this would have been possible: Janek, Valentin and Andrea. You have created a supporting and cooperative environment, where no one takes themselves too seriously, which I have enjoyed being a part of. Thank you, Janek, for our trustful relationship, especially in times of dire work-space and personal situations. Your cheeky spirit has brought a lot of joy to this work and I greatly appreciate that you always took the time to give me coding advice. Also, I now have a fond memory of the Transformers soundtrack, which is something I surely would have never expected! Thank you, Valentin, for joining our experiment with your enthusiasm and carefree attitude at such a crucial time. It was inspiring to witness how quickly you have helped us in the lab, especially with your understanding for the theoretical models behind our work. Andrea, your curiosity for physics is infectious, and I have drawn a lot of inspiration and motivation from our discussions and shared need for an intuitive picture for everything. Your have often helped us to keep track of the greater goals, when we got lost in the details, which I greatly appreciate.

I would like to thank the former members of the Fermi experiment, Nicola, Marcel, Jeffrey and Jens, who have taught me how to operate –and especially debug– this experiment. Thank you, Nicola, for your guidance and supervision of my Bachelor and Master thesis, which has motivated me to start this PhD project.

I would like to thank the members of the AQO group for nice discussions over a cup of coffee and our shared lunch breaks: Felix, Pascal, Jonas, Steffen, Ralf, Martin, Moritz B., Moritz S., and Andreas. In particular, I would like to thank Thorsten and Santhosh, for proofreading parts of this thesis. Thank you, Tobias, for sharing my love for futsal and your support when lunch discussions went a bit crazy. A special thanks to Daniel, for nerves of steel on the snowy roads of Utah and a very memorable trip.

Thank you Akos, for always helping us with any electronics problem in oftentimes truly creative ways. I will always remember how we have assembled the insulation for the LBO crystal by using a self-made soldering machine.

I greatly appreciate the support on the theory side from Corinna and Ameneh, who have initiated and supported our investigation of periodically-driven double wells.

Finally, I would like to thank my family for always supporting me and believing in me. You have

given me the confidence to tackle and finish this truly challenging and sometimes overwhelming task and seemed always interested when I have talked about egg cartons. Thank you, Marlene, for being an incredibly supportive and understanding partner throughout the most difficult times of this project. Especially during the writing of this thesis you have supported me tremendously, for which I am truly grateful.

Contents

CHAPTER 1

Introduction

The observation of high-T_C superconductivity in cuprates in the year 1986 [1] has sparked an enduring research interest for now almost 40 years. The observed critical temperatures of up to 147 K were so much larger than that of the known conventional superconductors $\sim$ 30 K, that the underlying mechanism was clearly a different one [2]. And indeed, while conventional superconductivity in the Bardeen-Cooper-Schrieffer (BCS) theory [3] is based on weakly attractive interactions between electrons enabled by cooper pairing, the high T_C superconductivity appears in a system of large repulsive interactions and strong electron localization. This so-called strongly correlated regime –where phenomena cannot be explained by single-particle behavior alone, but are inherently many-body– makes the description challenging and contributes to the fact that a comprehensive understanding of the processes behind the observed high-T_C superconductivity is still missing.

Cuprates serve as an exceptional example of the unconventional nature of strongly correlated systems [4]. These ceramics consist of two-dimensional layers of copper oxides as its parent compound and various constituents that introduce charge doping to the layer. Contrary to what one would expect from a system at half-filling in a single-particle description, cuprates do not exhibit a metallic state. Instead, they form an antiferromagnetic Mott insulating state, where strong electron interactions suppress all dynamics. Upon doping the system with electron holes, a superconducting phase with d-wave symmetry emerges, though the exact pairing mechanism remains unknown. The microscopic processes driving these novel phases are naturally of great interest, but isolating them within the complex crystalline structure of real materials remains challenging.

In 1963, J. Hubbard proposed a conceptually simple model to describe strongly-correlated electrons in solids [5]. In this tight-binding model, the kinetic energy of the electrons is described by tunneling events between adjacent lattice sites, and they interact with each other when occupying the same site. Despite the model's simplicity, the interplay of these processes provides valuable insight into the microscopic processes behind the novel phases of strongly-correlated matter, like the cuprates. For instance, the Hubbard model predicts an insulating phase at half-filling with large repulsive interactions, which for low enough temperatures exhibits anti-ferromagnetic order driven implicitly through a second-order tunneling process known as superexchange. Away from half filling, Scalapino et al. predicted that the Hubbard model features a d-wave superconducting phase in three dimensions [6]. These findings suggest that the solution of the Hubbard model could potentially explain the high-T_C superconductivity observed in cuprates [7]. Unfortunately, theoretical investigations of the Hubbard model are notoriously difficult, as the Hilbert space grows exponentially with the number

of particles. Exact solutions are only available in very specific cases, like one-dimensional systems, and numerical calculations require assumptions from which the actual model is extrapolated [7, 8]. Therefore, even 60 years after its initial formulation, the exact phase diagram of the two-dimensional Hubbard model, particularly for doped systems, remains a topic of ongoing debate.

Quantum simulation offers a complementary approach to the theoretical study of strongly correlated systems like the Hubbard model. This concept was first envisioned by Feynman in 1982 [9], when he suggested: "Let the computer itself be built of quantum mechanical elements [...]." He proposed the idea of a "universal" (or digital) machine capable of simulating any quantum mechanical system [10]. However, a more specialized machine –an analogue quantum simulator– can be used to study specific systems. This analogue quantum simulator [11] is a quantum-mechanical emulation of a model system, that is governed by the same Hamiltonian, while being built of different constituents. It provides excellent control over system parameters, and excels at giving qualitative insights into debated topics.

Ultracold atomic gases in optical lattices present a highly suitable platform for analogue quantum computation of strongly-correlated systems [12–14]. In this setup, a periodic lattice structure is created by interfering laser beams, which is then filled with a quantum-degenerate atomic gas, mimicking the behavior of electrons in solids. The platform enables a clean emulation of various model Hamiltonians with exceptional control over the system parameters, like the lattice depths and interaction strength. Furthermore, the timescales of the atoms, in the kHz range, and the lengths scales, in the µm range, are easily experimentally accessible compared to those in real materials. However, to realize a quantum-mechanical system, the atomic cloud must be cooled to quantum degeneracy –typically around 100 nK– where the de Broglie wavelength of the atoms exceeds the inter-particle distance, causing the system's properties to be governed by quantum statistics.

The journey from a neutral atom gas at room temperature to quantum degeneracy had its breakthrough with the discovery of laser cooling, for which the Nobel Prize was awarded in 1997 [15–17]. Shortly thereafter, the development of evaporative cooling brought the onset of quantum degeneracy with the observation of Bose-Einstein condensation [18, 19] and Fermi-degeneracy [20]. Finally, in 2005, the realization of a quantum degenerate Fermi gas in an optical lattice [21] established the groundwork to emulate the Hubbard model. Since then, quantum simulations of the Hubbard model with ultracold atomic gases have achieved several groundbreaking results, from the observation of a Mott insulator in 2008 [22, 23] to long-range antiferromagnetic correlations [24, 25] and, recently an antiferromagnetic phase transition [26]. Moreover, quantum gas microscopy [27] has recently expanded the experimental control to the level of individual atoms, providing direct access to correlations between atoms that are otherwise elusive. Despite these technological advances, the lowest temperatures achieved in current experiments are around $k_B T/t = (0.25 \pm 0.02)$ [26, 28], which remains significantly above the proposed critical temperature for the superconducting phase, estimated at approximately $k_B T/t \sim 0.05$ [7].

Extensions to the Hubbard model are often necessary to emulate the physics of real materials, as evidenced by the absence of a superconducting phase in the pure two-dimensional Hubbard model [29]. For example, density-assisted tunneling is required to accurately map the three orbital cuprates onto a single band model [30]. The study of non-standard Hubbard models, that incorporate processes beyond conventional nearest-neighbor tunneling and on-site interactions, has improved our understanding of the physics in real materials. For instance, the creation of a Bilayer Hubbard model, by coupling two two-dimensional Hubbard layers, showed the competition of magnetic order between and within the coupled layers [31].

In this work, we have developed a phase-stable in-plane superlattice to explore physics beyond the standard Hubbard model. A superlattice, typically a bi-chromatic structure with two characteristic tunneling amplitudes, has been used to observe a wide range of phenomena, from superexchange dynamics [32, 33], to quantized transport in topological models [34, 35], and cooling mechanisms for bosons in a tilted superlattice [36]. Moreover, Kantian et al. [37] proposed using superlattices to create a superconducting condensate of η-pairs [38] in an optical lattice. However, to observe novel phenomena in optical superlattices, sufficient phase stability is necessary to prevent excessive lattice heating. We present the setup and calibration of a superlattice with excellent phase stability, exceeding 3 mrad, which is comparable to the best reported realizations [39, 40].

A periodic drive of the superlattice can fundamentally alter the system's properties. Under fast modulation, effective systems with properties vastly different from their static counterpart can be realized, a concept known as Floquet engineering [41]. Floquet engineering has been used to invert the sign of magnetic correlations [42], to study artificial gauge fields in optical lattices [43, 44], and famously, to achieve dynamic localization [45, 46], where single-particle tunneling is completely suppressed.

In this work, we demonstrate experimental control over pair tunneling in the double well, which forms the unit cell of the superlattice, using periodic modulation in a strongly interacting system. For a drive that is resonant to the interaction energy, we realize density-assisted tunneling in the absence of single-particle tunneling. Moreover, we show this behavior for various harmonic orders of the resonance condition and validate that the effective dynamic timescales are governed by Bessel functions of different orders. We then introduce effective interactions to the system by detuning the driving frequency. This allows us to observe a Floquet engineered crossover from density-assisted tunneling to dominant pair tunneling, thereby realizing a system where dynamics are restricted to atom-pairs while single particles remain localized over a wide range of effective interactions. Remarkably, the effective pair-tunneling rate is enhanced not only compared to the suppressed single particle tunneling, but also exceeds the static superexchange.

This work represents a first step towards the realization of many-body systems with dominant pair tunneling, such as the Penson-Kolb Hubbard model [47], which exhibits η-pairing superconductivity [48, 49]. In the future, observing and characterizing these exotic superconducting phases may provide insights into the mystery of high T_C superconductivity in cuprates.

Thesis Structure

In this work, I present an investigation of ultracold fermionic potassium atoms in both periodically-driven and static superlattices. To achieve this, we have extended our three-dimensional optical lattice setup by incorporating an in-plane superlattice. The primary focus of this work is the study of interacting fermions in periodically-driven double wells and the necessary setup and calibration of the static superlattice to enable this investigation. The contents of this thesis are summarized briefly below. Each chapter begins with a short introduction to the topic, followed by an outline of the chapter, so this overview will remain brief.

In Chapter 2, we discuss the theoretical framework behind our experimental quantum simulator. This includes the concept of optical lattices and the experimental control over interactions via magnetic Feshbach resonances. We also present the newly adapted tight-binding theory for interacting fermions in the superlattice.

Chapter 3 provides a brief summary of the experimental apparatus, most of which was assembled

before this work. We place particular focus on the new implementation of the phase-stable superlattice and the realization of suitable experimental observables.

In Chapter 4, we discuss experiments conducted in the one-dimensional static superlattice. We calibrate the tight-binding parameters of the superlattice in an array of isolated double wells. Additionally, we demonstrate the excellent phase stability of our superlattice and discuss the preparation and detection of repulsively-bound pairs in the double well.

In Chapter 5, we explore periodically driven double wells from both theoretical and experimental standpoints. We present experimental control over effective single-particle tunneling and report density-assisted tunneling for a resonant drive of various harmonic orders.

In Chapter 6, we examine the impact of effective interactions on the periodically driven system. We discuss a Floquet-engineered crossover from density-assisted to dominant pair tunneling and investigate the enhancement of pair tunneling compared to the static counterpart.

Finally, Chapter 7 provides a conclusion and outlook for future work.

This work was conducted on an experimental apparatus that has been developed by a series of PhD students over the last decades. The scientific investigations presented in this thesis were carried out by the team of Valentin Jonas, Janek Fleper, and me. In this thesis, we newly implemented and characterized an in-plane superlattice which was utilized to conduct the scientific investigations of this work. I made the main contributions to the experimental and theoretical study of interacting fermions in both static and periodically-modulated double wells, which are detailed in Chapters 4, 5 and 6. My colleague Valentin Jonas developed the scheme to periodically modulate the superlattice by programming an arbitrary waveform generator, as detailed in Chapter 3, and adapted the theory to describe driven double wells in Chapter 5. Janek Fleper developed the environmental feed-forward system to stabilize the superlattice phase, as summarized in Chapter 3, and led the programming efforts necessary to operate and evaluate an experiment of this scale. Finally, the LaTeXtemplate for this thesis was provided by Prof. Dr. Ian Brock [50].

Publications

During this work I have co-authored the following paper:

[51] **N. Klemmer***, J. Fleper*, V. Jonas, A. Sheikhan, C. Kollath, M. Köhl and A. Bergschneider, "Floquet-driven crossover from density-assisted tunneling to enhanced pair tunneling" (Currently under review at Physical Review Letters)

*These authors contributed equally

CHAPTER 2

Ultracold atoms in optical lattices

Ultracold atomic atoms in optical lattices present an exceptional platform for simulating strongly correlated matter [13, 27, 52]. In this context, neutral atoms confined in the periodic potential of an optical lattice mimic the behavior of electrons in the crystalline structure of a solid. This emulation effectively captures the quantum mechanical statistics of the system, provided the atoms are sufficiently cold such that their de Broglie wavelength exceeds the inter-particle distance. Furthermore, this platform offers control over the lattice geometries and dimensions as well as the interaction, via magnetic Feshbach resonances [53]. The experimental observables are readily accessible as the lattice spacing typically falls within in the µm range and the timescales are in the kHz regime. This setup creates a scalable and clean emulation of various quantum mechanical models, including the prominent Fermi-Hubbard model.

The Hubbard model [7, 8] is arguably conceptually the simplest model to describe strongly-correlated electrons in solids. In this model, electrons express their kinetic energy through tunneling events between neighboring lattice sites, interacting only if they occupy the same site (cf. figure 2.1 a). The intricate interplay between the tunneling energy t, the interaction energy U, and the Pauli principle governing fermions of the same spin gives rise to a rich phase diagram (cf. figure 2.1 b and the caption below). Most of the phase diagram at half filling, where each lattice site is on average filled by one particle, is well-established and has been successfully observed. For example, cold-atom experiments have realized the Mott insulating phase [22, 23] and observed antiferromagnetic spin order [24–26]. However, the phase diagram for doped systems remains a topic of ongoing debate [14], and the existence of a superconducting phase was recently questioned [29].

Non-standard Hubbard models [54], which incorporate processes beyond the conventional tunneling t and on-site interaction U, offer a more nuanced description of the complex physics observed in real materials. To explore these richer physics, we have enhanced the emulation capabilities of our experimental apparatus by introducing an optical superlattice. A superlattice is formed by superimposing two optical lattices with commensurate lattice spacing, creating a bi-chromatic structure. This setup enables the study of topological systems [55], which led to the observation of quantized transport in Thouless pumps for both bosons [34, 56] and fermions [35]. Additionally, a superlattice serves as a versatile tool for implementing a periodic drive to the system [41], which allowed for the manipulation of magnetic correlations [42] and the study of gauge fields [57, 58].

In this chapter, we explore the theoretical framework behind our quantum simulator, with a particular emphasis on the optical superlattice. We discuss the band structure of the optical lattices and detail

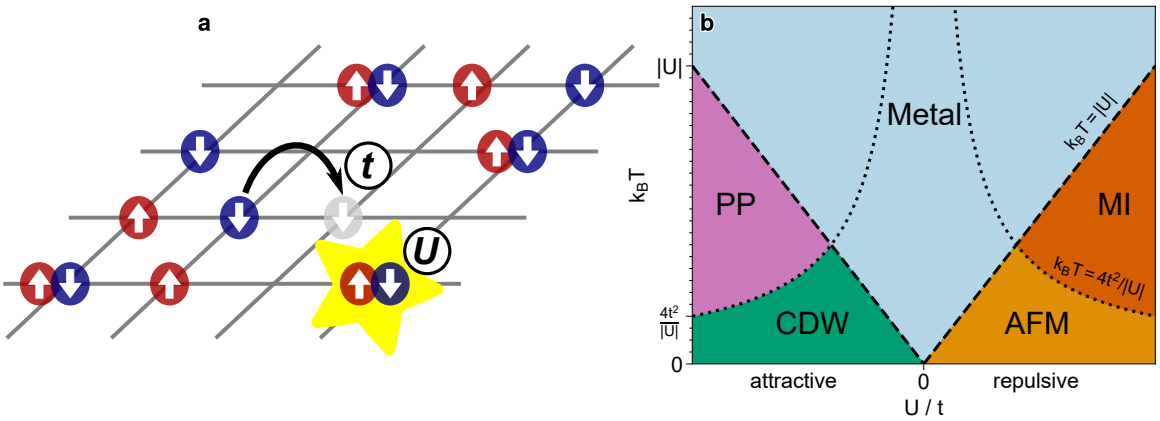

Figure 2.1: **The two-dimensional Hubbard model:** (a) In this description, strongly correlated matter is governed by the interplay of two fundamental processes: The nearest neighbor tunneling t and the on-site interaction U. (b) Schematic phase diagram of the two-dimensional Hubbard model at half-filling, for various temperatures k_BT and interaction strengths. The density sector contains three distinct phases that are separated by the approximate critical temperature $k_BT = |U|$ (dashed line): (i) The unordered metallic phase for weak attractive and repulsive interactions, (ii) the Mott insulator (MI) for large repulsive interactions, where double occupancies are suppressed and (iii) the preformed pairs (PP) for strong attractive interactions, where double occupancies are favoured. If the temperature is lowered below the superexchange energy scale $J = 4t^2/U$ (dotted line), an antiferromagnetic phase (AFM), with antiparallel spin alignment, arises for repulsive interactions. On the attractive site, this leads to a checkerboard structure of doublons and holes in the charge density wave (CDW). This subfigure was adapted from [13, 52].

the experimental techniques used to control it. Additionally, we introduce the interaction mechanism of neutral atoms, expressing how these interactions are manipulated by magnetic Feshbach resonances. Finally, we compute the many-body Hamiltonian of the superlattice in the tight-binding description, demonstrating how each parameter can be experimentally controlled. We specifically focus on the interplay between the interaction strength U and the underlying trapping potential.

2.1 Atom-light interaction

In this section, we discuss the interaction of an atom with a light field, focusing on how atoms can be trapped by light while minimizing heating.

There are two fundamental processes of atom-light interaction, which we first highlight qualitatively. One process is absorption (and consequential emission) of the light, which changes the momentum of the atom. The alternative is a refraction of light, where the atom acts as a dispersive material towards the photons. Intuitively, the detuning $\Delta = \omega - \omega_0$ of the photons with respect to the atomic resonance ω_0 plays a pivotal role in the interplay of these two processes: On resonance, the atoms absorb the photons and therefore the refractive process is irrelevant. For a large detuning, the absorption process is suppressed, the atoms become transparent and interact with the light in a refractive manner.

In the following, we briefly summarize the atom light interaction for a quantum mechanical two-level system as discussed in *Atomic Physics* by C.J.Foot [59]. An electric field $\boldsymbol{E} = E_0 \cos(\omega t - kx)\, \hat{e}_z$ propagating along the x-direction with a linear polarization along the z-axis induces a dipole moment

$\boldsymbol{d}$ at the atom

$$\boldsymbol{d} \equiv -e\boldsymbol{r} = \epsilon_0 \chi_\mathrm{a} E_0 \cos(\omega t - kx)\, \hat{e}_z \tag{2.1}$$

with the polarizability $\epsilon_0 \chi_\mathrm{a}$. The induced dipole then interacts with the electric field as

$$U = -\boldsymbol{d} \cdot \boldsymbol{E} = -\frac{1}{2}\epsilon_0 \chi_\mathrm{a} E_0^2. \tag{2.2}$$

The quantum-mechanical force $\bar{F}_x$, that the atoms experience from this interaction is then obtained by the differentiation of this interaction energy and the time average over many oscillations[59]. This force

$$\bar{F}_x = F_\mathrm{dipole} + F_\mathrm{scatt}. \tag{2.3}$$

separates into the dipole force and the scattering force. The dipole force

$$F_\mathrm{dipole} = -\frac{\hbar\Delta}{2} \frac{\Omega}{\Delta^2 + \Omega^2/2 + \Gamma^2/4} \frac{\delta\Omega}{\delta x}, \tag{2.4}$$

with the Rabi frequency Ω and the linewidth Γ that vanishes for resonant light $\Delta = 0$. On the other hand, the scattering force

$$F_\mathrm{scatt} = \hbar k \frac{\Gamma}{2} \frac{\Omega^2/2}{\Delta^2 + \Omega^2/2 + \Gamma^2/4} \tag{2.5}$$

decreases with the detuning $\sim 1/\Delta^2$.

Therefore, it is suitable to work in the far-detuned regime $\Delta \gg \Gamma, \Omega$ for trapping atoms in the dipole potential. In this regime, the dipole potential, or the *light shift* of the energy levels, is given as

$$U_\mathrm{dipole} = \pm\frac{\hbar\Gamma^2}{8I_\mathrm{sat}} \frac{I}{\Delta} \tag{2.6}$$

with the normalized intensity $I/I_\mathrm{sat} = 2\Omega^2/\Gamma^2$. Here, the positive sign corresponds to the ground state and the negative sign to the excited state. For red-detuning $\Delta < 0$, atoms in the ground state experience an attractive potential that changes with intensity. For blue-detuning $\Delta > 0$, the ground state is repelled from the high-intensity regions by a repulsive potential and vice versa for the excited state.

The scattering rate $R_\mathrm{scatt} = F_\mathrm{scatt}/\hbar k$ in the far-detuned regime approaches

$$R_\mathrm{scatt} = \frac{\Gamma^3}{8I_\mathrm{sat}} \frac{I}{\Delta^2}. \tag{2.7}$$

Relative to the dipole potential ($\sim 1/\Delta$), the scattering rate decreases faster with the detuning $\sim 1/\Delta^2$. Therefore, a large detuning allows for a trapping of atoms in the dipole potential, while the heating from scattered photons is suppressed.

Nonetheless, there is a remaining heating process in the dipole potential due to spontaneous emission from the excited state. In short, the trapped eigenstate of the two-level system in a driving field is a *dressed* state of the atomic level and the laser mode [60]. This dressed state has a small admixture of the excited state of the atom with a finite lifetime. In a radiative cascade, this excited state can decay

to trapped or untrapped states by spontaneous emission of a photon. This leads to fluctuations in the dipole force and is therefore a source of heating in the dipole potential.

2.2 Single-particle description of optical lattices

In this section, we explore how the dipole potential can be used to create optical lattices of different symmetries for neutral atoms. In particular, we discuss how the geometry of the interference changes the lattice spacing and how the superposition of bi-chromatic lasers leads to an optical superlattice. Moreover, we calculate the band structure of these periodic potentials using Bloch's theorem. Finally, we compare two different basis sets of the optical lattice: The delocalized Bloch functions and the localized Wannier functions.

A monochromatic optical lattice is created by interfering two laser beams of the same wavelength $\lambda = 2\pi/k$ and with wave vectors $\boldsymbol{k}$, $\boldsymbol{k}'$. The simplest interference geometry is given by two counter-propagating plane waves $\boldsymbol{k} = -\boldsymbol{k}'$ along the y-direction (cf. figure 2.2 a), which creates a periodic intensity pattern

$$I(y) = \frac{c\epsilon_0}{2}\left|E_0 e^{i(ky-\omega t)} + E_0 e^{-i(ky+\omega t)}\right|^2 = I_0 \cos^2(ky). \tag{2.8}$$

When the frequency of the lasers is far-detuned from the atomic resonances, this intensity pattern creates a periodic optical dipole potential (compare equation 2.6)

$$V_{\text{latt}}(y) = \pm V_0 \cos^2\left(\frac{\pi y}{a}\right), \tag{2.9}$$

with the lattice spacing $a = \lambda/2$ and the light shift amplitude V_0. The sign of V_{latt} is given by the detuning and creates either repulsive (blue detuned) or attractive (red detuned) potentials.

The spacing a of the optical lattice can be adjusted using a shallow-angle interference geometry (cf. figure 2.2 b). For an interference angle of 2γ, the interference also creates an optical potential according to equation 2.9, but the periodicity of the lattice is given by

$$a = \frac{\lambda_{\text{eff}}}{2} = \frac{\lambda}{2\sin(\gamma)}. \tag{2.10}$$

The obtained lattice spacing is minimal for counter-propagating beams and increases with finite interference angles.

An optical superlattice is created by superimposing two optical lattices with commensurate wavelengths $\lambda_l = m\lambda_s$ (cf. figure 2.2 c), which we denote the *long* and *short* wavelength respectively. In our realization, the superlattice potential is created by a blue-detuned short lattice and a red-detuned long lattice of twice the wavelength, resulting in the superlattice potential

$$V_{\text{sup}}(x) = -V_l \cos^2(k_l x + \phi) + V_s \cos^2(2k_l x) \tag{2.11}$$

with the superlattice phase ϕ. This potential is a bipartite structure consisting of lattice sites and sublattice sites. The infrared lattice defines a lattice site that is 'split' into two sublattice sites (*left* and *right*) by the green lattice.

The superlattice phase defines the symmetry of the potential. In the symmetric configuration $\phi = 0$, the potential minimum of the attractive infrared lattice coincides with the potential maximum of the

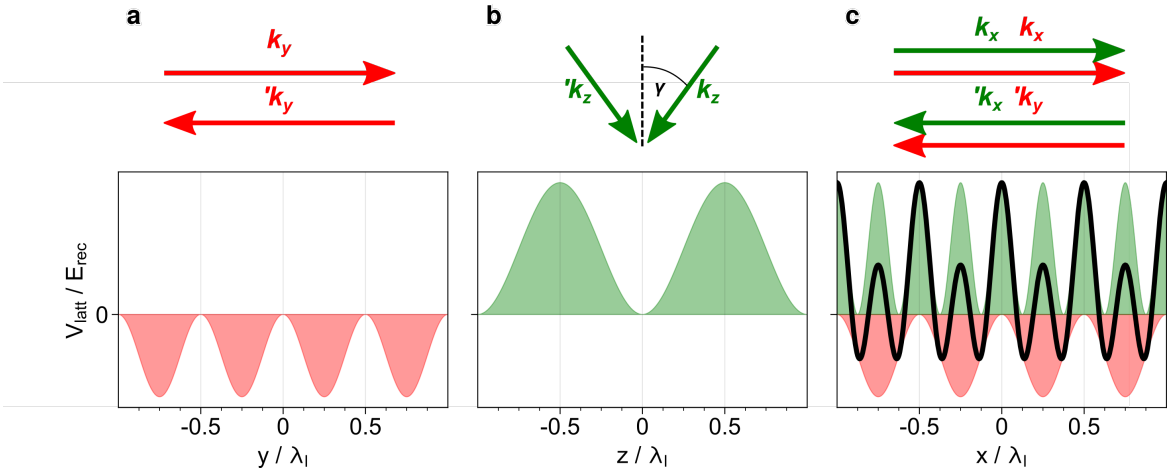

Figure 2.2: **Various types of optical lattices in the experimental setup:** The lattices along the x, y and z direction have different lattice geometries and lattice spacings compared to the wavelength $\lambda_l = 1\,064\,\text{nm}$. (a) A monochromatic optical lattice along the y-direction is created by interference of two counter-propagating laser beams with wavelength λ_l. (b) A shallow-angle optical lattice along the z-direction is created by interference of two laser beams with wavelength $\lambda_s = \lambda_l/2$ under an angle $2\gamma = 24°$. (c) An optical superlattice is created along the x-direction by superimposing two monochromatic lattices of harmonic wavelengths $\lambda_l = 2\lambda_s$. In this experiment, the *short* wavelength lattice is blue detuned and the *long* lattice is red detuned.

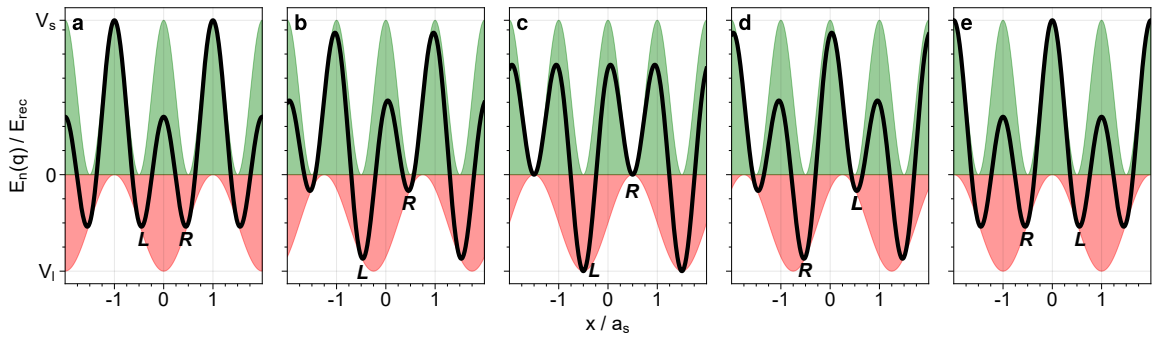

Figure 2.3: **Periodicity of the optical superlattice:** The potential of an optical superlattice according to equation 2.11 changes its symmetry with the superlattice phase ϕ. (a) For a symmetric superlattice $\phi = 0$, the left and right sublattice sites are energetically degenerate. Increasing the superlattice phase $\phi = \pi/8$ (b) introduces an asymmetry until the completely asymmetric phase is reached at $\phi = \pi/4$ (c). (d) The asymmetry is reduced, when increasing the phase even further$\phi = 3\pi/8$. (e) After one period $\phi = \pi/2$, the symmetric configuration is restored, but the unit cell has shifted by one short lattice length a_s.

green lattice (cf. figure 2.3 a).[1] This results in the same potential energy of the left and right sublattice site. In the completely asymmetric configuration $\phi = \pi/4$, both intensity minima coincide, resulting in the maximal energy difference between the sublattice sites (cf. figure 2.3 c). For a superlattice phase of $\phi = \pi/2$, the symmetric configuration is restored, however, the unit cell has shifted by one short lattice spacing a_s.

[1] Subplots in this thesis are created using ProPlot [61], an enhanced wrapper for Matplotlib.

The optical lattice depth is typically given in units of the recoil energy $E_{\mathrm{rec}} = h^2/(8ma^2)$, with Planck's constant h. This describes the energy an atom with mass m obtains by absorbing a photon from the lattice with spacing a. The benefit of this description is a normalized energy scale for atoms in optical lattices that allows for the comparison of lattices with different spacing (or atomic species). We have a three-dimensional optical lattice, where the lattice depths are denoted s_z, s_y, V_s, and V_l, with the latter two depths referring to the superlattice along the x-direction.

2.2.1 Band structure of optical lattices

In this subsection, we explore the eigenenergies and eigenstates of a single particle in an optical lattice. The Hamiltonian for a one-dimensional optical lattice

$$\hat{H}(x) = \hat{H}_{\mathrm{kin}} + V_{\mathrm{latt}}(x) \tag{2.12}$$

is given by the kinetic energy operator $\hat{H}_{\mathrm{kin}}$ and the periodic lattice potential $V_{\mathrm{latt}}(x+a) = V_{\mathrm{latt}}(x)$. The eigenstates of a periodic system can be constructed according to the Bloch theorem [62]. It states, that the eigenfunctions are given by plane wave states e^{iqx} with wave vector q multiplied by an envelope function $u_q(x)$ that inherits the lattice periodicity.

Band structure of a monochromatic lattice

In the following, we will determine the specific wave vector q and the envelope function for the monochromatic optical lattice. For this purpose, it is beneficial to decompose the lattice potential (equation 2.9) in its Fourier components

$$V_{\mathrm{latt}} = \frac{V_0}{4}\left(e^{iGx} + e^{-iGx} + 2\right) \tag{2.13}$$

with the reciprocal lattice vector $G = 2k$. This decomposition shows, that the lattice Hamiltonian of equation 2.13 couples plane wave states with a momentum difference corresponding to multiples of the reciprocal lattice vector G. Therefore, the *discrete* translational symmetry of the lattice leads to a conservation of the *quasi-momentum* q, which is defined as the momentum modulo the reciprocal lattice vector G. Now, we can use the Bloch theorem to construct a basis set

$$|q, m\rangle \equiv u_m(x)\, e^{iqx} = e^{i(q+mG)x} \tag{2.14}$$

that corresponds to plane waves with an overall momentum given by the quasi-momentum q plus integer multiples m of the reciprocal lattice vector G.

In this basis, the matrix elements of the kinetic operator

$$\langle q', m' |\, \hat{H}_{\mathrm{kin}} \,| q, m\rangle = \frac{\hbar^2}{2m}\,(q+mG)^2\, \delta_{q,q'}\, \delta_{m,m'} \tag{2.15}$$

are diagonal. On the other hand, the matrix elements of the optical potential follow directly from equation 2.13:

$$\langle q', m' |\, V_{\mathrm{latt}} \,| q, m\rangle = \frac{V_0}{2}\, \delta_{q,q'}\, \delta_{m,m'} + \frac{V_0}{4}\, \delta_{q,q'}\, \delta_{m\pm1,m'} \tag{2.16}$$

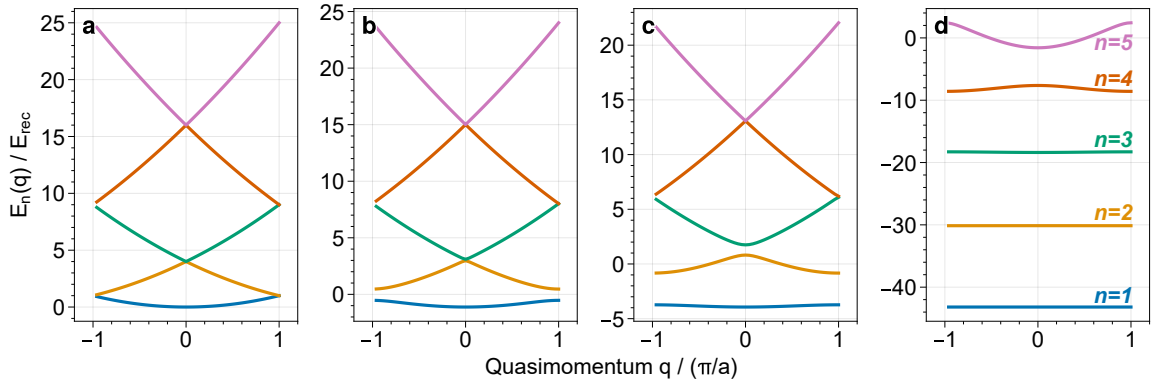

Figure 2.4: **Band structure of monochromatic optical lattice:** The eigenvalues of the lattice Hamiltonian $E_n(q)$ are plotted versus the quasimomentum q. The quasimomentum is restricted to the first Brillouin zone $q \in (-\pi/a, \pi/a]$ due to the discrete translation invariance of the optical lattice. This spectrum is shown for various lattice depths $V_0 = 0,\ 2,\ 6$ and $50\, E_{\text{rec}}$ in subfigures a, b, c and d respectively.

and showcase again the coupling between different plane wave states, while conserving the quasimomentum. For a given quasimomentum q, we construct the lattice Hamiltonian in matrix form for discrete values of $m \in [-10, 10]$. Diagonalizing this Hamiltonian yields the eigenstates and eigenvalues of the optical lattice, which are described by the following equation

$$\hat{H}(x)\,\psi_n(q,x) = E_n(q)\,\psi_n(q,x), \tag{2.17}$$

where $n \in \mathbb{N}$ represents the band index, a new quantum number introduced in this formalism.

In the following, we investigate the single particle energy spectrum $E_n(q)$ of the optical lattice: the *band structure*. In figure 2.4, we plot the spectrum of a monochromatic lattice for increasing lattice depths V_0. For a shallow lattice (subfigure a), the spectrum resembles a parabola that is folded at the edge and center of the Brillouin-zone (BZ) where $q = m\pi/a$. This corresponds to the free particle dispersion relation with a restriction to the first BZ due to the definition of the quasi-momentum $q \in (-\pi/a, \pi/a]$. Increasing the lattice depth (subfigures b to c), opens one or more gaps at the points of degeneracy, effectively separating the spectrum into energy bands, hence the name. This gap opening is caused by the optical lattice that couples the eigenstates and creates avoided crossings at the points of degeneracy. The spectrum above the lattice depth still resembles a free particle dispersion relation and is therefore referred to as the *continuum*. For very deep lattices (subfigure d), the lowest bands become flat and thus show no dispersion. These deep lattices are referred to as *frozen*, as they suppress all dynamics.

Band structure of a bi-chromatic superlattice

The band structure of a bi-chromatic superlattice is obtained in a manner similar to that for the monochromatic lattice.

We start by considering a monochromatic lattice of the short wavelength with the reciprocal lattice vector $G_s = 2k_s$ and the corresponding quasi momentum $|q_s| \leq \pi/a_s$. The lattice Hamiltonian is given by equation 2.13 with the repulsive lattice depth V_s. Next, we introduce the attractive lattice of

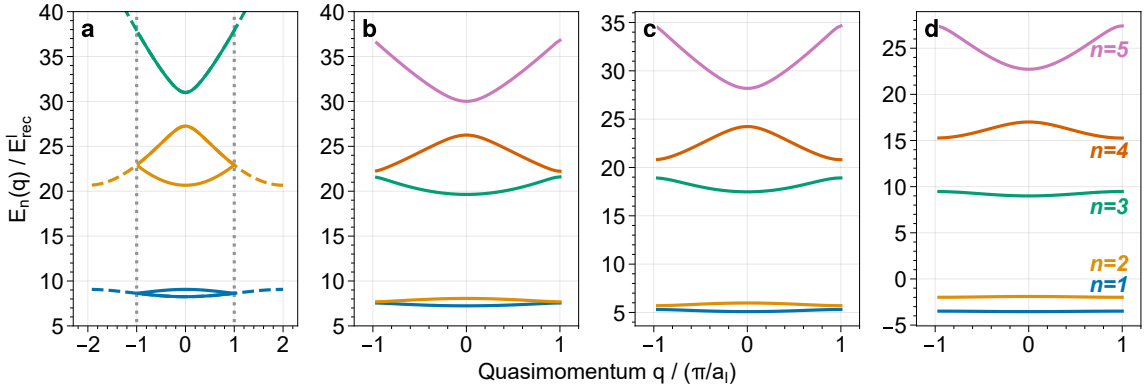

Figure 2.5: **Band structure of bichromatic optical superlattice:** The eigenvalues of the superlattice Hamiltonian $E_n(q)$ are plotted versus the quasimomentum q. The quasimomentum is restricted to the first Brillouin zone $q \in (-\pi/a_l, \pi/a_l]$. This spectrum is shown in a symmetric configuration $\phi = 0$ for a short lattice depth $V_s = 6\,E_{\text{rec}}$ and various long lattice depths $V_l = 0,\ 2,\ 6$ and $20\,E_{\text{rec}}$ in subfigures a, b, c and d respectively.

the long wavelength with the halved reciprocal lattice vector $G_l = G_s/2$ and halved Brillouin zone $|q_l| \leq \pi/2a_s$. This gives the Fourier components of the superlattice potential as

$$V_{\text{sup}} = \frac{V_s}{4}\left(e^{iG_s x} + e^{-iG_s x} + 2\right) - \frac{V_l}{4}\left(e^{i(G_s/2x+\phi)} + e^{-i(G_s/2x+\phi)} + 2\right). \tag{2.18}$$

The introduction of the long-wavelength lattice leads to an additional coupling between plane wave states with a momentum difference of $G_s/2$, the halved reciprocal lattice vector. The solution of the superlattice Hamiltonian is then analogue to the monochromatic scenario [2].

In general, the band structure of the superlattice depends on three parameters: the two lattice depths V_s, V_l and the superlattice phase ϕ. In figure 2.5, we consider a symmetric superlattice $\phi = 0$ with a constant short lattice depth $V_s = 6\,E_{\text{rec}}$ and increasing long lattice depths. The smaller Brillouin zone of the long lattice leads to an additional folding at the new edge of the Brillouin zone $q = \pm\pi/a_l$ (dotted vertical lines in subfigure a). Increasing the long lattice depth V_l (subfigure b to d), opens another gap at the edges of the smaller Brillouin zone, creating band-pairs (or mini-bands) with a small band gap.

The resulting mini-band structure is a direct consequence of the bi-chromatic lattice configuration, which introduces both lattice and sublattice sites. Compared to the monochromatic lattice, this substructure effectively splits each band into two mini-bands. This behavior will be explored in greater detail in the next section, where we discuss the eigenstates of the superlattice.

2.2.2 Bloch waves in optical lattices

The eigenfunctions of a single particle in an optical lattice are the Bloch waves $\psi_n(q,x)$ for a given band n and quasi momentum q. As postulated in the Bloch theorem, they are plane waves that inherit the periodicity of the underlying potential by the envelope function $u_q(x)$. Therefore, the Bloch waves

[2] For a detailed calculation and discussion of the superlattice band structure, please refer to my Master thesis [63].

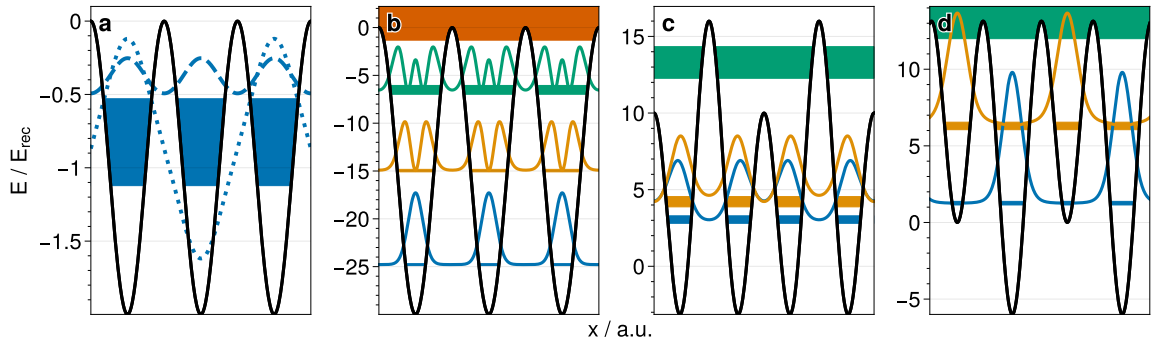

Figure 2.6: **Bloch waves of different optical lattices:** The eigenfunctions of the optical lattice are plotted qualitatively into the optical lattice potential and offset by their eigenenergies. (a) In a shallow monochromatic lattice $V_0 = -2\,E_{\mathrm{rec}}$, the Bloch waves $\psi_n(q,x)$ of the lowest band $n = 1$ (blue shaded region) depend strongly on the quasimomentum $q = 0$ (dashed line) or $q = \pi/a$ (dotted line). (b) For a deep lattice $V_0 = -30\,E_{\mathrm{rec}}$, the probability density $|\psi_n(q,x)|^2$ is strongly peaked at the lattice sites and the band index n dictates the number of nodes. The different bands are indicated by the color coding, and the probability density is offset by the energy of the corresponding band. (c) In the symmetric superlattice configuration ($V_s = 4\,E_{\mathrm{rec}}$, $V_l = 6\,E_{\mathrm{rec}}$, $\phi = 0$), the Bloch waves of the lowest two bands are coupled and delocalized over both sublattice sites. (d) In the completely asymmetric superlattice configuration $\phi = \pi/4$, the Bloch waves of the two lowest bands are localized on one specific sublattice site.

can be written as

$$\psi_n(q,x) = \sum_m u_{qmn} e^{i(q+mG)x} \tag{2.19}$$

with the relative weight u_{qmn}. The characteristics of the Bloch waves change with the quasi momentum and band index. The quasimomentum defines the phase of the plane wave states at neighboring lattice sites: For $q = \pi/a$, the plane waves accumulate a phase factor of -1 between adjacent lattice sites, whereas for $q = 0$ the sign stays the same. The band index is the dominant energy scale and defines the number of nodes in the wave function.

We show the Bloch waves $\psi_n(q,x)$ of the lowest band ($n = 1$) in figure 2.6 a for a shallow lattice of $V_0 = 2\,E_{\mathrm{rec}}$. Here, the energy band is indicated by a colored region and the corresponding Bloch waves by a dashed line ($q = 0$) and a dotted line ($q = \pi/a$), showcasing the different phases between adjacent lattice sites. Moreover, the Bloch waves are delocalized over the lattice and inherit its periodicity. However, they still have finite probabilities at the high intensity regions due to the small lattice amplitude that results in a large bandwidth. For a deep monochromatic lattice $V_0 = 30\,E_{\mathrm{rec}}$, this bandwidth decreases significantly (cf. figure 2.6 b). Therefore, the Bloch waves are sharply peaked at the lattice sites, as the probability density $|\psi_n(q,x)|^2$ (solid line) is negligible in the high intensity regions. The band index n changes the number of nodes of the Bloch wave, in strong resemblance of the harmonic oscillator wave functions.

In an optical superlattice, the characteristics of the Bloch waves change with the superlattice phase. In a symmetric superlattice $\phi = 0$, the Bloch waves of the lowest two bands are delocalized over all (sub)lattice sites (cf. figure 2.6 c). They only differ in their probability density between the sublattice sites. The reason for this similarity is the coupling of the two bands that is indicated by the small band gap. The coupling is related to the energy degeneracy of the two sublattice sites, which we

will investigate further in the next section. For the completely asymmetric configuration $\phi = 0$, this degeneracy is lifted and the two bands decouple (cf. figure 2.6 d). Here, the Bloch waves of the first (second) band are localized at the left (right) sublattice sites. A thorough (theoretical) investigation of the Bloch waves in optical superlattices can be found in the Master thesis of F. Görg [64].

2.2.3 Wannier functions in optical lattices

So far, we have described optical lattices using the Bloch basis. As discussed, Bloch waves are completely delocalized across the lattice and posses fixed quasi-momenta. Alternatively, the lattice can be described in a localized basis, known as the Wannier basis [65], which is constructed as a superposition of all momenta. Wannier functions are localized at specific lattice sites, thereby discretizing the lattice. It should be stressed, that these functions are not the eigenfunctions of the system as their localization is energetically costly. However, they are typically used as a basis for many-body lattices theory with local interactions in a *tight-binding* description, like the Fermi-Hubbard model.

In the following, we introduce the Wannier functions for monochromatic and bichromatic lattices. The obtained wave functions will serve as the basis for the tight-binding description of the optical superlattice in section 2.4. The Wannier function of band n that is localized at site l is typically defined as

$$w_l^n(x) = \frac{1}{\sqrt{N_L}} \sum_q e^{-iqla} \psi_n(q,x), \text{ with } q \in \left(-\frac{\pi}{a}, \frac{\pi}{a}\right] \tag{2.20}$$

with the number of lattice sites N_L [66]. This definition is practically a Fourier transformation of the Bloch waves of one specific band. In the monochromatic lattice, this procedure gives Wannier functions that are localized at one lattice site, as shown in figure 2.7 a. However, in a symmetric superlattice the Wannier functions of the two lowest bands (blue and orange line) are delocalized over both sublattice sites (cf. figure 2.7 b). The reason for this remaining delocalization is the aforementioned coupling between these two bands, which makes the definition of equation 2.20 unsuited for the superlattice.

For the optical superlattice, we define the Wannier functions as the eigenfunctions of the band projected position operator (BPO), as introduced by S.Kivelson [67]. The obtained Wannier functions are maximally localized [68], and were applied to superlattices by U.Bissbort [69] and F.Görg [64]. The band projected position operator $\hat{x}_{\mathcal{M}}$ for a band manifold $\mathcal{M}$ is defined as

$$\hat{x}_{\mathcal{M}} = \hat{P}_{\mathcal{M}} \hat{x} \hat{P}_{\mathcal{M}} \tag{2.21}$$

with the manifold projection operator

$$\hat{P}_{\mathcal{M}} = \sum_{n \in \mathcal{M}} \sum_q |q,n\rangle \langle q,n| \tag{2.22}$$

and the Bloch waves $|q,n\rangle$. The maximally localized Wannier functions $|l,m\rangle_{\mathcal{M}}$ then solve the eigenvalue equation

$$\hat{x}_{\mathcal{M}} \, |l,m\rangle_{\mathcal{M}} = x_{lm} \, |l,m\rangle_{\mathcal{M}} \tag{2.23}$$

with their center of mass position x_{lm}, the lattice site index l and the generalized band index $m \in \mathcal{M}$.

At the heart of this method is the appropriate choice of the band manifold $\mathcal{M}$ that includes the

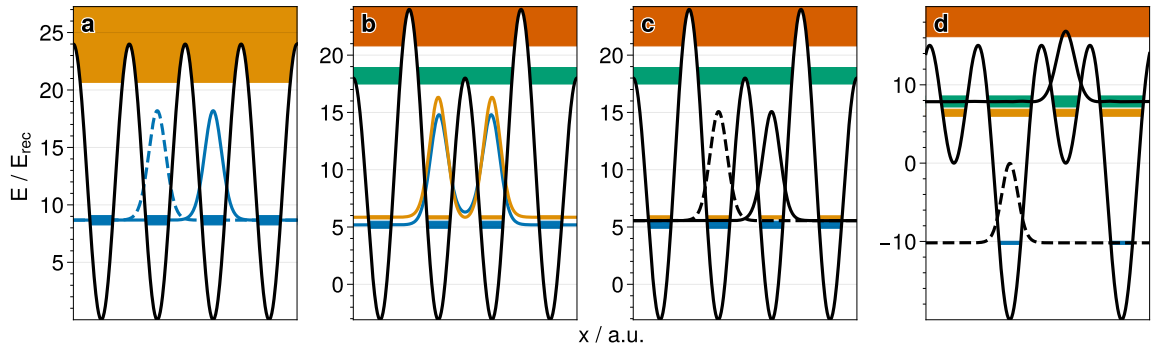

Figure 2.7: **Wannier functions of different optical lattices:** The probability densities of different Wannier functions $|w_l^n(x)|$ are plotted into the potential of various optical lattices and are offset by their energy. (a) In a monochromatic lattice $V_0 = 24\,E_{\mathrm{rec}}$, the Wannier functions of the lowest band are localized at one lattice site. (b) In a bichromatic superlattice ($V_s = 6\,E_{\mathrm{rec}}$, $V_l = 6\,E_{\mathrm{rec}}$, $\phi = 0$), the single-band Wannier functions ($n = 1, 2$) are localized at one lattice site but delocalized over both sublattice sites. (c) Considering a band manifold $\mathcal{M} \in \{1, 2\}$ in the calculation of the Wannier functions, results in two wave functions that are localized on the left (dotted line) and right (dashed line). (d) In a completely asymmetric superlattice (($V_s = 6\,E_{\mathrm{rec}}$, $V_l = 20\,E_{\mathrm{rec}}$, $\phi = \pi/4$)), the Wannier function on the right well is calculated using the manifold $\mathcal{M} \in \{2, 3\}$.

coupled bands. For example, in the symmetric configuration of the superlattice, the lowest two bands are chosen as the manifold $\mathcal{M} \in \{1, 2\}$ to obtain Wannier functions that are localized on one sublattice site (cf. figure 2.7 c). However, the choice of the manifold depends on the superlattice phase. For a completely asymmetric superlattice, the second and third band are coupled (cf. figure 2.7 d). Here, the Wannier function on the lower well is calculated from the first band and the one on the upper well from the manifold $\mathcal{M} \in \{2, 3\}$.

To circumvent the necessity of choosing the right manifold, we have developed the multiband description which considers manifolds of more than two bands. The method is described in detail in my master thesis [63]. In short, the larger manifold size gives more than one localized function per sublattice site. Therefore, an additional calculation step is required in which the multiple Wannier functions per sublattice site serve as a basis for the actual maximally localized Wannier function. The final result is a maximally localized Wannier function at lattice site l, which now also differentiates between sublattice sites

$$|l,\, m\rangle_{\mathcal{M}} \equiv w_l^m(x) = \alpha \sum_q \sum_{n \in \mathcal{M}} d_{lm}^{qn}\, \psi_n(q, x) \tag{2.24}$$

with the Bloch functions $\psi_n(q, x)$ of band n and quasi momentum q and their weight d_{lm}^{qn}, the generalized band index m and a normalization constant α.

In general, the Wannier functions are three-dimensional just as the lattice structure that they describe. However, the lattices are (almost) orthogonal and therefore their band structure as well as the Wannier functions separate

$$w_{i,j,k}(x, y, z) = w_i(x) \cdot w_j(y) \cdot w_k(z), \tag{2.25}$$

where we have neglected the generalized band indices for better readability.

2.3 Interacting particles in optical lattices

At the heart of quantum simulation lies the study of interacting matter. In this section, we focus on the interaction mechanisms between neutral atoms and methods to experimentally control these interactions. Although the study of interactions typically spans the complex fields of quantum chemistry and molecular physics, we will see that the low temperatures characteristic of ultracold atomic gases provide a substantial simplification [70]. This simplification allows us to describe the interaction process using a single key parameter: the scattering length.

First, we discuss the quantum mechanical treatment of collisional interactions in the scattering theory. Then, we explore the experimental control of the scattering length via magnetic Feshbach resonances. This section offers a brief overview of the vast topic of interacting ultracold atoms. For a more thorough investigation, readers are encouraged to consult the articles that inspired this section: "From van der Waals universality to Fano–Feshbach resonances" by J.Dalibard [70] and "Atomic, Molecular and Optical Physics" by M.Köhl [60].

2.3.1 Scattering theory

Ultracold atoms primarily interact through elastic two-body collisions, which are best described using quantum mechanical scattering theory. Scattering theory's simplicity lies in its reduction of complex molecular interactions to just one key parameter, the scattering length a. This simplification allows us to visualize the scattering process as though it were occurring off a hard sphere with radius a.

The molecular potential $V(\boldsymbol{r})$ characterizes the interaction between two neutral atoms and changes considerably with the distance r between them. For large inter-particle distances that exceed the Bohr radius ($r \gg a_0$), the atoms experience the weakly attractive van-der-Waals interaction $V_{\text{vdW}} \sim -r^{-6}$ by induced dipole-dipole interactions. Conversely, at short distances $r < a_0$, the two atoms strongly repel each other due to Pauli-blocking between the two electron clouds. Although an ab-initio determination of the exact molecular potential is difficult, it can be estimated with the Lennard-Jones potential (black line) in figure 2.8. We will see that an approximation of the inter-molecular potential is appropriate as the exact shape of the potential is irrelevant for low-energy collisions.

The scattering process between two particles is described typically in the relative coordinate frame $\boldsymbol{r} = \boldsymbol{r_1} - \boldsymbol{r_2}$, which gives the Hamiltonian

$$\hat{H}(\boldsymbol{r}) = \frac{-\hbar^2 \nabla_r^2}{2\mu} + V(\boldsymbol{r}), \tag{2.26}$$

with the reduced mass $\mu = \frac{m_1 m_2}{m_1 + m_2}$. For a radially symmetric interaction potential $V(r)$, the momentum of the scattering process is conserved [59]. Consequently, the eigenfunctions of the collision process separate into a radial and angular part $\psi(\boldsymbol{r}) = \psi(r)\, Y_{l,m}(\theta, \phi)$. In this expression, the spherical harmonics $Y_{l,m}(\theta, \phi)$ represent the angular part of the scattering process, which corresponds to an angular momentum transfer of l. The radial part of the wave function describes an incoming plane wave along the x-direction, that is scattered into a spherical wave

$$\psi(r) \propto e^{ikx} + f_k(\theta) \frac{e^{ikr}}{r} \tag{2.27}$$

with the scattering amplitude $f_k(\theta)$ for an azimuthal angle θ and momentum k.

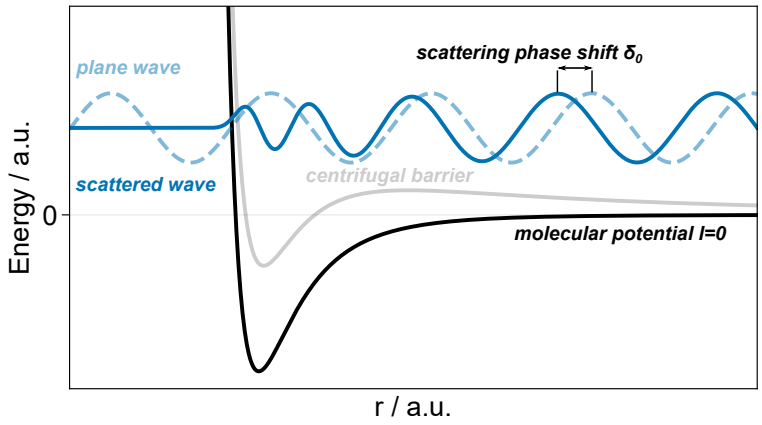

Figure 2.8: **Sketch of two-particle scattering process:** The two-particle interaction is dictated by the molecular potential as a function of the relative coordinate r. For s-wave scattering ($l = 0$), the molecular potential can be estimated by the Lennard-Jones potential (black line). If the particles exchange momenta ($l \neq 0$), the centrifugal barrier creates a local maximum that suppresses access to the attractive part of the potential. The scattered wave function (blue line) is perturbed by the molecular potential and approaches a plane wave for large inter-particle distances. Here, the impact of the scattering process is characterized by the scattering phase shift δ_0 compared to an unperturbed plane wave state (blue dashed line).

The scattering process is significantly simplified for low-energy collisions, as we will discuss. The influence of the orbital angular momentum can be incorporated into an effective interaction potential for the radial wave function, given by

$$V_{\text{eff}} = V(r) + \frac{\hbar^2 l(l+1)}{2mr^2}. \tag{2.28}$$

The second term of this expression is the *centrifugal-barrier*, which introduces a local potential maximum as indicated as the gray line in figure 2.8. This maximum $E_{max}/k_B \sim 1\,\text{mK}$ significantly exceeds the typical temperatures of ultracold gases [60] and suppresses access to the short-range molecular potential. Only for *s-wave scattering* (l=0), the centrifugal-barrier vanishes and the attractive part of the molecular potential is probed by the atoms. Therefore, ultracold atomic gases interact exclusively via s-wave scattering processes.

Interestingly, the de Broglie wavelength λ_{DB} of these s-wave atoms is much larger than the effective range of the molecular potential $r_c = 64.9\,\text{a}_0$ (for ^{40}K [53]). Therefore, the low-energy particles are insensitive to the details of the potential, and we can characterize the scattering process in the far-field regime $r \gg r_c$. Here, the effect of the collision is simply described by a phase shift $\delta_0(k)$, relative to the unperturbed plane wave (cf. figure 2.8). In general, the phase of the scattered particle advances more quickly in attractive potentials than for a free particle, which results in a positive phase shift $\delta_0 > 0$ and vice versa for repulsive potentials. This phase shift is then used to define the *scattering length* a as [70]

$$\frac{1}{a} = -\lim_{k\to 0} k\,\cot(\delta_0). \tag{2.29}$$

This scattering length can be considered as the radius of a hard-sphere potential that causes the

observed phase shift. However, the scattering length can be positive, negative, zero and infinite, and therefore the image of a hard sphere radius "is just a useful fiction that is mathematically equivalent to the scattering potential" [59].

Moreover, the scattering length can drastically change with the potential depth of an attractive potential [60]. For shallow potentials, the scattering length is negative and decreases with the potential depth. When the potential is sufficiently deep, a bound state energy becomes resonant with the energy of the incoming wave and the scattering length diverges as $\delta_0 = \pi/2$. After this resonance, the scattering length is positive until this behavior repeats itself for the next bound state. This phenomenon is called *resonant scattering* and is utilized in Feshbach resonances, which we discuss in the next section.

We have established, that the scattering process is characterized completely by the scattering length a and–in the case of s-wave scattering– the atoms do not sample the exact shape of the molecular potential. Therefore, it is beneficial (from a computational perspective) to replace the molecular interaction potential with a simpler potential that gives rise to the same scattering length. A suitable *pseudo potential* is the regularized contact potential

$$V_{\text{pseudo}}(\boldsymbol{r}) = g\delta(\boldsymbol{r})\frac{\delta}{\delta r}r \tag{2.30}$$

with the coupling strength $g = 2\pi\hbar a^2/m$.

2.3.2 Feshbach resonances

To realize a good quantum simulator, we need experimental control over the interaction strength and sign. However, for a given atomic species the molecular potential is fixed (for a specific hyperfine mixture) and so is the scattering length a. This limitation is overcome by the use of magnetic Feshbach resonances [53, 70] that effectively manipulate the scattering length with a magnetic field. In the following, we will discuss the use of magnetic Feshbach resonances for the fermionic potassium isotope ^{40}K.

Magnetic Feshbach resonances utilize the aforementioned *resonant scattering*, but the resonance is created between two collisional channels (cf. figure 2.9 a). The *open channel* describes a molecular potential between two hyperfine states (i.e. $|F = 9, m_F = -9/2\rangle$ and $|F = 9, m_F = -7/2\rangle$), which is energetically lower than the kinetic energy, and hence the name. The *closed channel* corresponds to a different hyperfine state mixture (i.e. $|F = 9, m_F = -9/2\rangle$ and $|F = 7, m_F = -7/2\rangle$) which is energetically inaccessible at large distances. However, at short distances, a bound state of the closed channel can be resonant to the scattering particles of the open channel. This modifies the scattering length, if the two channels couple to one another by spin-exchange interactions, for which the sum of the magnetic quantum number m_F must be conserved [60].

Conveniently, the resonance condition can be manipulated using an external magnetic field, as the two different channels experience a relative Zeeman shift due to their different magnetic momenta. This allows for a precise control of the s-wave scattering length a around a magnetic Feshbach resonance according to [70]

$$a(B) = a_{\text{bg}}\left(1 - \frac{\Delta B}{B - B_0}\right). \tag{2.31}$$

The background scattering length a_{bg} describes the behavior far from the resonance and is spin

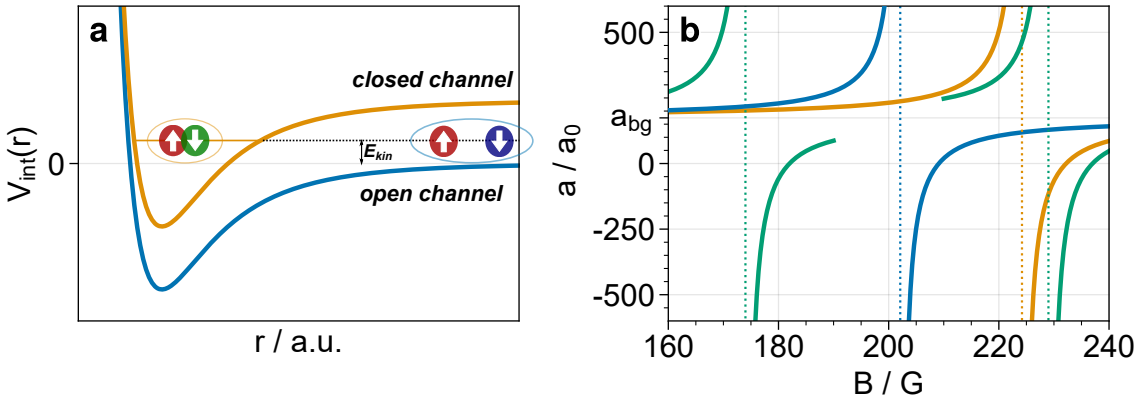

Figure 2.9: **Magnetic Feshbach resonances:** (a) Resonant scattering between two collisional channels. The *open channel* is given by the initial hyperfine mixture which is energetically lower than the kinetic energy of the colliding particles. The *closed channel* for a different hyperfine mixture is energetically inaccessible for large inter particle distances r, but the bound state can be resonant to the collisional energy. If the two hyperfine mixtures couple to one another by a spin-exchange interaction, resonant scattering is induced which alters the scattering length significantly. The energy difference between both channels is controlled by an external magnetic field as this changes the relative Zeeman shift. (b) Magnetic Feshbach resonances of ^{40}K. The three lowest hyperfine mixtures $|9,\ 7\rangle$, $|9,\ 5\rangle$ and $|7,\ 5\rangle$ are depicted in blue, orange, and green.

independent. For ^{40}K, the background scattering length was measured to be $a_{\mathrm{bg}} = (174 \pm 7)\ \mathrm{a}_0$ [71]. The position and width of the magnetic Feshbach resonance are denoted by B_0 and ΔB, respectively. In general, these parameters are determined experimentally and a list of all relevant parameters for fermionic potassium is given in [72].

We plot the magnetic Feshbach resonances according to equation 2.31 for the three lowest hyperfine mixtures in figure 2.9 b. The mixture of the lowest two hyperfine states $|m_F = -9/2\rangle$ and $|m_F = -7/2\rangle$ is denoted as $|9,\ 7\rangle$ and shown in blue, $|9,\ 5\rangle$ is shown in orange, and $|7,\ 5\rangle$ is shown in green. Clearly, magnetic Feshbach resonances are an excellent tool to adjust the scattering length over a large parameter range. It should be noted, that the scattering length between the two resonances of the $|7,\ 5\rangle$ hyperfine mixture is not modelled correctly by equation 2.31. Instead, in this region one should rely on experimental data of the scattering lengths [73, 74].

2.4 Tight binding description of optical lattices

After discussing the periodic potential of optical lattices and the interaction mechanism of ultracold atoms, we can explore the many-body physics in optical lattices using the tight-binding description. This approach assumes that the atoms are well localized at the lattice sites, which significantly simplifies the analysis: The atoms can only tunnel between neighboring sites and only interact if they occupy the same site. This procedure leads to the paradigmatic Hubbard model for monochromatic lattices and the Rice-Mele model for superlattices. We start this section, by calculating the parameters of the single-band tight-binding models and exploring how they can be controlled by the optical lattices and the scattering length. Then, we discuss how the population of higher bands leads to second-order processes in the model and why they are negligible for typical configurations. Finally,

we explore the interplay between interactions and the underlying potential, focusing on how it changes the observed interaction strength.

We start with the quantum many-body Hamiltonian in second quantization [13] for an optical (super)lattice potential $V(\boldsymbol{r})$ (equation 2.11), and the contact interaction $V_{\text{pseudo}}(\boldsymbol{r})$ (equation 2.30)

$$\hat{H} = \sum_{\sigma} \int d\boldsymbol{r}\ \hat{\psi}^{\dagger}_{\sigma}(\boldsymbol{r}) \left[\frac{-\hbar^2 \nabla^2}{2m} + V(r) \right] \hat{\psi}_{\sigma}(\boldsymbol{r}) + g \int d\boldsymbol{r}\ \hat{\psi}^{\dagger}_{\uparrow}(\boldsymbol{r}) \hat{\psi}^{\dagger}_{\downarrow}(\boldsymbol{r}) \hat{\psi}_{\downarrow}(\boldsymbol{r}) \hat{\psi}_{\uparrow}(\boldsymbol{r}), \tag{2.32}$$

with the field operator $\hat{\psi}^{\dagger}_{\sigma}(\boldsymbol{r})$ that creates a particle at position $\boldsymbol{r}$ with spin $\sigma \in \{\uparrow, \downarrow\}$. We emulate the spin with a pseudo-spin, where $\downarrow$ corresponds to the ground state of the hyperfine manifold $|F = 9/2,\ m_F = -9/2\rangle$ and $\uparrow$ is given by $|F = 9/2,\ m_F = -7/2\rangle$. The first term of the many-body Hamiltonian describes the kinetic energy and the potential landscape, while the two-particle interactions are incorporated in the second term.

We express the quantum many-body Hamiltonian in the Wannier basis, using the fermionic field operator in one dimension

$$\hat{\psi}^{\dagger}_{\sigma}(x) = \sum_{j} w_j(x)\, \hat{c}^{\dagger}_{j\sigma} \tag{2.33}$$

with the Wannier function localized at lattice site j according to equation 2.24 and the fermionic creation operator $\hat{c}^{\dagger}_{j\sigma}$ of a particle with spin σ. In general, this is a suitable basis as long as the lattice depth is large enough to realize strongly peaked wave functions at the lattice sites. Moreover, the appropriate band manifold $\mathcal{M}$ depends on the energy scales of the atomic cloud, namely the temperature and interaction strength. Typically, these energy scales are smaller than the band gap of the monochromatic lattice which allows for a single-band treatment in this case. However, for the superlattice, the manifold choice is more delicate due to the small band gap between mini-bands as discussed in section 2.2.3. Therefore, we consider a band-manifold of four bands and use the energetically lowest one (generalized band index $m = 1$) as our Wannier basis.

The single-band many-body Hamiltonian of equation 2.32 is given in the Wannier basis as

$$\hat{H} = -\sum_{\langle i,j\rangle,\sigma} t_{ij} \left(\hat{c}^{\dagger}_{i\sigma} \hat{c}_{j\sigma} + h.c. \right) + \sum_{i,\sigma} E_i \hat{n}_{i\sigma} + U \sum_{i} \hat{n}_{i\uparrow} \hat{n}_{i\downarrow}, \tag{2.34}$$

with the number operator $n_{i\sigma} = c^{\dagger}_{i\sigma} c_{i\sigma}$ and the sum over neighboring lattice sites $\langle i, j\rangle$. The particles express their kinetic energy by tunneling events between neighboring sites with amplitude t. They experience an onsite energy E_i at lattice site i, and if two particles of opposing spin occupy the same site, they experience the interaction energy U.

The parameters t, E, and U characterize the tight-binding Hamiltonian and are typically referred to as Hubbard parameters. The tunneling amplitude between two sites i and j and along the direction x is given by

$$t_{ij} = \int dx\ w^{*}_{i}(x) \left[\frac{-\hbar^2 \nabla^2}{2m} + V(x) \right] w_j(x). \tag{2.35}$$

This tunneling amplitude depends on the spatial overlap between the Wannier functions of the two sites. Therefore, the restriction to tunneling between neighboring sites is reasonable in the tight-binding picture as the Wannier functions are exponentially localized. For the special case of $i = j$, equation

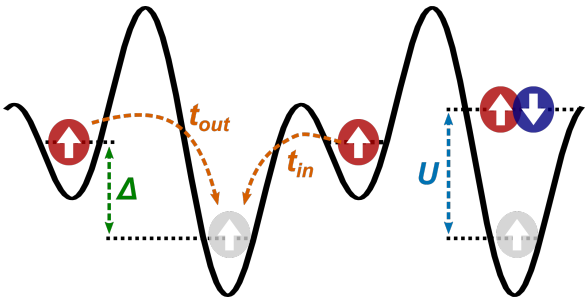

Figure 2.10: **Interacting Rice-Mele model in one dimension** The tight-binding Rice-Mele model describes fermions in a superlattice potential with four characteristic energy scales. The particles can tunnel within one unit cell with the rate t_{in}/h and out-of the unit cell with t_{out}/h. If two particles occupy the same lattice site they experience an on-site interaction U. The energy offset between both lattice sites of a unit cell is twice the tilt 2Δ.

2.35 gives the onside energy E_i.

The interaction energy U at lattice site i is given by

$$U = \frac{4\pi\hbar^2 a}{2m} \int d\boldsymbol{r}\ |w_i(\boldsymbol{r})|^4 \tag{2.36}$$

with the scattering length a. Here, it is important to note that the interaction energy depends on the three-dimensional Wannier function unlike the directional tunneling amplitude of equation 2.35.

The definition of these parameters holds for both monochromatic and superlattices. However, for the superlattice, two characteristic tunneling amplitudes exist due to the sublattice structure: The tunneling within a lattice site t_{in} and the out-of-site tunneling t_{out} (cf. figure 2.10). Moreover, the onside energy can differ significantly between the sublattice sites, which is typically encaptured by the tilt $\Delta = (E_i - E_{i+1})/2$.

The tight-binding model for a superlattice structure is given by the Rice-Mele model

$$\begin{aligned}\hat{H}_{\text{RM}} = &-\sum_i \left(t_{in}\, \hat{a}^\dagger_{i\sigma}\hat{b}_{i\sigma} + t_{out}\, \hat{a}^\dagger_{i\sigma}\hat{b}_{i-1\sigma} + h.c.\right) \\ &+ \frac{\Delta}{2}\sum_{i,\sigma}\left(\hat{n}^a_{i\sigma} - \hat{n}^b_{i\sigma}\right) \\ &+ U\sum_i \left(\hat{n}^a_{i\uparrow}n^a_{i\downarrow} + \hat{n}^b_{i\uparrow}n^b_{i\downarrow}+\right)\end{aligned} \tag{2.37}$$

with the lattice index i and the number operator at the left sublattice site $\hat{n}^a_{i\sigma} = \hat{a}^\dagger_{i\sigma}\hat{a}_{i\sigma}$ and at the right sublattice site $\hat{n}^b_{i\sigma}$. For a balanced system $\Delta = 0$ the model is referred to as the Su-Schrieffer-Heeger (SSH) model, which is a paradigmatic topological model. Notably, the Hubbard model is a special case of the Rice-Mele model ($t_{\text{in}} = t_{\text{out}}$ and $\Delta = 0$) and we will restrict the further discussion to the richer Rice-Mele model.

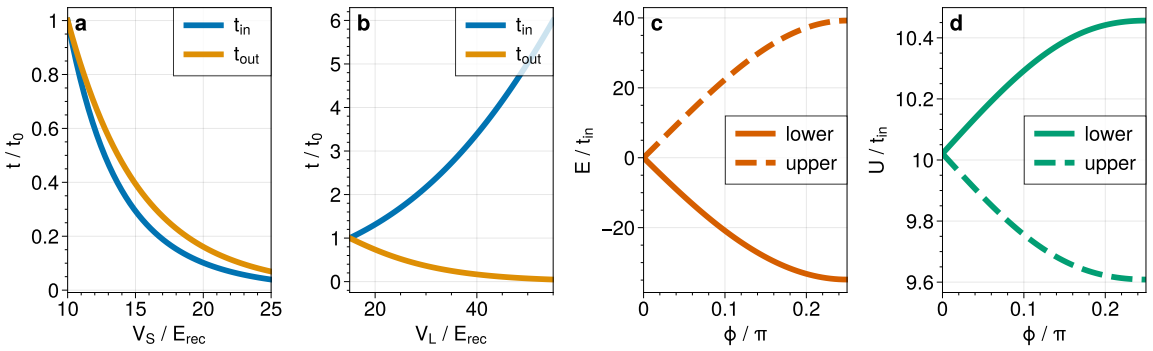

Figure 2.11: **Hubbard parameters vs. superlattice parameters:** The Hubbard parameters are calculated for a superlattice configuration of $V_S = 10\,E_{\mathrm{rec}}$, $V_L = 15\,E_{\mathrm{rec}}$, $\phi = 0$, and scattering length $a = 265\,a_0$. (a) The short lattice depth V_S supresses both tunneling amplitudes t_{in} (blue) and t_{out} (orange) exponentially. (b) The long lattice depth enhances t_{in} and suppresses t_{out}. (c) A superlattice phase $\phi \neq 0$ lifts the energy degeneracy between sublattice sites. The energy of the lower (upper) well is decreased (increased) as indicated by the solid (dashed) orange line. (d) The interaction energy U of the lower well (solid green line) increases with the superlattice phase $\phi \neq 0$, as the Wannier function is squeezed by the tighter confinement. This behavior is inverted for the upper well as indicated by the dashed line. Note that for the calculation of the interaction energy additional lattice depths of $V_y = 60\,E_{\mathrm{rec}}$ and $V_z = 110\,E_{\mathrm{rec}}$ have been considered.

Experimental control over the tight-binding parameters

The tight binding parameters can be controlled precisely with the superlattice properties V_S, V_L, ϕ, and the scattering length a. From equation 2.36 we see that the interaction can be changed linearly with the scattering length a and also depends on the shape of the Wannier function. We will see in the next section that this linear scaling with the scattering length is only true for small scattering lengths. But for now, we explore the scaling of the Hubbard parameters with the superlattice parameters.

We start with the symmetric superlattice configuration $\phi = 0$. Here, the tunneling within a lattice site t_{in} exceeds t_{out}. The reason for this is that the potential barrier within a lattice site is created by the superposition of the attractive and repulsive potential that partially cancel each other (cf. figure 2.3 a). The lattice depths of the short and long lattice then change both tunneling amplitudes in different ways. Increasing the short lattice depth enhances confinement at all lattice sites, leading to a stronger localization of the Wannier functions and an exponential suppression of both tunneling amplitudes (cf. figure 2.11 a). On the other hand, increasing the depth of the long lattice effectively shifts the Wannier functions toward the center of each lattice site, resulting in an increase of t_{in}, while simultaneously decreasing t_{out} (cf. figure 2.11 b).

Introducing a superlattice phase $\phi \neq 0$ breaks the symmetry of the superlattice. The onside energy changes differently for the sublattice sites as one is energetically lowered while the other is raised (cf. figure 2.11 c). This energy imbalance is often characterized by the energy tilt $\Delta = E_i - E_{i+1}$, which scales linearly with small superlattice phases. Moreover, already for small phases $\phi = 0.05\pi$, the tilt dominates the tunneling $\Delta \gg t_{\mathrm{in}}$, thereby suppressing all dynamics.

The degeneracy of the interaction energy U between sublattice sites is lifted by a non-zero superlattice phase $\phi \neq 0$ (cf. figure 2.11 d). In this configuration, the Wannier function on the lower well experiences a tighter confinement, and therefore, the interaction energy is increased and vice versa for the upper well. Additionally, the interaction energy U is sensitive to the lattice depths, as

these alter the confinement within the superlattice. For more detailed plots illustrating the dependence of the Hubbard parameters on the superlattice parameters, please refer to Appendix A.

Higher band corrections to tight-binding model

So far, we have considered the tight-binding model in the single-band picture (or two band picture for the superlattice). This description is accurate for deep lattice configurations, where all energy scales are smaller than the gap to the next band $k_B T, U \ll E_{\text{gap}}$. However, there are second-order tight-binding parameters, that describe additional processes in optical lattices, where the higher bands are populated [54]. Here, we introduce these parameters and show that they are negligible for our typical lattice configuration of $V_s = 10\,E_{\text{rec}}$, $V_l = 15\,E_{\text{rec}}$, $s_y = 60\,E_{\text{rec}}$, $s_z = 110\,E_{\text{rec}}$, and $\phi = 0$. Nonetheless, for periodically driven systems these higher-band processes can become significant as we show in chapter 6.

We start the discussion with the tunneling between lattice sites beyond the nearest-neighbor limit. The dominant process is between next-to-nearest neighboring lattice sites t_{ii+2}, as defined in equation 2.35, which is negligible as $t_{ii+2}/t_{\text{in}} \sim 5 \times 10^{-3}$. Therefore, it is a reasonable assumption to restrict the tight-binding model to tunneling between nearest-neighboring lattice sites.

The interactions also influence the dynamics in the system by changing the shape of the wave functions and therefore, also the overlap of wave functions between neighboring lattice sites. This results in an additional density-dependent part in the tight-binding Hamiltonian

$$-\delta t \sum_i \left(\hat{c}_i^\dagger (\hat{n}_i + \hat{n}_{i+1}) \hat{c}_{i+1} + h.c \right) \tag{2.38}$$

which is referred to as density-dependent or density-assisted tunneling, and was observed in optical lattices [75, 76]. Therefore, we incorporate a correction to the single particle dynamics $t'_{\text{in}} = t_{\text{in}} + \delta t$ with

$$\delta t = \frac{4\pi\hbar^2 a}{m} \int d\boldsymbol{r}\, |w_i(\boldsymbol{r})|^2 \cdot w_i(\boldsymbol{r}) w_{i+1}(\boldsymbol{r}) \tag{2.39}$$

for half-filled lattice systems (cf. figure 2.12 a). The amplitude of the density-assisted tunneling δt depends linearly on the scattering length, and therefore, is relevant for large interaction strengths. However, for typical interaction strengths $U/t = 8$, the density-assisted tunneling correction is rather negligible $\delta t/t_{\text{in}} \sim 7 \times 10^{-2}$.

The remaining corrections are the nearest neighbor interaction $\hat{V}_{\text{nn}}$, the direct exchange $\hat{V}_{\text{de}}$ that introduces spin flips between neighboring sites, and the correlated tunneling $\hat{V}_{\text{ct}}$ [77] (cf. figure 2.12 b and c), which are given as

$$\begin{aligned}
\hat{V}_{\text{nn}} &= V_{\text{nn}} \sum_i \left(\hat{n}_{i\uparrow} \hat{n}_{i+1\downarrow} + h.c. \right), \\
\hat{V}_{\text{de}} &= V_{\text{de}} \sum_i \left(\hat{c}_{i\uparrow}^\dagger \hat{c}_{i+1\uparrow} \hat{c}_{i+1\downarrow}^\dagger \hat{c}_{i\downarrow} + h.c. \right) \\
\hat{V}_{\text{ct}} &= V_{\text{ct}} \sum_i \left(\hat{c}_{i\uparrow}^\dagger \hat{c}_{i+1\uparrow} \hat{c}_{i\downarrow}^\dagger \hat{c}_{i+1\downarrow} + h.c. \right),
\end{aligned} \tag{2.40}$$

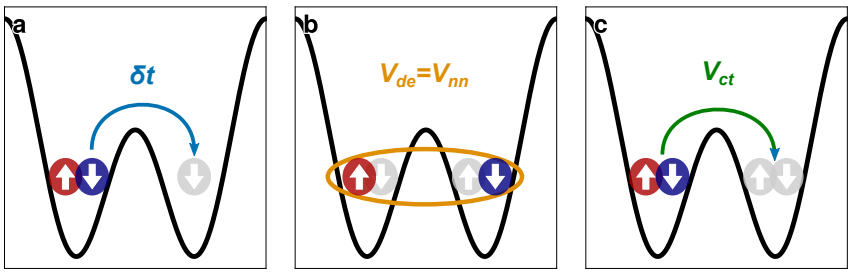

Figure 2.12: **Higher-band corrections to tight-binding model** (a) Density-assisted tunneling δt modifies the tunneling dynamics of half-filled lattices. (b) The nearest neighbor interaction V_{nn} is of the same strength as the direct exchange interaction V_{de} that introduces effective spin flips. (c) The correlated tunneling V_{ct} describes an explicit pair hopping.

with an equal amplitude for all three processes

$$V_{\mathrm{nn}} = V_{\mathrm{de}} = V_{\mathrm{ct}} = \frac{4\pi\hbar^2 a}{m} \int d\boldsymbol{r}\, |w_i(\boldsymbol{r})|^2 \cdot |w_{i+1}(\boldsymbol{r})|^2. \tag{2.41}$$

For static lattices with $U/t_{\mathrm{in}} = 8$, these corrections are negligible $V_{\mathrm{ct}}/t_{\mathrm{in}} = 8 \times 10^{-4}$, however, we will show in chapter 6, that for a periodic drive, the correlated tunneling can be enhanced significantly exceeding the effective single particle tunneling.

It is important to note, that we have calculated the Hubbard parameters with the non-interacting Wannier functions. This basis was obtained from the single particle description of the optical lattice and, therefore, does not account for the distortion of the wave functions by interactions apart from the density induced tunneling. We will address this inaccuracy in the next section.

2.4.1 Interplay between interactions and the underlying potential

So far, we have separated the interaction process from the calculation of the lattice energy spectrum. In particular, we have used the Wannier functions of the single-particle band structure to determine the interaction strength U according to equation 2.36. However, we didn't account for the fact, that the interactions also influence the wave functions in the lattice.

Intuitively, we would expect a broadened version of the Wannier function for repulsive interactions, as this would minimize the additional interaction energy. This would in turn, lead to an increase of the potential energy, as the broadened wave function penetrates further in the high intensity regions of the lattice. We can imagine this energy-interplay to happen iteratively until the wave function that minimizes the overall energy is found, which differs from the non-interacting wave function used in the previous chapter.

To explore interactions in the presence of an underlying potential, we study two fermions that interact via the contact potential of equation 2.30 in a harmonic confinement, which serves as a good approximation of a deep lattice site. This model was solved analytically for an isotropic harmonic oscillator by Busch et al. [78] and adapted to cylindrical symmetries by Idziaszek and Calarco [79], which was used to model the behavior in our monochromatic two-dimensional lattices [72, 80]. However, the symmetry of the superlattice potential is completely anisotropic, for which the

analytic solution was recently published by Chen et al. [81], and was applied to our system in this work. The anisotropy of a typical superlattice configuration ($V_S = 10\,E_{\mathrm{rec}}$, $V_L = 15\,E_{\mathrm{rec}}$, $V_y = 60\,E_{\mathrm{rec}}$, $V_z = 110\,E_{\mathrm{rec}}$ and $\phi = 0$) is characterized by the different trap frequencies

$$\omega_z \sim 23\,\mathrm{kHz},\ \eta_x = \frac{\omega_x}{\omega_z} = 4.41,\ \eta_y = \frac{\omega_y}{\omega_z} = 2.95, \tag{2.42}$$

where we have introduced the aspect ratios η_i. In a monochromatic lattice, the trapping frequency is directly derived from the lattice depth $\omega_i = 2\sqrt{V_i\,E_{\mathrm{rec}}}/\hbar$ [13]. In contrast, for a superlattice, while the trapping potential remains approximately harmonic, it depends on both the lattice depths and the phase of the superlattice. To determine the trapping frequency in this case, we fit a harmonic oscillator potential to the specific well under consideration.

We use the solution presented in [81] to solve the anisotropic harmonic oscillator with interactions for our specific trap symmetry. We compute the energy spectrum as a function of the scattering length a, and relative to the ground state energy of the non-interacting harmonic oscillator E_0 in figure 2.13 a. For non-interacting systems ($a = 0$), we observe an energy spacing of $\Delta E = 2\hbar\omega_z$, which corresponds to every second non-interacting harmonic oscillator level. This energy spacing is caused by the symmetry of the interaction potential, which couples only states with even parity $n \in 0, 2, 4, \ldots$.

We discuss interacting systems for the example of the lowest harmonic oscillator level $n = 0$, which corresponds to the lowest band of the lattice. Introducing a finite repulsive scattering length, linearly increases the energy for small scattering lengths and vice versa for attractive scattering lengths. For large scattering lengths $|a| \gg 1\,l^z_{HO}$, where the harmonic oscillator length is defined as $l^z_{\mathrm{HO}} = \frac{\hbar}{m\omega_z} \sim 1\,900\,\mathrm{a_0}$, the energy saturates. The change in energy relative to the non-interacting case gives the interaction energy $U_{\mathrm{HO}} = E - E_0$. This model clearly demonstrates that the linear scaling of interaction energy with scattering length, as postulated in equation 2.36, only holds true for small scattering lengths. Moreover, there exists a bound state for repulsive interactions $a \leftarrow 0^+$, which can be used to create Feshbach molecules [82].

We can gain further insight into the model by studying the relative wave functions along the z-direction, as depicted in figure 2.13 c to g. The relative wave functions are plotted for increasing scattering lengths and energies, which are indicated by orange dots in the spectrum shown in subfigure a. We start our discussion with the wave function of the non-interacting system (subfigure e), which corresponds to the non-interacting ground state of the harmonic oscillator. If we include interactions, the eigenstate responds to the interaction potential by coupling to higher bands of the harmonic oscillator. For repulsive interactions, the relative wave function minimizes the density in the interaction region and becomes broader (subfigure f), and vice versa for attractive interactions (subfigure d). This broadening of the wave function happens until the restoring force of the harmonic potential balances the repulsion of the interaction in the saturated region. For attractive interactions, the kinetic energy counteracts the interaction induced localization of the wave function leading to the observed saturation. Note that the positive parity of the wave functions is conserved for all scattering lengths, due to the aforementioned parity of the pseudo potential.

Still, the obtained interaction energy overestimates the interactions in an optical lattice, as the confinement is slightly stronger in the harmonic oscillator [83]. As a consequence, the eigenfunctions of the harmonic oscillator, the Gauss functions, are more localized than the Wannier functions. To account for this inaccuracy, we employ a correction factor $\mathcal{A}$ [83] to determine the interaction energy

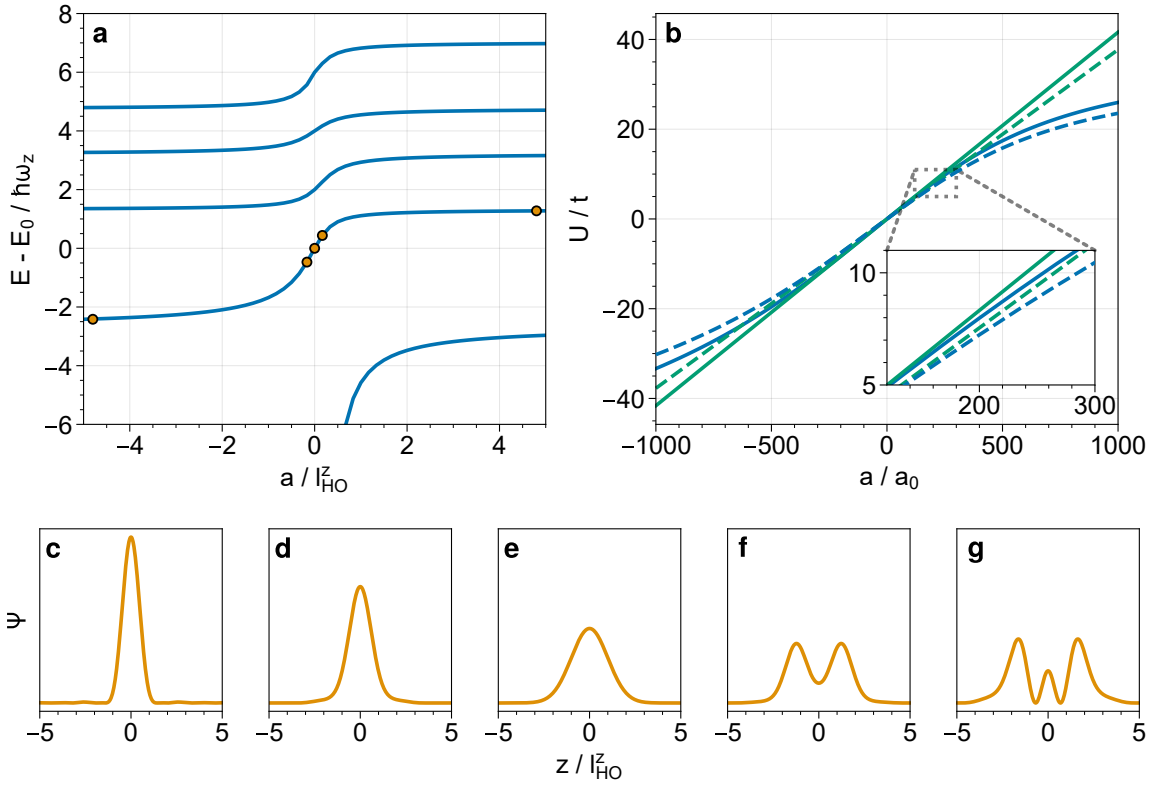

Figure 2.13: **Anisotropic harmonic oscillator spectrum and corrected interaction strength:** (a) The spectrum of an anisotropic harmonic oscillator with aspect ratios $\eta_x = 4.4$ and $\eta_y = 3$ is plotted versus the scattering length a in units of the harmonic oscillator length l^z_{HO} along the z-axis. The energy zero is set to the energy of the lowest band in the non-interacting limit E_0. The relative wave function for the eigenstates of the lowest band (orange dots) are plotted in (c) to (g) along the z-direction. (b) Interaction energy U in a three-dimensional lattice configuration for different computation methods. The interacting anisotropic harmonic oscillator is shown as a solid blue line, and including the correction for Wannier functions as a dashed blue line. The calculations with non-interacting wave functions is shown for a Gaussian wave function as a solid green line and for a Wannier function as a dashed green line. The inset shows the behavior for repulsive interactions that are typically used in our experiment. The considered lattice configuration for both subplots is $V_S = 10\,E_{\mathrm{rec}}$, $V_L = 15\,E_{\mathrm{rec}}$, $V_y = 60\,E_{\mathrm{rec}}$, $V_z = 110\,E_{\mathrm{rec}}$, and $\phi = 0$.

in an optical lattice from the harmonic oscillator

$$U_{\text{latt}} = \mathcal{A}\, U_{\text{HO}}, \text{ with } \mathcal{A} = \frac{U_W}{U_G} = \frac{\int d\boldsymbol{r} |w_i(\boldsymbol{r})|^4}{\int d\boldsymbol{r} |g_i(\boldsymbol{r})|^4}, \tag{2.43}$$

where we have introduced the Gaussian function

$$g_i(\boldsymbol{r}) = g_i(x) g_i(y) g_i(z), \text{ with } g_i(x) = \frac{1}{\sqrt[4]{\pi l_x^2}} e^{\frac{-(x-x_i)^2}{2l_x^2}}. \tag{2.44}$$

We compare the different methods to determine the interaction strength for various scattering lengths in figure 2.13 b. The linear scaling is evident in both non-interacting calculations using Gaussian functions U_G (solid green line) and Wannier functions U_W (dashed green line). Notably, $|U_G| > |U_W|$, highlighting the aforementioned overestimation of the confinement for the harmonic trap. Additionally, we observe the impact of the correction factor, that adjusts U_{HO} (blue line) to give the actual interaction strength in the lattice U_{latt} (blue dashed line).

Moreover, the saturating behavior of U_{HO} becomes significant for large scattering lengths $|a| \gtrsim 500\, \text{a}_0$. The inset provides a zoomed-in version of the plot for typical repulsive interaction strengths in an experiment ($U/t \sim 8$), where the various interaction strengths only differ by $\sim t$. This minor discrepancy is caused by the strong confinement of the considered lattice configuration, with the deviation being more pronounced for shallower lattices, where higher band contributions are more significant [80].

In this work, we use the interaction energy U_{latt} to calculate the interactions in our system. The calibration of the interaction energy is discussed in section 4.2.2, where we find great agreement between this theory and our experimental data.

CHAPTER 3

Experimental apparatus

In this chapter, we discuss the experimental apparatus used to study ultracold fermionic atoms in a three-dimensional optical lattice. We begin by summarizing the process of transforming a hot atomic vapor of potassium atoms into a quantum-degenerate fermionic gas confined in the optical lattice. Then, we explore the implementation of an in-plane superlattice, which is central to the research presented in this thesis. Finally, we discuss the detection methods used in this work.

At the start of this work, this experimental setup was already assembled and had been refined by many generations of PhD students. Therefore, most components of the apparatus are only briefly reviewed here, with detailed descriptions available in the work of my predecessors [72, 80, 84–90]. During this work, we newly implemented a phase-stable and periodically-drivable superlattice (section 3.2) and investigated its observables (section 3.3.4).

3.1 Creation of a quantum-degenerate Fermi-gas in an optical lattice

In this section, we discuss the preparation of ultracold fermionic potassium atoms in a three-dimensional optical lattice for quantum simulation. Achieving this requires cooling the atoms so that their behavior is primarily governed by quantum mechanics. This necessitates a high phase space density, which is more challenging for fermions than for bosons due to the Pauli exclusion principle.

The Pauli exclusion principle dictates that the many-body fermionic wave function, composed of a spin and a spatial wave function, must be antisymmetric under particle exchange. As a result, s-wave scattering, which requires a symmetric spatial wave function (compare section 2.3.1), can only occur between fermions with different spins. Consequently, identical fermions cease to interact at increasingly low temperatures.

To overcome this thermalization issue, we prepare a spin mixture during the various cooling processes. This approach ensures that the fermionic atoms can interact and thermalize effectively, allowing us to reach the necessary phase space density for quantum simulation.

In the following, we explore the techniques employed to cool a hot atomic gas of potassium to quantum-degeneracy in more detail. The cooling process begins with a magneto-optical trap and laser cooling. Subsequently, the atoms undergo evaporative cooling in magnetic and optical traps. Finally, we discuss the atom transfer into a two-dimensional optical lattice, which serves as the starting point for the experiments conducted in this thesis.

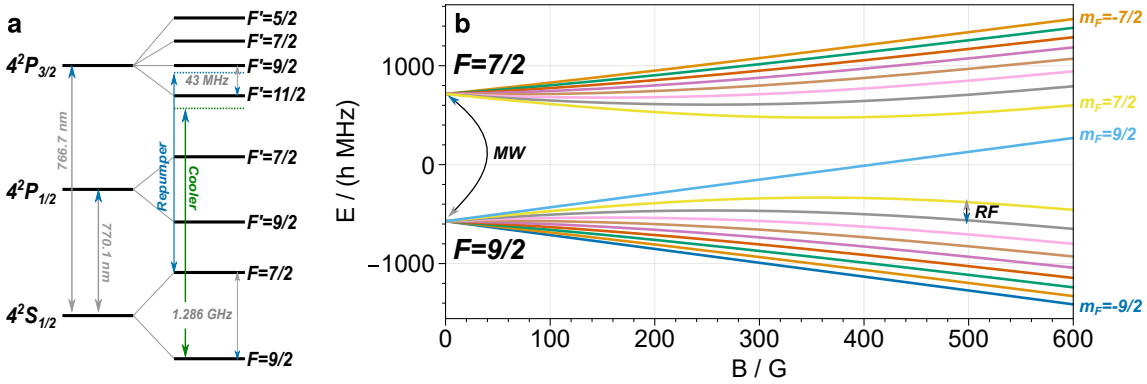

Figure 3.1: **Level Structure of ^{40}K with and without external magnetic field:** (a) Level Scheme of ^{40}K without a magnetic field. The atoms are primarily cooled on the $|F = 9/2\rangle \rightarrow |F' = 11/2\rangle$ transition of the D2 Line with an additional repumper laser that is necessary due to the small energy splitting of the excited state manifold. Both lasers are red detuned by 32 MHz with respect to their transitions and therefore contribute to the cooling of the atom cloud. (b) Breit-Rabi diagram of the two lowest hyperfine manifolds in an external magnetic field. The energy difference between (within) the two manifolds is in the microwave (radio-frequency) regime.

3.1.1 Properties of potassium-40

We conduct our experiments with the fermionic isotope of potassium ^{40}K. This Alkali atom has one valence electron and a nuclear spin $I = 4$. The consequential level structure is shown in figure 3.1 and is particularly suited for laser cooling. The ground state $4^2S_{1/2}$, with a total angular momentum quantum number $J = 1/2$, composes of two hyperfine-manifolds $|F = 9/2\rangle$ and $|F = 7/2\rangle$. We laser cool the atoms primarily on the $|F = 9/2\rangle \rightarrow |F' = 11/2\rangle$ transition of the D2 Line (766.7 nm). However, due to the relatively small level spacing in the excited states, some atoms are off-resonantly excited to the $|F' = 9/2\rangle$ state from which they can decay to the $|F = 7/2\rangle$ state. Therefore, a second laser is used to re-pump the atoms back into the primary cooling cycle. Both lasers are red detuned by 32 MHz to provide an effective cooling force.

Introducing an external magnetic field $\boldsymbol{B} = B\hat{e}_z$ lifts the energy degeneracy of the ground state. In particular, for the two hyperfine manifolds of the ground state, the Hamiltonian in an external magnetic field is given by

$$\hat{H}_{HF} = \frac{A}{\hbar^2}\hat{I}\cdot\hat{J} + \frac{1}{\hbar}(g_J\mu_B m_J - g_I\mu_N m_I)B. \tag{3.1}$$

For the magnetic fields used in typical quantum-gas experiments of up to a few hundred Gauss, the hyperfine Hamiltonian crosses from the low-field (Zeeman) regime to the high-field (Paschen-Back) regime. In the low-field regime, the hyperfine constant dominates the magnetic coupling $A \gg g_J\mu_B B$, causing the electron and nuclear angular momenta to couple into the total angular momentum F. In the high-field regime $A \ll g_J\mu_B B$, the external magnetic field dominates, and both momenta couple individually to the external field. Although the good quantum numbers differ between these two regimes, the magnetic quantum number m_F remains a valid quantum number in both. The energy spectrum in this system is known as the Breit-Rabi spectrum [60, 91] and is depicted in figure 3.1 b.

For small magnetic fields, the eigenenergies scale linearly with the magnetic field. Here, the atoms are in the Zeeman regime, where their energy scales with the magnetic quantum number m_F.

However, in the high-field regime $> 500\,G$ the eigenenergies depend mostly on the electronic angular momentum m_J which can have a different slope and sign. In this work, we mostly work in the regime around $\approx 200\,G$, where the Feshbach resonance of the lowest two m_F states is located (cf. figure 2.9). Here, in between the two magnetic-field regimes, the level splitting between the different m_F is not equidistant, allowing for selective transfers between the states by radio-frequency (RF) pulses (section 3.3.1). On the other hand, the energy difference between the F states is in the GHz regime, which allows for microwave (MW) transfers.

3.1.2 Magneto-optical trap and transfer to the science cell

The first step in the experimental sequence to cool our atom from room temperature to quantum-degeneracy is the magneto-optical trap (MOT), which is described in detail in [84, 85, 92]. We use enriched Potassium with approximately 10 percent ^{40}K that is directly loaded from the background gas into our MOT.

The MOT consists of three pairs of counter propagating laser beams and a magnetic field gradient created by a pair of coils in anti-Helmholtz configuration. This creates a position dependent force, simultaneously trapping and cooling the atoms depending on the detuning of the lasers from the D2 line. In the first step, a large detuning is chosen to realize a large capture range, when initially confining the atoms. Then, the density of the cloud is increased by decreasing the detuning. Finally, the intensity of the repumper is reduced drastically, which realizes a *dark MOT* [93], where only a small fraction of the atoms are actively part of the cooling cycle. This increases the atomic density further, as the repulsive forces from rescattered photons are decreased.

Loading the MOT directly from the background gas has the upside of fast loading cycle that produces approximately 500×10^6 atoms in 5 s with a temperature close to the Doppler temperature

$$T_D = \frac{\hbar\Gamma}{2k_B} = 150\,\mu\text{K}. \tag{3.2}$$

However, the downside is a relatively high vacuum-pressure of $\sim 10^{-9}$ mbar. As a result, the collision rate of the atomic cloud with the background gas is too high to reach quantum-degeneracy. Therefore, the atoms are transported mechano-magnetically from the MOT-chamber to the science-chamber. The science chamber consists of a glass-cell in an ultrahigh vacuum system with a background-pressure of $\sim 10^{-11}$ mbar. The transport is realized by moving a magnetic trap between the two chambers mechanically on a ballscrew-based translation stage.

To load the atoms from the MOT into the magnetic trap, they need to be in trappable low-field seeking state $m_F > 0$. However, after the MOT they populate all m_F states equally which is addressed by an optical pumping procedure after turning off the MOT. Here, σ^+ light is shone onto the atoms while creating a homogenous magnetic along the z-axis, defining the quantization axis. This pumps the atoms dominantly to the $|m_F = 9/2\rangle$ and $|m_F = 7/2\rangle$ states that are then trapped in the minimum of a magnetic quadrupole field created by two coils in anti-Helmholtz configuration. This coil-pair is attached to the motorized translation stage that moves the atoms to the science chamber.

3.1.3 Evaporative cooling to quantum-degeneracy

We perform two evaporative cooling steps in the UHV science chamber: the first is conducted in a magnetic trap and the second in an optical dipole trap. Evaporative cooling in general follows the

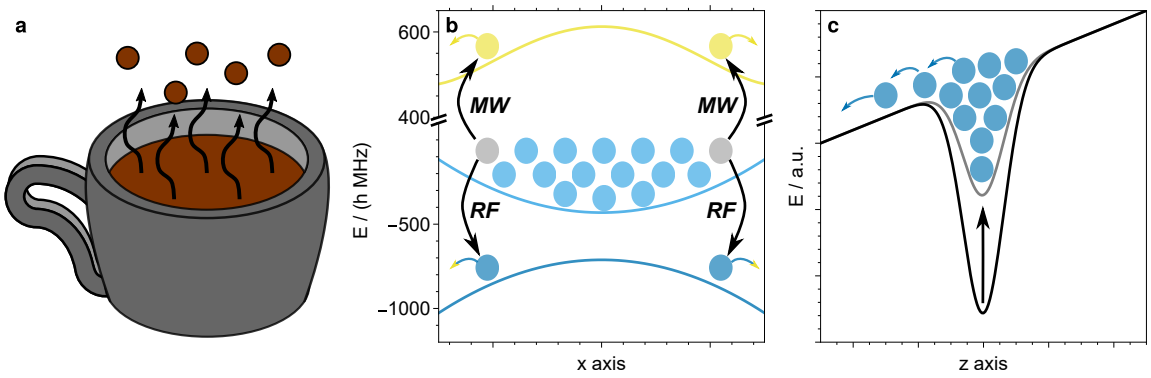

Figure 3.2: **Schematics of various evaporative cooling techniques:** (a) Evaporative cooling of a hot cup of coffee. The hottest atoms evaporate from the cup, effectively lowering the temperature. (b) Forced evaporative cooling technique in the magnetic trap around 100 G. Atoms in the $|F = 9/2, m_F = 9/2\rangle$ state (light blue) occupy different regions of the trap depending on their temperature. First, the hot atoms are selectively transferred by a MW pulse to the untrappped $|F = 7/2, m_F = 7/2\rangle$ state (yellow). In a second evaporation step, a RF transition to the untrapped $|F = 9/2, m_F = -9/2\rangle$ state (blue) is utilized for lower temperatures. (c) Evaporative cooling in an optical dipole trap. Gravity tilts the confining potential of the dipole trap for low intensities. Reducing the optical power spills the hottest atoms from the optical dipole trap. This sub-figure was inspired by [88].

same working principle as cooling down a hot cup of coffee (compare figure 3.2). Initially, the trapped ensemble consists of atoms at various temperatures that follow the Boltzmann distribution. Selectively removing the hottest atoms allows the ensemble to thermalize to a lower temperature, where the high energy states are populated by fewer atoms. Repeating this process then iteratively reduces the population of the high energy states and thus continuously lowers the temperature of the ensemble. This principle holds true for all trap designs, however, the selective removal technique can range from blowing into a cup for your morning coffee to applying a radio frequency pulse in a magnetic trap.

At first, the atoms are confined in an Ioffe-Pritchard trap, a magnetic trap with a non-zero field minimum [84, 85]. This design has the advantage of absent Majorana-losses at the field minimum and a large mode overlap with the dipole traps of the next cooling step. Initially, the removal process is forced by a microwave transfer to the untrapped high-field seeking states ($B < 200\,G$) of the $|F = 7/2\rangle$ manifold (compare figure 3.1). During this process atoms with higher temperatures are selected by choosing a microwave frequency for large magnetic fields that are only experienced by the hot atoms on the edges of the trap (compare figure 3.2 b). An interesting advantage of this process is that it removes the population of the unwanted low m_F states that more likely populate the outer regions of the trap due to their smaller magnetic moment [85]. This MW evaporation is followed by a radio-frequency evaporation to the lowest m_F states of the $|F = 9/2\rangle$ manifold that is more efficient for lower temperatures. After the evaporative cooling in the magnetic trap, we obtain roughly 10×10^6 atoms at $3\,\mu K$.

In the next step, the atoms are transferred from the magnetic trap to a crossed-beam optical dipole trap (compare section 2.1). These traps have the advantage over a magnetic trap, that their depth is not dependent on the internal state of the atoms. The two red-detuned beams in use are the horizontal dipole trap (Dth) and the dimple dipole trap (Dtd), both with a wavelength of 1 064 nm. First, the atoms are transferred from the magnetic trap to the Dth, which has a similar confinement as the

Axis	Lattice type	Lattice spacing	Laser source
x	retro reflection	$a_x^{1064} = 532\,\text{nm}$ $a_x^{532} = 266\,\text{nm}$	NKT Koheras Adjustik + Boostik Y10 SHG + Coherent Mephisto MOPA 55W
y	retro reflection	$a_y^{1064} = 532\,\text{nm}$	Innolight Mephisto MOPA 20W
z	shallow-angle	$a_z^{1064} = 2\,129\,\text{nm}$ $a_z^{532} = 1\,064\,\text{nm}$	Innolight Mephisto Coherent Verdi V10

Table 3.1: **Parameters of three-dimensional optical lattice setup**

magnetic field due to the small beam waist along the z-direction $w_z = 12.5\,\mu\text{m}$. Here, we transfer the atoms from the highest m_F states to the two lowest hyperfine states $m_F \in \{-9/2, -7/2\}$ via a Landau-Zener sweep (compare section 3.3.1). We perform up to three spin-mixing pulses [88], to ensure a balanced population of our quasi-spin states for the following experiments.

Then, we include the dimple to deepen the potential of the optical trap. In particular, the additional laser increases the confinement along the z-direction of our optical dipole trap and ensures a high phase-space density throughout the following evaporation process. This evaporation is performed simply by lowering the intensity of both dipole lasers. As a consequence, the high-temperature atoms are pulled from the trap by gravity along the z-direction figure 3.2.

This evaporation is performed in two steps: first at repulsive interactions ($B = 235\,G$) and then at attractive interactions ($B = 204\,G$). This final attractively-interacting evaporation has the benefit of higher atomic densities at the trap center and therefore better band-insulator fidelities in the optical lattice. We characterize the final evaporation step in a thermometry measurement by ballistic expansion [72, 80, 94] that gives

$$100 \times 10^3 \text{ atoms, at } T \lesssim 0.1\,T_F \tag{3.3}$$

with the Fermi temperature T_F. With these temperatures well below the Fermi-temperature, we have reached the quantum-degenerate regime, where the behavior of the fermionic cloud is dictated by quantum statistics. For a detailed discussion of the current evaporation process in the dipole traps, please refer to [88].

3.1.4 Loading into a two-dimensional optical lattice

At the heart of the experimental apparatus lies a three-dimensional optical lattice setup. The lattices along the x- and y-direction are created by means of retro reflection, while along the z-direction a shallow-angle lattice is created by interfering two beams under an angle of 29° (cf.figure 3.3). In general, we either use red-detuned infrared lasers with a wavelength of 1 064 nm or blue-detuned green lasers with a wavelength of 532 nm to create the optical lattices.

In the following, we discuss the experimental sequence to create a quantum-degenerate Fermi gas in a two-dimensional optical lattice. This is the starting point of all experiments discussed in this thesis. We start by loading the three-dimensional Fermi gas from the optical dipole traps into the green lattice along the z-direction within 3 second. Here a further evaporation procedure is realized by the interplay of the attractive dipole traps and the repulsive lattice beam [80]. In particular, the repulsive nature of the lattice introduces additional local minima of the potential from which the hot

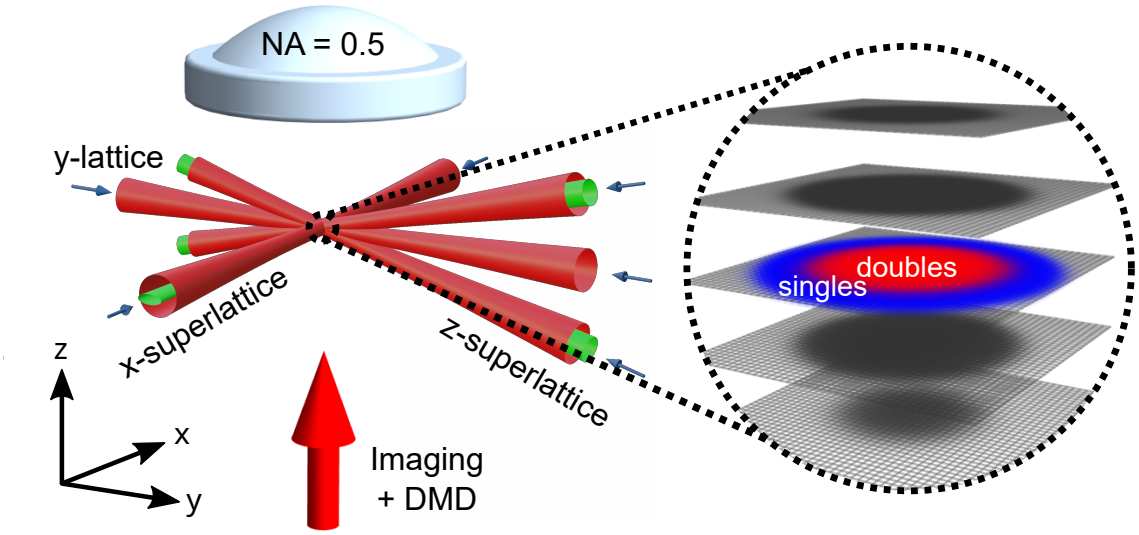

Figure 3.3: **Three-dimensional optical lattice setup:** The green shallow-angle lattice along the z-direction separates the cloud into a *pancake* structure. Two infrared lattices along the x- and y-direction are created by retro reflection and realize a two-dimensional optical lattice. The apparatus is extended further, by superimposing an infrared (green) laser along the z-(x-)direction, which creates an optical superlattice. Details on the specific lattice parameters are given in table 3.1. This figure was adapted from [72].

atoms are able to escape. This additional evaporation step is necessary, as the loading itself is not sufficiently adiabatic which leads to higher band populations of the lattice.

In the second-step, the infrared in-plane lattices are ramped within 500 ms to $6\,E_{\mathrm{rec}}$. This time was optimized to be the shortest timescale for which the system has thermalized in the lattice. To this end, two different thermometers in the lattice were compared: the spin correlations via the staggered structure factor (SSF) and the temperature extraction from the density profile. The spin correlations are measured in an auto-correlation analysis of the spin states after a Ramsey-type sequence [95]. On the other hand, the density thermometer extracts the temperature from the fitted equation of state [96].

For loading times larger than 500 ms, both thermometers measure a constant heating rate of $(0.37 \pm 0.05)\,\mathrm{t/s}$ [1]. In contrast, for smaller loading times, only the spin-thermometer detects the linear scaling whereas the density-thermometer measures much higher temperatures. This deviation is accounted to density redistributions during the thermalization process that are detected by the density-sensitive thermometer. The realized temperatures in the 2D Fermi-Hubbard model depend on the relative interaction strength U/t and the absolute timescale t defining the thermalization time. For a repulsive interaction of $U/t = (8.2 \pm 0.5)$, [2] my colleagues have measured temperatures from $k_B T/t = (0.96 \pm 0.02)$ [98] down to $k_B T/t = (0.63 \pm 0.02)$ [96] showcasing a quantum-degenerate fermionic gas in a two-dimensional optical lattice.

With this procedure we have prepared a two-dimensional realization of the Fermi-Hubbard model in the quantum-degenerate regime. This serves as the starting point for all experiments conducted

[1] This heating rate is extrapolated for a constant lattice depth.

[2] At this specific interaction, the highest temperature $k_B T/t \sim 0.3$ for the occurrence of anti-ferromagnetic ordering is expected [97].

during this thesis.

It should be noted, that there is also a digital micro-mirror device (DMD) installed in the experimental apparatus. We use a far detuned laser at 730 nm to image the almost arbitrary pattern of the DMD onto the atomic cloud along the z-imaging axis. This was successfully used to create potential barriers separating the high-density from the low-density regions of the two-dimensional lattice [31, 88, 90]. However, when compensating for the Gaussian envelope of the lattice beams with the DMD, the atoms localize and become immobile [99]. This observation is accounted to disorder in the DMD potential on length-scales that are not observable due to our limited resolution. The DMD was not used in the experiments discussed in this work, and the reader is referred to the aforementioned works of my colleagues, for more detailed information.

3.2 Superlattice setup

We have implemented an optical superlattice along the x-direction of our three-dimensional lattice setup during this work. This superlattice is created by superimposing a 1 064 nm and a 532 nm laser, forming a bi-chromatic lattice structure through retro-reflection from the same mirror.

The infrared laser in use is a NKT photonics *Koheras Adjustik/Boostik Y10* with a linewidth reduced to less than 3 kHz. The green laser is created by second-harmonic generation (SHG) from a Coherent *Mephisto MOPA 55W* 1 064 nm pump laser. This procedure provides us with a green laser source that inherits the small line width of its pump laser (1 kHz over 100 ms [100]) which are superior to other commercially available green lasers like the *Verdi* laser systems with a linewidth in the MHz regime [101]. Detailed experimental information on this SHG in a monolithic bow-tie cavity can be found in my Bachelor thesis [102].

This section is organized as follows. First we introduce the optical setup to create an intensity-stable optical superlattice in the atom-plane. Next, we discuss the relative-phase control of both lasers on short and long timescales independently. This enables stable superlattice phases that can be modulated quickly for the realization of Floquet-driven systems.

3.2.1 Optical setup of the in-plane superlattice

The optical setup of the superlattice is separated into two parts. On the *laser table*, both lasers are intensity- and phase-stabilized before being coupled into optical fibers going to the *experimental table*. On the experimental table, the lasers are superimposed and used to create an optical superlattice at the atom position.

Optical setup on the laser-table

The optical setup on the laser table to obtain an intensity stable pair of 1 064 nm and 532 nm lasers is shown in figure 3.4. It was initially set up during my Master thesis [63] and significantly updated since. The following paragraph describes this optical setup and is partially extracted from my Master thesis.
X1064: The pair of half-wave plate ($\frac{\lambda}{2}$) and polarization dependent beam splitter (PBS) splits the laser power in two parts. The majority of the light is sent through an acousto-optic modulator (AOM) in double-pass configuration before being coupled into the fiber towards the experiment. The purpose of this AOM is two-fold: Firstly, it is used to stabilize the intensity of the laser on the experimental side. For this purpose, a photodiode on the experimental table (see figure 3.5) monitors the intensity

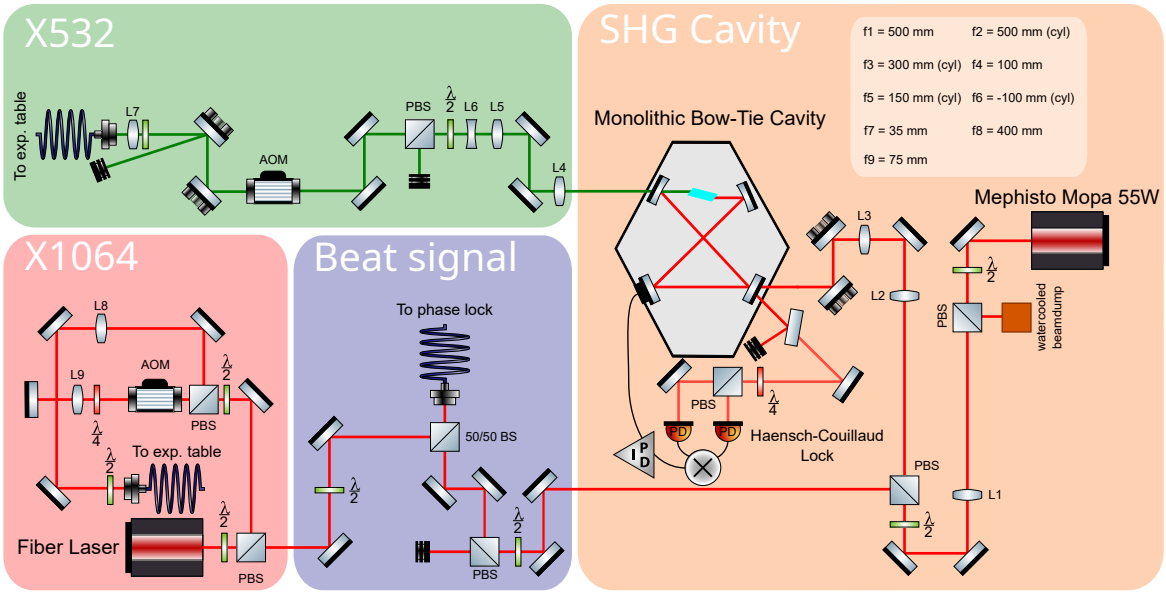

Figure 3.4: **Superlattice setup on laser table:** Optical setup to create a phase and intensity stable pair of 1 064 nm and 532 nm lasers. This graphic is adapted from [63].

of the laser and changes the RF input power of the AOM in a feedback loop accordingly. Secondly, the frequency of the AOM can be changed to control the frequency of the infrared laser in a rapid fashion, which will be discussed in more detail in the next section.

SHG Cavity: The infrared laser is mode matched and coupled into the monolithic-bow-tie cavity. Here, the SHG is performed using a Lithium Triborate (LBO) crystal with a high damage threshold lager than 10 GW/cm^2 [103]. A Haensch-Couillaud lock [104] ensures that the optical path length inside the cavity is kept resonant to the pump laser frequency using a piezo chip behind one of the cavity mirrors. The principle of the lock itself is the following: The cavity represents a polarization filter due to the Brewster cut of the LBO crystal, resulting in a clean p-polarization inside the cavity. Therefore, when probing the beam reflected from the cavity, the light that picked up the phase inside the cavity is orthogonally polarized to the directly reflected beam. These two parts get mixed again using a quarter-wave plate, a PBS and a balanced photodiode *PDB210A/M* from Thorlabs resulting in an error signal which is fed back to the piezo mirror. In the current configuration, pumping the cavity with $\sim$ 18 W leads to $\sim$ 5 W green laser power.

X532: The cavity output beam is divergent and elliptic which is compensated by a collimation lens right after the cavity and a cylindrical telescope of 2/3 x magnification (in the p-axis). This results in a $1/e^2$ beam diameter of $\sim$ 2 mm. The light is coupled through an AOM to create an intensity stabilization scheme similar to the aforementioned one. Finally, a single-mode polarization-maintaining photonic-crystal fiber *LMA-PM-15* from NKT photonics guides the light to the experiment table. We have observed a drastic dependence of the fiber-coupling efficiency on the minimal bending radius of this photonic crystal fiber. Therefore, we ensure a minimal bending radius $>$ 30 cm and achieve a fiber coupling efficiency of $>$ 65 %. We attribute this limited coupling efficiency to the remaining ellipticity of the beam profile.

Beat signal: A small fraction of the X1064 laser power and the X532 pump laser power is used

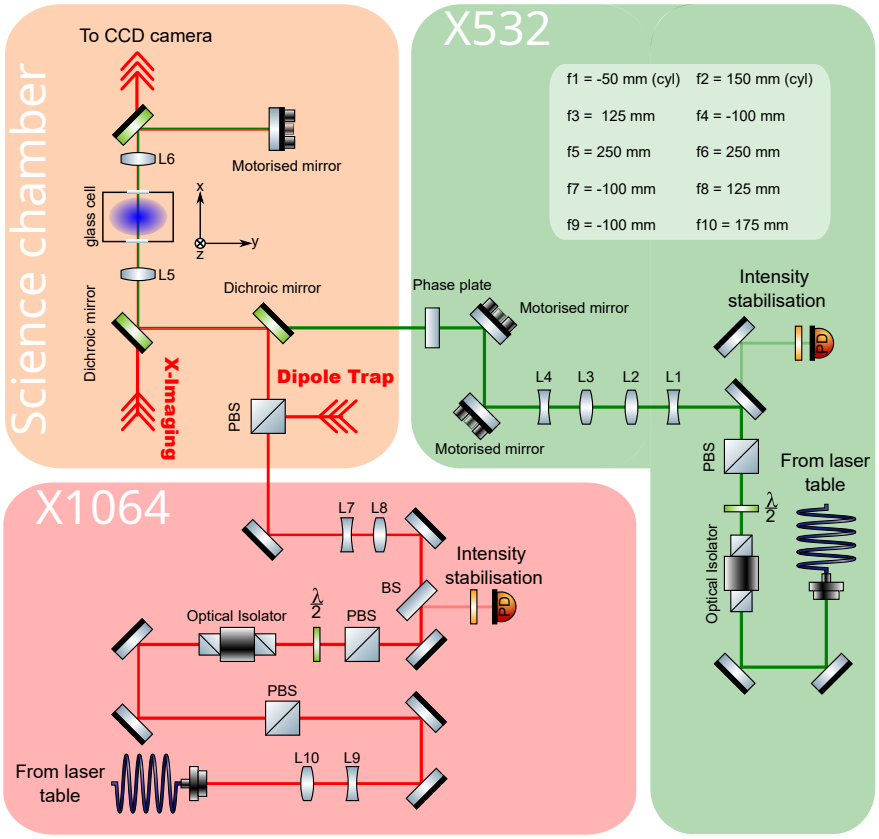

Figure 3.5: **Superlattice setup on experimental apparatus:** Optical setup to create a bi-chromatic superlattice by retro-reflection from the same mirror. This graphic is adapted from [63].

to create a beat signal. In particular, both infrared beams are overlapped using a 50/50 BS and coupled into the same fiber leading to a fiber-coupled avalanche photodiode DET08CFC/M with 5 GHz bandwidth from Thorlabs. This creates a beat signal of the frequency difference of both lasers that is used in a phase-lock scheme to stabilize the frequency and phase difference of both lasers (compare section 3.2.2).

Optical setup on the experiment-table

The optical setup of the x-direction superlattice on the experimental side is shown in figure 3.5. The infrared lattice along the x-direction was implemented many years ago [72, 80], while the green lattice was initially set up during my Master thesis [63]. Therefore, the following paragraph is partially extracted from this work with updates according to the significant changes.

X1064: The infrared beam is polarization cleaned and beam-shaped after the out-coupling from the fiber. An optical isolator (*M714* from *conoptics inc.*) prevents back-reflections into the fiber. A fraction of the laser power is split, wavelength filtered using a line filter and monitored on a photodiode (PD). This PD signal is used for the intensity stabilization of the lattice laser. In particular, intensity fluctuations at the PD are compensated in a feedback loop with the AOM on the laser table. After another beam shaping telescope, the lattice laser is sent to the science chamber.

Science chamber: The infrared beam is overlapped with the horizontal dipole trap using a PBS and subsequently aligned and focused onto the atom cloud. Moreover, the last dichroic mirror before the chamber enables imaging along the x-direction. After the glass cell, the beams are collimated by the achromatic doublet *YAP-250* from *CVI Laser Optics* with a focal length of 250 mm. Then another dichroic mirror transmits the imaging wavelength 767 nm to a CCD camera which images the atom plane. However, a small fraction of the infrared and green light is also transmitted enabling a monitoring of the beam profile at the place of the atoms. Finally, a motorized mirror, which will be referred to as retro-mirror, retro-reflects the lattice lasers resulting in a standing wave intensity pattern at the position of the atoms.

X532: The green lattice setup also consists of an optical isolator and an intensity stabilization photodiode. A cylindrical telescope creates an elliptical beam shape with an aspect ratio of $w_z/w_y \sim 0.4$ in the atom plane. This ellipticity allows for the creation of deeper lattices for a given power at the cost of a decreased Rayleigh length. However, due to the small extend of the atomic cloud along the z-direction the larger beam divergence is acceptable. The green beam is superimposed with the infrared beam by two motorized mirrors before the dichroic mirror. Finally, a 10 mm thick anti-reflection coated window from *Eksma optics* in a motorized mount from *Newport Agilis* is used to displace the beam. This displacement leaves the position of the beam at the atoms-position unchanged while it varies its angle. In section 4.1.2 we demonstrate, that this *X532-displacement plate* angle can change the superlattice phase spatially in the atom plane.

3.2.2 Superlattice phase control

The final and most challenging task in the setup of the optical superlattice is the phase stability. This superlattice phase ϕ controls the symmetry of the optical potential

$$V_{\text{sup}}(x) = V_L \cos(k_L x + \phi)^2 + V_S \cos(k_S x)^2 \tag{3.4}$$

with the lattice depths V_i and wave vectors $k_S = 2k_L$. However, the individual phases of the lattice potentials cannot be altered directly. Specifically the retro-reflection that generates the standing-wave intensity pattern creates a node at the mirror position, thereby the lattice phases. Instead, a relative phase at the atom position is accumulated by detuning the laser frequency of the infrared lattice $k_L \rightarrow k_L + \delta_k$, which is sketched in figure 3.6. This detuning induces the superlattice phase

$$\phi = L \cdot \delta_k = L \cdot \frac{2\pi\delta_\nu}{c} \tag{3.5}$$

with the optical path length between the atom cloud and the retro-mirror $L \sim 50$ cm. The periodicity of our superlattice configuration is $\pi/2$ (cf. figure 2.3), which requires a frequency change of $\delta_\nu \sim 150$ MHz.

We achieve experimental control over the superlattice phase by the frequency of the infrared laser in a two-fold approach. Firstly, we lock its frequency to the infrared pump laser for the SHF in an optical phase locked loop [105]. In this process, we also account for changes in the optical path length due to environmental parameters (i.e. pressure, temperature) in a feed-forward mechanism. Secondly, we adjust the frequency of the infrared lattice laser with a double-pass AOM after the phase-lock. This serves as a secondary tuning knob for the superlattice phase which we use to realize periodically modulated superlattice potentials.

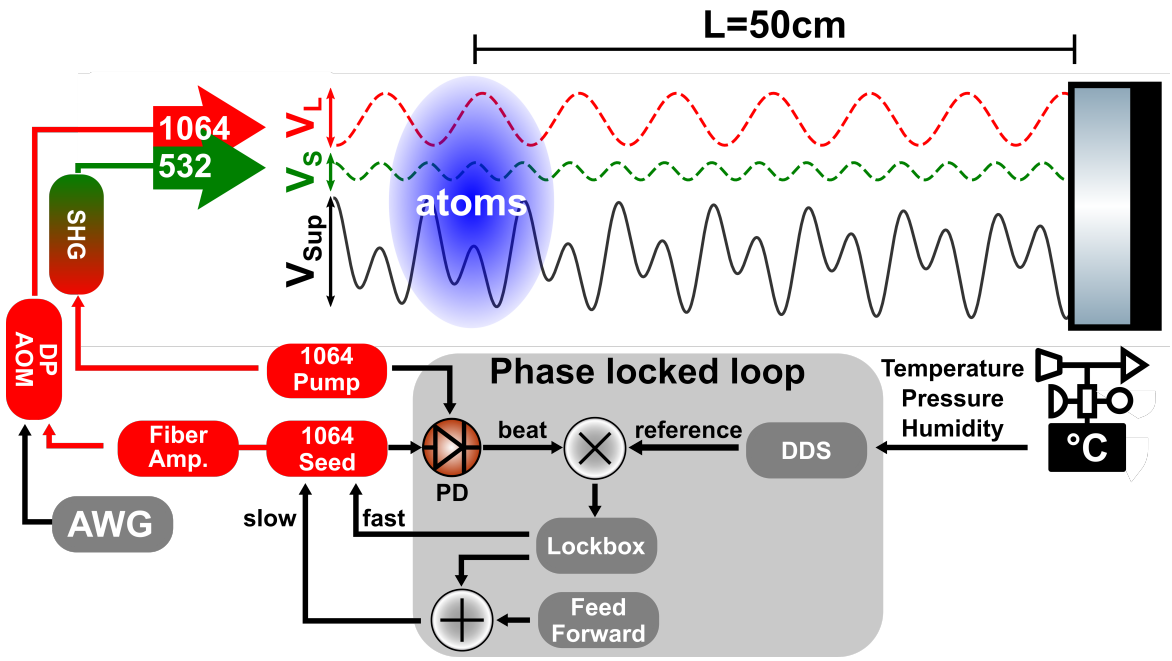

Figure 3.6: **Superlattice phase stability schematic:** Detailed information is given in the text.

Phase locked loop and environmental feed-forward

We experimentally achieve a stable superlattice phase by an optical phase locked loop (PLL) [105], as depicted in figure 3.6. In short, the beat signal $\Delta\nu$ between the infrared lattice laser *1064 Seed* and the infrared pump laser for the SHG *1064 pump* is compared to a reference frequency ν_{ref} and feed-back to the former laser.

The reference frequency is created by a direct digital synthesis device (DDS) *AD9914* that uses an external 10 MHz clock and digital-to-analog conversion to create analog frequency signals of up to 1.4 GHz [106]. The DDS creates a variable reference frequency that can also be swept linearly to create phase ramps.

The mixed signal of the beat and the reference frequency is then split in a fast and a slow feedback loop. For the fast feedback loop we use a fast analog linewidth control unit *mFALC110* from *Toptica* with a bandwidth of up to 100 MHz. This is connected to the current modulation port of the *1064 Seed*, a self-built interference filter laser [107], that is connected to the fiber amplifier from NKT photonics. We have replaced the commercial seed laser from NKT because of its limited frequency modulation linewidth of ~ 20 kHz.

For the slow feedback loop, we use a self-built PID lock box with a sufficient bandwidth of ~ 15 kHz that is connected to the piezo of the seed laser. Moreover, we have the possibility to apply a feed-forward voltage directly to the piezo of the seed laser. This is necessary for fast linear ramps of the superlattice phase that otherwise risk the lasers to fall out of lock.

In practice, our phase locked loop has the purpose to create a minimal linewidth beat signal as the phase stability itself is given by the aforementioned node at the retro-mirror. We observe a locked beat signal with a bandwidth (FWHM) $\ll 1$ kHz that greatly exceeds the former results of our frequency offset lock ~ 10 kHz [63].

This linewidth is 5 orders of magnitude smaller than the periodicity of the superlattice, which suggests an excellent stability of the superlattice phase. However, this statement is only true for the precision of the phase and not the accuracy. The accuracy of the superlattice phase is greatly worsened by the change of the optical path length L by the environmental parameters: temperature T, pressure P and humidity H. These parameters change the relative refractive index of air (and glass) between the lattice lasers and thus the relative optical path length.

We measure the environmental parameters with a *BME280* sensor from *Bosch* on the optical table close to the retro-mirror. The temperature on the optical table is regulated by a filter fan unit (FFU) in combination with an AC system and therefore only drifts on the order of $\sim 0.1\,^{\circ}\mathrm{C}$. The pressure in the lab is not regulated and therefore changes according to the whether which can be on the orders of a few 10 mbar over the course of a day. The humidity in the lab is also not regulated but limited by dehumidifiers below typically 40 %. Typical changes in the humidity over the course of a day are on the order of a few percent.

In the following, we discuss the impact of the environmental parameters on the two main constituents of the optical path: air and various glasses. We use a calculation based on the Ciddor equations [108] to model the refractive index change of air with the environmental parameters [109] for the two wavelengths. According to these equations the refractive index is linear within all environmental parameters, which we therefore reference to

$$T_0 = 23\,^{\circ}\mathrm{C},\ P_0 = 1\,000\,\mathrm{mbar},\ H_0 = 25\,\%. \tag{3.6}$$

We calculate the change of the superlattice phase with the environmental parameters using equation 3.5 and the geometrical path length in air $l_{\mathrm{air}} = 45.8\,\mathrm{cm}$:

$$\frac{\delta\phi}{\delta P} = -1.04\,\mathrm{MHz/mbar},\ \frac{\delta\phi_{\mathrm{air}}}{\delta T} = 2.09\,\mathrm{MHz}/^{\circ}\mathrm{C} \text{ and } \frac{\delta\phi}{\delta H} = -0.08\,\mathrm{MHz}/\%. \tag{3.7}$$

Clearly, for the optical path in air the aforementioned pressure changes have the largest impact on the superlattice phase.

The optical path also propagates through the L6 lens (cf. figure 3.5) that consists of 13 mm NBK7 and 4 mm NSF11 glass as well as through 4 mm UVFS of the glass cell. The refractive index of these glasses changes significantly with temperature, while it remains constant for pressure and humidity changes. We calculate the change of the superlattice phase contribution of glass from the Sellmeier equation

$$\frac{\delta\phi_{\mathrm{glass}}}{\delta T} = -12.3\,\mathrm{MHz}/^{\circ}\mathrm{C},\ \text{which gives}\ \frac{\delta\phi}{\delta T} = \frac{\delta\phi_{\mathrm{glass}}}{\delta T} + \frac{\delta\phi_{\mathrm{air}}}{\delta T}. \tag{3.8}$$

We measure the environmental parameters once per experimental cycle and compare them to the reference values T_0, P_0 and H_0. Then, we adjust the set value of the DDS according to the calibrated slopes of the superlattice phase. We discuss the characterization of the superlattice phase in section 4.1.2, where we show the successful compensation of the environmental changes. This environmental feed-forward was primarily developed by my colleague Janek Fleper [110].

Superlattice phase modulation

We modulate the superlattice phase with an AOM in double-pass configuration. This double-pass configuration is realized by coupling the deflection of the AOM in a cat-eye configuration back through

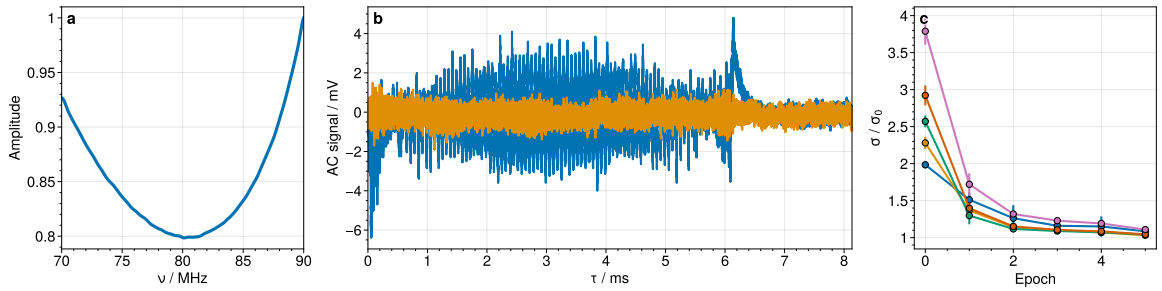

Figure 3.7: **Calibration of the superlattice phase modulation:** (a) For a given RF amplitude the observed intensity at the regulation PD varies with the carrier frequency, showcasing the frequency dependent diffraction efficiency of the AOM. This is compensated by an amplitude rescaling (blue) that limits the power to the minimal observed power. (b) Time calibration of a modulation signal. In the first three milliseconds the modulation amplitude is ramped linearly to $A^{\nu}_{\mathrm{mod}} = 5\,\mathrm{MHz}$. For the next two milliseconds the signal is modulated at full amplitude with a driving frequency of $\nu_{\mathrm{mod}} = 15\,\mathrm{kHz}$. Finally, the amplitude is ramped down in the same fashion as before. The observed AC signal on the photodiode is shown without compensation (blue) and after the fifth compensation step (orange). (c) The standard deviation σ of the AC coupled signal is compared to the static noise floor σ_0 for various compensation epochs. The different modulation amplitudes $A^{\nu}_{\mathrm{mod}} = 2,\ 4,\ 6$ and $8\,\mathrm{MHz}$ are shown in blue, orange, green, red and pink.

the AOM. With this setup, the frequency of the acoustic-wave in the AOM –and therefore the frequency of the laser beam– can be changed without beam steering. The AOM in use is a *3080-199* from *G&H* with a carrier frequency of 80 MHz and a bandwidth of 20 MHz. Compared to the periodicity of the superlattice in the MHz regime and usual tunneling amplitudes of a few hundred Hz, this is a very suitable setup for fast modulation of the superlattice phase.

We generate the RF source for the AOM with an arbitrary-waveform generator (AWG) board *M4i.6631-x8* from *spectrum instrumentation*. This AWG has a sampling rate of 1.25 GSamples/s and a bandwidth of 400 MHz on two output channels. We program [3] the AWG to write segments of sinusoidal signals with variable amplitudes and phases, that are output one after another. In the static scenario, the AWG outputs a sinusoidal signal with a frequency of 80 MHz. For a periodic modulation, we change the carrier frequency also in a sinusoidal manner while preventing phase slips of the signal between the different segments.

It is crucial to avoid lattice-heating during the periodic modulation. Therefore, we minimize the intensity noise of the optical lattice during the modulation-sequence in a two-step procedure. First, we compensate the carrier-frequency dependent diffraction efficiency of the AOM, as shown in figure 3.7 a. For this purpose, we measure the lattice intensity at the experiment-PD for various carrier frequencies and compensate lower diffraction efficiencies with increased RF power. This procedure also compensates power losses due to residual beam-steering at the cost of maximal lattice depth. The calibration itself is dependent on the overall RF-power, but otherwise stable over months.

In the second step, we compensate for time-dependent intensity fluctuations that occur for fast changes of the carrier-frequency. The lower limit for frequency changes is given by the rise time of the AOM which is in our case a few hundred nanoseconds for a beam diameter of 1 mm and the speed of sound in the crystal material *TeO2* 4.2 mm/µs. However, also for frequency changes that are slower than the rise time, we observe intensity fluctuations. We account these ripples in the laser intensity to

[3] For details on the programming of the AWG please refer to [111].

interference effects between forward-going and reflected acoustic wave with different frequencies. These ripples are strongly dependent on the specific modulation parameters and must therefore be compensated for each modulation scheme individually.

At the beginning of each experimental sequence a time calibration for the specific modulation scheme is performed. First, the modulation signal is applied to the AOM and the response of the lattice intensity is observed on the PD (compare figure 3.7 b). Then, the RF-amplitude of the different frequencies is adjusted to compensate for the intensity fluctuations. This procedure is repeated in usually five epochs to converge to an acceptable intensity profile. The ultimately obtained signal is then used for the experimental realization a few seconds later. We compare the noise floor of the modulated signal by the standard deviation of the ac coupled signal σ to the corresponding un-modulated intensity noise σ_0 in figure 3.7 c. For an uncompensated signal the noise floor strongly depends on the modulation amplitude of the modulated signal and can exceed the static counterpart by more than a factor of three. However, after the compensation procedure we achieve lattice intensities with a relatively small noise increase of $\sigma/\sigma_0 \sim 1.1$. This procedure was developed by my colleague Valentin Jonas [112].

3.2.3 Lattice potential characterization

The final step in the setup of our optical superlattice is the calibration of the lattice potential at the atom position.[4] For this purpose, we determine the lattice depths at the trap center as well as the waists of the lattices.

We calibrate the lattice depth by a lattice modulation spectroscopy measurement. In short, we load the atoms in the lowest band of the lattice and then modulate the lattice depth at a variable frequency. When the energy of the driving photons is resonant with a transition from the first- to a higher-band, we observe an atom loss. Finally, we compare the resonance frequencies with band structure calculations (as introduced in section 2.2.1) to determine the corresponding lattice depth. In the past, we have performed this lattice-modulation spectroscopy with a global evaluation technique based on adiabatic band mapping (compare section 3.3.4). This method is explained in detail in my Master thesis [63] but only calibrates the lattice depth at the trap center, which leaves the lattice waist to be determined. For the superlattice, we perform the spectroscopy measurement first for the infrared lattice and then for the superlattice. This way, the infrared lattice depth is already calibrated for the superlattice spectroscopy and the number of free variables is reduced.

The lattice waists are determined in a trap frequency measurement (for details refer to [90]), that determines the overall underlying lattice potential. This potential structure is governed by the Gaussian envelope of the beams, as well as a running-wave component of the lattice beams. The latter is created by a power imbalance γ of forward-going and retro-reflected beam that is caused by losses at the optical components, and which we calibrate directly with a power meter. For the trap-frequency measurement we prepare a spin polarized cloud and deflect the cloud from the center with a magnetic field kick along one axis direction. Along this direction we only create a dipole potential, by blocking the retro-reflected beam, which allows the atoms to perform a sloshing motion in the remaining harmonic confinement. From the frequency of the harmonic oscillation, we calibrate the last uncertainty of the underlying potential: the waist of the lattice beam.

Recently, we have implemented an in-situ lattice modulation spectroscopy. This measurement

[4] This procedure is necessary for all optical lattices but is discussed exemplary for the superlattice.

resolves the lattice depth locally and therefore directly measures the lattice depths and waists. Therefore, it has replaced the two-fold characterization technique with just one measurement. The implementation of this method will be discussed in the thesis of my colleague Janek Fleper [110].

For the optical superlattice, the lattice potential can be characterized even more rigorously by a direct measurement of the Hubbard parameters t, Δ and U. In general, these parameters can be calculated for a given superlattice depth, phase and scattering length, as introduced in section 2.4. However, a direct measurement can be used to verify, or – if necessary– calibrate these theoretical calculations. We discuss this characterization technique in chapter 4.

3.3 Detection methods

The first step for an analogue quantum simulator is to assemble an experimental apparatus that realizes the system of choice. We have discussed this setup to create an ultracold fermionic gas in an optical (super-) lattice in the first two chapters. To further study the system of choice, it is crucial to implement detection methods that extract its characteristic observables.

In this section, we discuss the specific detection methods that were applied in this work. Most of these methods were set up during previous PhD works and will only be shortly summarized. However, the adiabatic band mapping technique (section 3.3.4) to observe sublattice populations in an optical superlattice was newly implemented.

3.3.1 Radio-frequency transfers between hyperfine states

The manipulation of the hyperfine states of the atoms is a fundamental part of every experimental cycle. We have introduced the preparation of the lowest two hyperfine states with high fidelities in the first section of this chapter. However, for the detection procedure we need to change the hyperfine states i.e. to differentiate sites with double occupation from singly occupied sites.

We implement adiabatic transfers between the hyperfine states with RF sweeps. These transfers are can address specific hyperfine transitions as the energy spectrum around $\sim 200\,G$ is not equidistant (cf.3.1) and differs typically by more than 2 MHz. Moreover, we ensure the adiabaticity by implementing Landau-Zener sweeps with a *HS1* pulse form of the RF sweep. This pulse form is used in nuclear magnetic resonance (NMR) spectroscopy [113] and modulates the amplitude and the frequency of the signal.

This state transfer becomes more delicate when considering interactions. For example, we prepare the lowest two hyperfine states and transfer the $|m_F = -7/2\rangle$ to the $|m_F = -5/2\rangle$ state. The two hyperfine mixtures before and after the transfer have different interaction strengths as their Feshbach resonance positions differ (cf. figure 2.9 b). Therefore, the resonance frequency of doubly occupied sites $\nu_{\delta U}$ is shifted by $\Delta U/h = (U_{\text{final}} - U_{\text{initial}})/h$ with respect to the resonance for singly occupied sites ν_s (compare figure 3.8). With this occupation-dependent splitting, we can selectively transfer singly and doubly occupied sites, which gives the name of *singles-doubles spectroscopy* (SD).

This interaction shift is usually on the order of a few kHz and therefore, the pulse width must be chosen carefully. On the one hand, it must be small enough to avoid a transfer of singly occupied sites while it must be large enough to sample the spatially varying interaction shift (cf. figure 6.5). As a compromise, typical Singles-Doubles separation pulses have a width of 1 kHz. Alternatively, a large pulse width of typically 175 kHz is chosen for a transfer of both site occupations.

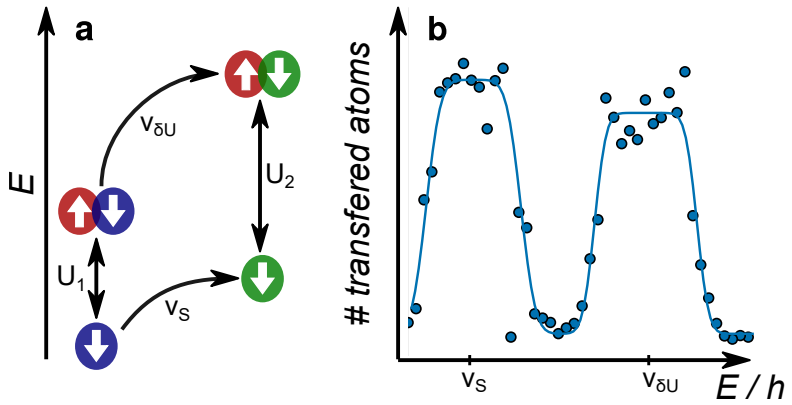

Figure 3.8: **Singles-doubles (SD) spectroscopy:** (a) The hyperfine states have different energies in the external magnetic fields and can be changed by a radio-frequency transfer with frequency ν_S. In a monochromatic lattice configuration, the interaction energy U_i depends on the hyperfine mixture- Therefore, the frequency for a transfer of double occupied sites is different $\nu_{\delta U} \neq \nu_S$ (b) Typical signal for radio-frequency spectroscopy of the differential interaction energy $\Delta U = U_2 - U_1 = h(\nu_{\delta U} - \nu_S)$.

The small pulse width of the SD separation leads to strong requirements on the magnetic field stability: The differential slope between the $|m_F = -7/2\rangle$ and $|m_F = -5/2\rangle$ state of the Breit-Rabi diagram at $200\,G$ is $h \cdot 170\,\mathrm{Hz/m}G$. Therefore, magnetic field stabilities on the order of mG are realized by a μ-metal shielding of the experimental chamber and a low-noise magnetic coil design. For details on the design of the magnetic coils please refer to [72, 80].

It should be noted that these transfers are sensitive to the frequency sweep direction, which can cause unwanted coupling to higher lattice bands [80]. Finally, the RF transfer scheme can also be used as a spectroscopy method for the rich band structure of interacting particles in optical superlattices. We will discuss this RF spectroscopy technique in section 4.2.2.

3.3.2 Strong saturation absorption imaging

We observe the atomic density via absorption imaging on the D_2 line of potassium $4^2S_{1/2} \rightarrow 4^2P_{3/2}$. In short, the atoms are exposed to resonant imaging pulses that imprint a shadow of the atomic cloud onto the imaging beam. We use circularly polarized light σ^- with a wavelength of $\lambda = 766.7$ nm to transfer atoms from $|F = 9/2,\ m_F = -9/2\rangle$ to $|F = 11/2,\ m_F = -11/2\rangle$ in a closed imaging transition.

The optical density (od) is a dimensionless measure of the light absorption that is defined as the intensity difference of the imaging beam before and after the measurement $I_{i,f}$. Using Beers Law [59], the optical density for a low-intensity imaging beam along the z-direction is given as

$$od(x,y) = -\ln(I_f(x,y)/I_i(x,y)) = \sigma_0 n(x,y) \tag{3.9}$$

with the absorption cross-section σ_0 and the column density $n(x,y)$. However, in reality the cross-section of the realized two-level system is intensity dependent

$$\sigma(I) = \frac{\sigma_0}{1 + I/I_{\mathrm{sat}}} \tag{3.10}$$

with the saturation intensity I_{sat}. This gives the modified Beer's law [114]

$$\frac{dI}{dz} \equiv -n\sigma(I(x,y))I(x,y) = -n(x,y)\sigma_0^* \frac{I(x,y)}{1 + I(x,y)/I_{\mathrm{sat}}^*} \tag{3.11}$$

with the effective saturation intensity $I_{\mathrm{sat}}^* = \alpha^* I_{\mathrm{sat}}$ and effective absorption cross-section $\sigma_0^* = \sigma_0/\alpha^*$ induced by the imaging correction parameter α^*, that accounts for all imaging imperfections in the experimental apparatus. Integrating the modified Beer's law and performing a separation of variables then gives the optical density for saturated absorption imaging

$$od(x,y) = -\alpha^* \ln\left(\frac{I_f(x,y)}{I_i(x,y)}\right) + \frac{I_i(x,y) - I_f(x,y)}{I_{\mathrm{sat}}}. \tag{3.12}$$

This strong saturation absorption imaging scheme was developed by Reinaudi et al. [114] and applied to our experiment by J. Drewes [89], L. Miller [80] and E.Cocchi [72] including the crucial calibration of α^*.

3.3.3 High-resolution in-situ imaging

We employ a high-resolution imaging apparatus along the z-direction to obtain an image of the atoms in the two-dimensional optical lattice. This apparatus was already in place and calibrated before this work [72, 80, 89]. Here, we will briefly summarize the setup and the calibration results that are relevant for this work.

At the heart of the imaging setup are two commercially available aspheric lenses (*Thorlabs 352240-B*) glued inside the glass cell (cf. figure 3.9). The high numerical aperture $NA = 0.5$ is achieved using a small working distance of 5.92 mm to the position of the atomic cloud. The achromatic doublet outside the glass cell sets the magnification $\mathcal{M}$ and creates a first image plane at its focal point. Here, a mask of two razor blades defines the image frame that is projected onto a CCD camera chip using a 1:1 relay. This exposes only a third of the camera chip, while the masked area is used as a storage area. The fast kinetics mode of the Andor camera allows us to take three images in fast succession during one experimental cycle. The first two frames are used to image optical densities *OD1* and *OD2* while the third frame is a bright image to calibrate the spatially varying intensity of the imaging beam. To account for intensity fluctuations between the three imaging pulses, we compare the imaging intensities in a mask of the imaging frame without atoms and rescale them accordingly. Moreover, a $\lambda/4$ plate is placed before the 1:1 relay to prevent interference effects from back reflections and a line filter is used to discard non-resonant light.

During the imaging of the lowest hyperfine state we want to avoid off-resonant scattering of the imaging light. For this purpose, we employ a *microwave-shelving* technique that transfers the other hyperfine state to the far-detuned $|F = 7/2\rangle$ state by a broad microwave sweep. Note, that during the shelving process atoms from both hyperfine states on doubly occupied sites are lost due to spin-changing collisions. Therefore, the microwave-shelving is usually combined with a SD separation. After the first imaging procedure, a second MW sweep brings the shelved atoms back to the initial hyperfine state, which is followed by the second imaging pulse. We showcase the *microwave-shelving* in a sketch of the experimental sequence for η-pair observations in figure B.1.

Our imaging system is characterized by its magnification $\mathcal{M}$ and the imaging resolution. The former is determined by a time of flight image revealing the fermionic anti-bunching at the edges of

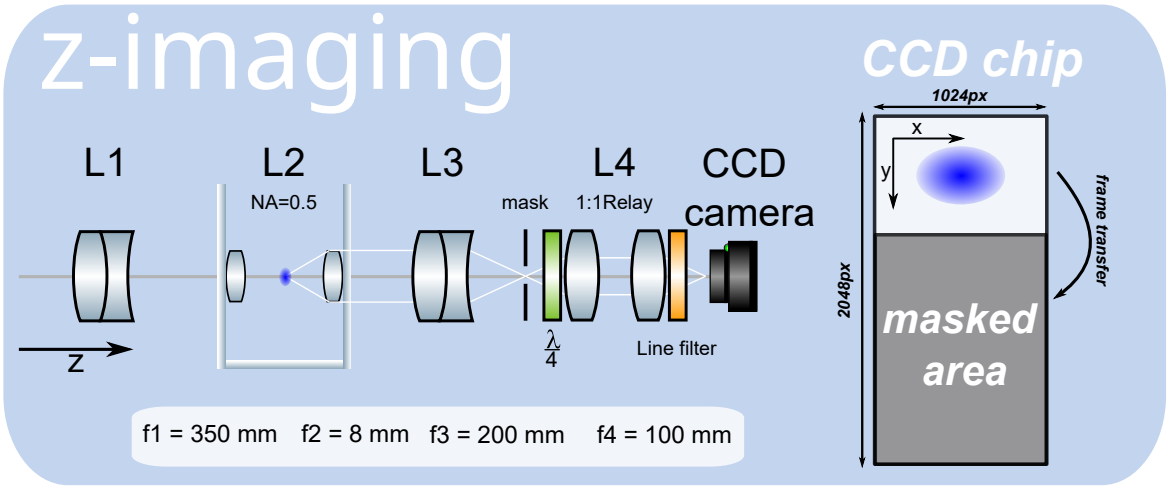

Figure 3.9: **High resolution imaging system:** Left: Schematics of the imaging system along the z-axis. The CCD camera in use is the *Andor Ixon 888* with a schematic of the CCD chip shown on the right-hand side. A mask at the first image plane of the imaging system defines the image frame and exposes only a third of the CCD chip. Using the fast kinetics mode of the camera, an image can be transferred to the masked area after the exposure allowing for three images in total for each experimental run. The schematics are adapted from [89].

the Brillouin-zone [115], from which we can deduce the magnification of our setup [89]

$$\mathcal{M} = (22.69 \pm 0.01). \tag{3.13}$$

With this magnification one lattice site with spacing $a_{x,y}^{1064} = 532\,\text{nm}$ corresponds to approximately 0.93 pixels with size $a_{px} = 13\,\mu\text{m}$.

The imaging resoultion, on the other hand, is more delicate to determine. The Rayleigh criterion gives a first estimate of the diffraction limited resolution of $r = 1.22\lambda/NA = 0.94\,\mu\text{m}$. A more elaborate measure of the imaging quality is the point-spread-function (PSF). The PSF $\mathcal{P}(r)$ characterizes the smearing of the actual atomic density $n(r)$ when observed in the camera frame

$$n_{\text{exp}}(r) = \int dr' n(r')\mathcal{P}(r' - r) \tag{3.14}$$

due to contributions from atoms at lattice site r'. Experimentally, the point spread function is determined by in-situ density fluctuations revealing the modulation transfer function (MTF) [116] and consequentially the PSF. For our imaging apparatus the calibrated FWHM radius of the Airy-disk-like PSF is [89]

$$\mathcal{P}_{FWHM} = 2.5\,\mu\text{m} \approx 4.7\,a_{x,y}^{1064} = 9.4\,a_x^{532}. \tag{3.15}$$

This shows, that while the magnification would theoretically allow for an imaging of individual lattice sites, the atomic density is smeared over roughly 5 lattice sites radially. The most plausible cause for this larger PSF is that the atoms are not located exactly at the working distance of the high NA lenses. Unfortunately, neither the atomic position, which is determined by the magnetic field of the Ioffe-Pritchard coils, nor the lenses are movable.

In general, our in-situ imaging technique resolves the atomic densities along the x- and y-direction

while integrating over the z-direction. However, the different planes along the z-direction have vastly different fillings and therefore realize different two-dimensional systems. Thus, we apply a *radio-frequency tomography* to selectively address atoms from one specific plane. First, a magnetic field of roughly 214 G is applied, and the atoms are transferred to a $|m_F = -7/2\rangle$, $|m_F = -5/2\rangle$ mixture. At this specific magnetic field the transition frequency for a $|m_F = -5/2\rangle \rightarrow |m_F = -3/2\rangle$ transfer is the same for singly and doubly occupied sites. Then, a strong magnetic field gradient of 33 G/cm is applied along the z-direction, which separates the transition frequency between the different planes. In particular, for the green z-lattice the spacing between two planes of $a_z^{532} = 1\,064\,\mathrm{nm}$ leads to a relative detuning of the transition frequency of $\sim 600\,\mathrm{Hz}$. This detuning can be increased further by a factor of two using the superlattice along the z-direction to only occupy every second plane [88, 90]. Note that this tomography was also used during the aforementioned determination of the PSF.

3.3.4 Adiabatic band mapping in time-of-flight (TOF) imaging

The limited in-situ imaging resolution is an even bigger challenge with respect to the smaller lattice spacing of the superlattice $a_x^{532} = 266\,\mathrm{nm}$. In particular, dynamic measurements of population density oscillations between neighboring lattice sites are not resolvable in-situ with a PSF of $9.4\,a_x^{532}$. Therefore, we have adapted the adiabatic band mapping measurement technique [32, 117, 118] that effectively resolves the density in momentum- instead of position-space. While this allows for a discrimination between sublattice sites, it is a global measurement averaged over the three-dimensional optical lattice.

The concept of the adiabatic band mapping is most intuitively explained by localized, spin-polarized particles in one unit cell of the superlattice.[5] First, the atoms are localized by freezing the optical superlattice after the experiment. Here, they are described by Wannier functions of different Bloch bands (compare section 2.2.3), depending on the lattice configuration. Adiabatically removing the optical lattice, unfolds the Band structure and maps the different bands, initially folded at the edge of the Brillouin-zone, to the free space momentum (cf. figure 3.10 a and d). Ballistic expansion for $t_{\mathrm{tof}} = 6\,\mathrm{ms}$, then maps the position to quasimomentum in a time-of-flight (TOF) measurement. Here, the quasimomentum q is given in the camera-frame as

$$q = \frac{px \cdot d_{px}}{M} \cdot \frac{m}{t_{\mathrm{tof}} k} \tag{3.16}$$

with the pixel px, the pixel size d_{px}, the magnification M, the mass of the atoms m and the lattice momentum k. We integrate the measured density along the y-axis, to obtain the quasimomentum distribution of the superlattice q_x.

We calibrate the adiabatic band mapping technique as follows. For the symmetric superlattice configuration (subfigure a and d), the Wannier functions of the left and right sublattice cannot be distinguished, as both sites are given by the superposition of the first and second Bloch band. Here, the quasimomentum density (gray line in subfigure d) is the same for atoms prepared on either sublattice site. Therefore, we diabatically ramp the phase of the superlattice to $\phi = \pi/4$, where the Wannier function of the upper (lower) site is mapped to the second (first) Bloch band. This mapping is reproduced experimentally by the measurements of the quasimomentum density in figure 3.10 e: The

[5] The procedure also works for the delocalized eigenfunctions of the optical superlattice: the Bloch wave functions.

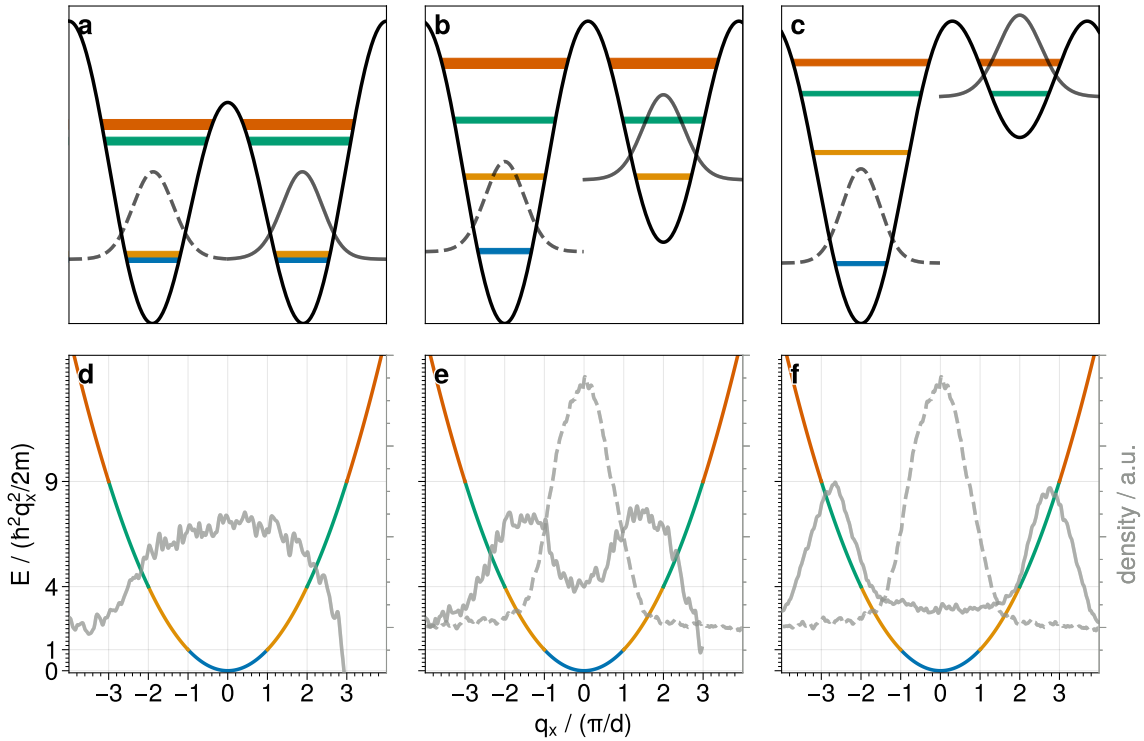

Figure 3.10: **Adiabatic band mapping in the optical superlattice:** The particles localized on the different sites of the superlattice unit-cell are described by Wannier functions (gray lines) of different Bloch bands depending on the lattice configuration (a to c). The adiabatic band mapping technique [32, 117] maps the band-structure of the optical superlattice to the free space momentum. For this purpose, the lattice depths are ramped down in 1 ms seconds practically unfolding the band-structure to the free space dispersion relation (d to f). The mapping of the Bloch bands to the different quasi momenta is indicated by the color code. Ballistic expansion for 6 ms before taking the absorption image (time-of-flight measurement) allows to determine the quasimomentum occupation. The atom density is plotted versus the quasimomentum, that correspond to the Wannier functions shown above. The lattice configurations are (a, d): $V_s = 12\,E_{\mathrm{rec}}$, $V_l = 15\,E_{\mathrm{rec}}$, $\phi = 0$, (b, e): $V_s = 12\,E_{\mathrm{rec}}$, $V_l = 15\,E_{\mathrm{rec}}$, $\phi = \pi/4$, (c, f): $V_s = 12\,E_{\mathrm{rec}}$, $V_l = 45\,E_{\mathrm{rec}}$, $\phi = \pi/4$.

atoms prepared on the left well are detected in the first BZ (dashed line) and the atoms on the upper well are detected mostly in the second BZ (solid line). However, both density profiles are not sharply restricted to their theoretically expected Brillouin-zones, which makes a clear distinction between the two sublattice sites difficult. The reason for this is most likely that we are not perfectly in the far-field regime and instead the initial density distribution impacts the quasimomentum mapping. Usually, the far-field limit is ensured by large expansion times t_{tof}, however, this is not possible in our scenario due to the large magnification of the imaging setup. To amplify the resolution between the two sublattice sites, we quench the long lattice depth to $V_l = 45\, E_{\mathrm{rec}}$ (c and f). This maps the Wannier function of the upper well to a superposition of the third and fourth band, allowing us to differentiate the population on both sublattice sites.

Finally, we characterize the relative detection efficiency between the two sites. For this purpose, we prepare the atoms either on the lower site or perform an additional diabatic phase ramp to prepare them on the upper well. We observe a relative detection efficiency of (0.91 ± 0.05) on the upper site with respect to the lower site. We account this detection efficiency difference to atom losses on the higher site during the lattice quench. Note that during this calibration we have considered, that the dark counts for the first Brillouin zone are approximately four times larger than for the third and fourth Brillouin zone combined. This spatial dependency on dark counts can be accounted to the rescaling region which is applied of-center for the time-of-flight images, and therefore works worse for the first BZ.

It is important to note, that this adiabatic band mapping technique was evaluated for a spin polarized atom cloud. The mapping from quasimomentum to free-space momentum would be altered by interactions between different spin species during the ballistic expansion [119]. Nonetheless, we use this technique to observe dynamic signals of interacting particles by introducing an additional spin cleaning pulse, as we will discuss in section 5.3.2.

In summary, we have adapted the adiabatic band mapping technique in this work to successfully detect the population on sublattice sites for interacting and non-interacting atomic samples.

CHAPTER 4

Ultracold fermions in a static array of double wells

An optical superlattice, created by a superposition of two optical lattices with commensurate lattice constants, has proven to be a versatile extension of monochromatic lattices. For example, it was used in the realization of a bilayer Hubbard model [31], allowed for the study of topological models [34, 35, 120] and recently to engineer Hubbard couplings [40] and to realize a quantum register [121]. Additionally, optical superlattices are ideal for studying driven systems by periodically modulating the frequency of one of the lasers. We will discuss these Floquet systems in chapters 5 and 6.

In this chapter we utilize our superlattice to study and characterize the Rice-Mele model (cf. figure 4.1), which represents the single-band tight-binding model of the superlattice, as defined in equation 2.37. For the characterization of the superlattice, it is beneficial to depart from the many-body system and isolate the individual processes. For this purpose, we suppress the out-of-cell tunneling t_{out}, thereby creating an array of decoupled double wells (DW). These double wells are the fundamental building block of the Hubbard model as they resemble a minimal lattice consisting of two-sites [122, 123]. Their study has led to the observation of atom interferometry of a Bose Einstein condensate [124] and second-order tunneling [32, 33] as well as quantum computing operations [125, 126].

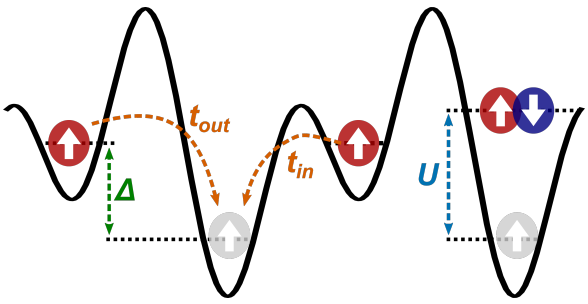

Figure 4.1: **Rice-Mele model of fermions in a superlattice potential** The tight-binding Rice-mele model describes fermions in a superlattice potential with four characteristic energy scales. The particles can tunnel within one unit cell with the rate t_{in}/h and out-of the unit cell with t_{out}/h. If two particles occupy the same lattice site they experience an on-site interaction U. The energy offset between both lattice sites of a unit cell is the tilt Δ.

This chapter is organized as follows: First we study non-interacting fermions in double wells. We characterize the inner-cell tunnel coupling t_{in} via Rabi oscillations and the stability of the superlattice phase. Then we explore the interacting double well. We start with the theoretical discussion followed by the characterization of the interaction energy via density assisted tunneling. We conclude the characterization procedure by a radio-frequency (RF) spectroscopy of the interacting double well. Finally, we discuss the preparation and detection of repulsively bound atom pairs in double well.

4.1 Non-interacting fermions in an array of double wells

In this section, we examine non-interacting fermions in double wells from both theoretical and experimental perspectives. This investigation serves as a preliminary step towards exploring interacting fermions in double wells, as outlined in section 4.2. We explore this non-interacting model to characterize the Hubbard parameters of our experimental apparatus, specifically the tunnel coupling t within the double well and the energy differential Δ between the lattice sites. Initially, we study a single fermion in a double well theoretically. Subsequently, we detail the experimental characterization of the Hubbard parameters through Rabi oscillations.

4.1.1 Theoretical description of a single fermion in a double well

We study a single fermion in a double well in the Wannier basis (compare section 2.4) of a particle localized on either the left site $|L\rangle$ or on the right site $|R\rangle$. In this basis, this gives the Hamiltonian of a single particle in the double well

$$H = \begin{pmatrix} \Delta/2 & -t \\ -t & -\Delta/2 \end{pmatrix} \tag{4.1}$$

with the tunneling between lattice sites t and the difference of the on-site energy between the lattice sites - the *tilt* Δ. Despite the simplistic nature of this model, it is suited to showcase fundamental properties of quantum mechanics: In a balanced system $\Delta = 0$, the tunneling between the lattice sites energetically favors a delocalization of the particles. Therefore, the eigenstates of the system are the symmetric and antisymmetric superposition of the basis states:

$$\psi_{\pm} = \frac{1}{\sqrt{2}}(|L\rangle \pm |R\rangle) \tag{4.2}$$

with energies $E_{\pm} = \mp t$. As a side note, these eigenstates are in direct analogy to the eigenstates of the H_2^+-molecule, where the node in the wave function was unfavorable due to the increased kinetic energy [59, 60]. On the other hand, the tilt decouples the lattice sites resulting in localized particles for strong tilts $\Delta \gg t$. This interplay of the tilt and the tunneling leads to a spectrum with an avoided crossing like behavior at $\Delta = 0$ with a gap of $2t$ as depicted in figure 4.2.

4.1.2 Experimental characterization of non-interacting double wells

We experimentally determine the Hubbard parameters t and Δ for the non-interacting double well using a fermionic spin-polarized cloud within an optical superlattice As previously described in section 2.4, this superlattice is characterized by three parameters in the tight binding model t_{in}, t_{out} and Δ. In our experiments, we choose the lattice depths of the superlattice V_s and V_l to suppress the out-of-well

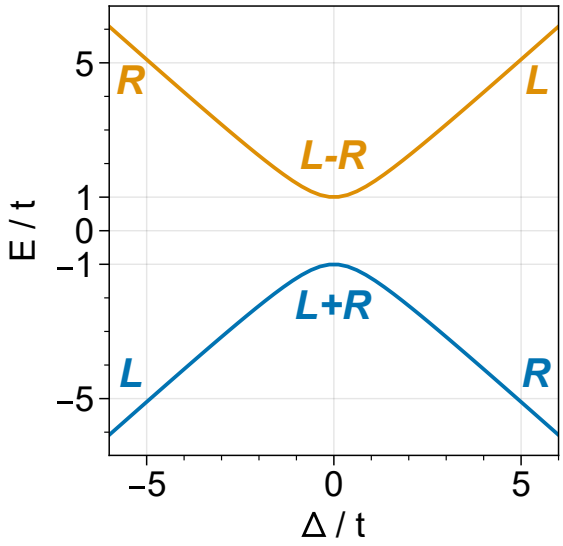

Figure 4.2: **Spectrum of a singly occupied double well vs. tilt:** The eigenvectors and eigenvalues of the ground state (blue) and excited state (orange) change with the tilt of the double well Δ. For strongly tilted systems $-\Delta \gg t$, the ground (excited) state decreases (increases) its energy linearly with the tilt and can be described by a particle localized at the lower (upper) well $|L\rangle$ ($|R\rangle$). In a balanced, configuration the ground (excited) state is delocalized in the double well with an even (odd) parity superposition $|L\rangle + |R\rangle$ ($|L\rangle - |R\rangle$) and lowers (increases) its energy by t.

tunneling $t_{\mathrm{out}}/t_{\mathrm{in}} \ll 1$. For example, a typical lattice configuration of $V_s = 12\,E_{\mathrm{rec}}$, and $V_l = 15\,E_{\mathrm{rec}}$ gives an intra-well tunneling $t_{\mathrm{in}} \sim 480\,\mathrm{Hz}$ that dominates the out-of-well tunneling $t_{\mathrm{in}}/t_{\mathrm{out}} = 5.6$. This configuration effectively isolates each double well, with a characteristic tunneling $t \equiv t_{\mathrm{in}}$.

We directly measure this tunnel coupling t through Rabi oscillations. Furthermore, we refine the Rabi oscillations technique to determine the *symmetry point*, where the superlattice phase ϕ is adjusted to ensure that double wells are balanced $\Delta = 0$. This method also allows us to calibrate the phase stability of the superlattice.

Rabi oscillations of non-interacting fermions in double wells

The non-interacting double well at half filling resembles the quantum-mechanical two-level system. Hence, if it is not prepared in one of it eigenstates, Rabi oscillations [90] with frequency

$$f_{\mathrm{R}} = \sqrt{4t^2 + \Delta^2}/h \tag{4.3}$$

and peak-to-peak amplitude

$$A_{\mathrm{R}} = \frac{1}{2}\frac{1}{1 + (\Delta/2t)^2} \tag{4.4}$$

occur. In the following, we will discuss how we probe these oscillations and determine t and Δ.

We prepare a spin-polarized atom cloud in the lowest Bloch band of an optical superlattice with lattice depths $V_s = 12\,E_{\mathrm{rec}}$ and $V_l = 15\,E_{\mathrm{rec}}$. The lattices along the y- and z-axis are frozen ($s_y = 55\,E_{\mathrm{rec}}$

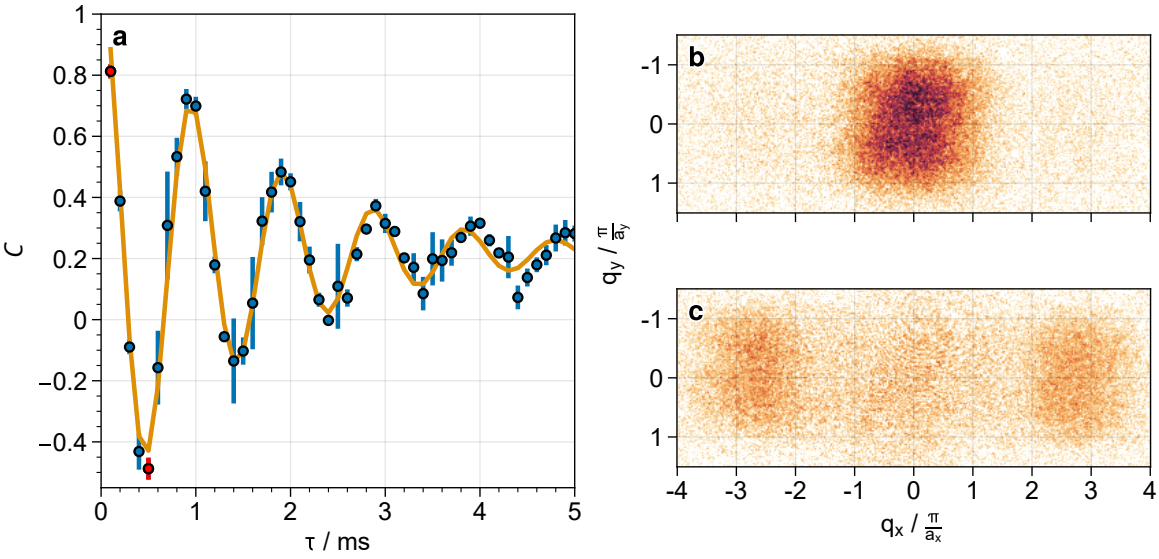

Figure 4.3: **Rabi oscillations of non-interacting fermions:** (a) The population contrast C oscillates with the holding time τ (blue data points). The fitted damped sinusoidal function (orange line) gives a Rabi frequency $f_R = (1\,040 \pm 4)$ Hz. (b) Initially (first red data point), almost all atoms occupy the first Brillouin-zone. (c) After half a period (second red data point), most atoms occupy the third- and fourth-Brillouin-zone.

and $s_z = 110\,E_{\mathrm{rec}}$). Initially, we choose the superlattice phase ϕ such that all dynamics are frozen $\Delta \gg t$. Then, we diabatically remove the lattice tilt and prepare the atoms at one site of the double i.e. $|L\rangle$. As discussed, this induces Rabi oscillations between the lattice sites. After a holding time τ we project the system back onto the $|L\rangle$, $|R\rangle$ basis by diabatically introducing a tilt $\Delta \gg t$. Unfortunately, we cannot resolve the density on the individual lattice sites of the double well as they are 266 nm apart and the point-spread function of our imaging system is 2.5 µm (FWHM) [89]. Therefore, we use the adiabatic band mapping technique, as introduced in section 3.3.4, to detect the lattice site occupation. With this technique, we map the $|L\rangle$ lattice site to the first Brillouin-zone (BZ) and $|R\rangle$ to the third- and fourth BZ. Measuring the occupations of these Brillouin-zones N_i then gives the global observable of the population contrast

$$C = \frac{N_1 - N_{34}}{N_1 + N_{34}}. \tag{4.5}$$

We observe oscillations in the population contrast with one characteristic frequency and a pronounced dephasing (cf. figure 4.3 a). Initially, the atoms are almost exclusively in the first BZ (figure 4.3 b) and after half a period the third- and fourth BZ is dominantly occupied (figure 4.3 c). The dephasing stems from the Gaussian nature of our lattice beams resulting in spatially dependent parameters $t(\boldsymbol{x})$ and $\Delta(\boldsymbol{x})$. Therefore, the global observable is averaged over several DWs with various Rabi frequencies and amplitudes resulting in the observed dephasing.

To extract the characteristic frequency of the oscillation, we fit a damped sinusoidal function to the data

$$a e^{-\tau/\tau_0} \cdot \cos(2\pi f_{\mathrm{R}} \cdot \tau) + b, \tag{4.6}$$

with the amplitude of the oscillation a, the decay constant τ_0, the Rabi frequency $f_{\mathrm{R}} = 2t/h$ and

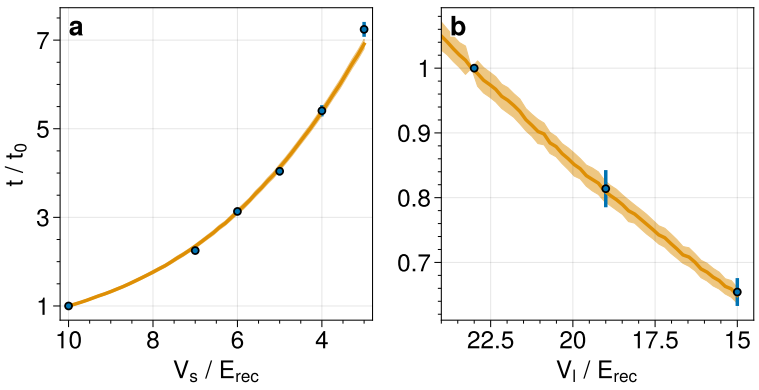

Figure 4.4: **Tunneling rate as a function of the lattice depths:** (a) Normalized tunneling rate as a function of the short lattice depth V_s for a long lattice depth $V_l = 30\,E_{\mathrm{rec}}$. (b) Normalized tunneling rate as a function of the long lattice depth V_l for a short lattice depth $V_s = 10\,E_{\mathrm{rec}}$. For both subplots, the data is shown in blue and the 1σ confidence interval of the theoretical simulation is indicated in orange.

the offset b. The offset is necessary to account for the imperfect detection efficiency of $|L\rangle$ and $|R\rangle$ (compare section 3.3.4) and for residual tilts Δ, which we will address in the next section. The fitted damped-sinusoidal function is shown as an orange line in figure 4.3 a, and agrees very well with the observed signals within the first three periods. Moreover, the extracted frequency of $f_{\mathrm{R}} = (1\,040 \pm 4)\,\mathrm{Hz}$ agrees roughly with the theoretical expectation of $(961 \pm 14)\,\mathrm{Hz}$, but shows, that a direct calibration is necessary. Note, that the theoretical tunneling rate is calculated from the Wannier functions of the lattice according to equation 2.35, where we have considered a lattice-depth uncertainty of 1 %.

We further compare our direct measurements of the tunneling rate t with the theoretical expectations by changing the two lattice depths V_s, V_l independently. Here, we observe that our observed scaling of the tunneling rate agrees with the theory excellently (cf. figure 4.4 a and b). The observed deviation for very small short lattice depths might be caused by a breakdown of the tight-binding approximation. In this case, the green lattice depth is not large enough to ensure two well-separated lattice sites of the double well.

To conclude, we have directly measured the tunneling rate and verified its theoretically expected scaling. Our experimental data shows good agreement with the theoretical expectations.

Phase-stability of the superlattice

The discussed Rabi oscillations can also be used to characterize the tilt of the double well. We are especially interested in studies of balanced double wells and therefore in the *symmetry-point* ϕ_0, where the superlattice phase ϕ is chosen such that the double well is balanced $\Delta = 0$.

At the symmetry-point, the Rabi frequency f_R is minimal (compare equation 4.3) and the amplitude A_R maximal (compare equation 4.4). We visualize this in figure 4.5 a, where we compute the population contrast for various tilts theoretically. To determine the symmetry point, we choose a fixed holding time τ on the first decreasing slope, near the minimum of the Rabi oscillation (black vertical line) and vary the tilt, which creates a signal with a minimal population contrast at the symmetry point, where $\Delta = 0$ (compare figure 4.5 b).

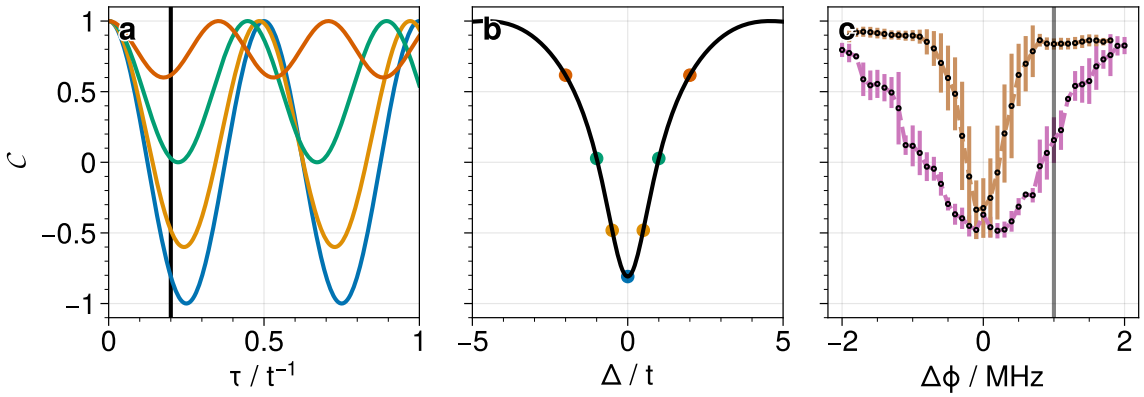

Figure 4.5: **Symmetry-point measurements:** (a) Theoretical calculations of Rabi oscillations in the population contrast C for various tilts $\Delta/t = 0$, $\Delta/t = 0.5$, $\Delta/t = 1$, and $\Delta/t = 2$ are shown in blue, orange, green and red as a function of the time *tau*. (b) Theoretical calculation of a symmetry-point measurement at time $\tau = 0.2/t$ (as indicated as a black vertical line in subfigure a) for various tilts Δ/t. The data points corresponding to the dynamic traces of subfigure a, are plotted in the same color coding. (c) Experimental symmetry-point measurements for two different lattice configurations: $V_s = 10\,E_{\mathrm{rec}}$, and $V_l = 15\,E_{\mathrm{rec}}$ (pink), as well as $V_s = 14\,E_{\mathrm{rec}}$, and $V_l = 30\,E_{\mathrm{rec}}$ (brown). The lattice configurations differ in the tilt they realize at a superlattice phase $\Delta\phi = 1$ MHz (gray vertical line), which is $\Delta/t = 1.5$ for the shallow lattice (pink) and $\Delta/t = 4$ for the deep lattice (brown). The data set consists of 32 measurements (pink) and 80 measurements (brown), that were re-binned according to the deviation of the data point from the fitted symmetry point $\Delta\phi$ for better visibility.

In the experiment, we use the superlattice phase to change the tilt and observe the minimum in the population contrast, which we then extract by fitting a Gaussian function. We show an averaged signal for a lattice configuration of ($V_s = 10\,E_{\mathrm{rec}}$, and $V_l = 15\,E_{\mathrm{rec}}$), as the pink data points in figure 4.5 c. Here, the population contrast is plotted versus the deviation of the superlattice phase from the symmetry point $\Delta\phi = \phi - \phi_0$, for better visibility. The width of the signal is dictated by the lattice configuration, which creates a tilt of $\Delta_s/t = 1.5$ for a superlattice phase of $\Delta\phi = 1$ MHz (vertical gray line). For a deeper lattice configuration ($V_s = 15\,E_{\mathrm{rec}}$, and $V_l = 10\,E_{\mathrm{rec}}$), the tilt at the same superlattice phase is much larger $\Delta_d/t = 4$, and therefore, the symmetry-point signal is more narrow (brown data points). The ratio of the fitted Gaussian widths is directly the inverse of the tilt ratios $w_s/w_d \sim 2.7 \sim \Delta_d/\Delta_s$, which verifies experimentally, that the sensitivity of the symmetry-point signal is governed by the ratio Δ/t at a given superlattice phase $\Delta\phi$.

Theoretically, we can use a lattice configuration with large Δ/t determine the symmetry-point with extreme precision. However, the symmetry-point drifts over time significantly due to the optical path length changes with the environmental parameters: temperature, pressure and humidity. As introduced in section 3.2.2, we account for this by an environmental feed-forward (FF) [110]. Nonetheless, the symmetry-point still fluctuates due to imperfections of this environmental FF. We categorize these fluctuations into long-term drifts and short-term shot-to-shot variations, the latter occurring on timescales shorter than a single measurement of the symmetry point, which usually consists of approximately 10 sequences.

The long-term behavior of the symmetry-point and the applied FF over a period of 40 h is depicted in figure 4.6. The peak to peak amplitude of the applied FF of roughly 5 MHz shows that it is crucial for the stability of the superlattice phase, especially when comparing it to the width of the symmetry

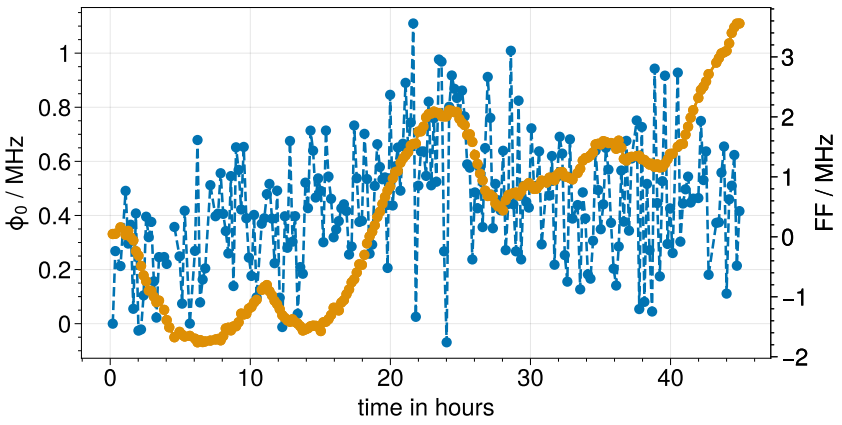

Figure 4.6: **Symmetry-point long term fluctuations:** The symmetry point ϕ_0, compared to the first measured value, changes over the course of over 40 h (blue data points and left axis), despite the applied environmental feed-forward (orange data points and right axis). The chosen lattice configuration was $V_s = 10\,E_{\mathrm{rec}}$, and $V_l = 15\,E_{\mathrm{rec}}$.

point signals in figure 4.5 c. We quantify the remaining fluctuations of the symmetry point with the mean value and the standard deviation

$$\overline{\phi_0} = 0.45\,\mathrm{MHz},\ \sigma_{\Delta\phi} = 0.22\,\mathrm{MHz} = 2.4\,\mathrm{mrad}. \tag{4.7}$$

The mean value expresses a drift of the symmetry point compared to the first measurement, while the standard deviation quantifies the fluctuations. However, compared to the periodicity of our superlattice (148.9 ± 0.1) MHz, both values show excellent stability. In general, we could improve the feedforward by minimizing the standard deviation of the symmetry-point measurements, with respect to the parameters of the FF. However, to ensure a global optimum we would need a lot of data to optimize the three-dimensional environmental parameter space. As we cannot control these parameters this would require too much measurement time to be feasible.

The shot-to-shot fluctuations are difficult to determine directly, as they occur on faster timescales than our symmetry-point measurement. Therefore, we try to estimate them by statistical means. We perform the symmetry-point measurement 80 times and fit the symmetry point to each individual data set. Then, we determine the population contrast as a function of the deviation of the superlattice phase from the symmetry point $\Delta\phi = \phi - \phi_0$. We bin $\Delta\phi$ in intervals of 0.2 MHz and average, resulting in a very clear signal as depicted in figure 4.7 a. Interestingly, the standard deviation of the population contrast shows a double-peak signature (cf. figure 4.7 b) with a local minimum at $\Delta\phi = 0$. This is a clear indication of shot-to-shot fluctuations that lead to larger standard-deviations on the slopes of the symmetry-point signal.

We compare this data to Monte-Carlo (MC) simulations of the shot-to-shot fluctuations in the symmetry-point measurement. For this purpose, we perform our usual symmetry-point fit to the averaged signal and simulate the shot-to-shot fluctuations as uncertainties on $\Delta\phi$ with various standard deviations σ_ϕ. We show the standard deviation of a MC simulated symmetry-point signal with shot-to-shot fluctuations of $\sigma_\phi = 0.2$ MHz as the green trace in (cf. figure 4.7 b). Then, we calculate the difference of the standard deviation profile between the experimental data and the MC simulated

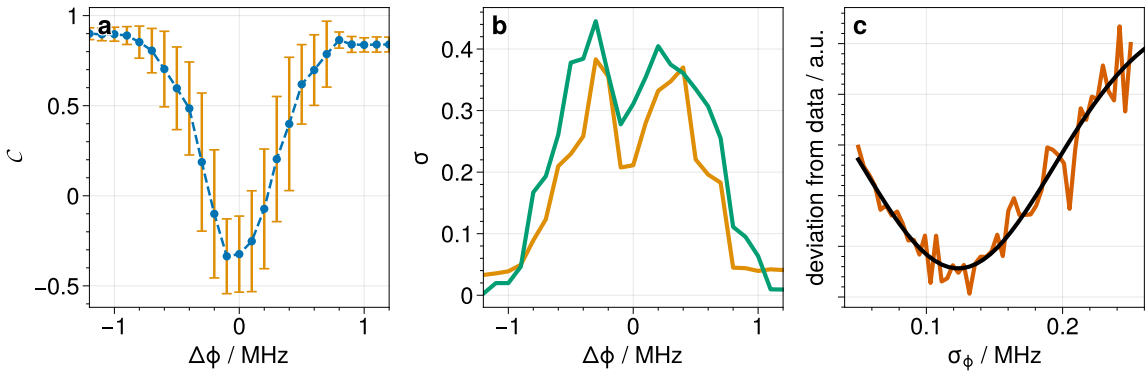

Figure 4.7: **Shot-to-shot fluctuations of the symmetry point:** (a) Average of the population contrast as a function of the deviation of the superlattice phase from the fitted symmetry-point $\Delta\phi$. (b) Standard deviation σ of the population contrast as a function of $\Delta\phi$ (orange) compared to Monte-Carlo simulated symmetry-point measurements with shot-to-shot fluctuations of $\sigma_\phi = 0.2\,\mathrm{MHz}$ (green). (c) Difference of the standard deviation profile shown in (b) between the experimental data and MC data for various MC simulated standard deviations σ_ϕ (red line). We fit a Gaussian function (black line) to extract the estimate of the shot-to-shot fluctuations at the minimal difference. The chosen lattice configuration was $V_s = 14\,E_\mathrm{rec}$, and $V_l = 30\,E_\mathrm{rec}$.

data for various shot-to-shot fluctuations σ_ϕ on the $-0.5 \leq \Delta\phi \leq 0.5$ interval. This deviation is shown in figure 4.7 c and shows a clear minimum at

$$\sigma_\phi = (0.12 \pm 0.01)\,\mathrm{MHz} = (1.3 \pm 0.1)\,\mathrm{mrad}, \tag{4.8}$$

which is our estimate for the shot-to-shot fluctuations.

With these measurements, we have determined the phase fluctuations on long and short timescales in an averaged measurement over the whole cloud to be $< 3\,\mathrm{mrad}$. Compared to other reported stabilities of optical superlattices (4.5 mrad [40], 9.4 mrad [39]), the presented results are excellent. Moreover, for typical lattice configurations of $V_s = 10\,E_\mathrm{rec}$ and $V_l = 15\,E_\mathrm{rec}$, the shot-to-shot fluctuations correspond to a tilt of $\Delta = 0.18\,\mathrm{t}$, which shows that the fluctuations are also acceptable on an absolute scale.

In-situ symmetry-point measurement

In previous measurements of the symmetry-point, we used global observables that did not provide insight into local variations of the symmetry point. Here, we discuss a method to measure the symmetry-point in-situ, providing local information. This method is also based on the aforementioned Rabi oscillations but with a different detection scheme, which we discuss in the following.

After the Rabi oscillations the system is projected onto the $|L\rangle$, $|R\rangle$ basis by the diabatic introduction of a tilt $\Delta \gg t$. Then, the long-lattice depth is increased rapidly to $V_l = 54\,E_\mathrm{rec}$, which maps the $|R\rangle$ basis to the third and fourth band, as depicted in figure 4.8 a. In this configuration, the energy gap between the third- and fourth- and the second energy band is $23\,E_\mathrm{rec}$. This is resonant with the gap from the first band to the continuum in the y-lattice (cf. figure 4.8 b). The coupling between the x- and y-bands is usually assumed to be suppressed, however, it is possible due to the imperfect orthogonality of $\approx 84^\circ$ [90]. Next, this configuration is held for 1.04 s to allow the atoms in the $|R\rangle$ state to leave

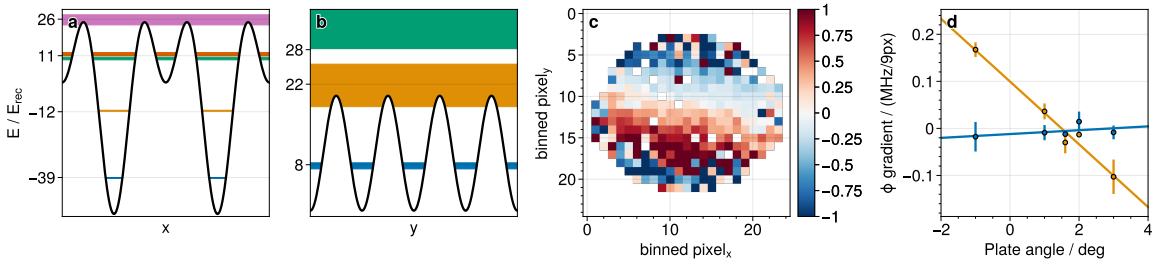

Figure 4.8: **In-situ symmetry point measurement:** (a) Band structure of the superlattice along the x-direction for $V_s = 15\,E_{\mathrm{rec}}$ and $V_l = 54\,E_{\mathrm{rec}}$. The atoms on the $|L\rangle$ sites are in the first band and frozen, while the atoms on the $|R\rangle$ sites are in a superposition of the third and fourth band. The energy difference between the third and fourth and the second band is $\approx 23\,E_{\mathrm{rec}}$ and corresponds to the energy difference from the first band to the continuum of the y lattice (b) for a lattice depth of $s_y = 20\,E_{\mathrm{rec}}$. (c) Map of the relative in-situ symmetry point $\Delta\phi$ for binned pixels of $9px \cdot 9px$ with significant phase gradient along the y-direction. The x-lattice has an angle of $(5.3 \pm 0.3)^\circ$ [90] to the camera frame, which causes the observed rotation of the map. (d) The angle of the *phase-plate* can be used to change the gradient along the y-direction, while keeping the gradient along x-direction constant.

the trap in y-direction via the continuum state, whereas the $|L\rangle$ state remains frozen. As we lose the atoms in the $|R\rangle$ state, it is not possible to calculate a population contrast between the two lattice sites. Instead, we measure the density of the left well N_L averaged over $\sim 10 \times 10$ lattice sites, due to the imaging resolution (compare section 3.3.3).

This measurement technique gives a map of the relative symmetry point $\Delta\phi$ over the cloud, as depicted in figure 4.8 c. We observe a symmetry-point map with a strong gradient along the y-direction of $(0.17 \pm 0.02)\,\mathrm{MHz}/9px$ and a slight rotation with respect to the camera frame. The rotation is caused by the angle between the x-lattice and the camera frame of $(5.3 \pm 0.3)^\circ$ [90]. We attribute the gradient to different angles of the incoming lattice beam and the retro reflected lattice beam, that result in spatially dependent optical path lengths [110]. To control the angle of the lattice beams at the atom cloud, we have installed a *phase-plate*, as introduced in section 3.2.1. In figure 4.8 we show, that by changing the angle of this phase-plate with respect to the lattice beam, we can change the phase-gradient along the y-direction linearly, while keeping the gradient along the x-direction almost constant.

There is an additional phase gradient along the x-direction, that is caused by the y-lattice. The y-lattice has a running wave component, due to the unavoidable power imbalance of forward-going and retro-reflected beam of approximately $\gamma_y = 0.77$. This creates an underlying attractive potential that changes along the x-direction due to the Gaussian beam profile of the y-lattice beam. Unfortunately, we cannot compensate this gradient with the phase plate due to its non-linear profile. In the future, we plan to compensate this inhomogeneity with light sheets, which will be discussed in the outlook of this thesis in more detail.

This in-situ symmetry-point measurement provides us with a spatially-resolved insight into the superlattice phase. Moreover, we control the phase-gradient along the y-direction with a phase-plate, allowing us us to create systems of double wells with almost homogeneous superlattice phases. [1]

[1] Unfortunately, this method is not suitable to measure the Rabi oscillations locally with high precision, as the long holding times and atom loss lead to noisy signals.

4.2 Interacting fermions in an array of double-wells

In this section, we explore the interplay between interactions and kinetic energy in the paradigmatic Hubbard model, focusing on its fundamental building block: the interacting double well. First, we theoretically analyze two interacting fermions in a double well. We examine the characteristic eigenstates and their dependence on the interaction energy U and the tilt Δ. Then, we experimentally determine the remaining Hubbard parameter U by means of density-assisted tunneling in tilted double wells. To conclude our calibration, we perform a relative spectroscopy of an array of repulsively interacting double wells for various tilts. Finally, we discuss the preparation and detection of repulsively-bound pairs in double wells.

4.2.1 Theoretical description of two interacting fermions in a double well

We study two interacting fermions of opposite spin in a double well potential. Here, the two-particle wave functions separate into a spatial- and a spin-part, as the Hamiltonian itself is spin independent

$$\psi(\boldsymbol{x}_1, \boldsymbol{x}_2, \sigma_1, \sigma_2) = \phi(\boldsymbol{x}_1, \boldsymbol{x}_2) \cdot \xi(\sigma_1, \sigma_2) \tag{4.9}$$

with the spin of the particles $\sigma = \{\uparrow, \downarrow\}$. The spatial wave function determines the energy spectrum, while the spin part describes the magnetic correlations of the system [90]. We obtain the tight-binding Hamiltonian of the double well by introducing the field operator [13]

$$\hat{\psi}_\sigma(\boldsymbol{x}) = \sum_{i=\{L,R\}} w_i(\boldsymbol{x})\, \hat{c}_{i\sigma} \tag{4.10}$$

with the fermionic annihilation operator $\hat{c}_{i\sigma}$ and the Wannier functions $w_i(\boldsymbol{x})$, as introduced in section 2.2.3, that are localized either on the left or right lattice site. In this work, we use the Fock basis [58]

$$\begin{aligned} |LL\rangle \equiv |\uparrow\downarrow, 0\rangle &= \hat{c}^\dagger_{L\downarrow}\, \hat{c}^\dagger_{L\uparrow}\, |0\rangle \\ |LR\rangle \equiv |\uparrow, \downarrow\rangle &= \hat{c}^\dagger_{R\downarrow}\, \hat{c}^\dagger_{L\uparrow}\, |0\rangle \\ |RL\rangle \equiv |\downarrow, \uparrow\rangle &= \hat{c}^\dagger_{R\uparrow}\, \hat{c}^\dagger_{L\downarrow}\, |0\rangle \\ |RR\rangle \equiv |0, \uparrow\downarrow\rangle &= \hat{c}^\dagger_{R\downarrow}\, \hat{c}^\dagger_{R\uparrow}\, |0\rangle \end{aligned} \tag{4.11}$$

which gives the Hamiltonian in matrix form

$$H_{\mathrm{DW}} = \begin{pmatrix} U + 2\Delta & -t & t & 0 \\ -t & 0 & 0 & -t \\ t & 0 & 0 & t \\ 0 & -t & t & U - 2\Delta \end{pmatrix} + H_{\mathrm{corr}} \tag{4.12}$$

with the higher-band corrections H_{corr}, as introduced in section 2.4. These corrections include the correlated tunneling V_{ct}, a nearest-neighbor interaction V_{nn} and the direct spin-exchange V_{de}, giving

$$H_{\text{corr}} = \begin{pmatrix} 0 & 0 & 0 & V_{\text{ct}} \\ 0 & V_{\text{nn}} & -V_{\text{de}} & 0 \\ 0 & -V_{\text{de}} & V_{\text{nn}} & 0 \\ V_{\text{ct}} & 0 & 0 & 0 \end{pmatrix}. \tag{4.13}$$

However, in the discussed single band picture, where the interaction energy U is much smaller than the band gap to higher Bloch bands they are negligible. Finally, there is a correction to the tunneling amplitude δt, also referred to as density-assisted tunneling, that considers the impact of interactions on the Wannier functions, which we consider implicitly $t \to t + t_{\text{corr}}$.

Two interacting fermions in the balanced double well

The interplay between interactions and kinetic energy is best studied in the balanced double well $\Delta = 0$. Here, it is convenient to change to a basis consisting of the singlet state $|s\rangle$, the (spin) triplet state $|t\rangle$ and two states of double occupancies $|d_+\rangle$ and $|d_-\rangle$ with different parity

$$\begin{aligned} |s\rangle &= \frac{1}{\sqrt{2}}(|\uparrow,\downarrow\rangle - |\downarrow,\uparrow\rangle) \\ |t\rangle &= \frac{1}{\sqrt{2}}(|\uparrow,\downarrow\rangle + |\downarrow,\uparrow\rangle) \\ |d_+\rangle &= \frac{1}{\sqrt{2}}(|\uparrow\downarrow,0\rangle + |0,\uparrow\downarrow\rangle) \\ |d_-\rangle &= \frac{1}{\sqrt{2}}(|\uparrow\downarrow,0\rangle - |0,\uparrow\downarrow\rangle). \end{aligned} \tag{4.14}$$

The triplet state $|t\rangle$ is an eigenstate of the (balanced) double well with zero energy $\langle t|H_{\text{DW}}|t\rangle = 0$, that doesn't couple to any other eigenstate. Moreover, the odd parity doubly-occupied state $|d_-\rangle$ is an eigenstate of the balanced double well with energy $\langle d_-|H_{\text{DW}}|d_-\rangle = U$. This state is of particular interest, as it resembles an η-pair which is a highly excited eigenstate of the Hubbard model with off-diagonal long range order [127] for repulsive interactions. We will discuss the preparation and detection of this repulsively-bound pair state in section 4.2.3.

The remaining two eigenstates are the ground state and the (most-)excited state and are superpositions of $|s\rangle$ and $|d_+\rangle$ that are coupled by the tunneling in the double well. The composition of the ground (excited) state depends on the interaction energy U, as illustrated in the spectrum of figure 4.9: For strong attractive interactions $-U \gg t$, double occupancies are energetically favorable, and therefore the ground state consists of $|d_+\rangle$. However, for strong repulsive interactions $U \gg t$ double occupancies are energetically more costly and thus the ground state is $|s\rangle$ and vice versa for the excited state. Of particular interest is the energy of these two eigenstates

$$E_{\text{g,e}}(U) = \frac{1}{2}\left(U \mp \sqrt{(4t)^2 + U^2}\right) \tag{4.15}$$

which gives the gap of the avoided crossing for non-interacting systems $\Delta E(U = 0) = 4t$. Moreover,

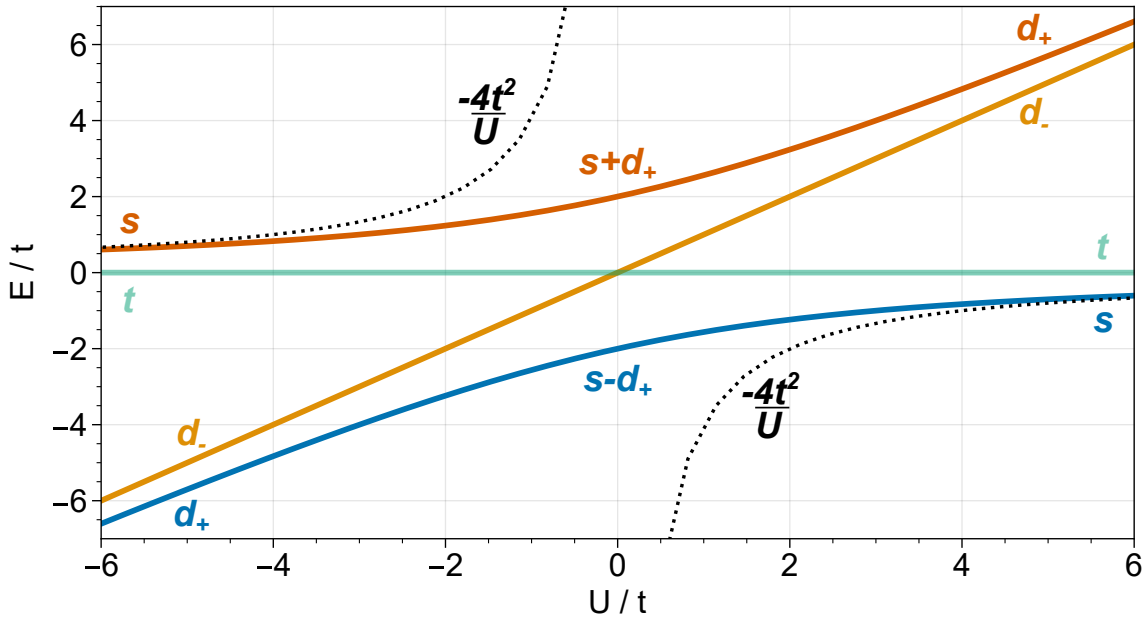

Figure 4.9: **Spectrum of a balanced doubly occupied double well vs. interaction strength:** The eigenvectors and eigenenergies of the system change with the interaction strength U. The $|d\_\rangle$ state (orange) is a superposition of the doubly occupied sites with uneven parity and has an energy of U. For strong attractive interactions $-U \gg t$, the ground state (blue) is described by the doubly occupied state with even parity $|d_+\rangle$ and has an energy of $U + 4t^2/U$. At these interactions, the excited state (red) is described by the There is an avoided crossing at vanishing interactions $U = 0$ between the ground and excited state The triplet state (green) is a superposition of the singly occupied sites with even parity has zero energy and does not couple to the other states.

in the strongly repulsively interacting limit $U \gg t$, the energy of the ground state defined in equation 4.15 approaches

$$E_g(U \to \infty) \approx \frac{-4t^2}{U}. \tag{4.16}$$

In this system, where single particle tunneling is suppressed by the strong repulsion, this ground state energy is lowered by a second order tunneling process: the *superexchange* [128, 129] with rate $J = \frac{-4t^2}{U}$ that is illustrated in figure figure 4.10 a. Here, the particles tunnel virtually from the singlet state to the doublet state and back, effectively interchanging the spins in the double well. This effective spin-spin interaction is only possible for the anti-ferromagnetic spin configuration of the singlet state (compared to the ferromagnetic order of the triplet) and therefore implicitly introduces magnetic order in the system.

However, the temperature restrictions to observe these antiferromagnetic correlations are very challenging: When the temperature is below the interaction energy $k_B T \ll U$, the double well is in the Mott-insulating regime and the doubly occupied states $|d_+\rangle$ and $|d\_\rangle$ are not populated. Only if we increase the temperature further below the superexchange energy $k_B T \ll J$, the singlet state is dominantly populated and antiferromagnetic correlations are dominant. These antiferromagnetic correlations in the double well are usually measured via *singlet-triplet oscillations* [130, 131], where

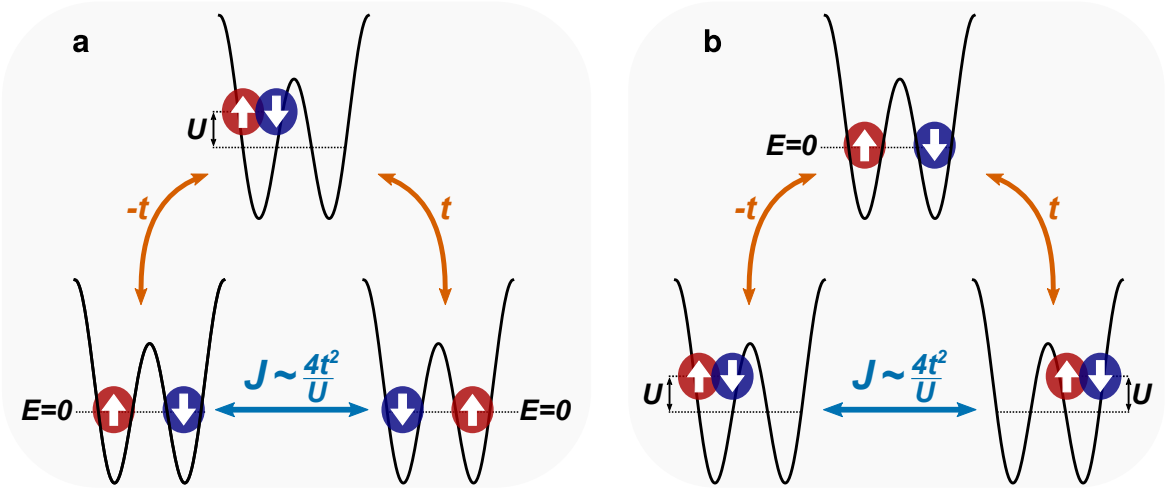

Figure 4.10: **The superexchange process in strongly interacting double wells:** (a) The superexchange J as an effective spin-spin interaction for the singlet state. While the single particle tunneling is suppressed by the strong interaction, this second order tunneling process virtually populates a doublet state resulting in a spin exchange. (b) The superexchange J as an effective pair tunneling for doublet states. The pair tunnels within the double well as two consecutive tunneling events via the virtual singlet state. This figure was inspired by [123].

an external magnetic field gradient lifts the degeneracy of the spin states and induces Rabi oscillations between the singlet and the triplet state. For more information on experimental studies of quantum magnetism with our experimental apparatus the reader is kindly referred to the thesis of my predecessors Nicola Wurz, Marcell Gall and Chun Fai Chan [87, 88, 90].

The introduced superexchange also describes a second-order pair-tunneling process for strongly interacting systems as illustrated in figure 4.10 b. This process of two consecutive single-particle tunneling events lowers (increases) the energy of the doublet state of even parity $|d_+\rangle$ compared to $|d_-\rangle$ for strong attractive (repulsive) interactions (cf. figure 4.9). We will show in Chapter 6, that this process can be enhanced by a periodic modulation of the system.

Two interacting fermions in the tilted double well

Introducing a tilt Δ to the repulsively interacting double well, changes the spectrum and eigenstates of the system significantly. The only exception is the triplet state $|t\rangle$, that remains at zero energy due to the lack of coupling to the other states (cf. figure 4.11 a). For a dominant tilt $-\Delta \gg U, t$ the system is in an insulating state with a localized ground state $|LL\rangle$ and excited state $|RR\rangle$. The state adiabatically connected to $|d_-\rangle$ is in the singlet state $|s\rangle$ and energetically degenerate with the triplet state. Decreasing the tilt leads to the first avoided crossing at $-2\Delta = |U|$ of the ground state and the state adiabatically connected to the $|d_-\rangle$-state. Here the ground state is dominantly in a superposition of the singlet state $|s\rangle$ and the localized doublet state $|LL\rangle$

$$|\psi_0(-2\Delta = U)\rangle \approx \frac{1}{\sqrt{3}}(|LL\rangle - |LR\rangle + |RL\rangle) + \epsilon\,|RR\rangle \tag{4.17}$$

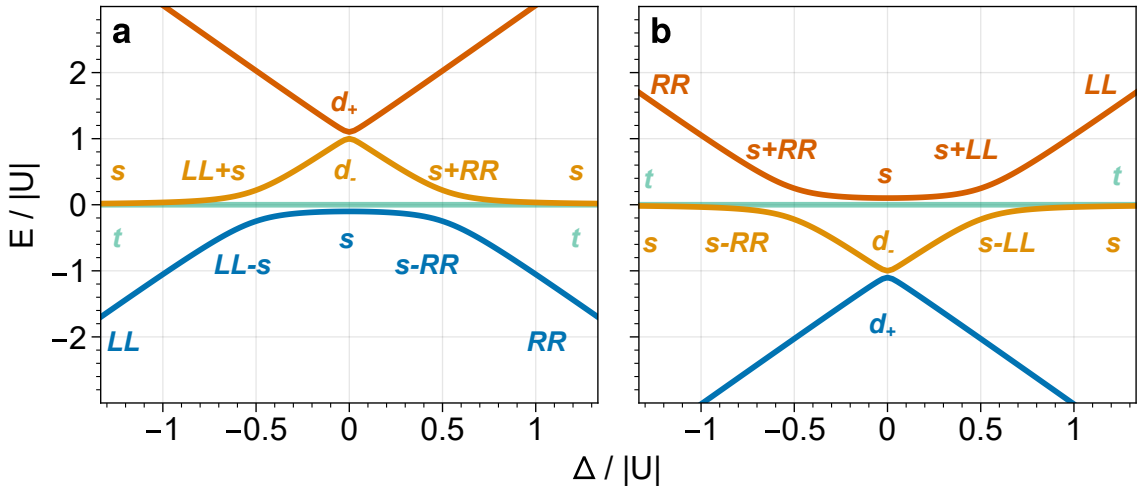

Figure 4.11: **Spectrum of an interacting doubly occupied double well vs tilt:** (a) Repulsively interacting double well with $U = 6t$. The ground state (blue) changes its energy and composition of basis states with the tilt Δ. There is an avoided crossing at $-2\Delta = U$ between the ground state and the state adiabatically connected to the $|d_-\rangle$ state (orange). For a balanced double well $\Delta = 0$, there is a second avoided crossing between the excited state (red) and the $|d_-\rangle$ state. The triplet state $|t\rangle$ (green) does not couple to the other states. (b) For the attractively interacting double well $U = -6t$ the spectrum is identical to the repulsive spectrum for $E \rightarrow -E$. Note that only the dominating part of the eigenstates is denoted in this graphic for simplicity.

with a negligible population ($\epsilon \ll 1$) of the localized doublet $|RR\rangle$. This results in the ground state energy

$$E_0(-2\Delta = U) = -\left(\frac{4}{3} + \epsilon\right) t, \tag{4.18}$$

which is solely dependent on the single particle tunneling t. Evidently, the interaction energy and the tilt cancel each other and (up to first order) allow for single particle tunneling in a virtually balanced double well. Decreasing the tilt further to $\Delta = 0$ leads to the second avoided crossing between the $|d_-\rangle$ state and the excited state. Here, the energy-gap is given by the superexchange J.

In the upcoming sections, we will leverage several aspects of the tilted interacting double well. First, we utilize the resonance condition $2\Delta = U$ for density-assisted tunneling, to calibrate the interaction strength U in section 4.2.2. Furthermore, we implement a new detection scheme for the population of the repulsively bound pairs ($|d_-\rangle$) in section 4.2.3. Here, we utilize that the $|d_-\rangle$ state is mapped to the singlet state for large tilts $\Delta \gg t, U$. Finally, we exploit the coupling of the ground state and the state adiabatically connected to the $|d_-\rangle$ state around $2 - \Delta = U$ to induce Rabi oscillations between these two states and verify the measured population.

4.2.2 Characterization of interacting fermions in double wells

We experimentally characterize the interacting double wells by measuring the characteristic Hubbard parameters t, Δ and U. Notably, we have determined t and Δ in the non-interacting double well setup, as discussed in section 4.1.2, leaving only the interaction strength U to be quantified. In the following subsection, we will explore the characterization of U through density-assisted tunneling in

the tilted double well. We conclude our experimental characterization of the interacting double well by performing a radio-frequency spectroscopy.

Density-assisted tunneling in tilted double wells

The variable tilt of the double well Δ allows for a direct measurement of the interaction strength U through density-assisted single particle tunneling in the virtually balanced double well. For this purpose, we prepare two fermions on one lattice site $|RR\rangle$ and choose the superlattice phase such that the tilt balances the interaction energy $|U - 2\Delta| = 0$. This allows for density-induced tunneling with a rate proportional to t [33, 123], as shown in figure 4.12 a and calculated in equation 4.18. We use this method to perform an experiment similar to the in-situ symmetry-point introduced in section 4.1.2, that determines the superlattice phase, where the single particle tunneling is resonant. However, the obtained resonance $\Delta\phi^U$ is shifted with respect to the symmetry-point measurement due to the interaction strength and the changed y-lattice depth $s_y = 55\,E_{\mathrm{rec}}$ (compared to $s_y = 20\,E_{\mathrm{rec}}$). Calculating the difference pixel wise with a bin size of 10×10 lattice sites, shows a spatial variation of $\Delta\phi^U$, due to the Gaussian nature of the lattice beams (figure 4.12 b). Then, we calculate the spatially varying tilt $2\Delta(\boldsymbol{x})$ from the calibrated lattice depths as well as the interaction strength $U(\boldsymbol{x}, a)$, as introduced in section 2.4. Finally, we minimize $|2\Delta(\boldsymbol{x}) - U(\boldsymbol{x}, a)|$ with respect to the scattering length a in the high density region, to calibrate the interaction strength.

We perform in-situ symmetry-point measurements and density-assisted tunneling calibrations in an alternating fashion, to be less susceptible for symmetry-point drifts. We use this procedure to observe the change of the scattering length a with the external magnetic-field strength B, as depicted in figure 4.12 c. Comparing our data to the calibrated Feshbach resonance [71, 72, 74] (orange line), shows great agreement. However, it should be noted that the magnetic field values in this plot are not calibrated but calculated from Biot-Savart's law for the applied currents to the magnetic field coils. The presented method is a direct measurement of the interaction strength U and consequentially the scattering length a. Therefore, it can be used to calibrate the Feshbach resonances of ^{40}K which will be discussed in the thesis of my colleague Janek Fleper [110].

Radio-frequency spectroscopy of interacting fermions in double wells

We conclude the characterization of the interacting double well at half filling with a spectroscopic measurement. Initially, we prepare a balanced mixture of the lowest two hyperfine states $|F = 9/2, m_F = -9/2\rangle$ and $|F = 9/2, m_F = -7/2\rangle$, for which we will use the shorthand notation $|9, 7\rangle$ from now on. For the chosen magnetic field $B \sim 209\,G$, this is a non-interacting hyperfine mixture with $U_{97} \sim 0t$. First, we prepare the atoms in the ground state of the strongly tilted $\Delta \gg t$ double well: $|LL\rangle$. Then, we adiabatically change the tilt to the desired final value and perform a radio-frequency transfer with small pulse width $\delta\nu_{SD} = 1\,\mathrm{kHz}$ to the repulsively interacting $|9, 5\rangle$ hyperfine mixture with interaction strength $U_{95} \approx 8.1\,t$. Interestingly, for a small tilt $\Delta \approx 3t$, this spectroscopy shows three distinct resonances as depicted in figure 4.13 a. The lowest frequency resonance corresponds to the singly occupied sites at frequency ν_S. Here, the RF-frequency is resonant with the energy difference of the different m_F states in the external magnetic field. From the singles-doubles (SD) spectroscopy in the monochromatic lattice (compare section section 3.3.1) we would expect just one second resonance shifted by $\Delta_U/h = |U_{95} - U_{97}|/h = U_{95}/h$. However, the richer spectrum of the double well allows for -a priori- four additional resonances, one for each

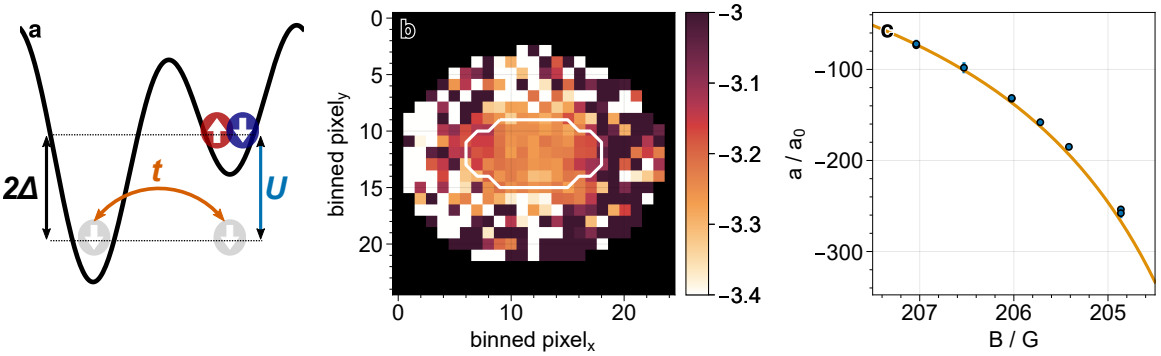

Figure 4.12: **Interaction strength U calibration:** (a) Density assisted tunneling, where $2\Delta = U$, in a tilted double well induces dynamics with the single particle tunneling rate t. (b) The superlattice phase for resonant density-assisted tunneling $\Delta\phi^U$ varies over the cloud due to the Gaussian nature of the lattice beams. The corresponding scattering length a is fitted in the high density region (white line). (c) The calibrated scattering lengths change with the external magnetic field B (blue data points) and agree with the expectation from the Feshbach resonance (orange line).

eigenstate.

We have performed this spectroscopy for several tilts and extracted the observed resonance frequencies by fitting a Gaussian to the peaks. The mean value of the singles peak was $\nu_S = (48.419 \pm 0.001)$ MHz which slightly deviates from the expected value of 48.429 MHz for a magnetic field of $B = 209.319\,G$. In particular, this measurement of the energy shift between the $|m_F = -7/2\rangle$ state and $|m_F = -5/2\rangle$ state is a suitable and very precise calibration method for the external magnetic field.

Extracting the energy difference of the additional resonances compared to the singles' resonance $h\Delta\nu$ gives the (relative) spectrum of the repulsively interacting double well (cf. figure 4.13 b). For small tilts $\Delta < 0.5\,U$, we observe two resonances. The energetically lower one (blue data points) scales almost linearly with the tilt, while the energetically higher one (orange data points) remains almost constant. For large tilts $\Delta > 0.5\,U$, we only observe the energetically lower resonance with an energy difference approaching the interaction energy U_{95} asymptotically. We compare these observed resonances with the theoretical expectation (shaded regions) for the differential spectrum between the energies of the repulsively interacting double well E_i^{95} and the ground state of the non-interacting double well E_0^{97}. Clearly, the observed energetically lower resonances correspond to a transfer between the two ground states (blue), whereas the energetically higher resonances correspond to a transfer to the $|d_-\rangle$ state (orange).

An insight into this relative spectrum, can be gained by comparing the spectra of the non-interacting and repulsively interacting double well in figure 4.14. The prepared ground state of the non-interacting double well (dashed blue line) changes its energy linearly with the tilt Δ. However, the ground state of the repulsively interacting double well (blue line) has a constant energy until the tilt is comparable to the interaction energy $\Delta > 0.5\,U_{95}$. Therefore, the energy difference between these two ground states changes linearly, until both states are localized on the lower lattice site $\Delta \gg 0.5U_{95}$, where the double well effectively reproduces the behavior of a monochromatic lattice.

The possibility of observing a transfer between the prepared ground state ψ_0^{97} and any final state

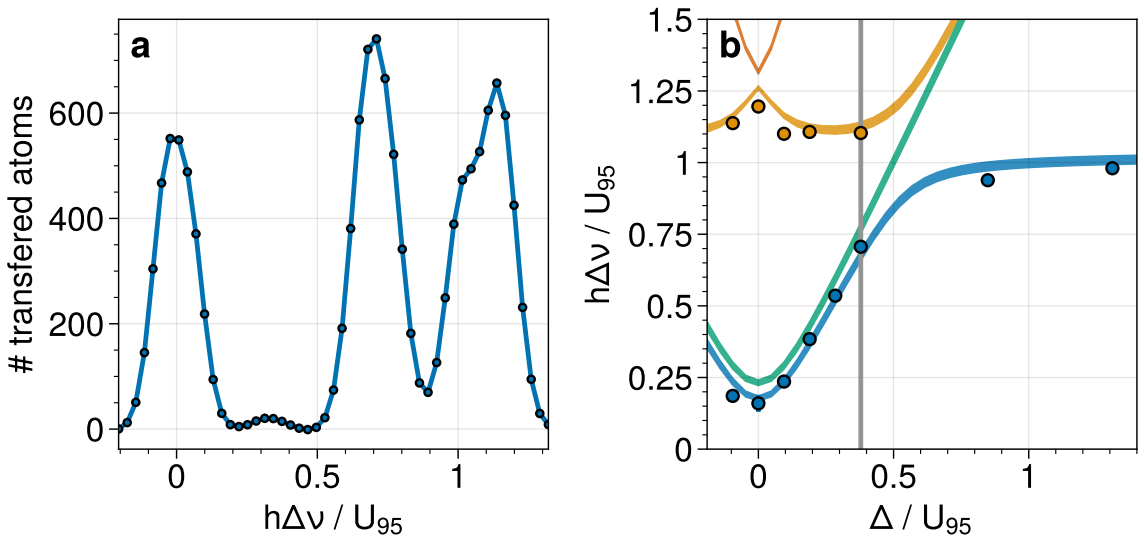

Figure 4.13: **Radio-frequency spectroscopy of interacting double well:** (a) Radio-frequency transfer from atoms in the $|9,7\rangle$ hyperfine mixture to the $|9,5\rangle$ hyperfine mixture. The magnetic field is chosen to create a non-interacting $|9,7\rangle$ hyperfine mixture and a repulsively interacting mixture $|9,5\rangle$ with $U_{95} \approx 8.1t$. The number of transferred atoms changes with the frequency detuning from the singles resonance $\Delta\nu = \nu - \nu_S$ and shows three distinct peaks for a tilt of $\Delta \approx 0.4U$. The resonances above the singles peak arise from transfers between doubly-occupied double wells with different interaction energies. (b) Relative spectroscopy signal of atoms prepared in the ground state of a non-interacting double well ψ_0^{97} that are transferred to various states of the interacting double well Ψ_i^{97}. The gray vertical line indicates the spectroscopy signal of subfigure a. For small tilts $\Delta/U_{95} < 0.5$, the atoms are only transferred to the ground state ψ_0^{97} (blue data points) and second-excited state Ψ_2^{97} (orange data points). The experimental data agrees well with the theoretical expectation obtained from Monte-Carlo simulations with the 1σ confidence interval indicated as shaded regions.

ψ_i^{95} is defined by the overlap between the states

$$A_i = \left|\left\langle \psi_0^{97} | \psi_i^{95} \right\rangle\right|^2, \tag{4.19}$$

as the utilized RF-transfer leaves the spatial wave function of the particles unchanged. This overlap changes drastically with the tilt Δ (cf. figure 4.14 b): For large tilts, there is only a finite overlap to the ground state of the repulsively interacting double well, which explains the observed single resonance. Moreover, for intermediate tilts $0 < \Delta/U_{95} \leq 0.5$, there is an additional significant overlap to the $|d_-\rangle$ state resulting in two possible transfers. For vanishing tilts $\Delta = 0$, the transfer to the $|d_-\rangle$ state should not be possible, which does not match our observations. However, this spectrum was averaged over the center region of the trap (20×20 lattice sites) and before we had control over the spatially varying superlattice-phase gradient. Therefore, it is reasonable to assume, that the number of double wells with vanishing tilt over the considered lattice sites is small.

This differential spectroscopy of the double well validates our calibration of the Hubbard parameters t, Δ, U of the interacting double well. Interestingly, we have seen that a transfer to a highly-excited eigenstate of the repulsively interacting double well is possible. We will explore the preparation and

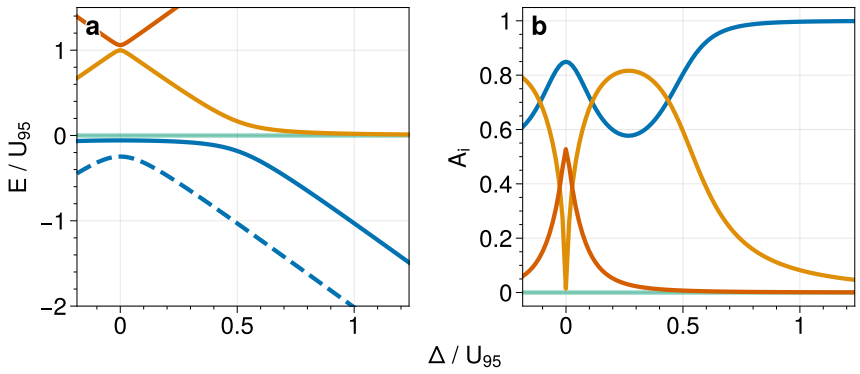

Figure 4.14: **Energies and wave function overlap for relative spectroscopy measurement:** (a) Non-interacting ground state energy E_0^{97} (blue dashed line) compared to the energies of the repulsively interacting double well E_i^{95} for various tilts Δ. Here, the interaction energy $U_{95} \approx 8.1\,t$ is chosen. (b) The overlap A_i between the non-interacting ground state wave function ψ_0^{97} and the wave functions of the repulsively interacting double well ψ_i^{95} are plotted for various tilts Δ. In both subplots, the ground state is shown in blue, the triplet state in green, the $|d_-\rangle$ state in orange and the excited state in red.

detection of this peculiar state in the next section.

4.2.3 Repulsively-bound pairs in double wells

In the last subsection, we have performed radio-frequency spectroscopy of interacting fermions in double wells, where we have observed transfers to highly excited eigenstates (orange data points in figure 4.13 b) for large repulsive interactions. For a balanced system $\Delta = 0$, this eigenstate is a coherently delocalized pair state, written as

$$|d_-\rangle = \frac{1}{\sqrt{2}}(|LL\rangle - |RR\rangle). \tag{4.20}$$

This highly excited eigenstate is peculiar, as it is a coherent pair state of fermions despite the large repulsive interactions. Therefore, we refer to this state as a repulsively-bound pair state [132]. In this section, we investigate the experimental preparation of this excited eigenstate and present a detection scheme to measure its population coherently. This will allow for a future investigation of the lifetime of these repulsively-bound pairs.

It should be stressed, that this excited eigenstate changes its composition of basis states with the tilt Δ, as we have shown by the orange trace in figure 4.11 a. For a balanced double well, it corresponds to the $|d_-\rangle$ state, while for a dominant tilt $\Delta \gg |U|$ it becomes the singlet state $|s\rangle$. To avoid confusion throughout this section, we always refer to this excited state as the $|d_-\rangle$ state.

Preparation and detection of repulsively-bound pairs

We experimentally prepare the repulsively-bound pairs in an array of double wells, that is created by the lattice configuration $V_s = 10\,E_{\mathrm{rec}}$, $V_l = 15\,E_{\mathrm{rec}}$, $s_y = 55\,E_{\mathrm{rec}}$ and $s_z = 110\,E_{\mathrm{rec}}$. We start in a balanced hyperfine mixture of $|F = 9/2,\, m_F = -9/2\rangle$ and $|F = 9/2,\, m_F = -7/2\rangle$ (shorthand notation

for the mixture is $|9, 7\rangle$), with negligible interactions $U_{97} \sim 0t$. Then, we prepare the $|d_-\rangle$ state of the double well by a RF Landau-Zener transfer to the hyperfine mixture of $|F = 9/2,\ m_F = -9/2\rangle$ and $|F = 9/2,\ m_F = -5/2\rangle$, that is repulsively interacting $U_{95} \sim 8t$. To ensure a significant overlap between the spatial wave functions (cf. figure 4.14 b), we choose a tilted double-well configuration $\Delta \sim -U_{95}/2$ during the RF-transfer. This preparation procedure allows for a preparation fidelity of the repulsively-bound pair-state of $0.93^{+0.07}_{-0.18}$. This preparation fidelity was determined by comparing the number of atoms transferred into the $|d_-\rangle$ with the initial number of atoms in doubly occupied double wells.

After the preparation, a planned experiment will measure the lifetime of the repulsively-bound pairs at arbitrary double-well tilts Δ. During this experiment, the pairs might decay to the ground state or get excited into a higher lying state by heating processes. To observe the state populations after the experiment, we adiabatically introduce a large tilt $\Delta \gg U, t$. In this configuration, the $|d_-\rangle$ state is adiabatically connected to the $|s\rangle$ state, whereas the ground- and excited state are mapped to the doubly occupied states $|LL\rangle$ and $|RR\rangle$ (cf. figure 4.11 a). The distinction of singly and doubly occupied lattice sites, using the SD separation introduced in section 3.3.1, allows for a detection of the $|d_-\rangle$ state population N_S compared to the added population of ground and excited state N_D. We use both populations to calculate the population contrast

$$C = \frac{N_D - N_S}{N_D + N_S}, \tag{4.21}$$

which is insensitive to fluctuations of the total atom number. This applied series of the preparation and detection scheme requires an elaborate series of RF transfers, the technical details for this are given in figure B.1 of Appendix B.

In this detection method based on the population of strongly-tilted double wells, singly occupied double wells (e.g. $|L\rangle$) cannot be distinguished from the $|d_-\rangle$ state, nor can incoherent doubly occupied states (e.g. $|LL\rangle$) be distinguished from the ground state populations. However, due to the possible decay mechanisms, it is not guaranteed that the prepared $|d_-\rangle$ state remains a pure state. Therefore, to measure the population of the pure state, we induce Rabi oscillations between the $|d_-\rangle$ state and the ground state, before the SD separation. The amplitude of this oscillation is a direct measure of the desired eigenstate populations, while other states like singly occupied double wells would result in an offset. To induce the Rabi oscillations between both states, we modulate the tilt of the double well [2] at their avoided crossing where $\Delta = -U_{95}/2$.

In the following, we briefly show that the periodic modulation of the double well induces Rabi oscillations between the $|d_-\rangle$ state and the ground state at their avoided crossing. The Hamiltonian of the double-well modulation is given as

$$H_{\mathrm{mod}}(\tau_{\mathrm{mod}}) = \Delta_{\mathrm{mod}} \cdot \cos(\omega\tau_{\mathrm{mod}}) \left(|LL\rangle\langle LL| - |RR\rangle\langle RR|\right), \tag{4.22}$$

with the tight binding modulation amplitude Δ_{mod} and frequency $\omega \equiv 2\pi\nu_{\mathrm{mod}}$. For a driving frequency ω close to the energy gap between the $|d_-\rangle$ state and the ground-state $\omega_0 = (E_{d-} - E_{\mathrm{GS}})/\hbar$, this system can be approximated by a driven two-level system. This simplification is possible, as the triplet state $|t\rangle$ can be neglected due to a lack of coupling and the participation of the excited state is suppressed by the large energy detuning $\Delta E \approx 2U$. In this approximate two-level system, at the

[2] For a fast modulation of the tilt, we change the superlattice phase via the double pass AOM, as introduced in section 3.2.2.

avoided crossing of the $|d_-\rangle$ state and the ground state, the two basis states are

$$|d_-\rangle \equiv \alpha\,|LL\rangle + \beta\,|s\rangle + \epsilon_{d-}\,|RR\rangle \equiv \begin{pmatrix}1\\0\end{pmatrix} \tag{4.23}$$

and

$$|GS\rangle \equiv \gamma\,|LL\rangle + \delta\,|s\rangle + \epsilon_{\mathrm{GS}}\,|RR\rangle \equiv \begin{pmatrix}0\\1\end{pmatrix} \tag{4.24}$$

with a negligible population of $|RR\rangle$, as $\epsilon_{d-}, \epsilon_{\mathrm{GS}} \ll \alpha, \beta, \gamma, \delta$. In this new basis, the Hamiltonian of the modulation can be written as

$$H_{\mathrm{mod}}(\tau_{\mathrm{mod}}) = \Delta_{\mathrm{mod}} \cos(\omega\tau_{\mathrm{mod}}) \cdot \begin{pmatrix}\alpha^2 & \alpha\gamma\\ \gamma\alpha & \gamma^2\end{pmatrix} + O(\epsilon^2) \tag{4.25}$$

where the population coefficients are considered to be real-valued. The off-diagonal elements of this Hamiltonian couple the two basis states and thus induce Rabi oscillations between them. Using the rotating-wave-approximation [60], the Hamiltonian of this driven two-level system is given in the rotating-frame as

$$H_{\mathrm{rot}} \approx \frac{\hbar}{2}\begin{pmatrix}-\delta_\omega & \Omega_R\\ \Omega_R & \delta_\omega\end{pmatrix}, \tag{4.26}$$

with the Rabi frequency $\Omega_R = \alpha\gamma\Delta_{\mathrm{mod}}/\hbar$ and detuning from resonance $\delta_\omega = \omega_0 - \omega$. This Hamiltonian of the driven system in the rotated frame is not diagonal, and therefore, the $|d_-\rangle$ state and the ground state are no eigenstates of this system. Therefore, when initially preparing the $|d_-\rangle$ state, the periodic modulation induces Rabi oscillations between the $|d_-\rangle$ state and the ground state with a frequency given as [60]

$$f = \frac{1}{2\pi}\sqrt{\delta_\omega^2 + \Omega_R^2}. \tag{4.27}$$

Evidently, we expect a Rabi oscillation with minimal frequency for a resonant drive $\delta_\omega = 0$. Moreover, increasing the amplitude of the modulation Δ_{mod} increases the Rabi frequency Ω_R and therefore the oscillation frequency f. Note that with this modulation technique, we solve the aforementioned problem of singly occupied double wells (e.g. $|L\rangle$ states) being detected in the same fashion as $|d_-\rangle$ states, via the SD separation. These singly occupied states do not change their state by the periodic modulation, and therefore are visible as an offset to the oscillation.

We experimentally probe the Rabi oscillations between the $|d_-\rangle$ state and the ground state for a tilted double well $\Delta = -U_{95}/2$. The population contrast C at the trap center (averaged over 20×20 lattice sites) oscillates during the modulation time τ_{mod}, as shown in figure 4.15 a, for an almost resonant drive. We observe a clear sinusoidal signal according to with one characteristic frequency and a pronounced dephasing due to the inhomogeneous lattice depths. This shows qualitatively, that we have coherently prepared and detected an excited eigenstate of this system.

We fit a damped sinusoidal function (compare equation 4.6) to the data to obtain a more quantitative measure of the oscillations. We extract an amplitude of (-0.66 ± 0.01) for the oscillation shown in figure 4.15 a. Compared to the maximal value of 1, this amplitude indicates a significant but improvable preparation of a coherent excited state. The reasons for this imperfection are most likely caused by the averaging over inhomogeneous double-wells, but this needs to be investigated in more detail in the future.

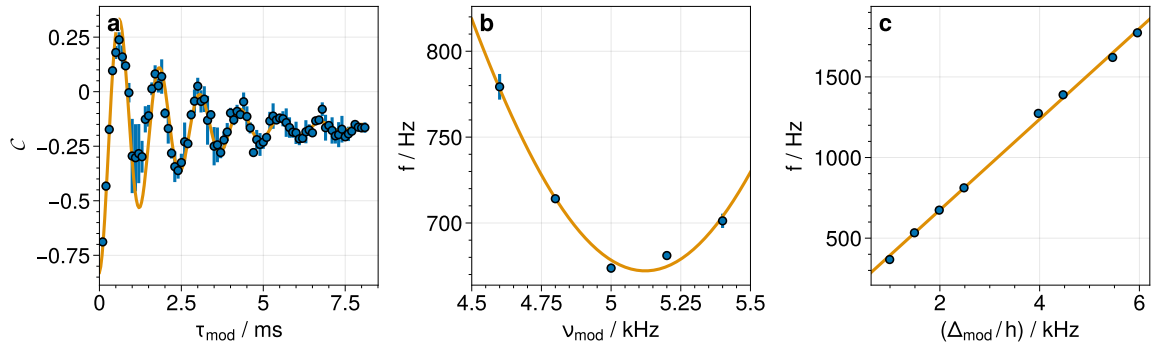

Figure 4.15: **Rabi oscillations between repulsively-bound pairs and the ground state of the double well:** (a) For a tilt modulation with amplitude $\Delta_{\mathrm{mod}}/h = 2.5\,\mathrm{kHz}$ and frequency $\nu_{\mathrm{mod}} = 5\,\mathrm{kHz}$, the population contrast C oscillates as a function of the time τ_{mod}. The data is shown in blue and a fitted sinusoidal function accordingis shown in orange. (b) The extracted oscillation frequency f (blue data points) changes with the modulation frequency ν_{mod} for a constant modulation amplitude of $\Delta_{\mathrm{mod}}/h = 2\,\mathrm{kHz}$. (c) For a resonant drive and constant driving frequency of $\nu_{\mathrm{mod}} = 5.4\,\mathrm{kHz}$, the observed oscillation frequency f changes linearly with the Rabi frequency $\Omega_R \propto \Delta_{\mathrm{mod}}/\hbar$. For subplots b and c, the fitted behavior according to equation 4.27 is shown in orange.

To determine the driving frequency for a resonant modulation $\delta_\omega = 0$, we vary ν_{mod} and compare the extracted frequencies (cf. figure 4.15 b). We fit equation 4.27 and extract the minimal oscillation frequency $f_{\mathrm{min}} = \frac{\Omega_R}{2\pi} = (672 \pm 3)\,\mathrm{Hz}$ at a driving frequency of $\nu_{\mathrm{mod}} = (5.12 \pm 0.01)\,\mathrm{kHz}$. Finally, we change the driving amplitude Δ_{mod} for a fixed driving frequency and observe the expected linear scaling of the Rabi frequency with the amplitude (cf. figure 4.15 c). Evidently, the driving induced Rabi oscillations change their oscillation frequency f with the driving frequency ν_{mod} and driving amplitude Δ_{mod} as theoretically expected.

We have successfully implemented a scheme to prepare repulsively bound atom pairs in an array of double wells using a radiofrequency transfer with high fidelity. Moreover, we have applied a tilt modulation scheme to drive coherent Rabi oscillations, that allow a transfer between the $|d\_\rangle$ state and the ground state of the system. We have demonstrated, that the observed Rabi oscillation frequency changes with the detuning Δ_ω and the driving amplitude Δ_{mod} according to the theoretical expectation, establishing our experimental control over this technique. In the future, we will use this technique to extract the pure state fraction of the prepared excited state. We will employ this technique to study the lifetime of repulsively-bound pairs in balanced double wells in the future.

CHAPTER 5

Periodically modulated double wells

A periodic modulation of a system can fundamentally alter its intrinsic properties. A famous classical example is a macroscopic ball on a saddle-point surface as depicted in figure 5.1. In the static scenario, the slightest deviation from the exact center position is unstable and makes the ball roll down. However, a periodic drive (in this case a rotation of the saddle point) creates an *effectively* stable potential if the frequency is much faster than the eigenfrequency of the system. Moreover, the ball performs a wiggly motion on an elliptical trajectory during the drive as it rolls to the time dependent potential minimum. The amplitude of this motion intuitively depends on the driving frequency and is usually referred to as a *micromotion*.

This description of a periodically driven system by a separation into a slow effective behavior and a fast motion within one driving period is the fundamental concept of Floquet physics [133, 134]. Moreover, the presented possibility to create effective systems with properties that go beyond their static counterparts is usually referred to as *Floquet engineering*. This concept is of natural interest across many physics disciplines. For instance, coupled waveguides were used to realize Floquet topological insulators [135] and to highlight the importance of dissipation in the context of quantized transport [136] in the photonics community [137]. In solid state physics, femtosecond laser pulses were used to demonstrate light-induced superconductivity [138] and manipulate magnetic order [139].

Quantum simulation using ultracold atoms is a particularly suitable platform for the study of periodically driven systems due to its excellent control over system parameters as well as timescales

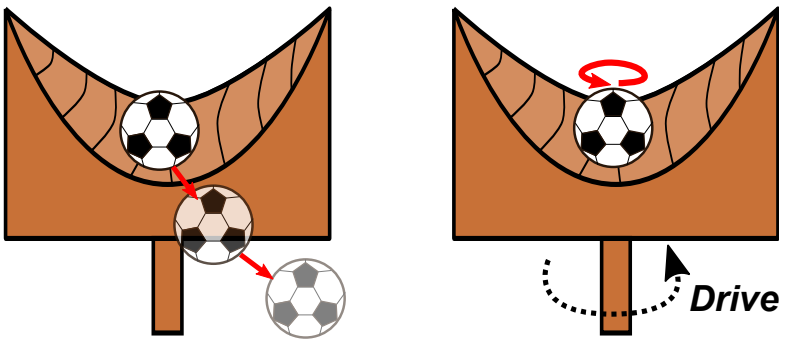

Figure 5.1: **Ball on a static and driven saddle-shaped potential:** This figure was inspired by [59].

in the kHz regime [41, 140]. For example, the dynamic properties of lattice systems were changed fundamentally by modulating the lattice position or the external magnetic field [141, 142]. Moreover, complex tunneling amplitudes were realized [57], that have enabled the study of quantized gauge fields [43, 44]. And recently, a periodically driven honeycomb-lattice was used to study an anomalous Floquet-topological system with topological edge modes despite a vanishing Chern number [143, 144].

In this chapter we are going to study periodically-modulated double wells [145–147] in the high-frequency and the resonantly-driven limit. We are going to briefly introduce Floquet theory [133, 134] and discuss the stroboscopic, as well as the effective description of periodically modulated systems. Then, we will apply this formalism to describe driven double wells as introduced in [77] and compare this to our experimental results: We will demonstrate the phenomenon of *dynamic localization* [45], where dynamics are frozen due a strong periodic drive, in the high frequency limit. Finally, we realize *density dependent* tunneling [75, 76] for resonantly driven double wells.

5.1 Floquet theory

In this section we are going to study the theoretical description of periodically driven systems following the works of Bukov et al. [134] and Goldman et al. [133]. These driven systems can be described by separable Hamiltonians

$$\hat{H}(\tau) = \hat{H}_0 + V(\tau) = \hat{H}_0 + V(\tau + T), \tag{5.1}$$

with the time independent part $\hat{H}_0$, and the time dependent part $V(\tau)$ with periodicity T. First, let's develop an intuitive understanding of a periodically driven system characterized by a driving frequency ν and amplitude K_0, by examining two contrasting regimes: In the adiabatic driving regime, where ν is significantly lower than the system's intrinsic frequencies, the eigenstates adapt to follow the driving frequency. Conversely, when the driving frequency surpasses any intrinsic frequency of the system, the response typically resembles that of an effective static potential. In its simplest form, this (effectively static) potential is equivalent to the time-averaged value $1/T \left(\int_0^T d\tau \hat{H}(\tau) \right) = \hat{H}_0$.

Even though Floquet physics describes periodically driven systems beyond these two extreme regimes, the connection is evident: In analogy to Bloch's Theorem, Floquet physics aims to decompose the time evolution of the periodically driven system into two parts: A slow motion governed by a time-independent Floquet Hamiltonian $\hat{H}_\mathrm{F}$ and a fast motion within the driving period T – the micromotion. As a consequence, the time evolution operator can be written as

$$\hat{U}(\tau_1, \tau_2) = e^{-i\hat{K}(\tau_2)} e^{-i\hat{H}_\mathrm{F}\cdot(\tau_1-\tau_2)} e^{i\hat{K}(\tau_1)}, \tag{5.2}$$

where $\hat{K}(\tau) = \hat{K}(\tau + T)$ is the time-periodic Kick operator. In general, there are several approaches to finding a Floquet Hamiltonian and corresponding Kick operator that fulfill equation 5.1. However, in this work we use the High-Frequency Expansion (HFE) to pertubatively calculate the effective Floquet Hamiltonian $\hat{H}_\mathrm{eff}$ and corresponding kick operator. In the next section we will start with the intuitive stroboscopic description of periodically driven systems and continue with the effective picture.

5.1.1 The stroboscopic and effective Floquet Hamiltonian

The basic concept of a stroboscopic description is that due to the periodicity of the drive, the time evolution for times corresponding to integer multiples of the periodicity $\delta\tau = nT$ is linear. However, there is a gauge freedom of the phase or the reference time within the modulation τ_0 at which the Floquet Hamiltonian $\hat{H}_F(\tau_0)$, which governs this linear time evolution, is applied. To determine the time evolution operator in the stroboscopic approach, we start with the evolution operator defined as

$$U(\tau_2, \tau_1) = \mathcal{T}_\tau e^{-i\int_{\tau_1}^{\tau_2} \hat{H}(\tau')d\tau'}, \tag{5.3}$$

with the time ordering operator $\mathcal{T}_\tau$ [134]. This evolution operator factorizes $U(\tau_2, \tau_1) = U(\tau_2, \tau_0) \cdot U(\tau_0, \tau_1)$ and fulfills $U(\tau_2, \tau_1) = U(\tau_2 + nT, \tau_1 + nT)$ for integer n due to the periodicity of the drive. With this, the general evolution can be written as

$$U(\tau_2, \tau_1) = U(\tau_2, \tau_0 + nT)\, e^{-i\hat{H}_F(\tau_0)nT}\, U(\tau_0, \tau_1), \tag{5.4}$$

illustrating that the time independent stroboscopic Floquet Hamiltonian $\hat{H}_F(\tau_0)$ describes the evolution for integer multiples of the driving period depending on the Floquet gauge choice. This gauge dependency of the Floquet Hamiltonian can be problematic in comparison to experimental observations, as an exact phase stabilisation between readout and modulation is difficult. Therefore, the phase dependency of the stroboscopic Floquet Hamiltonian can be gauged into the kick operators resulting in

$$U(\tau_1, \tau_2) = e^{-iK(\tau_2)} e^{-i\hat{H}_{\text{eff}}\cdot(\tau_1-\tau_2)} e^{iK(\tau_1)}, \tag{5.5}$$

with the gauge and time independent *effective Floquet Hamiltonian* $\hat{H}_{\text{eff}}$. This time evolution can be interpreted as a three-step procedure, starting with a transformation into a rotating frame. Here, the time evolution is governed by the effective Hamiltonian. After this evolution, the system is transformed to a measurement-time dependent final frame which causes the micromotion.

One main task of Floquet theory is the determination of the effective Hamiltonians and kick operators for a given driving scheme. In some situations, this is done in an iterative approach to solve the differential formulation of Floquet's theorem

$$\hat{H}_{\text{eff}} = e^{i\hat{K}(\tau)}\hat{H}(\tau)e^{-i\hat{K}(\tau)} + i\left(\partial\tau\, e^{i\hat{K}(\tau)}\right)e^{-i\hat{K}(\tau)}, \tag{5.6}$$

however, we are going to introduce a perturbative approach to face this problem.

Inverse frequency expansion

The Floquet Hamiltonian can only in rare cases be determined analytically. Therefore, for large driving frequencies, a perturbative approach is reasonable. For example, let's consider interacting fermions in a balanced double well with interaction energy U and tunneling t. If the driving frequency dominates $h\nu \gg U, t$, the system cannot absorb energy from the drive, which makes a perturbative approach resonable.

There are different expansion methods to pertubatively determine the Floquet Hamiltonians, depending on the Floquet gauge. Usually, the Magnus expansion is chosen to approximate the stroboscopic Floquet Hamiltonian [134]. However, in this work, we are going to focus on the effective

Floquet Hamiltonian. In this case, the High-Frequency Expansion is suitable to expand the effective Hamiltonian and kick operator as

$$\hat{H}_{\text{eff}} = \sum_{n=0}^{\infty} \hat{H}^n_{\text{eff}}, \quad K_{\text{eff}}(t) = \sum_{n=1}^{\infty} K^n_{\text{eff}}(t), \tag{5.7}$$

where $\hat{H}^n_{\text{eff}} \propto 1/\nu^n$ and $K^n_{\text{eff}} \propto 1/\nu^n$ [148]. In order to determine these expansion components, we start from the time evolution operator over a full driving cycle

$$U(T,0) = \mathcal{T}_\tau \exp\left(-i \int_0^T d\tau' \hat{H}(\tau')\right) = \exp\left(-i\hat{H}_{\text{eff}} T\right), \tag{5.8}$$

where we have used equation 5.5 for the second equality. Taking the logarithm and performing a Taylor expansion with regards to $1/\nu$ gives the first components of the effective Hamiltonian [149]

$$\hat{H}^0_{\text{eff}} = \hat{H}_0 = 1/T \int_0^T d\tau' \hat{H}(\tau'), \tag{5.9}$$

$$\hat{H}^1_{\text{eff}} = \frac{1}{2\pi\nu} \sum_{m=1}^{\infty} \frac{1}{m} \left[\hat{H}_m, \hat{H}_{-m}\right], \tag{5.10}$$

and the kick operator

$$K^1_{\text{eff}}(t) = \frac{1}{2\pi\nu} \sum_{m\neq 0} \frac{e^{i2\pi m\nu t}}{m} \hat{H}_m, \tag{5.11}$$

where we have introduced the Fourier components of the Hamiltonian $\hat{H}_m$. Evidently, for an infinitely high frequency drive, the effective behavior matches the intuitive picture: The effective Hamiltonian is described by the time average of the time dependent Hamiltonian and the kick operator is zero, suppressing the micromotion.

However, if one deviates from the high-frequency limit, the computational amount of the inverse frequency expansion increases drastically, as more terms of equation 5.7 are required to describe the effective Hamiltonian. In this work, we consider an inverse frequency expansion up to the third order $1/\nu^3$ to ensure a convergence of the expansion. Moreover, when computing the first order correction to the effective Hamiltonian $\hat{H}^1_{\text{eff}}$, the sum over the commutator needs to converge as well. This convergence depends on the driving amplitude, as the Fourier components of the Hamiltonian $\hat{H}_m$ are usually expanded in terms of Bessel functions. We consider Bessel functions $\mathcal{J}_j(K_0)$ for $j = 0, 1, 2, 3$ to realize converging Fourier components, which we have checked explicitly [112].

Eigenvalues and observables

The eigenvalues and eigenstates of the Floquet Hamiltonian are of particular interest in order to determine the expectation values of observables in driven systems. The (pertubatively) determined effective Hamiltonian fulfills the time independent Schrödinger equation

$$\hat{H}_{\text{eff}} |u_n\rangle = \epsilon_n |u_n\rangle \tag{5.12}$$

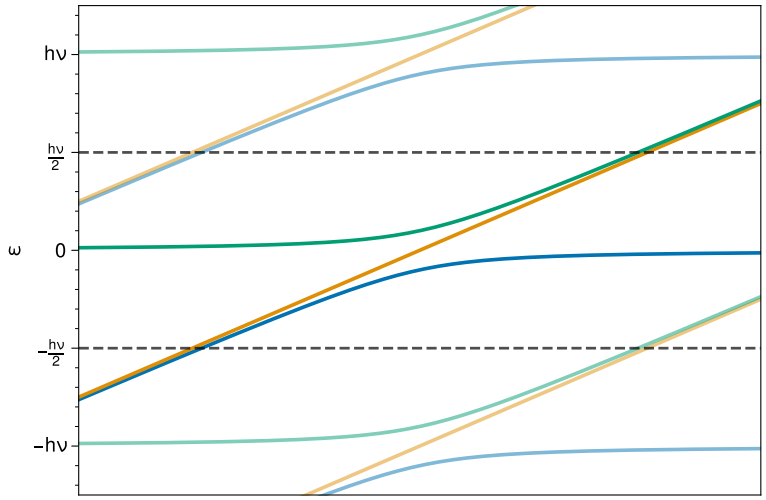

Figure 5.2: **Spectrum and Floquet zones of a periodically modulated double well:** The quasi energies ϵ of the effective Hamiltonian (blue, orange and green lines) are only defined mod $h\nu$. This causes the spectrum to contain infinite copies of quasi energies that are spaced by $h\nu$. Within one Floquet zone $(nh\nu - h\nu/2, nh\nu + h\nu/2]$ with integer n (dashed lines), the quasi energy is well-defined.

with the effective eigenvectors $|u_n\rangle$ and eigenvalues ϵ_n. Following Floquet's theorem the *Floquet states* are eigenstates of the time dependent Schrödinger equation and are defined as

$$|\psi_n(\tau)\rangle = e^{-i\epsilon_n \tau}\, e^{-iK(\tau)}\, |u_n\rangle \tag{5.13}$$

where the *Floquet mode* $|u_n(\tau)\rangle = e^{-iK(\tau)}\, |u_n\rangle$ is introduced. Evidently, the time evolution of the Floquet state is in analogy to Bloch's theorem separable into the slow time evolution with the quasi energies ϵ_n of the Floquet modes and their rapid time evolution with the micromotion. Moreover, the quasi energies are only defined up to multiples of $h\nu$ as adding or removing a driving quantum leaves the Floquet states unchanged [58]. This gives rise to a ladder-type spectrum (cf. figure 5.2) which has infinite rungs and therefore no well-defined ground state. Therefore, we restrict the quasi energies to the first Floquet zone $\epsilon_n \in (-h\nu/2, h\nu/2]$.

With the Floquet states we can compute the expectation value of an observable $\hat{O}$

$$\left\langle \hat{O} \right\rangle = \langle \psi(\tau)|\, \hat{O}\, |\psi(\tau)\rangle \tag{5.14}$$

$$= \langle u_n|\, e^{iK(\tau)} \hat{O} e^{-iK(\tau)}\, |u_n\rangle \tag{5.15}$$

which oscillates in similar fashion as the driving frequency. This phenomenon is called *micromotion*.

5.2 High frequently driven double wells

In this section we are going to discuss periodically driven double wells in the high frequency limit both theoretically and experimentally. First, we are computing the effective Hamiltonian in the high frequency expansion for a periodically modulated double well, following [77]. Then, we are

studying this model experimentally using a spin polarized cloud in an effectively one-dimensional optical superlattice with periodic drive. We are going to show observations of the rescaled tunneling amplitudes with the 0th order Besselfunction, the effect of dynamic localization and the effects of micromotion.

5.2.1 High frequency expansion of driven double wells

We study Floquet physics by applying a periodic modulation to the tilt of an array of double wells, as described in section 3.2.2. The application of the HFE to this model is discussed in detail in [77, 112] and will be shortly summarized in the following. This driven system can be described by the time dependent Hamiltonian

$$\hat{H}(\tau) = \hat{H}_0 + \hat{V}(\tau),\ \hat{H}_0 = \begin{pmatrix} U & -t & t & 0 \\ -t & 0 & 0 & -t \\ t & 0 & 0 & t \\ 0 & -t & t & U \end{pmatrix}, \tag{5.16}$$

where we have used the balanced, interacting double-well Hamiltonian $\hat{H}_0$, as introduced in section 4.2.1,[1] and the modulated on-site energy

$$\hat{V}(\tau) = h\nu K_0 \cos(2\pi\nu\tau)\, h_\Delta,\quad h_\Delta = \begin{pmatrix} 1 & 0 & 0 & 0 \\ 0 & 0 & 0 & 0 \\ 0 & 0 & 0 & 0 \\ 0 & 0 & 0 & -1 \end{pmatrix}, \tag{5.17}$$

in the usual Fock basis, where the normalized, dimensionless driving amplitude is denoted K_0 and the driving frequency ν. First, we will discuss the *high frequency limit* $h\nu \gg U, t$, however the amplitude of the periodic modulation also scales with the driving frequency. Therefore, a description in a rotating frame is necessary in order to make use of the high frequency expansion introduced in section 5.1. Introducing the rotation matrix

$$R_1(\tau) = \exp\left[-i \int \partial\tau V(\tau)\right] = \exp\left[-iK_0 \sin(2\pi\nu\tau) h_\Delta\right] \tag{5.18}$$

the Hamiltonian in the rotated frame is given by

$$\hat{H}_{\text{rot}}(\tau) = R_1^\dagger(\tau)\hat{H}_0 R_1(\tau) = \begin{pmatrix} U & -t(\tau) & t(\tau) & 0 \\ -t^*(\tau) & 0 & 0 & -t(\tau) \\ t^*(\tau) & 0 & 0 & t(\tau) \\ 0 & -t^*(\tau) & t^*(\tau) & U \end{pmatrix}, \tag{5.19}$$

[1] Here we have neglected the higher-band corrections V_{nn}, V_{de} and V_{ct} due to their vanishing amplitude.

with the time dependent tunneling amplitude $t(\tau) = t \exp\left[iK_0 \sin(2\pi\nu\tau)\right]$. The effective Hamiltonian in the lowest orders 5.9 of the HFE is then given by

$$\hat{H}^0_{\text{eff}} = \begin{pmatrix} U & -t\mathcal{J}_0(K_0) & t\mathcal{J}_0(K_0) & 0 \\ -t\mathcal{J}_0(K_0) & 0 & 0 & -t\mathcal{J}_0(K_0) \\ t\mathcal{J}_0(K_0) & 0 & 0 & t\mathcal{J}_0(K_0) \\ 0 & -t\mathcal{J}_0(K_0) & t\mathcal{J}_0(K_0) & U \end{pmatrix} \tag{5.20}$$

and $\hat{H}^1_{\text{eff}} = 0$ where we have used the definition of the Bessel functions of order ℓ

$$\mathcal{J}_\ell(x) = \frac{1}{T}\int_0^T \partial\tau \exp\left[i(x\sin(2\pi\nu\tau) + \ell 2\pi\nu\tau)\right]. \tag{5.21}$$

Evidently, the effective Hamiltonian in lowest order can be obtained by replacing $t \to t\mathcal{J}_0(K_0)$ in the static Hamiltonian, which clearly deviates from a mere time averaging of the potential. This interesting behavior arises since the driving amplitude is also frequency dependent in the applied driving scheme. The corresponding kick operator in the lowest order[2] is

$$K^1_{\text{rot}}(\tau) = 2i\frac{t}{h\nu}\mathcal{J}_1(K_0)\cos(2\pi\nu\tau)\begin{pmatrix} 0 & 1 & -1 & 0 \\ -1 & 0 & 0 & 1 \\ 1 & 0 & 0 & -1 \\ 0 & -1 & 1 & 0 \end{pmatrix} \tag{5.22}$$

with a dimensionless amplitude $A^1_{\text{rot}} \equiv t\mathcal{J}_1(K_0)/(h\nu)$ which is clearly vanishing in the high frequency limit. However, the transformation into the rotating frame leads to a second contribution to the micromotion that cannot be neglected in general [58, 77, 134]. This part of the micromotion changes our specific observables, which we will introduce in the next section, only perturbatively and was therefore neglected in the fitting procedures due to computational reasons [112]. Now that we have introduced the theoretical framework to describe the periodically driven double wells in the high frequency limit we can compare this to our experimental findings.

5.2.2 Spin-polarized fermions in periodically driven double wells

We study periodically driven double wells in the high frequency limit by loading a spin polarized cloud into our optical superlattice. As a consequence of the spin polarization, there is no interaction strength $U = 0$ and thus the driving frequency only needs to be larger than the tunnel coupling $\nu \gg t$ to realize the high-frequency regime. The experimental procedure follows section 4.1.2, where we have probed the tunneling dynamics in an array of double wells, with the addition of a periodic drive. We start with a cloud of polarized atoms at approximately unity filling in a three-dimensional lattice configuration $V_l = 15\,E_{\text{rec}}$, $s_y = 55\,E_{\text{rec}}$ and $s_z = 110\,E_{\text{rec}}$. The tunnel coupling in y- and z-direction is suppressed significantly compared to the x-direction $t_z/t_x < t_y/t_x \lesssim 0.01$, which allows us to describe the system as an array of one-dimensional systems.

We adiabatically load our atoms from the monochromatic lattice into the lowest Bloch band of the superlattice by ramping up the green lattice laser to $V_s = 30\,E_{\text{rec}}$ in 35 ms, as shown in figure 5.3. This

[2] The lowest order in this case means in terms of $1/\nu$ as well as Bessel functions up to the first order.

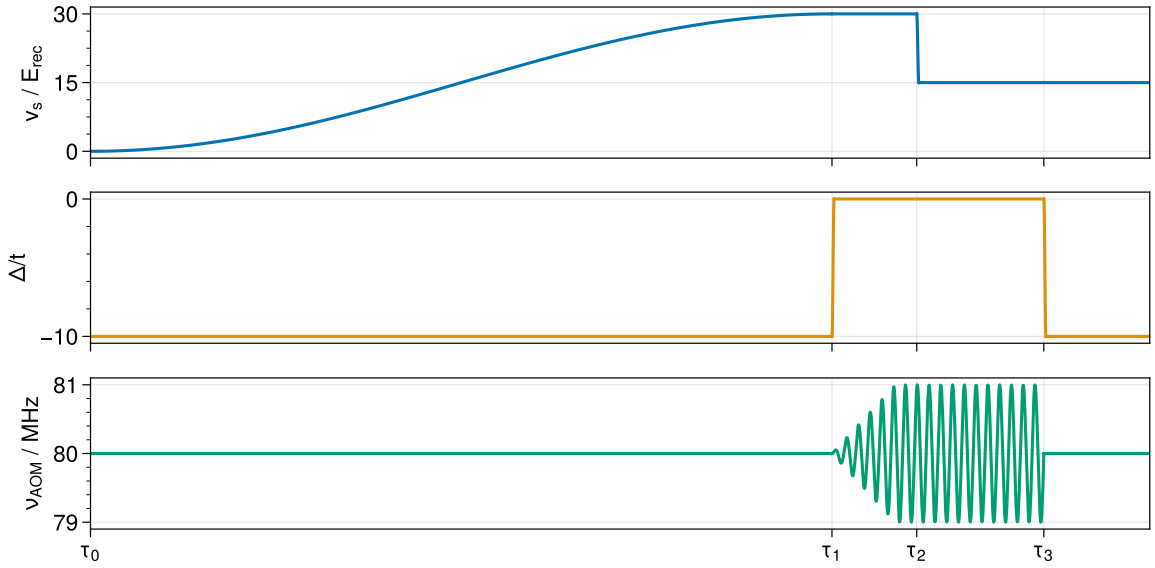

Figure 5.3: **Visualization of the experimental scheme to probe periodically modulated double wells:** The green lattice depth V_s is indicated as the blue trace. The energy offset, or tilt, of the double well Δ_0 is shown as the orange trace. The Floquet drive is implemented by modulating the frequency of the lattice AOM ν_{AOM} and shown as a green trace. The relevant timescales are $\tau_1 - \tau_0 = 35$ ms, $\tau_2 - \tau_1 = 3$ ms and the experiment time $\tau = \tau_3 - \tau_2$. For a detailed description of the scheme please refer to the text.

effectively splits every monochromatic lattice site into two sites with a maximal occupation of one particle per double well. The superlattice phase is chosen such that the energy offset within the double well dominates the tunnel coupling $\Delta_0 \gg t_{\mathrm{in}}$ and hence freezes all dynamics within the double well. This tilt is then removed diabatically, which projects the atoms onto one site of the double well.[3] As this projected state is no eigenstate of the double well, we expect to observe Rabi oscillations between the sublattice sites of the double wells. However, due to the large green lattice depths the tunnel rate is only $t_{\mathrm{in}}/h \approx 13$ Hz. This renders all manipulations of the system that are much faster than 70 ms to be effectively instantaneous.

We now want to adiabatically connect our static double well Hamiltonian to the Floquet Hamiltonian. For this purpose, we adiabatically ramp up the amplitude of the drive K_0 within 3 ms, according to [77]. Next, we unfreeze the green lattice diabatically within 200 µs to $V_s = 12\,E_{\mathrm{rec}}$. This enables tunneling dynamics with frequencies $t_{\mathrm{in}}/h = 480$ Hz, $t_{\mathrm{out}}/h = 65$ Hz within the double well.[4] After a holding time τ, the system is projected onto the $\{|L\rangle, |R\rangle\}$ basis by diabatically introducing a tilt within the double well $\Delta_0 \gg t_{\mathrm{in}}$. The population of left and right sublattice sites is measured using the adiabatic band-mapping technique, as introduced in section 3.3.4. Then, we use the obtained populations of the Brillouin zones N_i to compute our global observable, the time dependent population contrast

$$C^S(\tau) = \left[(N_{34} - N_1)/(N_{34} + N_1)\right]_\tau \tag{5.23}$$

[3] Without loss of generality, we consider the atoms to be initially on the left sublattice site $|L\rangle$.

[4] For this lattice configuration, the intra-well tunneling dominates the out-of-well tunneling $t_{\mathrm{in}} \gg t_{\mathrm{out}}$ and will be the only reference from now on $t \equiv t_{\mathrm{in}}$.

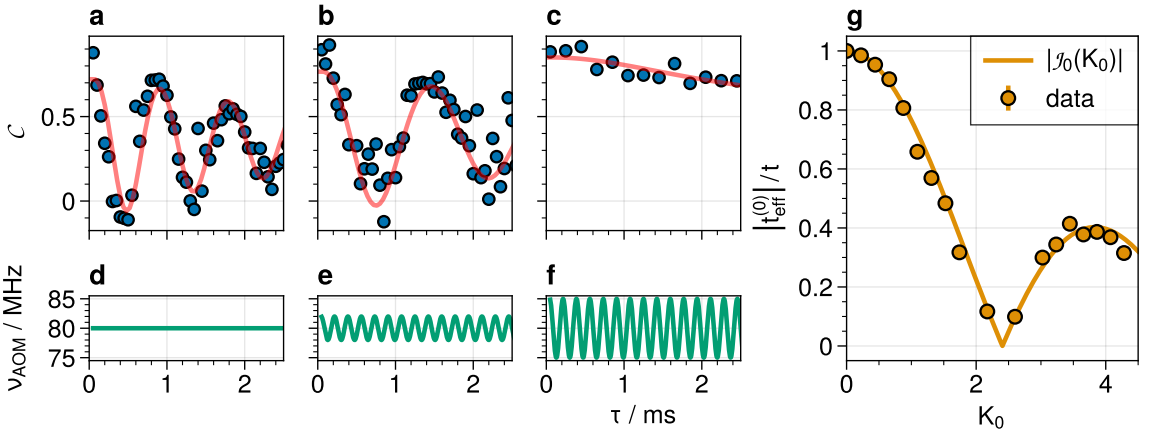

Figure 5.4: **Tunneling dynamics in driven double wells in the high frequency limit:** The population contrast C^S is shown as a function of the time τ for various driving amplitudes $K_0 = 0$, 1.3, 2.6 and fixed driving frequency $\nu = 5.8\,\mathrm{kHz}$ as blue data points(a to c). The fitted population contrast is shown as a red line and all uncertainties are omitted for better visibility. The corresponding periodic modulation of the AOM frequency ν_{AOM} is plotted below (d to f). (g) The observed effective tunneling rates are obtained from the fit to the population contrasts according to section 6.1 and compared to the 0th order Bessel function as a function of the driving amplitude K_0. Note that the uncertainties of the fit results are smaller than the marker size.

for the spin-polarized cloud.

We have measured the effective dynamics for a driving frequency $\nu = 5.8\,\mathrm{kHz}$ and various driving amplitudes K_0. This driving frequency is much larger than the relevant tunneling amplitude $h\nu \gg t$, which makes an effective description in the high-frequency limit appropriate. Moreover, the dimensionless micromotion amplitude in the lowest order is negligible $|A^1_{\mathrm{rot}}| \leq 0.04$. In this limit, we expect an effective behavior, that can be described purely by a rescaling of the tunneling rate as given by equation 5.20. Without any periodic modulation we see the expected oscillation in the contrast (cf figure 5.4 a, d) with an approximate periodicity of 1 ms and a dephasing due to the inhomogeneous lattice configuration, as discussed in section 4.1.2. As we introduce a driving amplitude of $K_0 = 1.1$, via a modulation of the AOM driving frequency with amplitude 2.5 MHz, the periodicity increases qualitatively (cf figure 5.4 b, e) while for a modulation amplitude $K_0 = 2.2$ the oscillation almost vanishes. Moreover, the signal shows no oscillations with the same frequency as the periodic drive, which confirms the expected suppression of the micromotion.

We evaluate this behavior quantitatively, by fitting the lattice depth V_s at the trap center and calculating the global contrast due to the calibrated lattice inhomogeneities. The fitted population contrast is shown as a red trace and matches the characteristics of our data excellently. The fitting procedure will be introduced in detail in section 6.1 for an interacting system. For this non-interacting case, the procedure treats our driven system like a static double well with a driving-amplitude dependent lattice depth $V_s(K_0)$. The fitted lattice depths are in turn used to calculate the driving-amplitude dependent effective tunneling $|t^{(0)}_{\mathrm{eff}}(K_0)|/t$ in the high frequency limit, as shown in figure 5.4 g. A comparison of the fitted rescaled tunneling with the 0th order Bessel function shows excellent agreement. Evidently, the driving amplitude in the high frequency limit can decrease the tunnel coupling until it is completely suppressed for an amplitude $K_0 = 2.4$. This phenomenon is called

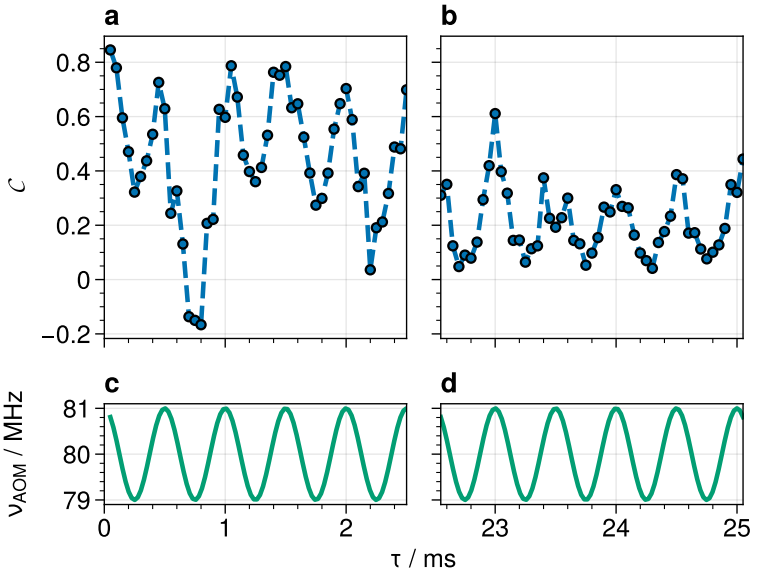

Figure 5.5: **Effects of the micromotion for spin polarized driven double wells:** The oscillations in the population contrast C_S are shown for a periodic drive with frequency $\nu = 2\,\mathrm{kHz}$ and amplitude $K_0 = 1.2$ for two holding time τ intervals (a and b). Note that the data points are connected as a guide to the eye and the uncertainties are omitted for better visibility. The corresponding periodic modulation of the AOM frequency ν_{AOM} is plotted below (c and d). The phase of the frequency modulation in c and d is uncertain and was adjusted in the plots to match the oscillation in the population contrast.

dynamic-localization [45] and has been first observed via the expansion of a Bose-Einstein condensate in an optical lattice [141].

So far, we have neglected the micromotion due to the negligible amplitude A^1_{rot} for the given driving amplitude $\nu = 5.8\,\mathrm{kHz}$. However, a direct observation of the micromotion is of interest to demonstrate control over the driven system in its entirety. For this purpose, we have probed the driven system as described before but with a driving frequency $\nu = 2\,\mathrm{kHz}$ and amplitude $K_0 = 1.2$ (cf. figure 5.5). The latter was chosen to observe the interplay between effective tunneling frequency and micromotion that scale with the 0th and first order Bessel functions respectively. Moreover, the micromotion amplitude is enhanced by more than a factor three compared to the 5.8 kHz drive. For short times, the oscillation of the population contrast shows a clear beating with the driving frequency, which is shown in figure 5.5 a and c. To isolate the effect of the micromotion, we observe the population contrast for large holding times $\tau > \frac{20}{t}$. This ensures that the oscillation due to the effective tunneling dynamics have dephased. However, the micromotion is not that sensitive to the inhomogeneities of the lattice as only its amplitude and not its frequency is affected. Therefore, for these large holding times the population contrast should only show dynamics due to the micromotion, which agrees very well with our observations in figure 5.5. In this qualitative demonstration of the micromotion, we have chosen the phase of the modulation arbitrarily. Nonetheless, a variation of the phase can have a significant impact on the observed oscillations, as we have observed and will be discussed in [112]. If the micromotion amplitude is small, however, the micromotion all together has a negligible impact and we will work in this regime from now on.

5.3 Resonantly driven double wells

In this section, we study interacting double wells with a periodic drive that is resonant to the interaction energy. First, we introduce the theoretical framework for near-resonantly driven double wells, as this includes the regime of a resonant drive. Next, we discuss our experimental scheme to probe resonantly driven double wells and compare our findings to the formerly introduced theory. Here, we show the realization of a double well with density-dependent tunneling of several harmonic orders.

5.3.1 Near-resonantly driven double wells in the high frequency expansion

In this section, we study the driven interacting double well in the near-resonant limit $U \approx \ell h\nu \gg t$ with the integer harmonic order ℓ theoretically, according to [77]. The driving frequency is still a dominant energy scale, and therefore, we start by a transformation to the rotating frame via equation 5.18. Unlike in the high frequency limit, we cannot directly expand the effective Hamiltonian in terms of the reverse frequency as the terms $\propto U/h\nu$ would not converge. We perform a second rotation to solve this problem via [133]

$$R_2(\tau) = \exp\left[-i\,2\pi\ell h\nu\tau\, h_U\right],\ h_U = \begin{pmatrix} 1 & 0 & 0 & 0 \\ 0 & 0 & 0 & 0 \\ 0 & 0 & 0 & 0 \\ 0 & 0 & 0 & 1 \end{pmatrix}. \tag{5.24}$$

Then we follow the procedure of section 5.2.1, where we perform two rotations instead of one $R_1(\tau) \rightarrow R_2(\tau)R_1(\tau)$. This gives the Hamiltonian in the co-rotating frame

$$\hat{H}_{\text{rot}} = \begin{pmatrix} U - \ell h\nu & -t_+(\tau,\ell) & t_+(\tau,\ell) & 0 \\ -t_+^*(\tau,\ell) & 0 & 0 & -t_-(\tau,\ell) \\ t_+^*(\tau,\ell) & 0 & 0 & t_-(\tau,\ell) \\ 0 & -t_-^*(\tau,\ell) & t_-^*(\tau,\ell) & U - \ell h\nu \end{pmatrix} \tag{5.25}$$

with $t_\pm(\tau,\ell) = t\exp\left[i(\pm 2\pi\ell h\nu + K_0\sin(2\pi\nu\tau))\right]$. Evidently, the tunneling in this frame gains a time- and harmonic order-dependent phase. Now this rotated Hamiltonian converges in an inverse frequency expansion as $h\nu \gg U - \ell h\nu, t$. Using equation 5.21 this gives the effective Hamiltonian of lowest order in the rotating frame

$$\hat{H}^0_{\text{eff}} = \begin{pmatrix} U_{\text{eff}} & (-1)^{\ell+1}\cdot t^\ell_{\text{eff}} & (-1)^{\ell}\cdot t^\ell_{\text{eff}} & 0 \\ (-1)^{\ell+1}\cdot t^\ell_{\text{eff}} & 0 & 0 & -t^\ell_{\text{eff}} \\ (-1)^{\ell}\cdot t^\ell_{\text{eff}} & 0 & 0 & t^\ell_{\text{eff}} \\ 0 & -t^\ell_{\text{eff}} & t^\ell_{\text{eff}} & U^0_{\text{eff}} \end{pmatrix} \tag{5.26}$$

with the effective interaction strength $U_{\text{eff}} = U - \ell h\nu$[5] and effective tunneling rate $t^\ell_{\text{eff}} = t\mathcal{J}_\ell(K_0)$.

These effective Hubbard parameters lead to some intriguing effects: The effective tunneling can be adjusted through the driving amplitude and the harmonic order of the drive, and it exhibits behavior

[5] Note, that in this theoretical framework the sign of the driving frequency ν is always the same as for the interaction strength U. However, this sign of the driving frequency is neglected in this work, as it is just a mathematical necessity.

distinct from that seen in the high-frequency limit. This phenomenon is usually interpreted as density-dependent tunneling: For a near-resonant drive $\ell h\nu \approx U \gg t$, a singly occupied double well is in the high frequency limit as it experiences no interaction energy and the effective Hamiltonian is governed by the 0th order Bessel function. In contrast, for a double well with half-filling, the tunneling is modified by the ℓth order Bessel function leading to a different tunneling rate. The effective interaction strength, on the other hand, changes linearly with the driving frequency and harmonic order. This adjustability allows for precise control over the interaction strength, enabling transitions from attractive to effectively repulsive interactions, and vice versa.

Surprisingly, there are sign changes of some of the effective tunnel coupling elements in 5.26, that change with harmonic order. This has implications on the coupling between the three relevant eigenstates of the double well

$$|s\rangle = \frac{1}{\sqrt{2}}(|LR\rangle - |RL\rangle),\ |d_-\rangle = \frac{1}{\sqrt{2}}(|LL\rangle - |RR\rangle) \text{ and } |d_+\rangle = \frac{1}{\sqrt{2}}(|LL\rangle + |RR\rangle). \tag{5.27}$$

For odd harmonic orders, the singlet state $|s\rangle$ couples to the negative parity doublet state $|d_-\rangle$. On the other hand, for even harmonic order the singlet $|s\rangle$ couples to the even parity double state $|d_+\rangle$, just like the static double well.

The consequences of this coupling change can be obtained by studying the spectra of driven double wells. In figure 5.6 a, we show the quasi-energy spectrum of an attractively interacting system with a periodic drive of frequency $h\nu = 10t$ but negligible driving amplitude $K_0 = 0$. Here, the singlet state $|s\rangle$ crosses two doublet states from another Floquet-zone that has an additional energy of $h\nu$. However, if we increase the driving amplitude $K_0 = 2.4$, $|s\rangle$ couples to $|d_-\rangle$. As a consequence, the spectrum shows an avoided crossing with a gap of $4t^\ell_{\text{eff}} = 4t\mathcal{J}_1(K_0)$ at $U = h\nu$ (cf. figure 5.6 b). Moreover, for the second harmonic order, we see a similar avoided crossing at $U = 2h\nu$ but with a gap of $4t^\ell_{\text{eff}} = 4t\mathcal{J}_2(K_0)$ (cf. figure 5.6 c).

These spectra resemble the one of a static double well with a few subtle but important differences. After the avoided crossing we see the doublet states increasing or decreasing in energy almost linearly, indicating the appearance of effective interactions with different sign as discussed. However, the gap between $|d_+\rangle$ and $|d_-\rangle$ is larger (smaller) for effective attractive (repulsive) interactions of first (second) harmonic order. Moreover, the gap between $|s\rangle$ and zero quasi energy is different for strong attractive and repulsive interactions. The reason for both phenomena are higher order Hubbard parameters V_{ct}, V_{nn} and V_{de} of significant amplitude that arise in the higher orders of the high frequency expansion and were included in this calculation. We will discuss their impact in more detail in Chapter section 6.3.

The kick operator in the rotated frame for harmonic order ℓ in the lowest order of the inverse frequency expansion cannot be written in a compact form anymore [112]. Intuitively, the two rotations with different frequencies $R_{1,2}$ cause a frequency beating between ν and $\ell\nu$ that shows in the kick operator. In addition, the Fourier components of this kick operator K^1_{rot} have amplitudes that scale with Bessel functions of orders that depend on the harmonic order ℓ. As an example we are considering the kick operator in the rotated frame for the lowest harmonic order $\ell = 1$. In the lowest order[6] of the

[6] This considers Bessel functions up to the first order.

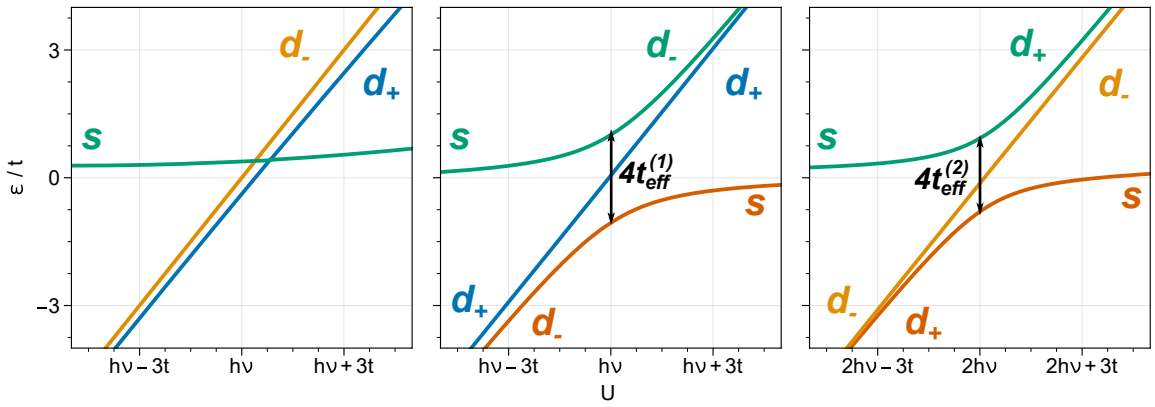

Figure 5.6: **Quasi-energy spectra of near-resonantly driven double wells:** For a periodic drive with driving frequency $h\nu = 10t$ the quasi-energy spectrum changes with the interaction strength U. (a) For a negligible driving amplitude $K_0 \approx 0$ and attractive interactions the singlet state $|s\rangle$ is crossed by two doublet states $|d-\rangle$ and $|d+\rangle$ of another Floquet zone with additional energy $h\nu$. (b) Introducing a finite driving amplitude $K_0 = 2.4$ couples $|s\rangle$ and $|d_-\rangle$ of the different Floquet zones and leads to an avoided crossing. The gap of size $4t\mathcal{J}_1(K_0)$ opens at $U = h\nu$. The resulting spectrum resembles the one of an interacting double well with changed parameters U_{eff} and t_{eff}. (c) For the second harmonic order $\ell = 2$ the singlet state $|s\rangle$ couples to $|d_+\rangle$ resulting in another avoided crossing around $U = 2h\nu$.

inverse frequency expansion, this kick operator is twofold $K^1_{\text{rot}}(\tau) = \kappa_1(\tau) + \kappa_2(\tau)$ [58] with

$$\kappa_1(\tau) = i\frac{t}{2h\nu}\mathcal{J}_1(K_0)\begin{pmatrix} 0 & e^{i4\pi\nu\tau} & -e^{i4\pi\nu\tau} & 0 \\ -e^{-i4\pi\nu\tau} & 0 & 0 & e^{-i4\pi\nu\tau} \\ e^{-i4\pi\nu\tau} & 0 & 0 & -e^{-i4\pi\nu\tau} \\ 0 & -e^{i4\pi\nu\tau} & e^{i4\pi\nu\tau} & 0 \end{pmatrix} \tag{5.28}$$

and

$$\kappa_2(\tau) = i\frac{t}{h\nu}\mathcal{J}_0(K_0)\begin{pmatrix} 0 & e^{i2\pi\nu\tau} & -e^{i2\pi\nu\tau} & 0 \\ -e^{-i2\pi\nu\tau} & 0 & 0 & e^{-i2\pi\nu\tau} \\ e^{-i2\pi\nu\tau} & 0 & 0 & -e^{-i2\pi\nu\tau} \\ 0 & -e^{i2\pi\nu\tau} & e^{i2\pi\nu\tau} & 0 \end{pmatrix}. \tag{5.29}$$

Both contributions scale with order $1/\nu$ and therefore the relative contribution to the micromotion depends mostly on the driving amplitude K_0.

This formalism is used to describe the effective behavior of resonantly driven $\ell h\nu = U$ half-filled double wells with attractive interactions in the next section. Moreover, it is used in the near-resonant regime $\ell h\nu \approx U$ to describe a Floquet driven crossover from density-induced tunneling to pair-tunneling, which is the topic of Chapter 6.

5.3.2 Interacting fermions in resonantly-driven double wells

We study attractively interacting fermions in resonantly-driven double wells using a degenerate mixture of the lowest two hyperfine states. The experimental procedure is the same as for the spin-polarized

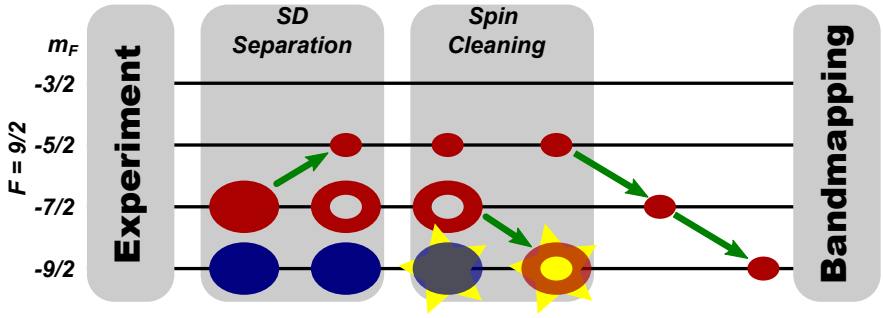

Figure 5.7: **Sketch of the spin cleaning procedure:** Between the experiment and the adiabatic band-mapping procedure the unwanted hyperfine states are *cleaned* via the imaging transition. First, a singles-doubles RF pulse transfers atoms in the $|-7/2\rangle$ to the $|-5/2\rangle$ hyperfine state if they are on doubly occupied sites. Then, the reference state $|-9/2\rangle$ and the residual atoms in the $|-7/2\rangle$ state are cleaned consecutively. The remaining atoms are only in one hyperfine state and are then imaged via the adiabatic band-mapping technique.

experiments described in section 5.2.2 with an adjusted detection method: The adiabatic band-mapping technique introduced in section 3.3.4 ends with a time-of-flight expansion. In short, the atoms expand freely with different momenta according to their quasimomenta in the lattice. This procedure is not directly applicable to interacting particles as the two spin species might interact during the expansion and the interactions might alter the mapping from quasimomentum to free-space momentum [119]. A typical approach to perform TOF-type measurements of interacting particles is a Stern-Gerlach procedure [22, 150], that separates the different hyperfine states during the expansion.

However, we have chosen a different approach to this problem using a *spin cleaning* procedure, as sketched in figure 5.7. After the experiment, we populate the lowest two hyperfine states of the $F = 9/2$ manifold $|-9/2\rangle$ and $|-7/2\rangle$ in the frozen lattice configuration $\Delta \gg t$. First, we perform a selective RF-transfer from the $|-7/2\rangle$ to the $|-5/2\rangle$ hyperfine state, for doubly doubly occupied sites (see section 3.3.1 for details). Then, we *clean* the $|-9/2\rangle$ hyperfine state via the closed imaging transition (see section 3.3.2 for details). This cleaning is repeated for the atoms in the initial $|-7/2\rangle$ state at singly occupied lattice sites after an additional RF swap. After this cleaning procedure, only the $|-5/2\rangle$ hyperfine state is populated and can be used for the usual adiabatic band-mapping procedure. This combination of bandmapping and selection of doubly-occupied sites allows us to measure in the $|LL\rangle$ and $|RR\rangle$ basis of the double well at half-filling. In this basis we determine the population contrast for half-filled double wells C^D according to equation 5.23.

Unfortunately, the spin cleaning procedure affects the atoms in the $|-5/2\rangle$ hyperfine state differently depending on their position in the double well $|LL\rangle$ or $|RR\rangle$. After the spin cleaning procedure we detect atoms on the upper well $|RR\rangle$ with a detection efficiency of (0.44 ± 0.08) normalized to the detection on the lower well $|LL\rangle$. The atoms on the upper well are less confined than in the lower well leading to larger tunneling rates. This might increase the possibility of losses during the cleaning procedure and cause the lower detection efficiency.

We probe the resonantly-driven double well for an attractive interaction strength of $U/t \approx -18$. For this purpose, we choose a lattice configuration $V_s = 12\,E_{\mathrm{rec}}$, $V_l = 15\,E_{\mathrm{rec}}$ which realizes the dominant tunneling frequency of $t_{\mathrm{in}}/h \approx 480\,\mathrm{Hz}$ and a suppressed out-of cell tunneling frequency of $t_{\mathrm{out}}/h \approx 65\,\mathrm{Hz}$. Without any driving amplitude, there is no clear sign of oscillations in the population contrast (cf. figure 5.8 a).

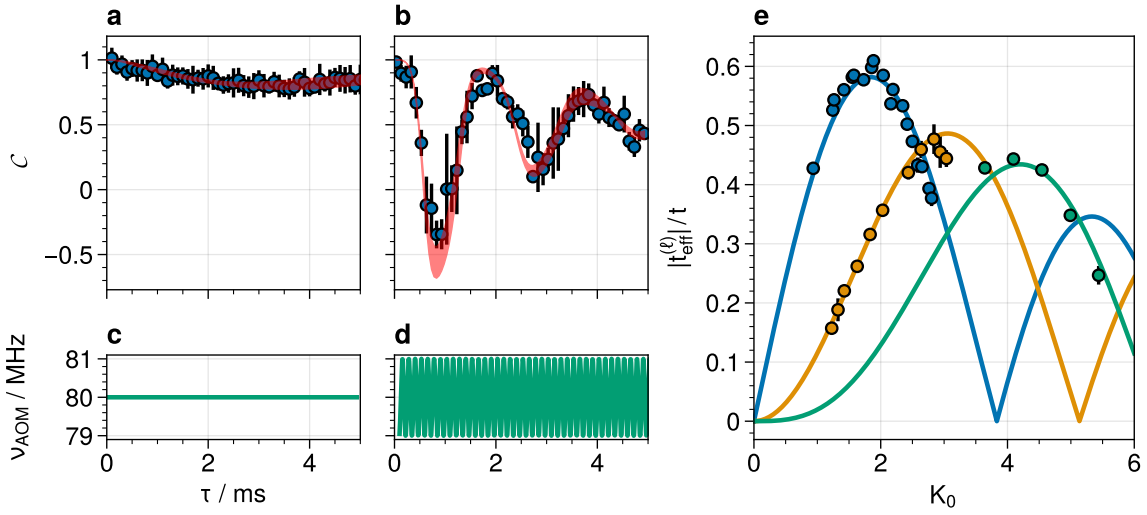

Figure 5.8: **Dynamic signals of resonantly driven double wells at half filling:** For an attractively interacting double well $U \sim 18t \sim h \cdot 8\,\mathrm{kHz}$, the population contrast C^D is shown for a resonant drive $U = \ell h\nu$ of first harmonic order with various driving amplitudes $K_0 = 0,\ 2.4$ (a, b). The fitted population contrast is shown as a red solid line with the shaded region indicating the 1σ confidence interaval. The corresponding periodic modulation of the AOM frequency ν_{AOM} is plotted below (c and d). The observed effective tunneling rates for various driving frequencies $\nu = 8,\ 4.325$ and $2.775\,\mathrm{kHz}$ (blue, orange, green) as a function of the driving amplitude are compared to Bessel functions of various harmonic orders (e). The first harmonic order is shown in blue, the second in orange and the third in green.

This behavior stems from the fact that our time evolution in the strongly attractive double well is described by the superexchange process with rate $J = \frac{2t^2}{U}$. This is a second-order process of two particles tunneling sequentially via a virtual state before recombining again emulating an effective pair tunneling [32, 33]. Nonetheless, it is the dominant process compared to the much faster single particle tunneling t as this process would come at a cost of the interaction U and is thus suppressed. This allows us to treat the interacting double well in the strongly attractive regime as an effective two-level system via the Schrieffer-Wolff [151] transformation of the half-filled double well. In the $\{|LL\rangle, |RR\rangle\}$ basis the two level system Hamiltonian reads:

$$\hat{H} = \begin{pmatrix} 2\Delta_0 & -J \\ -J & -2\Delta_0 \end{pmatrix}. \tag{5.30}$$

Note that compared to the singly occupied double well the tilt has an additional factor of two due to the higher particle number and the tunneling is replaced by the superexchange. Preparing the localized state $|LL\rangle$ induces Rabi oscillations within the double well with amplitude

$$A = \frac{1}{2}\frac{1}{1 + (2\Delta_0)^2/J^2}. \tag{5.31}$$

The superexchange rate for our lattice parameters is $J \sim 50\,\mathrm{Hz}$ and thus roughly 10 times lower than the tunneling rate. This makes the amplitude of the Rabi oscillations ~ 400 times more sensitive to

tilts compared to the quarter-filled double well. In combination with our position dependent tilts, due to the Gaussian nature of our lattice beams (compare section 6.1) and shot-to-shot fluctuations (compare section 4.1.2) this explains negligible oscillations in the population contrast.

Introducing a resonant periodic drive $\ell h\nu = U$ changes this behavior drastically: For a driving frequency $\nu = 8\,\mathrm{kHz}$ and amplitude $K_0 = 2.4$ the population contrast oscillates with a significant amplitude and periodicity of $\sim 2\,\mathrm{ms}$ (cf. figure 5.8 b, d). This observed behavior agrees with the expectation from the effective Hamiltonian of equation 5.26: The interaction energy is effectively balanced by the resonant driving quantum $U_{\mathrm{eff}} \approx 0$. Moreover, the effective tunneling is $t_{\mathrm{eff}} = t\mathcal{J}_1(K_0) \approx 0.5t$ which results in roughly twice the periodicity compared to the non-interacting dynamics (cf. figure 5.4 a). Thus, we have realized *density-assisted* tunneling by applying a resonant periodic modulation with driving amplitude $K_0 = 2.4$. The emphasis on *assisted* stems from the suppressed single particle tunneling in quarter-filled double wells, via the chosen driving amplitude K_0. This regime will be explored further in the next chapter 6, with the addition of effective interactions $U_{\mathrm{eff}} \neq 0$ by detuning the driving frequency from resonance.

Moreover, we have verified the rescaling of the effective tunneling amplitude with the Bessel function $\mathcal{J}_\ell(K_0)$ up to the third harmonic order $\ell = 1, 2, 3$ (cf.figure 5.8) The effective tunneling is determined in the same manner as for the spin polarized scenario and agrees excellently with the theoretical expectation. However, for higher harmonics the higher order frequency corrections play an increasingly important role, which made realizations for $\ell > 3$ not feasible for the chosen interaction strength. In comparison with the spin-polarized realization we have observed an effective tunneling with different scaling according to $t_{\mathrm{eff}} = t\mathcal{J}_\ell(K_0)$. This phenomenon is called *density dependent* tunneling and has been observed in tilted optical lattices [75] as well as periodically driven realizations [43, 76, 152].

CHAPTER 6

Floquet-driven crossover from density-assisted tunneling to enhanced pair tunneling

Understanding the fundamental properties of correlated quantum-many body states lies at the heart of our research. The Fermi-Hubbard model is famously capable of the description of correlated matter despite its simplistic nature: Particles can either tunnel between neighboring lattice sites or two-particles can interact with each other on the same lattice site as shown in figure 6.1. Quantum simulation [9] using ultracold atomic gases has shown great success in the study of Hubbard-model where theoretical calculations are not feasible anymore [12, 13]. The most famous achievements range from the study of Mott-insulators [153, 154] to superconductors [6] and quantum-magnets [14, 25, 155], to name only a few. However, the ultra-low temperatures required to study the postulated high-T_C superconductivity are still elusive despite the proposal of novel cooling schemes [156–158].

Therefore, the focus of current research has shifted towards extended Hubbard models which consider additional processes. For example, coupling two planes of two-dimensional Hubbard models realizes the Bilayer Fermi Hubbard model which more accurately resembles the lattice structure of real materials. Here, the competition of magnetic correlations [31] was studied as a first step towards the theoretically predicted superconducting pairing mechanism [159].

Another approach is to study systems with higher order tunneling processes that go beyond the single particle dynamics of Hubbard models [160–163]. One example is density-assisted tunneling, where the tunneling depends on the occupation of the lattice site, which was recently found to be essential for mapping a three-orbital model to a single-orbital model [30].

Moreover, the Penson-Kolb-Hubbard [47] model can induce superconducting $\eta-$pairing phases by including explicit pair hopping [48, 49]. This crucial process is only partially included in the regular Hubbard model as a second-order process for large interactions called superexchange (cf. figure 6.1 left column). It describes pair hopping as two sequential single-particle hopping events with a rate $J = 2t^2/U$ and is usually dominated by the single-particle tunneling.

In this chapter, we will explore how a near-resonant periodic drive can fundamentally alter the dominant dynamics of a double well. We will show a crossover from a regime with density-assisted tunneling (cf. figure 6.1 middle column) to enhanced pair tunneling (cf. figure 6.1 right column). Surprisingly, this pair tunneling can be enhanced not only compared to the Floquet-reduced single-particle tunneling but even beyond the static superexchange rate.

This chapter is organized as follows: First we will explore the dynamic signals of near-resonantly

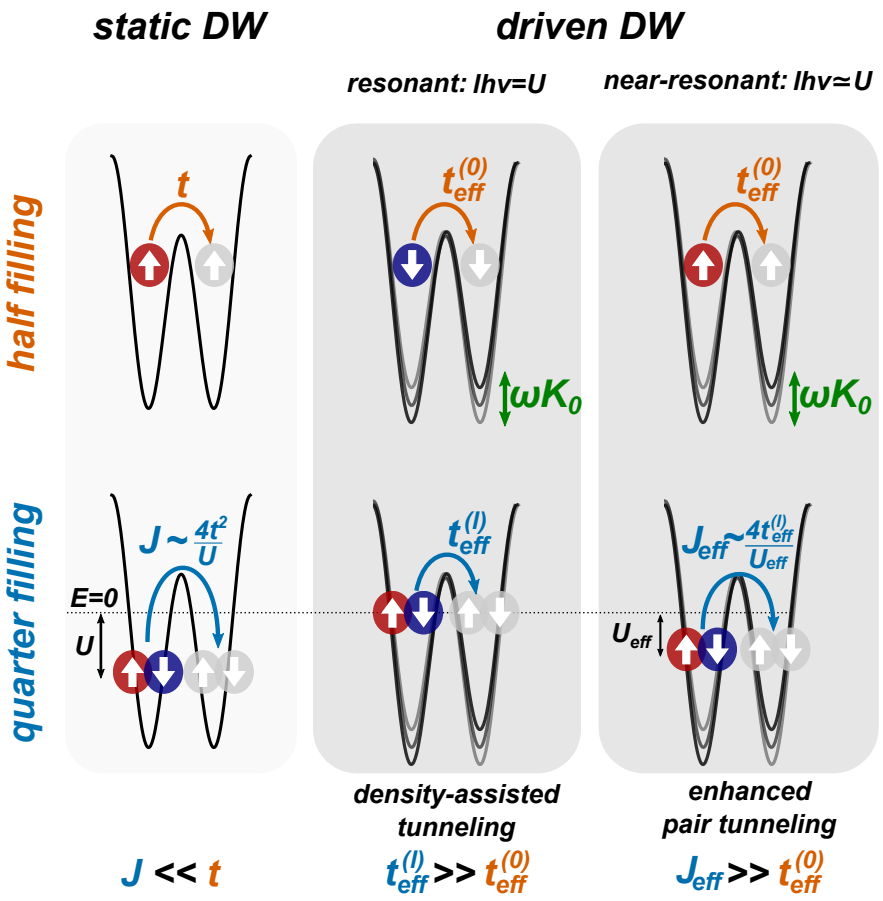

Figure 6.1: **Schematics of static and driven double wells (DW):** The static double well resembles the fundamental building block of the Fermi Hubbard model with nearest-neighbor tunneling t and on-site interaction U (left column). For strong interactions, the two-particle dynamics are governed by the superexchange $J \ll t$ (lower row, left column). A periodic drive with driving amplitude K_0 and driving frequency $\omega = 2\pi\nu$ can fundamentally alter these dynamics. For a quarter-filled double well, the single-particle tunneling is rescaled as $t_{\mathrm{eff}}^{(0)}$ (upper row, middle and right column). For a half-filled double well and a resonant drive $\ell h\nu = U$, the interaction energy is balanced $U_{\mathrm{eff}} = 0$ and the tunneling is rescaled $t_{\mathrm{eff}}^{(\ell)}$ depending on the harmonic order ℓ (lower row, middle column). This realizes *density-assisted* tunneling for a driving amplitude $K_0 = 2.4$ and is discussed in section 5.3.2. Detuning the driving frequency from resonance, gives rise to effective interactions $U_{\mathrm{eff}} \neq 0$ (lower row, right column) that induce pair tunneling. The driving amplitude K_0 can be chosen to enhance the effective two particle-tunneling above the effective single particle tunneling $J_{\mathrm{eff}} \gg t_{\mathrm{eff}}^{(0)}$.

driven double wells and the underlying effective Hamitlonians. We will discuss the evaluation of our data in detail and how we compute the global observables from a inhomogeneous system. Next, we investigate the spectra of the realized effective systems and extract the characteristic parameters. Finally, we explore and characterize the pair tunneling in the effective systems. Here, we discuss the pivotal role of higher order Hubbard parameters in the enhancement of the pair tunneling with respect to the static double well.

6.1 Dynamic signals of near-resonantly driven double wells

In this section, we explore the dynamics of periodically modulated double wells with effective interactions, by adjusting the driving frequency ν away from resonance. Initially, we will examine the dynamic signals from the driven double wells with effective interactions. Following this, we will outline the methodology for calculating and fitting the population contrast C^D. We begin by addressing the variation of Hubbard parameters across the atom cloud. Subsequently, we will explain how spatially and temporarily varying superlattice phases across the cloud are incorporated. Lastly, we present the fitting approach that accommodates these inhomogeneities and contrast these findings with our empirical observations.

Our experimental sequence is (apart from the changed driving frequency) the same as for the resonantly-driven interacting double well, as discussed in section 5.3.2. Additionally, we suppress single-particle tunneling via the driving amplitude $K_0 = 2.4$. The observed dynamic signals in the population contrast C^D for attractive interactions $U/t \approx -9$ and various driving frequencies are presented in figure 6.2. For an effectively non-interacting system with $\nu \approx |U|/h$ (see figure 6.2 a) the oscillation dynamics exhibit a single characteristic frequency. This indicates *density-assisted* tunneling, as introduced in figure 5.8. Upon introducing a small detuning of the driving frequency from the resonance, a beating becomes apparent in the contrast measurement (see figure 6.2 b-e). This beating becomes more pronounced with increasing detuning and is accompanied by a decrease in oscillation amplitude. When the driving frequency is approximately $\nu \approx U/(2h)$ (cf. figure 6.2 e), the oscillation amplitude increases again and the characteristic signature of frequency beating is less pronounced. This indicates that another effectively non-interacting system is realized by the second-harmonic resonance condition [43, 44].

We evaluate these dynamic signals by comparing them to the expectation from the effective Hamiltonian of a near-resonantly driven double well, as introduced in section 5.3.1. However, the population contrast is a global observable and therefore, we have to account for the inhomogeneous intensity distribution of our optical lattice in our theoretical analysis. Thus, we calculate the spatially dependent Floquet and Hubbard parameters $K_0(\boldsymbol{x})$, $t(\boldsymbol{x})$, $U(\boldsymbol{x})$, and $\Delta_0(\boldsymbol{x})$. With these parameters, we solve the different Floquet-driven double-well Hamiltonians and compute the time- and position-dependent contrast $C^D(\boldsymbol{x}, \tau)$. Then, we perform a density-weighted average over the inhomogeneous density distribution resulting in the global observable $C^D(\tau)$. To account for experimental fluctuations, this contrast is then fitted to our experimental data leaving the scattering length a and the green lattice potential depth at the trap center V_s as fit parameters. Moreover, this fit is repeated several times for various spatially varying superlattice phase maps, to account for phase fluctuations during the measurements. The mean values of the fitted results are presented as solid lines in figure 6.2, with the 1σ confidence interval indicated as a shaded region. The numerical data accurately replicates the dynamic features observed in our experimental data as well as a pronounced dephasing.

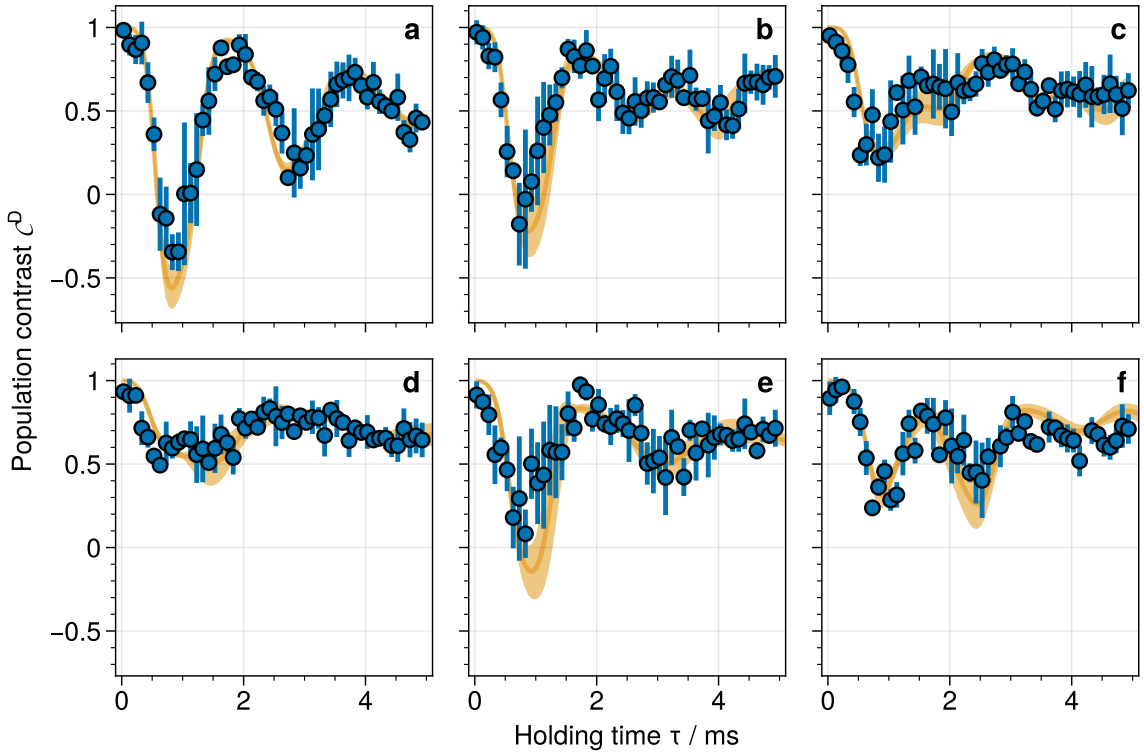

Figure 6.2: **Dynamic signals of near-resonantly driven double wells at half filling:** For attractive interactions $U \approx -9t \approx -4\,\mathrm{kHz}$, the measured population contrast C^D is shown as blue datapoints for a driving amplitude $K_0 = 2.4$ and various driving frequencies 4.05, 3.9, 3.6, 2.7, 2.25 and 2.05 kHz (a to f). The fitted population contrast is shown as an orange line with the 1σ confidence interval indicated as a shaded region.

This summarized fitting procedure will be discussed in more detail in the following subsection. The inhomogeneities are discussed in the xy-plane of the three-dimensional optical lattice, neglecting the changes along the z-direction. This is a reasonable simplification, as the atom cloud is compressed significantly along the z-direction compared to the waist of the Gaussian beams along this axis. In the following, we visualize the xy-plane in the z-imaging camera frame with a binning of 10×10 lattice sites to keep the computational effort at bay.

6.1.1 Calibration of the optical lattice setup

We start with the calibration of our optical lattice setup. First, we perform the in-situ lattice modulation spectroscopy to calibrate the lattice depths, as discussed in section 3.2.3. In table 6.1, we show the results of one specific setup during the Floquet experiments, as an example. The lattices are aligned very precisely to the center of the camera frame to achieve the most symmetric lattice setup as possible.

We determine the optical density profile in the chosen lattice configuration by an average over several in-situ images and the lattice-dependent interaction strength via the density-assisted single particle tunneling measurement, introduced in section 4.2.2. From the calibrated lattice depths and scattering length we can compute a grid of the relevant Hubbard parameters during one experimental cycle, as introduced in section 2.4. The results are shown in figure 6.3 with the high-density region of

	X532	X1064	Y1064	Z532
θ_x / °	-5.7	-5.7	–	–
θ_y / °	–	–	0.1	0.4
x_0 / px	–	–	1.4	4.2
y_0 / px	-7.3	-2.5	–	–
w_0 / µm	124	179	159	110

Table 6.1: **Lattice parameters during the Floquet experiments:** The properties of the four relevant lattices are listed for one exemplary realization: The angles $\theta_{x,y}$ and the center positions x_0, y_0 are given with respect to the camera frame and the waist of the Gaussian beams is given in µm.

doubly occupied sites od $\leq 0.1\,\max(\mathrm{od})$ indicated as a solid gray line and highlighting the relevant area of the Hubbard parameters. Clearly, the interaction energy $U(\boldsymbol{x})$ and intra-well tunneling $t_{\mathrm{in}}(\boldsymbol{x})$ vary significantly in the high-density region. Moreover, there is an additional tilt $\Delta_0^{\mathrm{latt}}(\boldsymbol{x})$ that stems from the Gaussian nature of the $y-$ and $z-$lattice and has a significant impact for effectively interacting systems. Finally, the out-of-well tunneling $t_{\mathrm{out}}(\boldsymbol{x})$ is suppressed significantly compared to the intra-well tunneling. Since the tunneling along the y-direction and z-direction are suppressed as well, we consider independent double wells, with spatially varying Hubbard parameters $t(\boldsymbol{x}) \equiv t_{\mathrm{in}}(\boldsymbol{x}) + t_{\mathrm{corr}}(\boldsymbol{x})$ and $U(\boldsymbol{x})$. Here we have introduced the correction of the tunneling rate due to interactions, as introduced in section 2.4.

6.1.2 Calibration of the superlattice phase fluctuations

The phase of the superlattice along the x-direction varies across the cloud. We calibrate these phase variations using the in-situ symmetry point measurement, as detailed in section 4.1.2. This gives the spatially varying superlattice phase relative to the set point of the experiment $\Delta\phi(\boldsymbol{x})$ in MHz (cf. figure 6.4 a). The given example shows a well-aligned superlattice resulting in a small mean deviation from the set symmetry point of (-0.15 ± 0.30) MHz. This relative superlattice phase is used to calculate the phase tilt $\Delta_0^{\phi}(\boldsymbol{x})$ (cf. figure 6.4 b), taking into account that the lattice dependent tilt Δ_0^{latt} is lattice depth dependent and thus different for the calibration method and the actual experiment. Finally, the overall tilt of the double wells $\Delta_0 = \Delta_0^{\phi} + \Delta_0^{\mathrm{latt}}$ is obtained by summation of the phase tilt Δ_0^{ϕ} with the lattice tilt Δ_0^{latt}

Unfortunately, the superlattice phase is despite the environmental feed forward [110] not exactly stable over time (compare section 4.1.2). To account for these phase fluctuations, we calibrate the phase tilt once per hour during the experimental cycle. This phase tilt changes significantly over time, as shown in figure 6.4 c which is 10 h after the first measurement. To account for these phase fluctuations, the different phase tilt grids are treated independently in the following fitting procedure.

Before we perform the actual fitting procedure, we ensure the validity of the phase-tilt measurements by statistical means: First, we characterize the phase maps via the mean phase tilt and their phase gradient along the x- and y-direction which gives us a quantitative measure for their inhomogeneity. Then, we drop statistical outliers with respect to these characteristics. By this procedure we ensure, that only phase-tilt maps with reasonable results are considered.

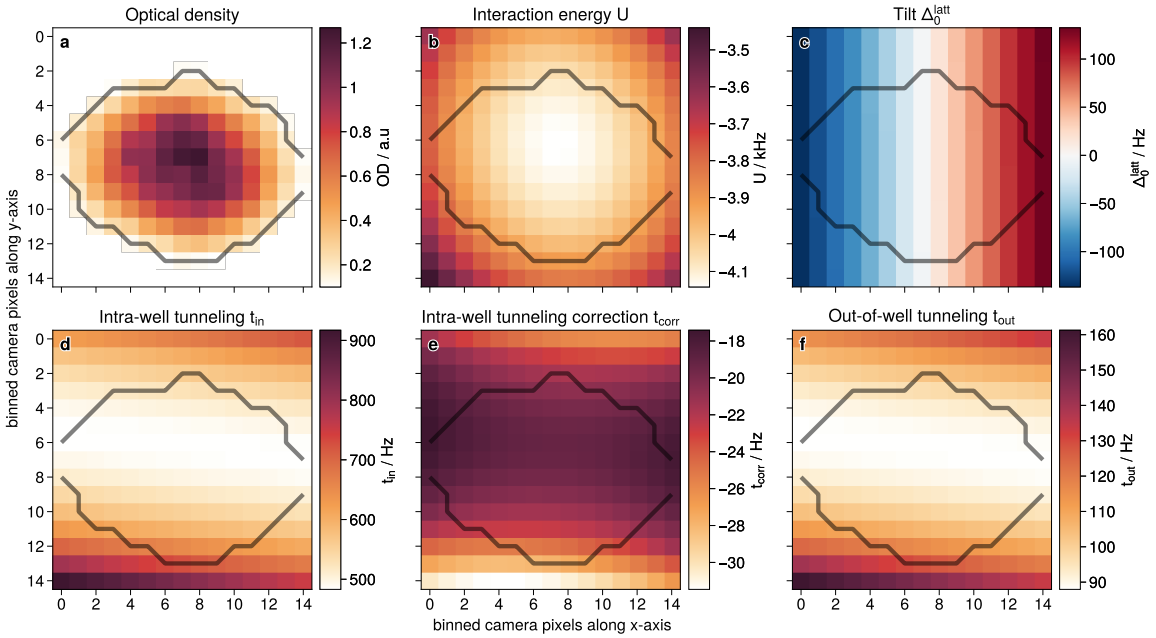

Figure 6.3: **Hubbard parameters during Floquet experiments:** The Hubbard parameters vary over the atom cloud due to the Gaussian nature of the lattice beams. These maps show these inhomogeneities along the $x-$ and $y-$direction binned over 10×10 lattice sites. The optical density for doubly-occupied sites indicates the trap center and dictates the area of interest of the optical lattices (a). The black line shows the boundary of the high density region $od \leq 0.1 \max(od)$. The Hubbard parameters (b to f) are calculated according to section 2.4 for the calibrated lattice parameters (compare table 6.1). They are calculated for $V_s = 12\,E_{\mathrm{rec}}$, $V_l = 15\,E_{\mathrm{rec}}$, $s_y = 55\,E_{\mathrm{rec}}$, $s_z = 110\,E_{\mathrm{rec}}$ and the scattering length $a = -131\,a_0$, which corresponds to $U/t \sim 9$.

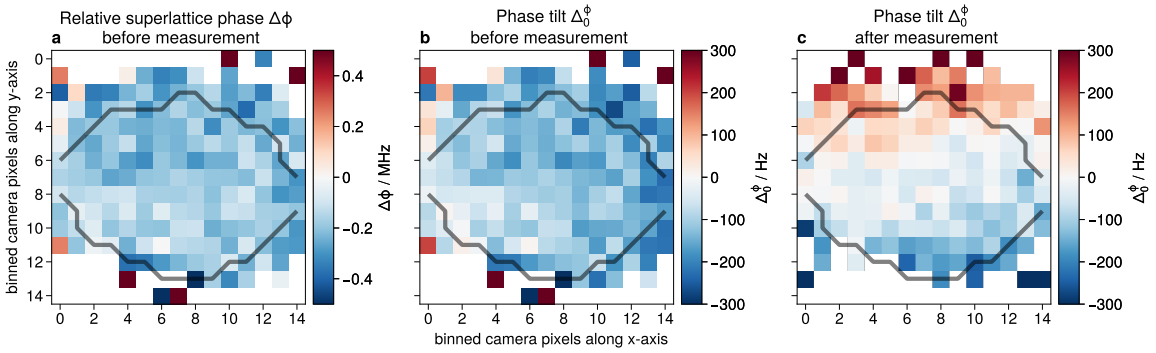

Figure 6.4: **Position-dependent superlattice phase during Floquet experiments:** The relative superlattice phase compared to the symmetry point $\Delta\phi$ is determined via the in-situ symmetry point measurements (a). The mean value of this relative superlattice phase is (-0.15 ± 0.30) MHz and indicates a well-adjusted superlattice before the experiment. The spatially varying phase tilt Δ_0^{ϕ} is calculated from the relative superlattice phase (b) but varies significantly over the course of an experimental cycle of 10 h (c).

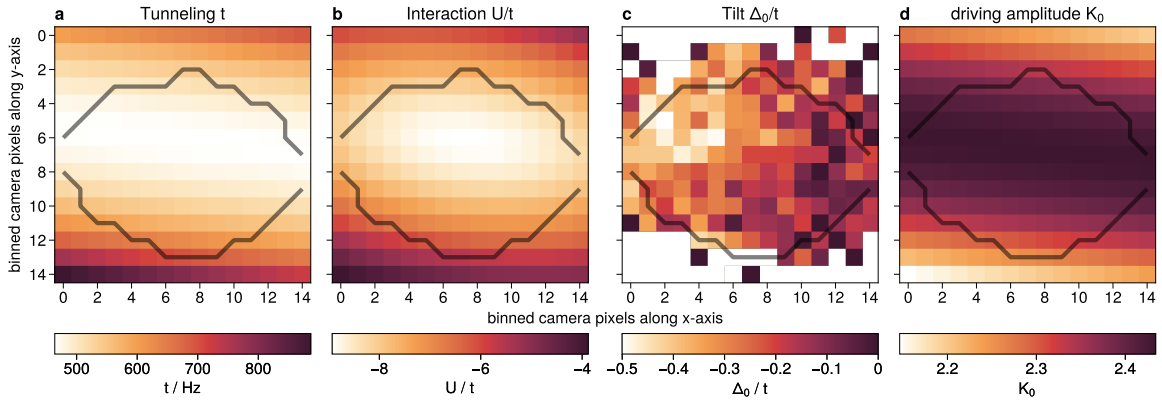

Figure 6.5: **Hubbard parameters considered in the fitting procedure:** The optical density for doubly occupied sites is used as a relative weight during averaging over the double wells and the boundary of high-density region od $\leq 0.1\,\max(\mathrm{od})$ is indicated as a gray line. The tunneling $t = t_{\mathrm{in}} + t_{\mathrm{corr}}$ (a) is determined from the intra-well tunneling t_{in} and the correction for interacting Wannier functions t_{corr}. (b) The normalized interaction U/t varies significantly from -9 to -7 within the high density region. The tilt $\Delta_0 = \Delta_0^{\phi} + \Delta_0^{\mathrm{latt}}$ is shown for one specific realization (c) and varies over time. The normalized driving amplitude K_0 also changes with the optical lattice depths (d), however, the driving frequency ν is constant.

6.1.3 Fitting the population contrast for an inhomogeneous array of double wells

In the fitting procedure, we perform a density weighted average of the spatially varying population contrast $C^D(\boldsymbol{x})$ to obtain the global observable C^D. For this purpose, we consider an array of independent near-resonantly driven double wells with the parameters $U(\boldsymbol{x})$, $t(\boldsymbol{x})$, $\Delta_0(\boldsymbol{x})$, $K_0(\boldsymbol{x})$ and ν (cf. figure 6.5). We solve the Hamiltonians (compare section 5.3.1) and obtain four eigenvalues ϵ_i and eigenvectors $|\psi_i\rangle$ per double well. This gives the time evolution for one double well initially prepared in $|LL\rangle$

$$|\Psi(\tau)\rangle = \sum_i \alpha_i e^{i\frac{\epsilon}{\hbar}\tau} |\psi_i\rangle \tag{6.1}$$

with $\alpha_i = \langle\psi_i|LL\rangle$. From this we compute the population contrast for each individual double well

$$C^D(\tau) = \frac{\langle\Psi(\tau)|LL\rangle - \langle\Psi(\tau)|RR\rangle}{\langle\Psi(\tau)|LL\rangle + \langle\Psi(\tau)|RR\rangle}, \tag{6.2}$$

and thus the spatially dependent population contrast $C^D(\tau, \boldsymbol{x})$.[1] Finally, the calibrated optical density is used for a density weighted average of the population contrast resulting in $C^D(\tau)$.

However, to account for experimental fluctuations, we allow for a variation of the green lattice depth V_s as well as the scattering length a and consequential fitting of the population contrast to our data. Moreover, we perform these fits for all tilt maps $\Delta_0(\boldsymbol{x})$ of one experimental cycle independently. We average over the individual fits to obtain the final result and its uncertainty shown as a solid line and a shaded region in figure 6.2. The fitted dynamic signals clearly reproduce the characteristics of our data. We compare our fitted lattice depths and scattering lengths for various driving frequencies with

[1] For the computation of the population contrast we consider the smaller detection efficiency on the upper well of (0.44 ± 0.08) normalized to the detection efficiency on the lower well $|LL\rangle$, as discussed in section 5.3.2.

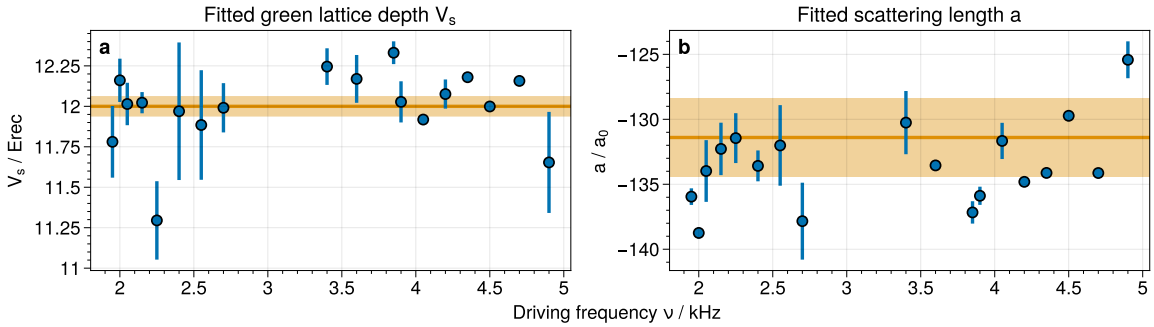

Figure 6.6: **Fitted lattice depth and scattering length:** For the attractive interaction $U \approx -9t \approx 4\,\mathrm{kHz}$ the fitted lattice depths V_s of the green lattice (a) agree well with the independent calibration $(12.0 \pm 0.1)\, E_{\mathrm{rec}}$. The fitted scattering lengths a agree excellently with the independently calibrated value $(-131.4 \pm 3.0)\, a_0$.

the expected values from independent calibrations in figure 6.6. Evidently, our obtained result agree very well with our expectations.

6.2 Spectra of near-resonantly driven double wells

We are interested in the effective processes that cause the observed dynamics in the driven systems. For this purpose, we extract the quasi-energy spectra of the fitted effective Hamiltonian at the trap center for half filling

$$\hat{H}_{\mathrm{eff}} = \begin{pmatrix} U_{\mathrm{eff}} + 2\Delta_0 & (-1)^{\ell+1} \cdot t_{\mathrm{eff}} & (-1)^{\ell} \cdot t_{\mathrm{eff}} & V_{\mathrm{ct}}^{\mathrm{eff}} \\ (-1)^{\ell+1} \cdot t_{\mathrm{eff}} & V_{\mathrm{nn}}^{\mathrm{eff}} & -V_{\mathrm{de}}^{\mathrm{eff}} & -t_{\mathrm{eff}} \\ (-1)^{\ell} \cdot t_{\mathrm{eff}} & -V_{\mathrm{de}}^{\mathrm{eff}} & V_{\mathrm{nn}}^{\mathrm{eff}} & t_{\mathrm{eff}} \\ V_{\mathrm{ct}}^{\mathrm{eff}} & -t_{\mathrm{eff}} & t_{\mathrm{eff}} & U_{\mathrm{eff}} - 2\Delta_0 \end{pmatrix} \tag{6.3}$$

with the effective tunneling t_{eff}, the effective interaction U_{eff}, the tilt Δ_0 and the effective higher-order Hubbard parameters: the explicit pair hopping $V_{\mathrm{ct}}^{\mathrm{eff}}$, the nearest-neighbor interaction $V_{\mathrm{nn}}^{\mathrm{eff}}$ and the direct spin exchange $V_{\mathrm{de}}^{\mathrm{eff}}$. Note, that these three higher-order Hubbard parameters are negligible in the static case $V_{\mathrm{nn}} = V_{\mathrm{de}} = V_{\mathrm{ct}} = 8 \times 10^{-4}\,\mathrm{t}$ and only arise in the higher orders of the high-frequency expansion of the effective Hamiltonian (compare equation 5.7) and will be discussed in detail in section 6.3.

The effective Hamiltonian provides us with three relevant quasienergies and a fourth value, corresponding to the spin-triplet state that we omit from display due to a lack of coupling. We show this spectrum for attractive interactions $U \approx -9t \approx -4\,\mathrm{kHz}$ and the first two harmonic orders $\ell = 1, 2$ in figure 6.7. As discussed in section 5.1.1, these quasienergies are only defined within one Floquet zone. Therefore, we normalize the quasienergies with the driving frequency and restrict the display to $-0.5 \leq \epsilon_i / h\nu \leq 0.5$. We compare our measurements to independent Monte-Carlo simulations with the 1σ confidence interval shown as shaded regions. In these simulations, we have considered the uncertainty of our lattice depths to be 0.5 % and of the scattering length to be $3\,a_0$, according to our calibrations.

We observe two distinct avoided-crossing-like behaviors around $h\nu/U \approx 1,\ 0.55$ corresponding to the first (second) harmonic resonance condition. Here, the intermediate quasi-energy is roughly

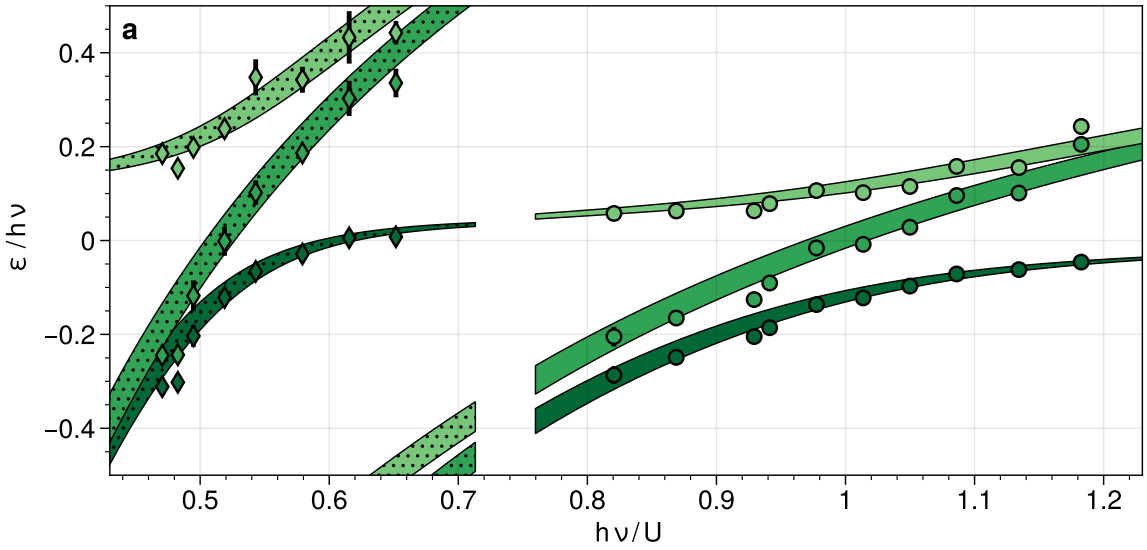

Figure 6.7: **Quasi-energy spectrum for a near-resonantly driven double well at half filling:** In an attractively interacting system $U \approx -9t \approx -4\,\mathrm{kHz}$ the energy eigenvalues $\epsilon_i/h\nu$ of the fitted Hamiltonians at the trap center are plotted for various driving frequencies $h\nu/U$. The driving amplitude is chosen to suppress tunneling in half-filled double wells $K_0 = 2.4$. The first (second) harmonic resonance is indicated by circles (diamonds) and the shades of green differentiate the various eigenenergies. The shaded regions indicate the 1σ confidence interval of independent Monte-Carlo simulations of the system.

equidistant to the lowest and highest quasi-energy, resembling a non-interacting double well. From the effective interaction strength up to the lowest order $U_{\mathrm{eff}} = U - \ell h\nu$ we would expect the second harmonic resonance to be at $h\nu/U \approx 0.5$. However, the observed deviation stems from the higher order corrections to the effective Hamiltonian, that are more relevant for the lower frequencies of the second harmonic order. Nonetheless, the linear scaling of this effective interaction is visible in the spectrum: Increasing the driving frequency from resonance, pushes the upper two quasi-energies up as their contribution of double occupancies increases their energies. On the other hand, decreasing the driving frequency realizes effective attractive interaction and thus pushes the lower two quasi-energies down. Moreover, the different slope of the intermediate state for the two harmonic resonances shows the expected behavior of the effective interaction with the harmonic order.

Note, that the periodicity of the quasienergies is visible in the theoretical spectrum of the second harmonic order. Here the highest two eigenenergies reach the upper edge of the Floquet zone around $\approx 0.65\, h\nu/U$ and seem to re-emerge at the lower edge of the Floquet zone. Moreover, in this intermediate regime between the two resonances, the near-resonant theory breaks down, as $U_{\mathrm{eff}} \ll h\nu$ is no longer valid. However, this regime might be of interest, as the repulsive branch of the second harmonic resonance approaches the attractive branch of the first harmonic resonance and thus, intuitively, the meaning of the effective interaction becomes unclear. Unfortunately, these regimes of large effective interactions –or in well-defined terms: large frequency detunings– are not experimentally accessible for us. As shown in figure 5.8 a (and the corresponding discussion), our global observable is not insightful in these regimes of large (effective) interactions, as the atoms localize in the double wells due to the residual tilt. Nonetheless, we see a great agreement of our

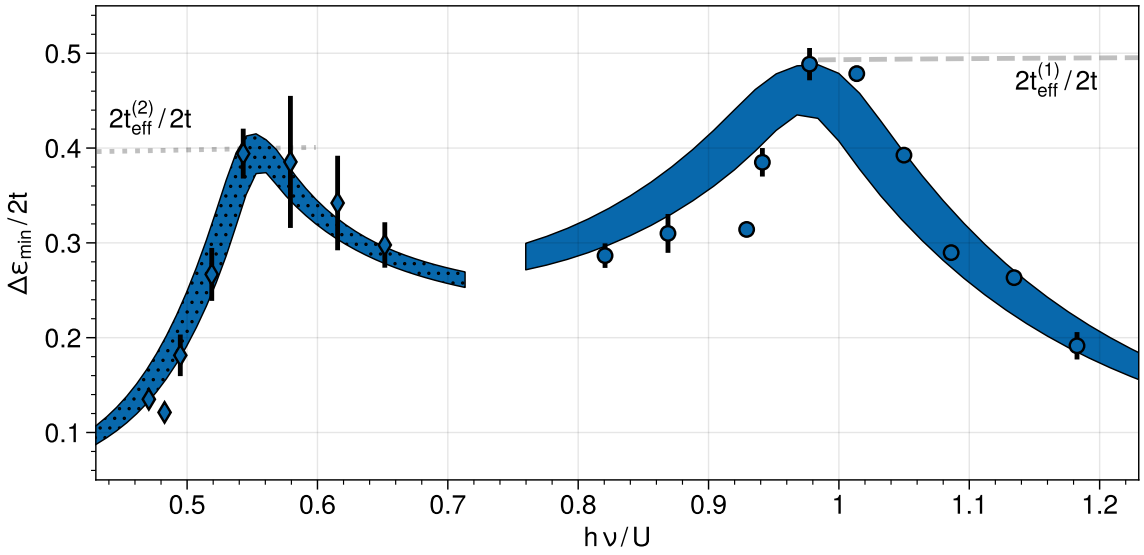

Figure 6.8: **Minimal quasi-energy difference for a near-resonantly driven double well:** In an attractively interacting system $U \approx -9t \approx -4\,\mathrm{kHz}$ the minimal quasi energy difference of the spectrum $\Delta\epsilon_{\mathrm{min}}/2t$ is plotted for various driving frequencies $h\nu/U$. The driving amplitude is chosen to suppress tunneling in half-filled double wells $K_0 = 2.4$. The first (second) harmonic resonance is indicated by circles (diamonds) and the shaded region denotes the 1σ confidence interval of an independent Monte-Carlo simulation. The dashed (dotted) line corresponds to the effective single particle tunneling for the effectively non-interacting systems of the first (second) harmonic resonance.

experimental data and the theoretical simulations within the observed regions.

We proceed with our analysis by determining the minimal quasienergy difference, $\Delta\epsilon_{\mathrm{min}}/2t$, from our spectra (refer to figure 6.8). We identify two distinct peaks at the same driving frequencies where the spectra exhibit avoided crossings. In this context, the minimal energies are associated with the density-assisted tunneling rates t_{eff}^{ℓ}, which vary according to the harmonic order ℓ, as previously introduced in figure 5.8 e. For large effective interactions the breaking of pairs is suppressed and the minimal quasi-energy difference corresponds to the effective pair tunneling rate $|J_{\mathrm{eff}}|$. Clearly this pair-tunneling rate is smaller than the density-assisted tunneling rate of the same harmonic order. However, it is dominant compared to the single particle tunneling which we suppress via the driving amplitude $K_0 = 2.4$. This already shows the crossover from a dominant density-assisted to pair-tunneling regime qualitatively. However, we will quantify this crossover more in detail in the next section. Note that we have also extracted the spectra of near-resonantly driven double wells for even larger attractive interactions $U_{\mathrm{eff}} \approx -18t$ and small attractive interactions $U_{\mathrm{eff}} \approx -6t$, that are presented in the appendix in figure C.1 and figure C.2. This shows, that our findings are reproducible for other interaction strengths as well.

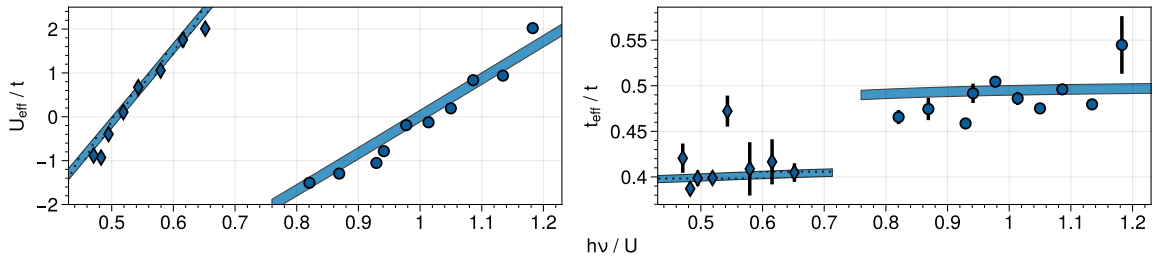

Figure 6.9: **Effective Hubbard parameters of near-resonantly driven double wells:** In an attractively interacting system $U \approx -9t \approx -4\,\mathrm{kHz}$ the effective interaction strength U_{eff} changes linearly with the driving frequency $h\nu$ (a). The first (second) harmonic order is indicated by circles (diamonds) and the shaded region denotes the 1σ confidence interval of an independent Monte-Carlo simulation. The driving amplitude is chosen to suppress tunneling in quarter-filled double wells $K_0 = 2.4$. (b) The effective tunneling t^{ℓ}_{eff} depends on the harmonic order ℓ and is almost independent of the driving frequency.

6.3 Floquet-driven crossover from density-assisted tunneling to enhanced pair tunneling

In this section we explore a Floquet-driven crossover from density-assisted tunneling to enhanced pair tunneling quantitatively using the effective Hubbard parameters. For this purpose, we consider the effective Hamiltonians at the trap center and extract the effective Hubbard parameters given in equation 6.3. With these effective parameters, we characterize the crossover using two properties of the two-particle dynamics: The pair-tunneling fidelity, which measures the relative amplitude of the pair-tunneling and the minimal energy difference of the spectrum, that corresponds to the characteristic frequency of the dynamics.

We start with the discussion of the effective Hubbard parameters. The dominant parameters are the effective interaction strength U_{eff} and the effective tunneling $t^{(\ell)}_{\mathrm{eff}}$, which we plot against the driving frequency ν in figure 6.9. This reproduces the qualitative analysis of the former section in a more quantitative fashion: The effective interaction is exactly balanced at the resonance conditions for the different harmonic orders and changes linearly with different slopes depending on the harmonic order, as shown in subfigure a. On the other hand, the effective tunneling is different for the harmonic order but otherwise not frequency dependent. With these two effective parameters per harmonic order we achieve comparability of the driven systems between each other and with respect to the static scenario, which we will apply in the following.

We have discussed the realized effective systems in the two regimes of balanced interactions and very strong interactions in the former section. Here, we have identified the density-assisted tunneling regime for $U_{\mathrm{eff}} = 0$, as well as the pair-tunneling regime $|U_{\mathrm{eff}}| \gg t^{(\ell)}_{\mathrm{eff}}$. To quantify this crossover and study also the intermediate regimes we introduce the pair tunneling fidelity

$$\mathcal{F}_{\mathrm{pair}} = 1 - 4 \cdot A_{\mathrm{split}} \tag{6.4}$$

with the time averaged population of split pairs

$$A_{\mathrm{split}} = \overline{|\langle LR|\Psi(\tau)\rangle|^2 + |\langle RL|\Psi(\tau)\rangle|^2}. \tag{6.5}$$

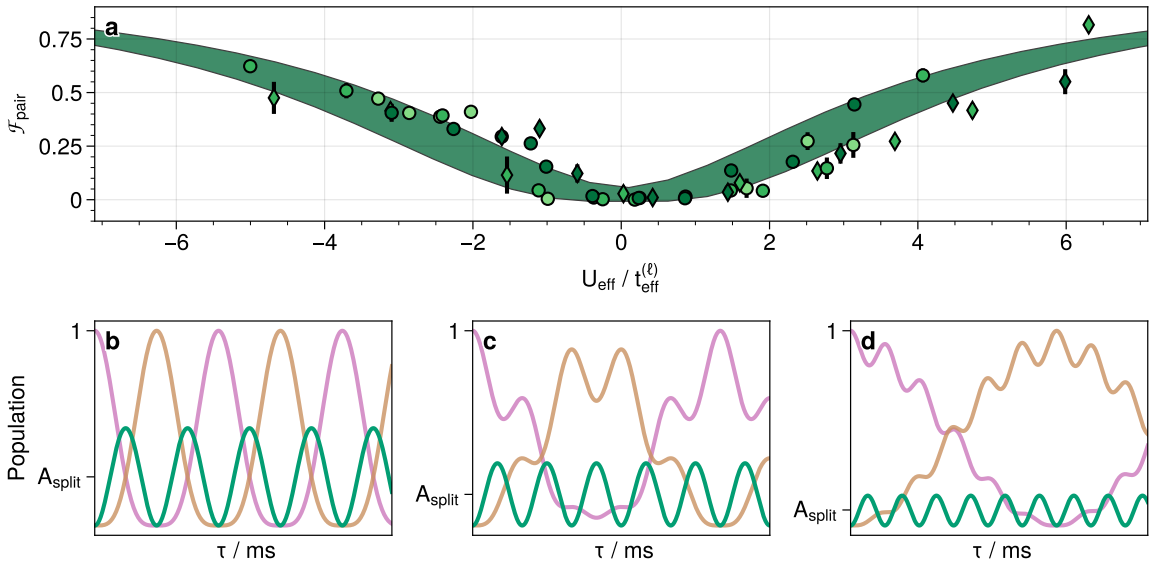

Figure 6.10: **Pair-tunneling fidelity of near-resonantly driven double wells:** The pair-tunneling fidelity $\mathcal{F}_{pair} = 1 - 4A_{split}$ quantifies the pair splitting during the tunneling dynamics. (a) $\mathcal{F}_{pair}$ is determined as a function of the normalized effective interaction strength $U_{eff}/t_{eff}^{(\ell)}$ for various interaction strengths $U/t \approx -9$ (dark green), $U/t \approx -18$ (green), $U/t \approx -6$ (light green) and harmonic orders $\ell = 1$ (circles) and $\ell = 2$ (diamonds). (b to d) Tunneling dynamics in systems with various interaction strengths $U/t = 0,\ 3,\ 6$. The pair tunnels from the left lattice site (brown) to the right lattice site (purple) via the split state (green). The time averaged population of the split pairs A_{split} changes with the interaction strength.

This fidelity measures the participation of the split pairs in the two-particle dynamics, as we show theoretically in figure 6.10 b to d. For an effectively non-interacting system (subfigure b), the atoms tunnel from the $|LL\rangle$ state (pink trace) to the $|RR\rangle$ state via the split states $|LR\rangle$ and $|RL\rangle$ (green). Here, the time averaged population of the split pairs is $A_{split} = 0.25$ leading to a pair-tunneling fidelity of $\mathcal{F}_{pair} = 0$. Increasing the effective interactions (subfigure c and d) suppresses the population of split pairs, thereby increasing the pair-tunneling fidelity which approaches unity for infinitely large effective interactions.

We present our measurements of the pair-tunneling fidelity as a function of the normalized effective interaction strength in figure 6.10 a. The data is shown for various interaction strengths and harmonic orders and compared to MC simulations, which are represented by the shaded region. Across all different realizations, the fidelity increases with the absolute value of the effective interaction strength, which suppresses the population of split pairs, matching our theoretical expectations. In effectively non-interacting systems within the density-assisted regime, we observe a vanishing fidelity. Increasing the effective interactions raises the pair-tunneling fidelity, until for $|U|/t > 5$ the pair tunneling fidelity exceeds 60 % significantly, rendering pair tunneling the dominant process in the system. With this pair-tunneling fidelity we have characterized the relative amplitude of the pair tunneling within the two-particle dynamics of the half-filled double well.

Next, we are interested in the frequency of the two-particle dynamics in the effective system, and how they compare to their static counterpart. For this purpose, we plot the minimal energy difference of the spectrum $\Delta\epsilon_{min}/2t_{eff}^{(\ell)}$ as a function of the effective interaction strength $U_{eff}/t_{eff}^{(\ell)}$ in figure

6.11 a. In the static double well, the minimal energy difference (gray line) corresponds to twice the single-particle tunneling for non-interacting systems and approaches the superexchange J for large interactions. We reproduce this behavior for near-resonantly driven systems of first harmonic order ($\ell = 1$) and different absolute interaction strengths $U/t = -9$ (dark blue) and $U/t = -18$ (light blue). Here, we have realized effective systems with two-particle dynamics that are comparable to the static double well over a wide range of interactions, but with completely suppressed single-particle tunneling (dotted line), via the driving amplitude of $K_0 = 2.4$. Especially for the large attractive effective interaction $U_{\text{eff}}/t_{\text{eff}}^{(1)} \sim -5$, where we have established pair tunneling to be the dominant process via the pair-tunneling fidelity, we have realized a system with dominant pair tunneling $J_{\text{eff}} > t_{\text{eff}}^{(0)}$.

Remarkably, the pair-tunneling rate in the driven systems can be enhanced not only compared to the localized quarter-filled double wells but also compared to its static counterpart. In figure 6.10 b, we show the minimal energy difference for a near-resonantly driven system of second harmonic order ($\ell = 2$) and absolute interaction strength $U/t = -9$ (dark blue). Interestingly, the repulsive branch exceeds its static comparison significantly for large effective interactions. In particular, for $U_{\text{eff}}/t_{\text{eff}}^{(2)} = 6$ this enhancement exceeds a factor of two. This effect is also directly visible when comparing the dynamic signals for the driven and static double well (cf. figure 6.10 c and d). Notably, the time averaged split population A_{split} is very similar for both scenarios, as it is only a measure of the (effective) interaction strength $U_{\text{eff}}/t_{\text{eff}}^{(\ell)}$, which is the same for both cases. Evidently, we have realized effective systems with a pair-tunneling rate that is enhanced not only compared to the suppressed single-particle tunneling but also compared to the superexchange of the static counterpart.

Driving induced enhancement of the correlated tunneling

We have observed, that for large effective interactions the minimal quasienergy difference, which corresponds to the pair-tunneling rate, can be enhanced above the superexchange rate of the static counterpart. To understand this enhancement, we compare the pair-tunneling rate of the driven systems with the static counterpart. We define the pair-tunneling rate as the quasienergy difference $\Delta\epsilon_{\text{pair}}$ between the two states that consist dominantly of pairs, for large effective interactions.[2]

In the static double well, the states with dominant pair occupancies are the $|d_-\rangle$ and the ground state (excited state) for attractive (repulsive) interactions, as shown in figure 4.9, and their energy difference is

$$\Delta E_{\text{pair}} = E_{\text{g,e}} - E_{d-} = -U/2 \pm \sqrt{16t^2 + U^2/4}. \tag{6.6}$$

For large interactions $|U| \gg t$, this energy difference approaches the superexchange $\Delta E_{\text{pair}} \sim \frac{4t^2}{U}$, which is the pair-tunneling rate of the static system.

In the driven double well, the states with dominant pair occupancies change with the harmonic order and with the sign of the interaction, as we have shown in figure 5.6 b and c. Note that the reason for this behavior is that the sign of the effective tunnel coupling changes with the harmonic order and therefore, the pair states that couple to the singlet state. The relevant quasienergy gap is given by

$$\Delta\epsilon_{\text{pair}} = \begin{cases} \epsilon_{g,e} - \epsilon_{d_+} & \ell \text{ odd} \\ \epsilon_{g,e} - \epsilon_{d_-} & \ell \text{ even} \end{cases}. \tag{6.7}$$

[2] This energy difference between states that consist dominantly of pairs is the same as the minimal energy difference, when neglecting the triplet state.

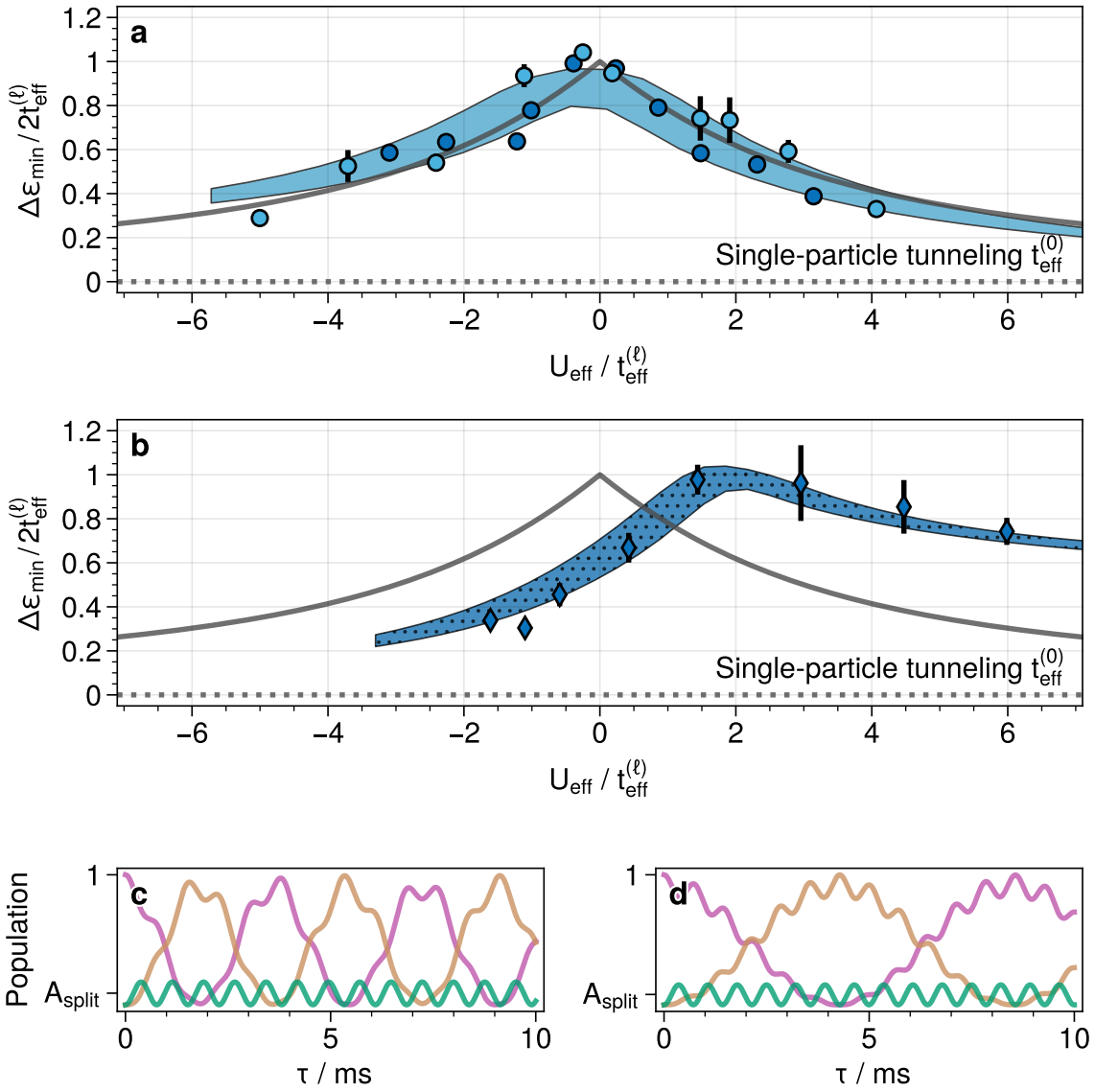

Figure 6.11: **Enhanced pair tunneling in near-resonantly driven double wells:** (a) For attractive interactions $U_{\text{eff}} \sim -9t \sim -4\,\text{kHz}$ (dark blue), and $U_{\text{eff}} \sim -18t \sim -8\,\text{kHz}$ (light blue) and driving amplitude $K_0 = 2.4$, the minimal quasi-energy difference $\Delta\epsilon_{\text{min}}/2t_{\text{eff}}^{\ell}$ changes with the effective interaction strength $U_{\text{eff}}/t_{\text{eff}}^{(\ell)}$ for a near-resonantly driven double well of first harmonic order $\ell = 1$. The shaded region denotes the 1σ confidence interval of an independent Monte-Carlo simulation for $U_{\text{eff}} \sim -18t$, while for $U_{\text{eff}} \sim -9t$ the MC simulation is not shown for better visibility. The behavior of the static double well (gray line) and the driven quarter-filled double well (dotted line) is shown for comparison. The second harmonic order $\ell = 2$ for $U_{\text{eff}} \sim -9t$ is shown in subfigure (b). (c and d) Comparison of tunneling dynamics in systems with and without periodic modulation. (c) In the driven double well with harmonic order $\ell = 2$ and $U/t_{\text{eff}}^{(2)} = 6$, the pair tunnels from the left lattice site (brown) to the right lattice site (purple) with only a minimal population of the split state (green). In comparison to the corresponding static double well (d), the dynamic timescale of the driven double well is enhanced significantly, whereas the split amplitude A_{split} remains almost the same.

Unlike in the static scenario, in the driven double well the higher-order Hubbard parameters can have significant amplitude, as we will show. Therefore, the quasienergy gap of the driven system also depends on the higher-order Hubbard parameters and is given as

$$\begin{aligned}\Delta\epsilon_{\text{pair}} = &\frac{-U_{\text{eff}} + (-1)^{\ell}\, 3\, V_{\text{ct}}^{\text{eff}} + 2\, V_{\text{nn}}^{\text{eff}}}{2} \\ &\pm \frac{\sqrt{16\, t_{\text{eff}}^2 + U_{\text{eff}}^2 + (-1)^{\ell}\, 2\, U_{\text{eff}}\, t_{\text{pair}}^{\text{eff}} - 4\, U_{\text{eff}}\, V_{\text{nn}}^{\text{eff}} + ((-1)^{\ell+1}\, V_{\text{ct}}^{\text{eff}} + 2\, V_{\text{nn}}^{\text{eff}})^2}}{2},\end{aligned} \tag{6.8}$$

where we have used $V_{\text{de}}^{\text{eff}} = V_{\text{nn}}^{\text{eff}}$ [77] and neglected the harmonic order ℓ superscript of the effective tunneling for better readability. Clearly this expression reproduces the result of the static double well of equation 6.7, when neglecting the higher order parameters. For large effective interactions $|U_{\text{eff}}| \gg t_{\text{eff}}, V_{\text{ct}}^{\text{eff}}, V_{\text{nn}}^{\text{eff}}$, this quasienergy difference approaches the effective-pair tunneling rate

$$J_{\text{eff}} \sim \frac{4t_{\text{eff}}^2}{U_{\text{eff}}} + (-1)^{\ell}\, 2\, V_{\text{ct}}^{\text{eff}} + O(U_{\text{eff}}^{-2}). \tag{6.9}$$

This effective pair-tunneling rate resembles the static superexchange rate with a harmonic order dependent correction by the effective correlated tunneling rate $V_{\text{ct}}^{\text{eff}}$. Whether the correlated tunneling rate leads to an enhancement –or rather a suppression– of J_{eff}, depends on the sign of the effective interaction strength, as well as the harmonic order.

The amplitude of the correlated tunneling determines, whether the correction to the pair tunneling is relevant. We show the amplitudes of the effective correlated tunneling for different interaction strengths and harmonic orders in figure 6.11 a. For the first harmonic order ($\ell = 1$) and both interaction strengths $U/t \sim -9$ (dark blue circles), and $U/t \sim -18$ (light blue circles) the effective correlated-tunneling rate is very small compared to the effective tunneling $t_{\text{eff}}^{(\ell)}$. On the other hand, for the second harmonic order and $U/t \sim -9$ (dark blue diamonds), the correlated tunneling rate is of significance $V_{\text{ct}}^{\text{eff}} > 0.2\, t_{\text{eff}}^{(2)}$ for all effective interaction strengths. For attractive interactions, this suppresses J_{eff} as the signs of the two summands differ. On the other hand, this enhances the pair-tunneling amplitude for repulsive interactions resulting in the asymmetric behavior observed in figure 6.11 b.

There remain two open questions about this driving induced enhancement of the correlated tunneling: Why is the effective correlated tunneling in the driven system sometimes large (dark blue diamonds in figure 6.10 a) and sometimes negligible (circles of both shades)? And why does the harmonic order change the sign of the contribution of the effective correlated tunneling to the effective pair tunneling in equation 6.9? In the following, we give answers to both questions, starting with the latter.

In short, the harmonic order dependent sign can be understood as the parity of our driving protocol changing the tunneling parity and thus interchanging the two basis states of the double well $|d_+\rangle$ and $|d_-\rangle$, if the harmonic order is uneven as shown in figure 5.6. Now, the pair tunneling operator $\hat{t}_{\text{pair}} = \hat{c}_{R\uparrow}^{\dagger}\hat{c}_{R\downarrow}^{\dagger}\hat{c}_{L\uparrow}\hat{c}_{L\downarrow}$ affects the two doublet states differently, as

$$\langle d_+|\hat{t}_{\text{pair}}|d_+\rangle = V_{\text{ct}} \text{ and } \langle d_-|\hat{t}_{\text{pair}}|d_-\rangle = -V_{\text{ct}}. \tag{6.10}$$

This quasi energy change then leads to an opening or closing of the gap between the two doublet states that depends on their initial quasi-energy hierarchy (cfs. figure 5.6 b and c).

Note that the other two higher-order Hubbard parameters V_{nn} and V_{de} are always of the same

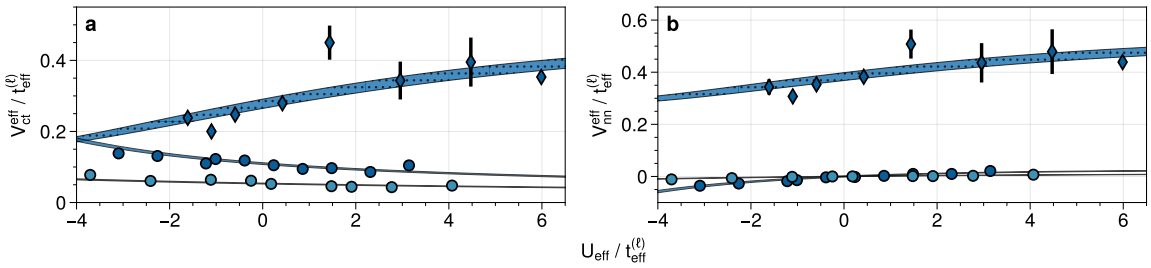

Figure 6.12: **Effective Hubbard parameters of higher orders for near-resonantly driven double wells** In a driven attractively interacting system $U \sim -9t \sim -4\,\mathrm{kHz}$ (dark blue) and $U \sim -18t \sim -8\,\mathrm{kHz}$ (light blue) the effective correlated tunneling $V_{ct}^{eff}/t_{eff}^{(\ell)}$ has a significant amplitude for the second harmonic order $\ell = 2$ (diamonds) compared to the first (circles) (a). The shaded region denotes the 1σ confidence interval of an independent Monte-Carlo simulation. (b) The effective nearest neighbor interaction V_{nn}^{eff} is much larger for the second harmonic than for the first harmonic order. Note that the effective direct exchange V_{de}^{eff} behaves in the exact same fashion as the effective nearest neighbor interaction. In the static scenario, these higher order parameters are negligible $V_{ct} = V_{nn} = V_{de} \leq 8.4 \times 10^{-4}\,t$.

amplitude and are also of relevance for our system (cf. figure 6.12 b). The corresponding operators only couple to the singlet state

$$\langle s|\hat{V}_{nn}|s\rangle = V_{nn} \text{ and } \langle s|\hat{V}_{de}|s\rangle = V_{de} \tag{6.11}$$

and thus increase the singlet states energy (cf. figure 5.6 c). In our system this has the consequence that the smallest energy gap at effectively non-interacting systems is lower than twice the effective tunneling (cf. figure 6.11 a). Moreover, these higher-order corrections to the singlet states energy were used in another experiment to change the magnetic correlations in a driven double well from antiferromagnetic to ferromagnetic [42, 164].

Finally, we investigate how the periodic modulation can cause a significant enhancement of the correlated tunneling rate in the effective system. For this purpose, we compute the effective correlated tunneling rate in the high frequency expansion resulting in

$$V_{ct}^{eff} = \frac{t^2}{h\nu}\left(\alpha^{(\ell)}\mathcal{J}_0(K_0)^2 + \beta^{(\ell)}\mathcal{J}_1(K_0)^2 + O(\mathcal{J}_{>1}(K_0)^2)\right) + O(1/\nu^2) \tag{6.12}$$

with the harmonic order dependent pre factors $\alpha^{(1)} = 2$, $\alpha^{(2)} = 1$, $\beta^{(1)} = -1$, and $\beta^{(2)} = -8/3$ [112]. Clearly, V_{ct}^{eff} decreases with the driving amplitude ν linearly and is therefore largest for the second harmonic order at smaller attractive interactions $U \sim -9t$ (diamonds in figure 6.12), as the driving frequency is the lowest. Therefore, to realize systems with effective higher-order Hubbard parameters of relevant amplitude small driving frequencies compared to the single particle tunneling are necessary. However, in this regime it is crucial to verify that the inverse frequency expansion is still valid [77], which we have done by testing the convergence of the effective parameters [112].

Summary and Outlook

In conclusion, we have utilized Floquet engineering to enhance pair tunneling both compared to the suppressed single-particle tunneling and compared to the superexchange rate of static double wells. Moreover, we have discussed and quantified a crossover from a density-assisted tunneling regime to the pair-tunneling regime by detuning the driving frequency. In particular, we have investigated the crucial role of higher-order Hubbard parameters in the enhancement of the pair tunneling.

In the future, this will allow for the realization of models with dominant pair tunneling beyond the usual Hubbard physics. For example, a system very similar to a ladder with dominant pair tunneling along the rungs and single-particle tunneling along the spars was theoretically predicted to have topologically protected edge states with Majorana-like properties [160, 161]. These Majorana fermions [165] are their own anti-particles and have been part of theoretical studies ranging from particle physics to condensed matter systems [166, 167] but have yet to be observed experimentally. In general, this ladder system could be emulated in our setup by unfreezing the tunneling along the y-direction and applying the near-resonant periodic drive to the double wells along the x-direction. However, several experimental aspects such as the homogeneity of the system and the possible observables still need to be resolved.

CHAPTER 7

Conclusion and Outlook

In this thesis, we have experimentally investigated the behavior of ultracold fermionic potassium atoms in both periodically-driven and static superlattices. We have observed novel physics beyond the standard Hubbard model of monochromatic lattices, which I will summarize in the following alongside the experimental achievements required for their realization.

In the course of this thesis, we have built and characterized a phase-stable in-plane superlattice, created by the superposition of an infrared and a green lattice. We have characterized the superlattices' tight binding parameters directly using Rabi oscillations, density-assisted tunneling and radio-frequency spectroscopy, validating our newly developed theoretical framework for the calculation of these parameters. Moreover, we have established significant control over the superlattice phase by employing a phase-locked loop with an environmental feed-forward. Notably, we have realized a phase-stability of the superlattice better than 3 mrad, which presents one of the best reported phase stabilities [39, 40].

Using the superlattice, we explored the dynamics in periodically-driven double-well potentials. In particular, we employed a low-noise periodic modulation of the onsite energy to study a Floquet-driven crossover from density-assisted tunneling to dominant pair tunneling. We demonstrated the realization of an effective Hamiltonian, where the effective tunneling amplitude varied with the driving amplitude following a Bessel function behavior. For a drive resonant with the interaction energy, we have observed density-assisted tunneling, fully suppressing single-particle dynamics for various harmonic orders. Detuning the drive from resonance introduced effective interactions and led to pair-tunneling in the absence of single-particle tunneling. Remarkably, we enhanced the pair tunneling in the driven system by more than a factor of two, compared to the static counterpart, due to a driving induced enhancement of the correlated tunneling.

Additionally, the superlattice offers the potential to discover new physics even in static configurations. In this work, we have newly developed a preparation and detection scheme for repulsively-bound pairs in array of tilted double-wells. We have prepared these pairs with high fidelity by a radio-frequency transfer between hyperfine states. Moreover, we have utilized a fast modulation of the double-well tilt to induce Rabi oscillations between the eigenstates of the system, coherently measuring the population of the repulsively bound pairs.

Exploring η-pairs using an in-plane optical superlattice In the future, the static in-plane superlattice offers the exciting possibility to study η-pairs [38], They are a unique eigenstate of the

Hubbard model, that posses off-diagonal long-range order [127], a property that is believed to be a characteristic of superconductivity [168]. In particular, they are delocalized pair-states with a π phase shift between neighboring sites and a characteristic center-of-mass momentum at the edge of the Brillouin zone of π/a [38].

The double well serves as a fundamental building block of the Hubbard model and is, therefore, particularly well-suited for studying η-pairs through a bottom-up approach. In the balanced double well, the η pair refers to the repulsively-bound pair state with negative parity

$$|\eta\rangle = |d_-\rangle = \frac{1}{\sqrt{2}}(|LL\rangle - |RR\rangle), \tag{7.1}$$

which is adiabatically connected to the excited state that we have prepared via a radio-frequency transfer as discussed in Chapter 4. In the future, adiabatic removal of the double-well tilt will prepare the η-pair and allow for the investigation of its properties using the established detection scheme based on Rabi oscillations.

The lifetime of these η-pairs in a many-body system is of natural interest. For this purpose, the η-pairs are initially prepared in the double wells. Then the infrared part of the superlattice can be ramped down adiabatically to probe the η-pairs in the extended green lattice [37], before employing the established detection technique. Varying the exposure time of the pairs in the extended lattice will determine their lifetime.

Another possibility is to probe the characteristic properties of the η-pair directly. To determine the center-of-mass momentum, the η-pairs could be transformed to Feshbach molecules by ramping the magnetic field close to the Feshbach resonance [169]. Performing a ballistic expansion of the created molecules would determine their momentum [170]. However, this would be a global measurement of the momenta and therefore is only ideal for a homogeneous system. Instead, one could measure the coherence (ODLRO) of the pairs. One approach would be a diabatic introduction of the tilt Δ for a variable time τ, after the preparation of the η-pair. This would introduce a time dependent phase $\phi(\tau) = \pm\Delta/\hbar\tau$ with different sign for the doubly occupied basis states ($|LL\rangle$ and $|RR\rangle$), while leaving the split states ($|LR\rangle$ and $|RL\rangle$) unchanged. The time dependent phase would induce Rabi oscillations between the η-state and the most excited state, as this state is essentially the η-state with positive parity. These Rabi oscillations would be a direct measure of their coherence, the Fourier transformation of the center-of-mass momentum [38].

Many-body systems with dominant pair tunneling Another interesting project is the study of many-body systems with dominant pair tunneling, that extend beyond regular Hubbard models. We have established a periodic modulation technique to create double wells with dominant pair tunneling, which can be applied to many-body systems as well. For example, unfreezing the y-lattice while periodically driving the double-wells along the x-direction, would create a ladder type system with dominant pair tunneling along the rungs and single-particle tunneling along the spars. Such a ladder system is theoretically predicted to exhibit topologically-protected edge states with Majorana-like properties [160, 161]. These Majorana fermions [165], are their own anti-particles and have been part of theoretical studies ranging from particle physics to condensed-matter systems [166, 167], but have yet to be observed experimentally.

Creating homogeneous lattice systems using light-sheets Both of the aforementioned future projects rely on a system that is homogeneous with respect to the superexchange interaction $J = 4t^2/U$, which is the characteristic energy scale. Only if the superexchange exceeds the energy offset between lattice sites, it governs the physics of the system. However, the Gaussian envelopes of the lattice beams create an underlying potential of approximately harmonic nature, which tends to dominate the superexchange. To compensate this harmonic confinement, we will employ light-sheets along the $x-$ and $y-$axes, with an intensity distribution inverse to the Gaussian envelopes of the lattice beams. These light-sheets will be created by superimposing multiple beams diffracted from an acousto-optic deflector (AOD) driven with several radio-frequencies at once, to create a smooth overall potential. By minimizing the number of diffracted beams, we can prevent disorder patterns observed in the past when a digital micromirror device (DMD) was used to compensate the harmonic confinement. The first steps towards the creation of a homogeneous lattice systems using light sheets are discussed in the upcoming Bachelor thesis of Juliane Reuter [171].

APPENDIX A

Hubbard parameters vs. Superlattice parameters

This appendix provides detailed plots of the tight-binding Hubbard parameters t_{in}, t_{out}, U and Δ for various lattice depths and scattering lengths. The calculation of these tight-binding parameters is discussed in detail in section 2.4.

In figure A.1, the two tunneling rates of the superlattice are plotted versus the lattice depth of the green lattice V_s and of the infrared lattice V_l. In figure A.2, the interaction strength is plotted versus the lattice depths of the three-dimensional lattice configuration V_s, V_l, s_y, s_z for a scattering length of $a = -265\,\mathrm{a}_0$. In figure A.3, the tilt of the superlattice is plotted versus the lattice depth of the green lattice V_s and of the infrared lattice V_l.

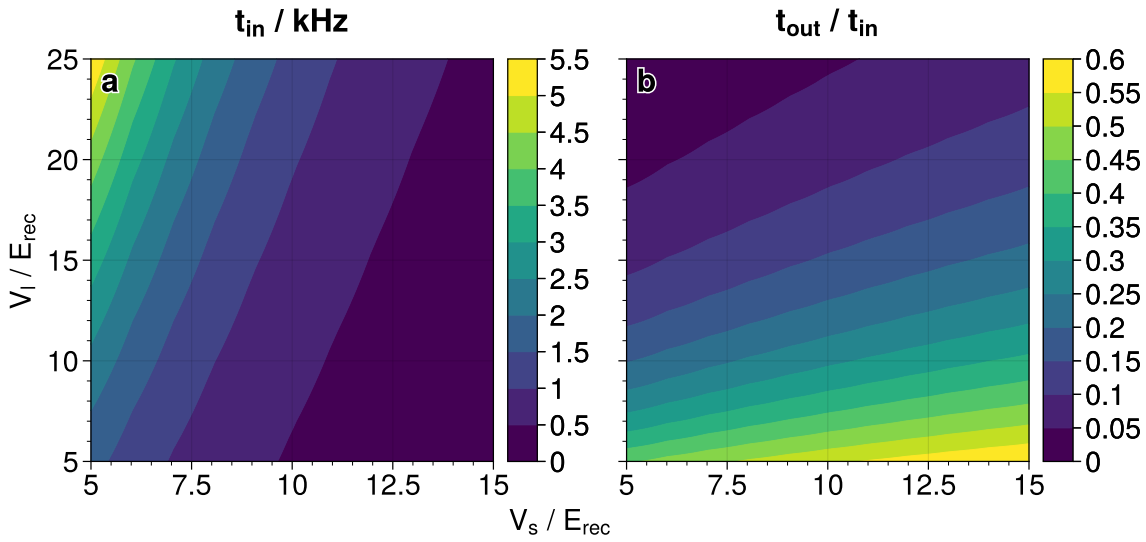

Figure A.1: **Tunneling vs. lattice depths:** (a) Tunneling between two sublattice sites t_{in} versus the short- and long-lattice depth (V_s and V_l respectively). The relative tunneling between lattice sites t_{out} is shown in (b)

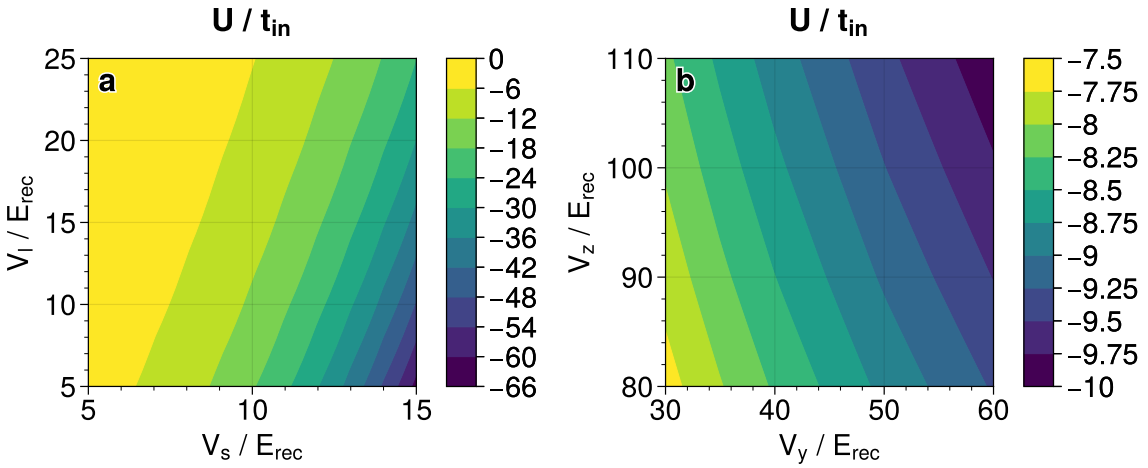

Figure A.2: **Interaction strength vs. lattice depths:** (a) Interaction strength U for a scattering length of $a = -265\,\mathrm{a_0}$ and lattice depths $s_y = 60\,E_{\mathrm{rec}}$ and $s_z = 110\,E_{\mathrm{rec}}$ versus the short and long lattice depths of the superlattice. (b) Interaction strength U for a scattering length of $a = -265\,\mathrm{a_0}$ and lattice depths $V_s = 10\,E_{\mathrm{rec}}$ and $V_l = 15\,E_{\mathrm{rec}}$ versus the lattice depth of the y- and z-lattice.

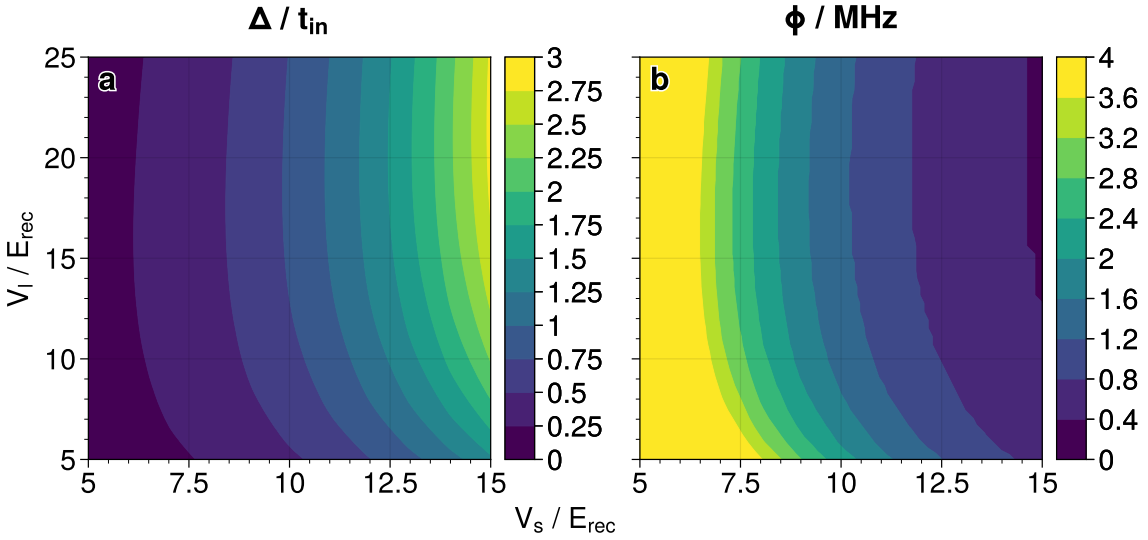

Figure A.3: **Tilt vs. lattice depths:** (a) Tilt between sublattice sites for a superlattice phase $\phi = 1\,\mathrm{MHz}$ relative to the dominant tunneling t_{in}. (b) Superlattice phase ϕ that is necessary to realize a tilt equal to the dominant tunneling $\Delta(\phi) = t_{\mathrm{in}}$.

APPENDIX B

Hyperfine populations during pair experiment cycle

This appendix provides a sketch of the hyperfine state population during the preparation and detection of repulsively-bound pairs in double-wells, according to section 4.2.3.

The elaborate series of radio-frequency transfers that are necessary to conduct these experiments are given in figure B.1. The most important aspects of this sequence are the *pair preparation* and *pair detection* phase. The detailed information on this sequence is given in the caption of the figure and in section 4.2.3.

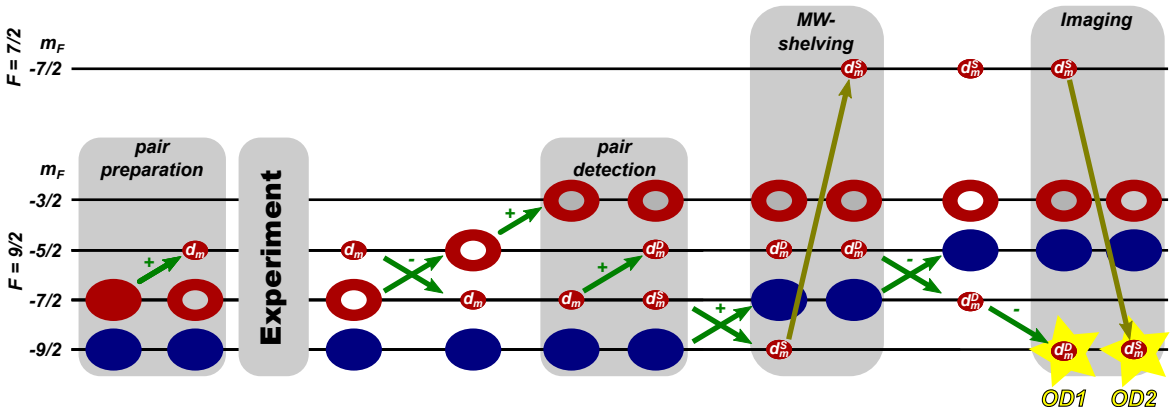

Figure B.1: **Sketch of hyperfine state populations during pair experiment cycle:** The $|d_-\rangle$ state is prepared by a RF-transfer with a pulse width of 3 kHz. After the experiment, the $|d_-\rangle$ state population is detected in a strongly tilted double well $\Delta \gg U, t$. Here, the $|d_-\rangle$ state is adiabatically connected to the singlet state $|s\rangle$ (denoted as d_m^S), whereas the excited- and the ground-state are connected to doubly occupied states (denoted as d_m^D). These states are differentiated by a singles-doubles separation pulse. Shelving the $|d_-\rangle$ states with singly occupations allows for the measurement of the remaining $|d_-\rangle$ state population N_S via OD2 compared to the sum of the population of excited- and ground-state N_D via OD1. The green arrows indicate radio-frequency transfers between the m_F states with the sign of the frequency detuning states above.

APPENDIX C

Additional spectra of near-resonantly driven double wells

This appendix provides additional two additional spectra of near-resonantly driven double wells as discussed in section 6.2. In figure C.1, we show the spectrum of a near-resonantly driven double well with large effective interactions $U \approx -18t \approx -8\,\mathrm{kHz}$. In figure C.2, we show the spectrum of a near-resonantly driven double well with small effective interactions $U \approx -6t \approx -8\,\mathrm{kHz}$.

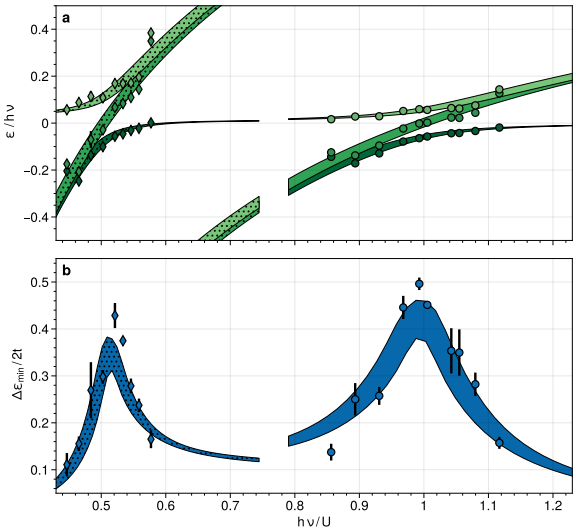

Figure C.1: **Quasi-energy spectrum for a near-resonantly driven double well with strong attractive interactions:** In an attractively interacting system $U \approx -18t \approx -8\,\mathrm{kHz}$ the energy eigenvalues $\epsilon_i/h\nu$ of the fitted Hamiltonians at the trap center are plotted for various driving frequencies $h\nu/U$ (a). The driving amplitude is chosen to suppress tunneling in half-filled double wells $K_0 = 2.4$. The first (second) harmonic resonance is indicated by circles (diamonds) and the shades of green differentiate the various eigenenergies. The shaded regions indicate the 1σ confidence interval of independent Monte-Carlo simulations of the system. (b) The minimal quasi energy difference of the spectrum $\Delta\epsilon_{\mathrm{min}}/2t$ is plotted for various driving frequencies $h\nu/U$ with the same color coding.

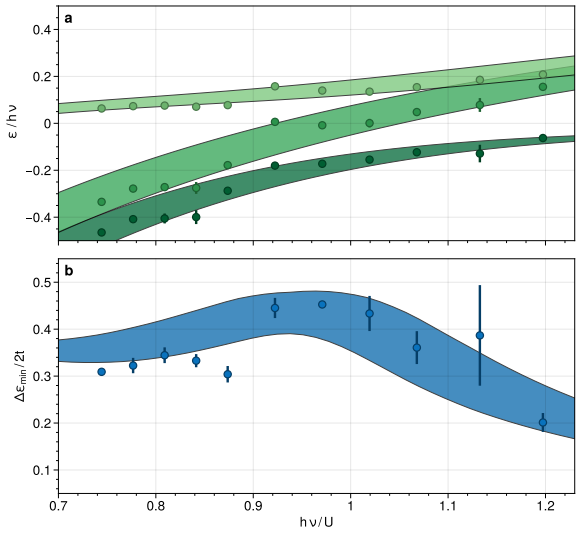

Figure C.2: **Quasi-energy spectrum for a near-resonantly driven double well with weak attractive interactions:** In an attractively interacting system $U \approx -6t \approx -2.8\,\mathrm{kHz}$ the energy eigenvalues $\epsilon_i/h\nu$ of the fitted Hamiltonians at the trap center are plotted for various driving frequencies $h\nu/U$ (a). The driving amplitude is chosen to suppress tunneling in half-filled double wells $K_0 = 2.4$. The first (second) harmonic resonance is indicated by circles (diamonds) and the shades of green differentiate the various eigenenergies. The shaded regions indicate the 1σ confidence interval of independent Monte-Carlo simulations of the system. (b) The minimal quasi energy difference of the spectrum $\Delta\epsilon_{\mathrm{min}}/2t$ is plotted for various driving frequencies $h\nu/U$ with the same color coding.

References

[1] J. G. Bednorz and K. A. Mueller,
Possible highT c superconductivity in the Ba-La-Cu-O system, en,
Zeitschrift fuer Physik B Condensed Matter **64** (1986) 189, ISSN: 0722-3277, 1434-6036,
URL: http://link.springer.com/10.1007/BF01303701 (visited on 18/04/2024).

[2] B. Keimer, S. A. Kivelson, M. R. Norman, S. Uchida and J. Zaanen,
From quantum matter to high-temperature superconductivity in copper oxides, en,
Nature **518** (2015) 179, ISSN: 0028-0836, 1476-4687,
URL: https://www.nature.com/articles/nature14165 (visited on 05/08/2024).

[3] J. Bardeen, L. N. Cooper and J. R. Schrieffer, *Theory of Superconductivity*, en,
Physical Review **108** (1957) 1175, ISSN: 0031-899X, URL:
https://link.aps.org/doi/10.1103/PhysRev.108.1175 (visited on 26/08/2024).

[4] D. A. Bonn, *Are high-temperature superconductors exotic?*, en, Nature Physics **2** (2006) 159,
ISSN: 1745-2473, 1745-2481,
URL: https://www.nature.com/articles/nphys248 (visited on 05/08/2024).

[5] J. Hubbard, *Electron correlations in narrow energy bands*, en, Proceedings of the Royal Society of London. Series A. Mathematical and Physical Sciences **276** (1963) 238,
ISSN: 0080-4630, 2053-9169,
URL: https://royalsocietypublishing.org/doi/10.1098/rspa.1963.0204
(visited on 27/08/2024).

[6] D. J. Scalapino, E. Loh and J. E. Hirsch,
d -wave pairing near a spin-density-wave instability, en, Physical Review B **34** (1986) 8190,
ISSN: 0163-1829, URL: https://link.aps.org/doi/10.1103/PhysRevB.34.8190
(visited on 18/04/2024).

[7] D. P. Arovas, E. Berg, S. A. Kivelson and S. Raghu, *The Hubbard Model*, en,
Annual Review of Condensed Matter Physics **13** (2022) 239, ISSN: 1947-5454, 1947-5462,
URL: https://www.annualreviews.org/doi/10.1146/annurev-conmatphys-031620-102024 (visited on 02/08/2024).

[8] M. Qin, T. Schäfer, S. Andergassen, P. Corboz and E. Gull,
The Hubbard Model: A Computational Perspective, en,
Annual Review of Condensed Matter Physics **13** (2022) 275, ISSN: 1947-5454, 1947-5462,
URL: https://www.annualreviews.org/doi/10.1146/annurev-conmatphys-090921-033948 (visited on 02/08/2024).

[9] R. P. Feynman, *Simulating physics with computers*, en,
International Journal of Theoretical Physics **21** (1982) 467, ISSN: 0020-7748, 1572-9575,
URL: http://link.springer.com/10.1007/BF02650179 (visited on 28/10/2020).

[10] S. Lloyd, *Universal Quantum Simulators*, en, Science **273** (1996) 1073,
ISSN: 0036-8075, 1095-9203,
URL: https://www.science.org/doi/10.1126/science.273.5278.1073 (visited on 02/08/2024).

[11] I. M. Georgescu, S. Ashhab and F. Nori, *Quantum simulation*, en, Reviews of Modern Physics **86** (2014) 153, ISSN: 0034-6861, 1539-0756, URL: https://link.aps.org/doi/10.1103/RevModPhys.86.153 (visited on 28/10/2020).

[12] I. Bloch, J. Dalibard and W. Zwerger, *Many-body physics with ultracold gases*, en, Reviews of Modern Physics **80** (2008) 885, ISSN: 0034-6861, 1539-0756, URL: https://link.aps.org/doi/10.1103/RevModPhys.80.885 (visited on 07/02/2020).

[13] L. Tarruell and L. Sanchez-Palencia, *Quantum simulation of the Hubbard model with ultracold fermions in optical lattices*, en, Comptes Rendus Physique **19** (2018) 365, ISSN: 16310705, URL: https://linkinghub.elsevier.com/retrieve/pii/S1631070518300926 (visited on 23/01/2024).

[14] A. Bohrdt, L. Homeier, C. Reinmoser, E. Demler and F. Grusdt, *Exploration of doped quantum magnets with ultracold atoms*, en, Annals of Physics **435** (2021) 168651, ISSN: 00034916, URL: https://linkinghub.elsevier.com/retrieve/pii/S0003491621002578 (visited on 18/04/2024).

[15] S. Chu, *Nobel Lecture: The manipulation of neutral particles*, en, Reviews of Modern Physics **70** (1998) 685, ISSN: 0034-6861, 1539-0756, URL: https://link.aps.org/doi/10.1103/RevModPhys.70.685 (visited on 01/08/2024).

[16] C. N. Cohen-Tannoudji, *Nobel Lecture: Manipulating atoms with photons*, en, Reviews of Modern Physics **70** (1998) 707, ISSN: 0034-6861, 1539-0756, URL: https://link.aps.org/doi/10.1103/RevModPhys.70.707 (visited on 01/08/2024).

[17] W. D. Phillips, *Nobel Lecture: Laser cooling and trapping of neutral atoms*, en, Reviews of Modern Physics **70** (1998) 721, ISSN: 0034-6861, 1539-0756, URL: https://link.aps.org/doi/10.1103/RevModPhys.70.721 (visited on 01/08/2024).

[18] W. Ketterle, *Nobel lecture: When atoms behave as waves: Bose-Einstein condensation and the atom laser*, en, Reviews of Modern Physics **74** (2002) 1131, ISSN: 0034-6861, 1539-0756, URL: https://link.aps.org/doi/10.1103/RevModPhys.74.1131 (visited on 01/08/2024).

[19] E. A. Cornell and C. E. Wieman, *Nobel Lecture: Bose-Einstein condensation in a dilute gas, the first 70 years and some recent experiments*, en, Reviews of Modern Physics **74** (2002) 875, ISSN: 0034-6861, 1539-0756, URL: https://link.aps.org/doi/10.1103/RevModPhys.74.875 (visited on 01/08/2024).

[20] B. DeMarco and D. S. Jin, *Onset of Fermi Degeneracy in a Trapped Atomic Gas*, en, Science **285** (1999) 1703, ISSN: 0036-8075, 1095-9203, URL: https://www.science.org/doi/10.1126/science.285.5434.1703 (visited on 01/08/2024).

[21] M. Köhl, H. Moritz, T. Stöferle, K. Günter and T. Esslinger, *Fermionic Atoms in a Three Dimensional Optical Lattice: Observing Fermi Surfaces, Dynamics, and Interactions*, en, Physical Review Letters **94** (2005) 080403, ISSN: 0031-9007, 1079-7114, URL: https://link.aps.org/doi/10.1103/PhysRevLett.94.080403 (visited on 15/10/2020).

[22] R. Jördens, N. Strohmaier, K. Günter, H. Moritz and T. Esslinger, *A Mott insulator of fermionic atoms in an optical lattice*, en, Nature **455** (2008) 204, ISSN: 0028-0836, 1476-4687, URL: https://www.nature.com/articles/nature07244 (visited on 10/04/2024).

[23] U. Schneider et al., *Metallic and Insulating Phases of Repulsively Interacting Fermions in a 3D Optical Lattice*, en, Science **322** (2008) 1520, ISSN: 0036-8075, 1095-9203, URL: https://www.science.org/doi/10.1126/science.1165449 (visited on 01/08/2024).

[24] D. Greif, T. Uehlinger, G. Jotzu, L. Tarruell and T. Esslinger, *Short-range quantum magnetism of ultracold fermions in an optical lattice*, Science **340** (2013) 1307, arXiv: 1212.2634, ISSN: 0036-8075, 1095-9203, URL: http://arxiv.org/abs/1212.2634 (visited on 28/07/2021).

[25] A. Mazurenko et al., *A cold-atom Fermi–Hubbard antiferromagnet*, en, Nature **545** (2017) 462, ISSN: 0028-0836, 1476-4687, URL: http://www.nature.com/articles/nature22362 (visited on 18/04/2022).

[26] H.-J. Shao et al., *Antiferromagnetic phase transition in a 3D fermionic Hubbard model*, en, Nature (2024), ISSN: 0028-0836, 1476-4687, URL: https://www.nature.com/articles/s41586-024-07689-2 (visited on 03/08/2024).

[27] C. Gross and I. Bloch, *Quantum simulations with ultracold atoms in optical lattices*, en, Science **357** (2017) 995, ISSN: 0036-8075, 1095-9203, URL: https://www.science.org/doi/10.1126/science.aal3837 (visited on 25/06/2024).

[28] C. S. Chiu et al., *String patterns in the doped Hubbard model*, en, Science **365** (2019) 251, ISSN: 0036-8075, 1095-9203, URL: https://www.science.org/doi/10.1126/science.aav3587 (visited on 03/08/2024).

[29] M. Qin et al., *Absence of Superconductivity in the Pure Two-Dimensional Hubbard Model*, en, Physical Review X **10** (2020) 031016, ISSN: 2160-3308, URL: https://link.aps.org/doi/10.1103/PhysRevX.10.031016 (visited on 04/08/2024).

[30] S. Jiang, D. J. Scalapino and S. R. White, *Density matrix renormalization group based downfolding of the three-band Hubbard model: Importance of density-assisted hopping*, en, Physical Review B **108** (2023) L161111, ISSN: 2469-9950, 2469-9969, URL: https://link.aps.org/doi/10.1103/PhysRevB.108.L161111 (visited on 07/03/2024).

[31] M. Gall, N. Wurz, J. Samland, C. F. Chan and M. Köhl, *Competing magnetic orders in a bilayer Hubbard model with ultracold atoms*, en, Nature **589** (2021) 40, ISSN: 0028-0836, 1476-4687, URL: http://www.nature.com/articles/s41586-020-03058-x (visited on 17/03/2022).

[32] S. Fölling et al., *Direct observation of second-order atom tunnelling*, Nature **448** (2007) 1029, ISSN: 1476-4687, URL: https://doi.org/10.1038/nature06112.

[33] S. Trotzky et al., *Time-Resolved Observation and Control of Superexchange Interactions with Ultracold Atoms in Optical Lattices*, en, Science **319** (2008) 295, ISSN: 0036-8075, 1095-9203, URL: https://www.science.org/doi/10.1126/science.1150841 (visited on 04/11/2022).

[34] M. Lohse, C. Schweizer, O. Zilberberg, M. Aidelsburger and I. Bloch,
A Thouless quantum pump with ultracold bosonic atoms in an optical superlattice, en,
Nature Physics **12** (2016) 350, ISSN: 1745-2481,
URL: https://www.nature.com/articles/nphys3584 (visited on 29/10/2019).

[35] S. Nakajima et al., *Topological Thouless pumping of ultracold fermions*, en,
Nature Physics **12** (2016) 296, ISSN: 1745-2481,
URL: https://www.nature.com/articles/nphys3622 (visited on 29/10/2019).

[36] B. Yang et al., *Cooling and entangling ultracold atoms in optical lattices*, en,
Science **369** (2020) 550, ISSN: 0036-8075, 1095-9203, URL:
https://www.science.org/doi/10.1126/science.aaz6801 (visited on 08/01/2024).

[37] A. Kantian, A. J. Daley and P. Zoller,
Eta Condensate of Fermionic Atom Pairs via Adiabatic State Preparation,
Physical Review Letters **104** (2010) 240406,
URL: https://link.aps.org/doi/10.1103/PhysRevLett.104.240406 (visited on 29/10/2019).

[38] C. N. Yang, *Eta pairing and off-diagonal long-range order in a Hubbard model*, en,
Physical Review Letters **63** (1989) 2144, ISSN: 0031-9007,
URL: https://link.aps.org/doi/10.1103/PhysRevLett.63.2144 (visited on 12/01/2024).

[39] M.-D. Li et al.,
High-powered optical superlattice with robust phase stability for quantum gas microscopy, en,
Optics Express **29** (2021) 13876, ISSN: 1094-4087,
URL: https://opg.optica.org/abstract.cfm?URI=oe-29-9-13876 (visited on 25/06/2024).

[40] T. Chalopin et al.,
Optical superlattice for engineering Hubbard couplings in quantum simulation,
Version Number: 1, 2024,
URL: https://arxiv.org/abs/2405.19322 (visited on 25/06/2024).

[41] C. Weitenberg and J. Simonet, *Tailoring quantum gases by Floquet engineering*,
Nature Physics **17** (2021) 1342, arXiv:2102.07009 [cond-mat, physics:quant-ph],
ISSN: 1745-2473, 1745-2481,
URL: http://arxiv.org/abs/2102.07009 (visited on 12/10/2023).

[42] F. Görg et al., *Enhancement and sign change of magnetic correlations in a driven quantum many-body system*, en, Nature **553** (2018) 481, ISSN: 0028-0836, 1476-4687,
URL: http://www.nature.com/articles/nature25135 (visited on 07/02/2023).

[43] C. Schweizer et al.,
Floquet approach to Z2 lattice gauge theories with ultracold atoms in optical lattices, en,
Nature Physics **15** (2019) 1168, ISSN: 1745-2473, 1745-2481, URL:
https://www.nature.com/articles/s41567-019-0649-7 (visited on 08/01/2024).

[44] F. Görg et al., *Realization of density-dependent Peierls phases to engineer quantized gauge fields coupled to ultracold matter*, en, Nature Physics **15** (2019) 1161, ISSN: 1745-2473, 1745-2481, URL: http://www.nature.com/articles/s41567-019-0615-4 (visited on 19/05/2023).

[45] D. H. Dunlap and V. M. Kenkre, *Dynamic localization of a charged particle moving under the influence of an electric field*, en, Physical Review B **34** (1986) 3625, ISSN: 0163-1829, URL: https://link.aps.org/doi/10.1103/PhysRevB.34.3625 (visited on 08/04/2024).

[46] A. Eckardt et al., *Exploring dynamic localization with a Bose-Einstein condensate*, en, Physical Review A **79** (2009) 013611, ISSN: 1050-2947, 1094-1622, URL: https://link.aps.org/doi/10.1103/PhysRevA.79.013611 (visited on 05/01/2024).

[47] K. A. Penson and M. Kolb, *Real-space pairing in fermion systems*, en, Physical Review B **33** (1986) 1663, ISSN: 0163-1829, URL: https://link.aps.org/doi/10.1103/PhysRevB.33.1663 (visited on 18/04/2024).

[48] S. Robaszkiewicz and B. R. Bułka, *Superconductivity in the Hubbard model with pair hopping*, en, Physical Review B **59** (1999) 6430, ISSN: 0163-1829, 1095-3795, URL: https://link.aps.org/doi/10.1103/PhysRevB.59.6430 (visited on 10/01/2024).

[49] G. I. Japaridze, A. P. Kampf, M. Sekania, P. Kakashvili and P. Brune, *Eta-pairing superconductivity in the Hubbard chain with pair hopping*, en, Physical Review B **65** (2001) 014518, ISSN: 0163-1829, 1095-3795, URL: https://link.aps.org/doi/10.1103/PhysRevB.65.014518 (visited on 10/01/2024).

[50] I. C. Brock, *Users Guide to Writing a Thesis in a Physics/Astronomy Institute of the University of Bonn*, URL: http://pi.physik.uni-bonn.de/pi_only/thesis.php.

[51] N. Klemmer et al., *Floquet-driven crossover from density-assisted tunneling to enhanced pair tunneling*, Version Number: 1, 2024, URL: https://arxiv.org/abs/2404.08482 (visited on 15/08/2024).

[52] T. Esslinger, *Fermi-Hubbard Physics with Atoms in an Optical Lattice*, en, Annual Review of Condensed Matter Physics **1** (2010) 129, ISSN: 1947-5454, 1947-5462, URL: https://www.annualreviews.org/doi/10.1146/annurev-conmatphys-070909-104059 (visited on 23/01/2024).

[53] C. Chin, R. Grimm, P. Julienne and E. Tiesinga, *Feshbach resonances in ultracold gases*, en, Reviews of Modern Physics **82** (2010) 1225, ISSN: 0034-6861, 1539-0756, URL: https://link.aps.org/doi/10.1103/RevModPhys.82.1225 (visited on 21/10/2020).

[54] O. Dutta et al., *Non-standard Hubbard models in optical lattices: a review*, Reports on Progress in Physics **78** (2015) 066001, ISSN: 0034-4885, 1361-6633, URL: https://iopscience.iop.org/article/10.1088/0034-4885/78/6/066001 (visited on 02/08/2024).

[55] N. Goldman, J. C. Budich and P. Zoller,
Topological Quantum Matter with Ultracold Gases in Optical Lattices,
(2016), Publisher: arXiv Version Number: 1,
URL: https://arxiv.org/abs/1607.03902 (visited on 13/08/2024).

[56] A. Hayward, C. Schweizer, M. Lohse, M. Aidelsburger and F. Heidrich-Meisner,
Topological charge pumping in the interacting bosonic Rice-Mele model, en,
Physical Review B **98** (2018) 245148, ISSN: 2469-9950, 2469-9969, URL:
https://link.aps.org/doi/10.1103/PhysRevB.98.245148 (visited on 12/08/2024).

[57] M. Aidelsburger et al.,
Realization of the Hofstadter Hamiltonian with Ultracold Atoms in Optical Lattices, en,
Physical Review Letters **111** (2013) 185301, ISSN: 0031-9007, 1079-7114,
URL: https://link.aps.org/doi/10.1103/PhysRevLett.111.185301 (visited on
12/04/2024).

[58] F. Görg, *Exploring and Floquet-Engineering the Driven Fermi-Hubbard Model with
Ultracold Atoms*, en, Artwork Size: 295 p. Medium: application/pdf Pages: 295 p.,
PhD thesis: ETH Zurich, 2019,
URL: http://hdl.handle.net/20.500.11850/361822 (visited on 05/06/2023).

[59] C. J. Foot, *Atomic Physics*, Oxford University Press, 2005.

[60] M. Köhl, "Atomic, Molecular, and Optical Physics".

[61] L. L. B. Davis, *ProPlot*, Language: en, 2021,
URL: https://zenodo.org/record/3873878 (visited on 16/04/2024).

[62] N. W. Ashcroft and N. D. Mermin, *Solid State Physics*, 1976.

[63] N. Klemmer, *Ultracold Fermions in an Optical Superlattice*,
MA thesis: Rheinische Freidrich-Willhelms-Universität, 2020.

[64] F. Görg, *Ultracold Fermionic Atoms in Optical Superlattices*, PhD thesis: TU München, 2014.

[65] G. H. Wannier, *The Structure of Electronic Excitation Levels in Insulating Crystals*, en,
Physical Review **52** (1937) 191, ISSN: 0031-899X,
URL: https://link.aps.org/doi/10.1103/PhysRev.52.191 (visited on 25/07/2024).

[66] N. Marzari, A. A. Mostofi, J. R. Yates, I. Souza and D. Vanderbilt,
Maximally localized Wannier functions: Theory and applications, en,
Reviews of Modern Physics **84** (2012) 1419, ISSN: 0034-6861, 1539-0756, URL:
https://link.aps.org/doi/10.1103/RevModPhys.84.1419 (visited on 02/11/2021).

[67] S. Kivelson, *Wannier functions in one-dimensional disordered systems: Application to
fractionally charged solitons*, en, Physical Review B **26** (1982) 4269, ISSN: 0163-1829, URL:
https://link.aps.org/doi/10.1103/PhysRevB.26.4269 (visited on 27/02/2020).

[68] N. Marzari and D. Vanderbilt,
Maximally localized generalized Wannier functions for composite energy bands, en,
Physical Review B **56** (1997) 12847, ISSN: 0163-1829, 1095-3795, URL:
https://link.aps.org/doi/10.1103/PhysRevB.56.12847 (visited on 04/03/2020).

[69] U. Bissbort, *Dynamical Effects and Disorder in Ultracold Bosonic Matter*,
PhD thesis: Johann Wolfgang Goethe-Universit Frankfurt, 2012.

[70] J. Dalibard, *From van der Waals universality to Fano–Feshbach resonances*, Lecture Series, Collège de France, 2021.

[71] T. Loftus, C. A. Regal, C. Ticknor, J. L. Bohn and D. S. Jin, *Resonant Control of Elastic Collisions in an Optically Trapped Fermi Gas of Atoms*, en, Physical Review Letters **88** (2002) 173201, ISSN: 0031-9007, 1079-7114, URL: https://link.aps.org/doi/10.1103/PhysRevLett.88.173201 (visited on 31/07/2024).

[72] E. Cocchi, *Analogue Quantum Simulation of the Two-Dimensional Hubbard Model with Ultracold Fermions*, PhD thesis: University of Cambridge, 2016.

[73] T. Tiecke, *Feshbach resonances in ultracold mixtures of the fermionic quantum gases 6Li and 40K*, PhD thesis: Universiteit van Amsterdam, 2009.

[74] A. Ludewig, *Feshbach resonances in 40K*, PhD thesis: Universiteit van Amsterdam, 2012, URL: https://staff.fnwi.uva.nl/j.t.m.walraven/walraven/theses_files/AntjeLudewig2012.pdf.

[75] O. Jürgensen, F. Meinert, M. J. Mark, H.-C. Nägerl and D.-S. Lühmann, *Observation of Density-Induced Tunneling*, en, Physical Review Letters **113** (2014) 193003, ISSN: 0031-9007, 1079-7114, URL: https://link.aps.org/doi/10.1103/PhysRevLett.113.193003 (visited on 15/08/2023).

[76] F. Meinert, M. J. Mark, K. Lauber, A. J. Daley and H.-C. Nägerl, *Floquet Engineering of Correlated Tunneling in the Bose-Hubbard Model with Ultracold Atoms*, en, Physical Review Letters **116** (2016) 205301, ISSN: 0031-9007, 1079-7114, URL: https://link.aps.org/doi/10.1103/PhysRevLett.116.205301 (visited on 05/01/2024).

[77] R. Desbuquois et al., *Controlling the Floquet state population and observing micromotion in a periodically driven two-body quantum system*, (2017), Publisher: arXiv Version Number: 2, URL: https://arxiv.org/abs/1703.07767 (visited on 07/02/2023).

[78] T. Busch, B.-G. Englert, K. Rzażewski and M. Wilkens, *Two Cold Atoms in a Harmonic Trap*, Foundations of Physics **28** (1998) 549, ISSN: 00159018, URL: http://link.springer.com/10.1023/A:1018705520999 (visited on 28/10/2021).

[79] Z. Idziaszek and T. Calarco, *Analytical solutions for the dynamics of two trapped interacting ultracold atoms*, en, Physical Review A **74** (2006) 022712, ISSN: 1050-2947, 1094-1622, URL: https://link.aps.org/doi/10.1103/PhysRevA.74.022712 (visited on 02/02/2021).

[80] L. A. Miller, *Ultracold Fermions in Two-Dimensional Optical Lattices: Quantum Simulation of the Hubbard Model*, PhD thesis: University of Cambridge, 2016.

[81] Y. Chen, D.-W. Xiao, R. Zhang and P. Zhang, *Analytical solution for the spectrum of two ultracold atoms in a completely anisotropic confinement*, en, Physical Review A **101** (2020) 053624, ISSN: 2469-9926, 2469-9934, URL: https://link.aps.org/doi/10.1103/PhysRevA.101.053624 (visited on 04/10/2021).

[82] M. Köhl, *Thermometry of fermionic atoms in an optical lattice*, en, Physical Review A **73** (2006) 031601, ISSN: 1050-2947, 1094-1622, URL: https://link.aps.org/doi/10.1103/PhysRevA.73.031601 (visited on 13/08/2024).

[83] P.-I. Schneider, S. Grishkevich and A. Saenz, *Ab-initio determination of Bose-Hubbard parameters for two ultracold atoms in an optical lattice using a three-well potential*, Physical Review A **80** (2009) 013404, arXiv: 0903.3185, ISSN: 1050-2947, 1094-1622, URL: http://arxiv.org/abs/0903.3185 (visited on 08/02/2021).

[84] M. Feld, *Low temperature phases of interacting fermions in two dimensions*, PhD thesis: University of Cambridge, 2011.

[85] B. Fröhlich, *A Strongly Interacting Two-Dimensional Fermi Gas*, PhD thesis: University of Cambridge, 2011.

[86] E. Vogt, *Collective Modes and Polarons in two-dimensional Fermi Gases*, PhD thesis: University of Cambridge, 2013.

[87] C. F. Chan, *Quantum simulation of strongly-correlated two-dimensional fermions in optical lattices*, PhD thesis: Rheinische Freidrich-Willhelms-Universität, 2019.

[88] M. Gall, *Quantum Simulation of the Bilayer Hubbard Model Using Ultracold Atoms*, PhD thesis: Rheinische Freidrich-Willhelms-Universität, 2020.

[89] J. H. Drewes, *Thermodynamics and correlations of ultracold fermions in a two-dimensional optical lattice*, PhD thesis, 2020.

[90] N. Wurz, *Quantum magnetism in the 2D Hubbard model and beyond*, PhD thesis: Rheinische Freidrich-Willhelms-Universität, 2021.

[91] T. Tiecke, *Properties of Potassium*, Appendix of PhD Thesis, 2019.

[92] M. Feld, *Laser system for the creation of an ultracold gas of fermionic atoms*, PhD First Year Report, 2008.

[93] W. Ketterle, K. B. Davis, M. A. Joffe, A. Martin and D. E. Pritchard, *High densities of cold atoms in a dark spontaneous-force optical trap*, en, Physical Review Letters **70** (1993) 2253, ISSN: 0031-9007, URL: https://link.aps.org/doi/10.1103/PhysRevLett.70.2253 (visited on 05/07/2024).

[94] W. Ketterle and M. W. Zwierlein, *Making, probing and understanding ultracold Fermi gases*, (2008), Publisher: arXiv Version Number: 1, URL: https://arxiv.org/abs/0801.2500 (visited on 08/07/2024).

[95] N. Wurz et al., *Coherent manipulation of spin correlations in the Hubbard model*, en, Physical Review A **97** (2018) 051602, ISSN: 2469-9926, 2469-9934, URL: https://link.aps.org/doi/10.1103/PhysRevA.97.051602 (visited on 21/10/2020).

[96] E. Cocchi et al., *Equation of State of the Two-Dimensional Hubbard Model*, en, Physical Review Letters **116** (2016) 175301, ISSN: 0031-9007, 1079-7114, URL: https://link.aps.org/doi/10.1103/PhysRevLett.116.175301 (visited on 11/02/2021).

[97] T. Paiva, R. Scalettar, M. Randeria and N. Trivedi, *Fermions in 2D Optical Lattices: Temperature and Entropy Scales for Observing Antiferromagnetism and Superfluidity*, en, Physical Review Letters **104** (2010) 066406, ISSN: 0031-9007, 1079-7114, URL: https://link.aps.org/doi/10.1103/PhysRevLett.104.066406 (visited on 11/07/2024).

[98] J. H. Drewes et al., *Antiferromagnetic Correlations in Two-Dimensional Fermionic Mott-Insulating and Metallic Phases*, en, Physical Review Letters **118** (2017) 170401, ISSN: 0031-9007, 1079-7114, URL: http://link.aps.org/doi/10.1103/PhysRevLett.118.170401 (visited on 11/07/2024).

[99] J. Fleper, *Long-range disorder in the non-interacting one-dimensional Fermi-Hubbard model*, MA thesis: Rheinische Freidrich-Willhelms-Universität, 2020.

[100] I. Coherent, ed., *Mephisto MOPA datasheet*, URL: https://www.coherent.com/assets/pdf/Mephisto-MOPA-Data-Sheet.pdf (visited on 12/10/2020).

[101] I. Coherent, ed., *Verdi Family datasheet*, URL: https://www.coherent.com/assets/pdf/Verdi-Family-Data-Sheet.pdf (visited on 12/10/2020).

[102] N. Klemmer, *Cavity design for high-power frequency doubling*, Bachelor thesis: Rheinische Freidrich-Willhelms-Universität, 2018.

[103] L. Lasercomponents, ed., *Lithium Triborate datasheet*, URL: https://www.lasercomponents.com/de/?embedded=1&file=fileadmin/user_upload/home/Datasheets/diverse-laser-optics/laser-rods-crystals/lbo.pdf&no_cache=1 (visited on 12/10/2020).

[104] T. Hansch and B. Couillaud, *Laser frequency stabilization by polarization spectroscopy of a reflecting reference cavity*, en, Optics Communications **35** (1980) 441, ISSN: 00304018, URL: https://linkinghub.elsevier.com/retrieve/pii/0030401880900693 (visited on 12/10/2020).

[105] L. Ricci et al., *A compact grating-stabilized diode laser system for atomic physics*, en, Optics Communications **117** (1995) 541, ISSN: 0030-4018, URL: http://www.sciencedirect.com/science/article/pii/003040189500146Y (visited on 29/10/2019).

[106] I. Analog Devices, ed., *AD9914 datasheet*, URL: https://www.analog.com/media/en/technical-documentation/data-sheets/AD9914.pdf (visited on 12/10/2020).

[107] M. Gilowski et al., *Narrow bandwidth interference filter-stabilized diode laser systems for the manipulation of neutral atoms*, en, Optics Communications **280** (2007) 443, ISSN: 00304018, URL: https://linkinghub.elsevier.com/retrieve/pii/S0030401807008577 (visited on 21/07/2024).

[108] P. E. Ciddor, *Refractive index of air: new equations for the visible and near infrared*, en, Applied Optics **35** (1996) 1566, ISSN: 0003-6935, 1539-4522, URL: https://opg.optica.org/abstract.cfm?URI=ao-35-9-1566 (visited on 17/07/2024).

[109] J. A. Stone and J. H. Zimmermann, *NIST online refractive index calculator*, 2001, URL: https://emtoolbox.nist.gov/Wavelength/Documentation.asp.

[110] J. Fleper, *Ultracold fermions in optical superlattices (preliminary title)*, PhD thesis: Rheinische Freidrich-Willhelms-Universität, to be submitted.

[111] V. Jonas, *Acousto-Optic Sculpturing of Optical Potential Landscapes for Ultracold Fermions*, MA thesis: Rheinische Freidrich-Willhelms-Universität, 2021.

[112] V. Jonas, *Ultracold fermions in optical superlattices (preliminary title)*, PhD thesis: Rheinische Freidrich-Willhelms-Universität, to be submitted.

[113] M. Garwood and L. DelaBarre, *The Return of the Frequency Sweep: Designing Adiabatic Pulses for Contemporary NMR*, en, Journal of Magnetic Resonance **153** (2001) 155, ISSN: 10907807, URL: https://linkinghub.elsevier.com/retrieve/pii/S1090780701923407 (visited on 22/07/2024).

[114] G. Reinaudi, T. Lahaye, Z. Wang and D. Guéry-Odelin, *Strong saturation absorption imaging of dense clouds of ultracold atoms*, en, Optics Letters **32** (2007) 3143, ISSN: 0146-9592, 1539-4794, URL: https://opg.optica.org/abstract.cfm?URI=ol-32-21-3143 (visited on 28/06/2024).

[115] T. Rom et al., *Free fermion antibunching in a degenerate atomic Fermi gas released from an optical lattice*, en, Nature **444** (2006) 733, ISSN: 0028-0836, 1476-4687, URL: https://www.nature.com/articles/nature05319 (visited on 03/07/2024).

[116] C.-L. Hung et al., *Extracting density–density correlations from in situ images of atomic quantum gases*, New Journal of Physics **13** (2011) 075019, ISSN: 1367-2630, URL: https://iopscience.iop.org/article/10.1088/1367-2630/13/7/075019 (visited on 03/07/2024).

[117] J. Sebby-Strabley et al., *Preparing and Probing Atomic Number States with an Atom Interferometer*, en, Physical Review Letters **98** (2007) 200405, ISSN: 0031-9007, 1079-7114, URL: https://link.aps.org/doi/10.1103/PhysRevLett.98.200405 (visited on 27/06/2024).

[118] D. Pertot et al., *Relaxation dynamics of a Fermi gas in an optical superlattice*, Physical Review Letters **113** (2014) 170403, arXiv: 1407.6037, ISSN: 0031-9007, 1079-7114, URL: http://arxiv.org/abs/1407.6037 (visited on 30/10/2019).

[119] S. S. Natu, D. C. McKay, B. DeMarco and E. J. Mueller, *Evolution of condensate fraction during rapid lattice ramps*, en, Physical Review A **85** (2012) 061601, ISSN: 1050-2947, 1094-1622, URL: https://link.aps.org/doi/10.1103/PhysRevA.85.061601 (visited on 10/04/2024).

[120] M. Atala et al., *Direct Measurement of the Zak phase in Topological Bloch Bands*, Nature Physics **9** (2013) 795, arXiv: 1212.0572, ISSN: 1745-2473, 1745-2481, URL: http://arxiv.org/abs/1212.0572 (visited on 16/01/2020).

[121] T. Hartke, B. Oreg, N. Jia and M. Zwierlein, *Quantum register of fermion pairs*, en, Nature **601** (2022) 537, ISSN: 0028-0836, 1476-4687, URL: https://www.nature.com/articles/s41586-021-04205-8 (visited on 18/04/2022).

[122] S. Murmann et al., *Two Fermions in a Double Well: Exploring a Fundamental Building Block of the Hubbard Model*, en, Physical Review Letters **114** (2015) 080402, ISSN: 0031-9007, 1079-7114, URL: https://link.aps.org/doi/10.1103/PhysRevLett.114.080402 (visited on 06/03/2023).

[123] A. Bergschneider, *Strong correlations in few-fermion systems*, PhD thesis, 2017.

[124] Y. Shin et al., *Atom Interferometry with Bose-Einstein Condensates in a Double-Well Potential*, en, Physical Review Letters **92** (2004) 050405, ISSN: 0031-9007, 1079-7114, URL: https://link.aps.org/doi/10.1103/PhysRevLett.92.050405 (visited on 11/05/2024).

[125] M. Anderlini et al., *Controlled exchange interaction between pairs of neutral atoms in an optical lattice*, en, Nature **448** (2007) 452, ISSN: 0028-0836, 1476-4687, URL: https://www.nature.com/articles/nature06011 (visited on 07/05/2024).

[126] C. J. Foot and M. D. Shotter, *Double well potentials and quantum gates*, en, American Journal of Physics **79** (2011) 762, ISSN: 0002-9505, 1943-2909, URL: http://aapt.scitation.org/doi/10.1119/1.3583478 (visited on 25/10/2022).

[127] C. N. Yang, *Concept of Off-Diagonal Long-Range Order and the Quantum Phases of Liquid He and of Superconductors*, en, Reviews of Modern Physics **34** (1962) 694, ISSN: 0034-6861, URL: https://link.aps.org/doi/10.1103/RevModPhys.34.694 (visited on 11/05/2024).

[128] H. Kramers, *L'interaction Entre les Atomes Magnétogènes dans un Cristal Paramagnétique*, fr, Physica **1** (1934) 182, ISSN: 00318914, URL: https://linkinghub.elsevier.com/retrieve/pii/S0031891434900239 (visited on 08/05/2024).

[129] P. W. Anderson, *Antiferromagnetism. Theory of Superexchange Interaction*, en, Physical Review **79** (1950) 350, ISSN: 0031-899X, URL: https://link.aps.org/doi/10.1103/PhysRev.79.350 (visited on 08/05/2024).

[130] S. Trotzky, Y.-A. Chen, U. Schnorrberger, P. Cheinet and I. Bloch, *Controlling and Detecting Spin Correlations of Ultracold Atoms in Optical Lattices*, en, Physical Review Letters **105** (2010) 265303, ISSN: 0031-9007, 1079-7114, URL: https://link.aps.org/doi/10.1103/PhysRevLett.105.265303 (visited on 18/08/2022).

[131] D. Greif, *Quantum Magnetism with Ultracold Fermions in an Optical Lattice*, PhD thesis, 2013.

[132] K. Winkler et al., *Repulsively bound atom pairs in an optical lattice*, en, Nature **441** (2006) 853, ISSN: 0028-0836, 1476-4687, URL: https://www.nature.com/articles/nature04918 (visited on 04/04/2024).

[133] N. Goldman, J. Dalibard, M. Aidelsburger and N. R. Cooper, *Periodically driven quantum matter: The case of resonant modulations*, en, Physical Review A **91** (2015) 033632, ISSN: 1050-2947, 1094-1622, URL: https://link.aps.org/doi/10.1103/PhysRevA.91.033632 (visited on 04/04/2024).

[134] M. Bukov, L. D'Alessio and A. Polkovnikov, *Universal high-frequency behavior of periodically driven systems: from dynamical stabilization to Floquet engineering*, en, Advances in Physics **64** (2015) 139, ISSN: 0001-8732, 1460-6976, URL: http://www.tandfonline.com/doi/full/10.1080/00018732.2015.1055918 (visited on 08/01/2024).

[135] M. C. Rechtsman et al., *Photonic Floquet topological insulators*, en, Nature **496** (2013) 196, ISSN: 0028-0836, 1476-4687, URL: https://www.nature.com/articles/nature12066 (visited on 11/04/2024).

[136] Z. Fedorova, H. Qiu, S. Linden and J. Kroha, *Observation of topological transport quantization by dissipation in fast Thouless pumps*, en, Nature Communications **11** (2020) 3758, ISSN: 2041-1723, URL: https://www.nature.com/articles/s41467-020-17510-z (visited on 12/04/2024).

[137] T. Ozawa et al., *Topological photonics*, en, Reviews of Modern Physics **91** (2019) 015006, ISSN: 0034-6861, 1539-0756, URL: https://link.aps.org/doi/10.1103/RevModPhys.91.015006 (visited on 12/04/2024).

[138] D. Fausti et al., *Light-Induced Superconductivity in a Stripe-Ordered Cuprate*, en, Science **331** (2011) 189, ISSN: 0036-8075, 1095-9203, URL: https://www.science.org/doi/10.1126/science.1197294 (visited on 17/01/2024).

[139] A. Kirilyuk, A. V. Kimel and T. Rasing, *Ultrafast optical manipulation of magnetic order*, en, Reviews of Modern Physics **82** (2010) 2731, ISSN: 0034-6861, 1539-0756, URL: https://link.aps.org/doi/10.1103/RevModPhys.82.2731 (visited on 11/04/2024).

[140] A. Eckardt, *Colloquium: Atomic quantum gases in periodically driven optical lattices*, en, Reviews of Modern Physics **89** (2017) 011004, ISSN: 0034-6861, 1539-0756, URL: http://link.aps.org/doi/10.1103/RevModPhys.89.011004 (visited on 08/01/2024).

[141] H. Lignier et al., *Dynamical Control of Matter-Wave Tunneling in Periodic Potentials*, en, Physical Review Letters **99** (2007) 220403, ISSN: 0031-9007, 1079-7114, URL: https://link.aps.org/doi/10.1103/PhysRevLett.99.220403 (visited on 08/04/2024).

[142] G. Jotzu et al., *Creating State-Dependent Lattices for Ultracold Fermions by Magnetic Gradient Modulation*, en, Physical Review Letters **115** (2015) 073002, ISSN: 0031-9007, 1079-7114, URL: https://link.aps.org/doi/10.1103/PhysRevLett.115.073002 (visited on 12/04/2024).

[143] K. Wintersperger et al., *Realization of an anomalous Floquet topological system with ultracold atoms*, (2020), Publisher: arXiv Version Number: 2, URL: https://arxiv.org/abs/2002.09840 (visited on 08/01/2024).

[144] A. Dutta, E. Sen, J.-H. Zheng, M. Aidelsburger and W. Hofstetter, *The anomalous Floquet Anderson insulator in a continuously driven optical lattice*, (2023), Publisher: [object Object] Version Number: 1, URL: https://arxiv.org/abs/2312.13589 (visited on 13/04/2024).

[145] M. Grifoni and P. Hänggi, *Driven quantum tunneling*, en, Physics Reports **304** (1998) 229, ISSN: 03701573, URL: https://linkinghub.elsevier.com/retrieve/pii/S0370157398000222 (visited on 08/01/2024).

[146] E. Kierig, U. Schnorrberger, A. Schietinger, J. Tomkovic and M. K. Oberthaler, *Single-Particle Tunneling in Strongly Driven Double-Well Potentials*, en, Physical Review Letters **100** (2008) 190405, ISSN: 0031-9007, 1079-7114, URL: https://link.aps.org/doi/10.1103/PhysRevLett.100.190405 (visited on 05/01/2024).

[147] Y.-A. Chen et al., *Controlling Correlated Tunneling and Superexchange Interactions with ac-Driven Optical Lattices*, en, Physical Review Letters **107** (2011) 210405, ISSN: 0031-9007, 1079-7114, URL: https://link.aps.org/doi/10.1103/PhysRevLett.107.210405 (visited on 16/01/2024).

[148] S. Rahav, I. Gilary and S. Fishman, *Effective Hamiltonians for periodically driven systems*, en, Physical Review A **68** (2003) 013820, ISSN: 1050-2947, 1094-1622, URL: https://link.aps.org/doi/10.1103/PhysRevA.68.013820 (visited on 04/04/2024).

[149] T. Mikami et al., *Brillouin-Wigner theory for high-frequency expansion in periodically driven systems: Application to Floquet topological insulators*, en, Physical Review B **93** (2016) 144307, ISSN: 2469-9950, 2469-9969, URL: https://link.aps.org/doi/10.1103/PhysRevB.93.144307 (visited on 04/01/2024).

[150] N. Strohmaier et al., *Observation of Elastic Doublon Decay in the Fermi-Hubbard Model*, en, Physical Review Letters **104** (2010) 080401, ISSN: 0031-9007, 1079-7114, URL: https://link.aps.org/doi/10.1103/PhysRevLett.104.080401 (visited on 10/04/2024).

[151] M. Bukov, M. Kolodrubetz and A. Polkovnikov, *Schrieffer-Wolff Transformation for Periodically Driven Systems: Strongly Correlated Systems with Artificial Gauge Fields*, en, Physical Review Letters **116** (2016) 125301, ISSN: 0031-9007, 1079-7114, URL: https://link.aps.org/doi/10.1103/PhysRevLett.116.125301 (visited on 12/10/2023).

[152] M. Messer et al., *Floquet Dynamics in Driven Fermi-Hubbard Systems*, en, Physical Review Letters **121** (2018) 233603, ISSN: 0031-9007, 1079-7114, URL: https://link.aps.org/doi/10.1103/PhysRevLett.121.233603 (visited on 28/06/2023).

[153] D. Greif et al., *Site-resolved imaging of a fermionic Mott insulator*, Science **351** (2016) 953, _eprint: https://www.science.org/doi/pdf/10.1126/science.aad9041, URL: https://www.science.org/doi/abs/10.1126/science.aad9041.

[154] L. W. Cheuk et al., *Observation of 2D Fermionic Mott Insulators of K 40 with Single-Site Resolution*, en, Physical Review Letters **116** (2016) 235301, ISSN: 0031-9007, 1079-7114, URL: https://link.aps.org/doi/10.1103/PhysRevLett.116.235301 (visited on 18/04/2024).

[155] M. Boll et al., *Spin- and density-resolved microscopy of antiferromagnetic correlations in Fermi-Hubbard chains*, en, Science **353** (2016) 1257, ISSN: 0036-8075, 1095-9203, URL: https://www.science.org/doi/10.1126/science.aag1635 (visited on 18/04/2024).

[156] J.-S. Bernier et al., *Cooling fermionic atoms in optical lattices by shaping the confinement*, en, Physical Review A **79** (2009) 061601, ISSN: 1050-2947, 1094-1622, URL: https://link.aps.org/doi/10.1103/PhysRevA.79.061601 (visited on 18/04/2024).

[157] C. S. Chiu, G. Ji, A. Mazurenko, D. Greif and M. Greiner, *Quantum State Engineering of a Hubbard System with Ultracold Fermions*, en, Physical Review Letters **120** (2018) 243201, ISSN: 0031-9007, 1079-7114, URL: https://link.aps.org/doi/10.1103/PhysRevLett.120.243201 (visited on 18/04/2024).

[158] A. Kantian, S. Langer and A. J. Daley, *Dynamical Disentangling and Cooling of Atoms in Bilayer Optical Lattices*, en, Physical Review Letters **120** (2018) 060401, ISSN: 0031-9007, 1079-7114, URL: https://link.aps.org/doi/10.1103/PhysRevLett.120.060401 (visited on 18/04/2024).

[159] R. T. Scalettar, J. W. Cannon, D. J. Scalapino and R. L. Sugar, *Magnetic and pairing correlations in coupled Hubbard planes*, en, Physical Review B **50** (1994) 13419, ISSN: 0163-1829, 1095-3795, URL: https://link.aps.org/doi/10.1103/PhysRevB.50.13419 (visited on 30/07/2021).

[160] C. V. Kraus, M. Dalmonte, M. A. Baranov, A. M. Läuchli and P. Zoller, *Majorana Edge States in Atomic Wires Coupled by Pair Hopping*, en, Physical Review Letters **111** (2013) 173004, ISSN: 0031-9007, 1079-7114, URL: https://link.aps.org/doi/10.1103/PhysRevLett.111.173004 (visited on 16/01/2024).

[161] N. Lang and H. P. Büchler,
Topological states in a microscopic model of interacting fermions, en,
Physical Review B **92** (2015) 041118, ISSN: 1098-0121, 1550-235X, URL:
https://link.aps.org/doi/10.1103/PhysRevB.92.041118 (visited on 08/01/2024).

[162] I. Dimitrova et al., *Enhanced Superexchange in a Tilted Mott Insulator*, en,
Physical Review Letters **124** (2020) 043204, ISSN: 0031-9007, 1079-7114,
URL: https://link.aps.org/doi/10.1103/PhysRevLett.124.043204 (visited on
04/11/2022).

[163] F. T. Lisandrini and C. Kollath,
Majorana edge modes in a spinful-particle conserving model, en,
Physical Review B **106** (2022) 245121, ISSN: 2469-9950, 2469-9969,
URL: https://link.aps.org/doi/10.1103/PhysRevB.106.245121 (visited on
18/04/2024).

[164] J. R. Coulthard, S. R. Clark, S. Al-Assam, A. Cavalleri and D. Jaksch,
Enhancement of superexchange pairing in the periodically driven Hubbard model, en,
Physical Review B **96** (2017) 085104, ISSN: 2469-9950, 2469-9969, URL:
http://link.aps.org/doi/10.1103/PhysRevB.96.085104 (visited on 06/07/2023).

[165] E. Majorana, *Teoria simmetrica dell'elettrone e del positrone*, it,
Il Nuovo Cimento **14** (1937) 171, ISSN: 0029-6341, 1827-6121,
URL: http://link.springer.com/10.1007/BF02961314 (visited on 23/04/2024).

[166] F. Wilczek, *Majorana returns*, en, Nature Physics **5** (2009) 614, ISSN: 1745-2473, 1745-2481,
URL: https://www.nature.com/articles/nphys1380 (visited on 08/01/2024).

[167] J. Alicea, *New directions in the pursuit of Majorana fermions in solid state systems*,
Reports on Progress in Physics **75** (2012) 076501, ISSN: 0034-4885, 1361-6633,
URL: https://iopscience.iop.org/article/10.1088/0034-4885/75/7/076501
(visited on 10/01/2024).

[168] H. Fan and S. Lloyd, *Entanglement and off-diagonal long-range order of an eta-pairing state*,
Journal of Physics A: Mathematical and General **38** (2005) 5285,
ISSN: 0305-4470, 1361-6447,
URL: https://iopscience.iop.org/article/10.1088/0305-4470/38/23/014
(visited on 17/05/2024).

[169] T. Stöferle, H. Moritz, K. Günter, M. Köhl and T. Esslinger,
Molecules of Fermionic Atoms in an Optical Lattice, en,
Physical Review Letters **96** (2006) 030401, ISSN: 0031-9007, 1079-7114,
URL: https://link.aps.org/doi/10.1103/PhysRevLett.96.030401 (visited on
26/06/2024).

[170] Y. Kiefer, M. Hachmann and A. Hemmerich,
Ultracold Feshbach molecules in an orbital optical lattice, en, Nature Physics **19** (2023) 794,
ISSN: 1745-2473, 1745-2481, URL:
https://www.nature.com/articles/s41567-023-01994-9 (visited on 26/06/2024).

[171] J. Reuter, *Akusto-optische Formung eines Lichtstrahls zur Kompensierung der Inhomogenität eines optischen Gitters*,
Bachelor thesis: Rheinische Freidrich-Willhelms-Universität, to be submitted.

List of Figures

List of Tables